
TESI DI DOTTORATO

MASSIMO FRITTELLI

Numerical methods for partial differential equations on stationary and evolving surfaces

Dottorato in Matematica ed Informatica, Salento (2018).

<http://www.bdim.eu/item?id=tesi_2018_FrittelliMassimo_1>

L'utilizzo e la stampa di questo documento digitale è consentito liberamente per motivi di ricerca e studio. Non è consentito l'utilizzo dello stesso per motivi commerciali. Tutte le copie di questo documento devono riportare questo avvertimento.



UNIVERSITÀ DEL SALENTO

DIPARTIMENTO DI MATEMATICA E FISICA "E. DE GIORGI"

Doctoral Thesis in Mathematics and Computer Science

**Numerical Methods
for Partial Differential Equations
on Stationary and Evolving Surfaces**

Tutor:

Chiar.ma Prof.ssa
Ivonne SGURA

Dottorando:

Massimo FRITTELLI

Coordinatore del Dottorato:

Chiar.mo Prof.
Giorgio METAFUNE

Direttore della Scuola di Dottorato:

Chiar.mo Prof.
Antonio LEACI

Dottorato di ricerca in Matematica ed Informatica XXX ciclo

Mathematics subject classification (2010): 35R01, 35B50, 65N12, 65N30, 65M12,
65M60, 65L20

To my family

Acknowledgements

First and foremost I vividly thank my supervisor, Prof. Ivonne Sgura, for patiently guiding my steps along the path of scientific and human maturation and for believing in me even when I was pessimistic and full of objections.

I am deeply grateful to Prof. Anotida Madzvamuse for spending time and resources for me in several circumstances. The first and most striking example is the invitation -without even knowing me- to spend a month at the Isaac Newton Institute (Cambridge, UK). The list continues with a one-month research period at the University of Sussex, several conferences, a seminar, and eventually three joint publications. I guess he does not regret that first blind invitation. As far as I am concerned, it is there in Cambridge that my PhD course took a new turn.

I wish to thank Dr. Chandrasekhar Venkataraman for his precious advice and for warmly inviting me to St. Andrews as a visiting student. Back in Cambridge, it is thanks to him that I came in touch with Smoller's book, which I had never heard of. The very day I first opened that book is when things started to work. Few pages of that big book inspired three joint publications on invariant regions and contributed to a fourth one on a model for electrodeposition. A large part of this thesis is based on these publications.

Special thanks go to Prof. Lourenço Beirão da Veiga for his valuable advice on the theory of virtual elements and for inviting me to several conferences, in which I had the honor of meeting the "virtual element community" and feeling extremely welcomed. I owe to him my very first invitation to give a talk at a conference, in which I also had the privilege of visiting wonderful Crete island.

I thank Profs. Benedetto Bozzini and Deborah Lacitignola for fruitful collaboration on the study of a model for electrodeposition on curved surfaces. One result on this problem is given in the present thesis.

One more round of acknowledgements goes to Profs. Anotida Madzvamuse and Lourenço Beirão da Veiga for patiently refereeing this thesis, thereby providing precious comments and improvements.

I wish to thank the members and the alternates of the final examination committee for their availability.

I am immensely thankful to my family, to which this result is dedicated. They will certainly appreciate it way more than I do.

Much gratitude goes to my friends, impossible to list in this context. Each one of them helped make me who I am.

Funding

I thank the Isaac Newton Institute for Mathematical Sciences (Cambridge, UK) for its hospitality during the programme “Coupling Geometric PDEs with Physics for Cell Morphology, Motility and Pattern Formation” funded by the EPSRC grant no. EP/K032208/1.

I acknowledge support from the University of Sussex (UK) during a one-month research period.

Ringraziamenti in italiano

Desidero ringraziare vivamente il mio supervisore, la Prof.ssa Ivonne Sgura, per avermi pazientemente guidato in questo percorso di maturazione scientifica e umana e per aver creduto in me anche quando ero pieno di pessimismo e obiezioni.

Esprimo profonda gratitudine al Prof. Anotida Madzvamuse per aver investito tempo e risorse per me in numerose occasioni. A cominciare dall'invito a trascorrere un mese all'Isaac Newton Institute dell'Università di Cambridge, senza neanche conoscermi. La lista continua con un periodo di ricerca di un mese presso l'Università del Sussex, diverse conferenze, un seminario, ed infine tre pubblicazioni congiunte. Ne deduco che non si sia pentito di quel primo invito a scatola chiusa. Per quanto mi riguarda, è lì a Cambridge che il mio corso di dottorato ha preso un'altra piega.

Ringrazio il Dott. Chandrasekhar Venkataraman per aver contribuito alla mia formazione matematica e per avermi calorosamente ospitato per un mese all'università di St. Andrews. Mi piace ricordare quel momento a Cambridge in cui mi indicò il libro di Smoller, di cui non avevo mai sentito parlare. Quando ho aperto quel libro, tutto ha cominciato a venire da sé. Poche pagine di quel grosso libro hanno ispirato tre pubblicazioni sulle regioni invarianti e contribuito a una quarta su un modello di elettrodeposizione. Gran parte di questa tesi è basata su queste pubblicazioni.

Ringrazio il Prof. Lourenço Beirão da Veiga per avermi incoraggiato e guidato nella ricerca sugli elementi virtuali e per avermi invitato a diverse conferenze, nelle quali ho avuto l'onore di conoscere la "comunità VEM" e sentirmene accolto. A lui devo il mio primo invito a parlare a una conferenza, con il privilegio aggiuntivo di visitare la meravigliosa isola di Creta.

Ringrazio i Proff. Benedetto Bozzini e Deborah Lacitignola per aver collaborato sullo studio di un modello di elettrodeposizione su superfici curve. Un risultato su questo problema è dato nella presente tesi.

Ai Proff. Anotida Madzvamuse e Lourenço Beirão da Veiga va un secondo ringraziamento per aver pazientemente revisionato questa tesi, fornendo preziosi commenti e miglioramenti.

Nel momento culminante dell'esame finale, desidero ringraziare i commissari e i loro supplenti per aver manifestato la loro disponibilità.

Un ringraziamento immenso va ai miei familiari, a cui dedico questo risultato. Loro

sapranno apprezzarlo più di me, che ormai mi sono abituato all'idea.

Concludo ringraziando infinitamente i miei amici, impossibili da elencare in questa sede. Ciascuno di loro ha contribuito a farmi diventare quello che sono.

Abstract

In this thesis we address two problems related to the numerical approximation of partial differential equations on stationary or evolving surfaces.

Firstly, we are concerned with geometric approximation of stationary surfaces. We approximate a given compact surface Γ with a piecewise flat surface with polygonal faces, called polygonation. Polygonations generalise the triangulations used in the surface finite element method [40]. We show two advantages of polygonations over standard triangulations: they simplify the approximation of simple surfaces and allow for simple mesh pasting. Based on our recent publication [58] we propose a novel numerical method for the Laplace-Beltrami equation, called Surface Virtual Element Method (SVEM) that is well-posed on polygonations. We prove that the method exhibits linear convergence in $H^1(\Gamma)$ seminorm. We provide numerical examples to experimentally show the convergence of the method and the advantages of polygonal meshes.

Secondly, for time-dependent partial differential equations on both stationary and evolving surfaces, we present the first numerical methods that preserve monotonicity properties under discretisation. For the case of stationary surfaces we present the results given in our publications [55, 56]. Specifically, we propose a Lumped Surface Finite Element Method (LSFEM) for the spatial discretisation of two parabolic problems on a stationary surface Γ : the semilinear heat equation and reaction-diffusion systems, with or without cross-diffusion (RDSs and RCDSs respectively). We derive a full discretisation by combining the LSFEM with an Implicit-Explicit (IMEX) Euler method. For the semilinear heat equation, both the spatially- and fully discrete methods preserve the maximum principle under discretisation. For RDSs and RCDSs, the methods preserve the invariant regions under discretisation. We prove quadratic convergence in space and linear convergence in time in $L^\infty([0, T]; L^2(\Gamma))$ norm, where T is the final time. We present numerical examples to confirm our findings in terms of convergence and preservation of monotonicity properties under discretisation.

For the case of evolving surfaces we present results from our publication [57]. In particular, we propose a Lumped Evolving Surface Finite Element Method (LESFEM) for the linear heat equation and for RDSs on an evolving surface. We introduce indicators, called dilation rates, that quantify the rate of expansion or contraction of the evolving surface. Under suitable conditions on the dilation rates, the linear heat equation fulfils the minimum-maximum principle at both the spatially and fully discrete levels. Similarly, for spatially and fully discretised RDSs we prove sufficient conditions on the dilation rates and the reaction kinetics, under which a given set in the phase-space is an invariant region. We apply our findings to determine classes of invariant regions for four RDSs on evolving surfaces existing in the literature. We provide numerical examples to confirm the preservation of monotonicity properties under discretisation and to empirically show the convergence of the method.

Contents

Acknowledgements	iv
Ringraziamenti in italiano	vi
Abstract	viii
1 Introduction	2
2 Partial differential equations on stationary surfaces	8
2.1 Introduction	8
2.2 Preliminaries and notations	8
2.3 Three model surface PDEs	13
2.4 The Laplace-Beltrami equation	14
2.5 The Surface Finite Element Method (SFEM) for the Laplace-Beltrami equation	15
2.5.1 Approximation of the surface and definitions	15
2.5.2 The SFEM space discretisation	18
2.5.3 Implementation	19
2.6 Survey on numerical methods for the semilinear heat equation and RDSs on stationary surfaces	21
2.6.1 Surface Finite Element Method	21
2.6.2 Kernel Methods	24
2.6.3 Spectral Method of Lines based on Spherical Harmonics	28
2.6.4 Planar parametrisation through spherical coordinates	30
2.6.5 Embedding methods and level set method	32
2.7 Conclusions	34
3 The Surface Virtual Element Method for the Laplace-Beltrami equation	36
3.1 Approximation of the surface and discrete function spaces	37
3.2 The SVEM space discretisation	39
3.2.1 Approximation of the $a(\cdot, \cdot)$ form	39
3.2.2 Approximation of the average-free condition	39
3.2.3 Approximation of the right-hand-side	40
3.2.4 Discrete formulation	40
3.3 Interpolation, projection and geometric error estimates	41
3.4 Existence, uniqueness and error analysis	47
3.5 Implementation	50

3.5.1	Constructing test problems	50
3.5.2	Constructing local matrices	51
3.5.3	Full-rank linear system associated to SVEM for the Laplace-Beltrami equation	52
3.6	Applications and numerical examples	54
3.6.1	Mesh pasting	54
3.6.2	Numerical examples	57
3.7	Conclusions	62
4	The heat equation on stationary surfaces	64
4.1	Introduction	64
4.2	The semilinear heat equation at the continuous level	65
4.3	The Lumped Surface Finite Element Method (LSFEM)	66
4.4	Time discretisation	67
4.5	Semi- and fully-discrete maximum principles	68
4.5.1	Mesh regularity assumption	68
4.5.2	Discrete maximum principles	70
4.6	Convergence analysis	72
4.7	Numerical examples	73
4.8	Conclusions	74
5	Reaction-cross-diffusion systems on stationary surfaces	76
5.1	Reaction-cross-diffusion systems on surfaces	78
5.1.1	Space discretisation	78
5.1.2	Time discretisation	79
5.2	Invariant convex polytopes for the semi- and fully-discrete schemes	80
5.3	Stability and error analysis	84
5.4	Numerical examples	93
5.5	Conclusions	102
6	Linear heat equation and reaction-diffusion systems on evolving surfaces	104
6.1	Introduction	104
6.2	Reaction-diffusion equations on an evolving surface	105
6.2.1	Preliminaries and basic results	105
6.2.2	Derivation of the reaction-diffusion model in strong form	107
6.2.3	Invariant regions and maximum principle	108
6.2.4	Derivation of the variational formulation	110
6.3	Lumped evolving surface finite element method	110
6.3.1	Surface triangulation and some definitions	110
6.3.2	Preliminary results on triangulated surfaces	112
6.3.3	Lumped evolving surface finite element method	113
6.3.4	Time discretisation	113
6.4	Characterisation of surface growth	114
6.4.1	Bounding the rate of change of the mass matrix in terms of the dilation rates	114
6.4.2	Characterising velocity flows in terms of the mappings G and G_h	115

6.4.3	Computing the dilation rates for the isotropic growth	116
6.5	Linear heat equation and discrete maximum principles	118
6.6	Reaction-diffusion systems and invariant regions	121
6.7	Velocity-induced invariant regions for RD models	124
6.7.1	RDS with <i>activator-depleted</i> kinetics	124
6.7.2	RDS with Thomas kinetics	125
6.7.3	Morphochemical RDS model for electrodeposition	126
6.7.4	RDS with Hodgkin-Huxley kinetics	128
6.8	Numerical examples	130
6.9	Conclusions	134

7 Conclusions and possible extensions 138

List of Figures

2.1	Normal and conormal vector fields on a surface with boundary	9
2.2	Surface Γ and respective Fermi stripe U	10
2.3	Tangential gradient	10
3.1	Illustration of the proof of Lemma 3.	43
3.2	Generating a polygonal mesh on the sphere	51
3.3	Pasting meshes along a straight line	55
3.4	Pasting meshes along an arbitrary curve	56
3.5	Laplace-Beltrami equation on sphere: convergence	59
3.6	Laplace-Beltrami equation on torus: convergence	61
3.7	Laplace-Beltrami equation on cylinder: mesh pasting and convergence	63
4.1	Delaunay mesh condition	69
4.2	Heat equation on sphere: convergence	75
5.1	Rosenzweig-MacArthur RDS on cyclide: invariant rectangle preservation	95
5.2	Rosenzweig-MacArthur RCDS on sphere: invariant parallelogram preservation	97
5.3	Schnakenberg RDS on sphere: convergence	100
5.4	Schnakenberg RDS on sphere: pattern formation	101
6.1	Plots of different growth functions	118
6.2	Heat equation on sphere: discrete maximum principle	131
6.3	Heat equation on sphere: convergence	132
6.4	Thomas RDS on logistically growing surfaces: invariant rectangle	133
6.5	Thomas RDS on logistically growing cyclide: numerical solution	135

List of Tables

1.1	Monotonicity properties: state of the art	7
4.1	Heat equation on sphere: discrete maximum principle	74
4.2	Heat equation on sphere: convergence	75
5.1	Rosenzweig-MacArthur RDS on cyclide: invariant rectangle violation	96
5.2	Rosenzweig-MacArthur RDS on cyclide: invariant rectangle preservation	96
5.3	Rosenzweig-MacArthur RCDS on sphere: invariant parallelogram violation	98
5.4	Rosenzweig-MacArthur RCDS on sphere: invariant parallelogram preservation	99
6.1	List of different growth functions	118
6.2	Thomas RDS on logistically growing cyclide: invariant rectangle violation	134
6.3	Thomas RDS on logistically growing cyclide: invariant rectangle preservation	136

Chapter 1

Introduction

Mathematical modelling of real phenomena through partial differential equations (PDEs) is an extremely wide field of mathematics. In many applications, the domain on which the phenomenon takes place is a surface embedded in \mathbb{R}^3 , rather than a flat domain [12, 19, 52, 53, 79, 125]. Moreover, in many cases the spatial domain -a flat domain or a curved surface- can be time-dependent or *evolving* [6, 14, 43, 45, 46, 85, 92, 136]. For this reason, the analysis and application of PDEs *on stationary or evolving surfaces* has become an active area of research over the last two decades.

Numerous classes of PDEs on surfaces have been considered in the literature, from both an analytical and a numerical point of view. The prototypical PDE on surfaces is the *Laplace-Beltrami* equation, that is the counterpart of the Laplace equation on surfaces [37, 125]. However, more general elliptic equations on surfaces have been considered [40, Section 3.1]. The basic time-dependent PDE on surfaces is the *diffusion- or heat equation* [68]. A more general class of parabolic PDEs on surfaces is that of *reaction-diffusion systems* (RDSs), which are extensively studied ever since Turing showed that such RDSs can exhibit the so called *diffusion-driven or Turing instability* [128]. It is worth mentioning some other remarkable time-dependent PDEs on surfaces that have been considered in the literature, such as the Navier-Stokes [125, Chapter 17], Allen-Cahn [35] and Cahn-Hilliard [44] equations.

The increasing number of applications of surface PDEs has stimulated the development of several numerical methods for their solution. The main challenge of devising efficient numerical methods for surface PDEs is to account for arbitrary geometries. For this reason, numerical methods for PDEs on general surfaces usually rely on the geometric approximation of the surface itself. The need of *discretising the surface* can be avoided only on particular geometries. For instance, some numerical methods are specifically designed for spherical geometries [19, 52, 53, 84, 99, 133] or for simple geometries that can be parametrised in closed form over planar domains, such as spheres, tori, cones, etc. [109]. For PDEs on arbitrary surfaces, several numerical methods have been developed. For instance, we mention the surface finite element method (SFEM) and its extensions [40], kernel methods [54], embedding methods [12, 24, 67, 90, 115]. In particular, we focus our attention on the SFEM. The method was first introduced in the pioneering work [37] for the Laplace-Beltrami equation. The SFEM was then extended to numerous classes of surface PDEs on stationary or evolving surfaces. We refer the interested reader to the survey paper [40]. The success of the method is due to its ability of coping with arbitrary geometries and for its algorithmic simpleness. In this thesis we

present three novel extensions of the SFEM: (i) the *surface virtual element method* (SVEM) for the Laplace-Beltrami equation, (ii) the *lumped surface finite element method* (LSFEM) for the semilinear heat equation, RDSs and RCDSs, and (iii) the *lumped evolving surface finite element method* (LESFEM) for the linear heat equation and RDSs on evolving surfaces. As discussed in the remainder of this introduction, the proposed numerical methods address two open problems in numerical analysis.

1) Polygonal approximation of geometry and applications

The aforementioned SFEM is based on the approximation of the surface through a *triangulated surface* or *triangulation* or *mesh*, i.e. a piecewise flat surface made up of triangles (called *elements*). On each element, the given PDE problem is locally discretised exactly as in the planar case using the finite element method (FEM). Consequently, the SFEM can be easily applied to arbitrary geometries and this justifies the success of the method. We face the problem of generalising the SFEM by considering polygonal approximation of surfaces. Before discussing the details of the novel numerical method, we motivate the need of considering polygonal approximation of surfaces. At first glance, it may appear that approximating an arbitrary surface with polygons is a cumbersome task with no advantage. In fact, any three not-aligned points span a (unique) triangle while, given $n \geq 4$ points, these do not span any n -gon if they do not belong to the same plane. However, there are at least two cases in which the process of meshing benefits from the possibility of choosing arbitrary polygonal elements.

The first application of polygonal meshes is the approximation of particular geometries such as cylinders, tori, cones, etc. We will show through numerical examples that approximating these simple surfaces with suitable quadrilaterals instead of triangles can lead to a significant reduction in the number of elements on equal number of nodes. This, in turn, translates into a reduction in the computational cost of the method, which is indeed proportional to the number of elements.

The second -and more interesting- proposed application of polygonal meshing is that of *mesh pasting*. If a surface is composed of simpler portions and a triangulation of each portion is available, it is desirable to simply paste the triangulated portions to obtain a triangulation of the overall surface. Unfortunately it is very unlikely that the triangulated portions match with each other along the boundaries, hence a naive pasting approach almost surely leads to a discontinuous or holed triangulation. An existing approach to overcome this issue is to suitably manipulate the boundaries of triangulated portions to let them match with each other. This is a complicated approach and some algorithms of this kind have been studied [75, 122]. We propose a pasting technique for which it is sufficient to juxtapose the triangulated portions without worrying about the discontinuities and the holes of the overall surface. Instead of manipulating and distorting the triangulations, we simply turn some triangular elements into polygonal elements by adding new nodes. Then we face the discontinuity of the overall triangulation by imposing a fictitious continuity condition on the numerical solution, called *virtual continuity*.

In order to exploit the aforementioned advantages of polygonal meshes we propose, based on our paper [58], a numerical method for the Laplace-Beltrami equation that is well-posed on such arbitrary polygonal surfaces, which we call Surface Virtual Element Method (SVEM). The method is an extension of the Virtual Element Method (VEM) introduced in [8] for the

numerical approximation Laplace equation on planar domains using polygonal meshes.

2) Numerical preservation of monotonicity properties under discretisation

The second problem that we address is the *numerical preservation of monotonicity properties under discretisation* for time-dependent PDEs. We start the discussion from the case of stationary surfaces. A scalar time-dependent PDE on a stationary surface that admits a strong solution $u(\mathbf{x}, t)$ is said to fulfil the *minimum-maximum principle* if, for any bounded initial datum $u_0(\mathbf{x})$, the solution fulfils

$$\min \left\{ 0, \min_{\mathbf{y} \in \Gamma} u_0(\mathbf{y}) \right\} \leq u(\mathbf{x}, t) \leq \max \left\{ 0, \max_{\mathbf{y} \in \Gamma} u_0(\mathbf{y}) \right\}, \quad (\mathbf{x}, t) \in \Gamma \times [0, T]. \quad (1.1)$$

For nonnegative initial data, the above definition reduces to the well-known notion of *maximum principle*:

$$\min_{\mathbf{y} \in \Gamma} u_0(\mathbf{y}) \leq u(\mathbf{x}, t) \leq \max_{\mathbf{y} \in \Gamma} u_0(\mathbf{y}), \quad (\mathbf{x}, t) \in \Gamma \times [0, T]. \quad (1.2)$$

We will refer to the minimum-maximum and maximum principles as *monotonicity properties*. The linear heat equation on stationary surfaces is known to fulfil the maximum principle [18]. From a numerical point of view, it is interesting to determine whether a numerical method for the heat equation preserves the maximum principle under discretisation. See Table 1.1 for a synoptic state of the art. In this thesis we present, based on our recent paper [56], a *lumped surface finite element method* (LSFEM) for the spatial discretisation of a *semilinear* heat equation and an implicit-explicit (IMEX) Euler-LSFEM for the full discretisation. The proposed methods preserve the maximum principle of the semilinear heat equation under discretisation.

For systems of PDEs, the monotonicity property which we are interested in is the *existence of invariant regions*. For a system of r , $r \in \mathbb{N}$ PDEs that admits a strong solution $\mathbf{u}(\mathbf{x}, t)$, a closed subset Σ of the phase-space \mathbb{R}^r is said to be an *invariant region* if, for any initial datum $\mathbf{u}_0(\mathbf{x})$ fulfilling $\mathbf{u}_0(\mathbf{x}) \in \Sigma$ for all $\mathbf{x} \in \Gamma$, the solution fulfils

$$\mathbf{u}(\mathbf{x}, t) \in \Sigma, \quad (\mathbf{x}, t) \in \Gamma \times [0, T]. \quad (1.3)$$

The two classes of systems of PDEs we will address in this thesis are *reaction-diffusion systems* (RDSs) and the more general *reaction-cross-diffusion systems* (RCDSs). For RDSs and RCDSs on planar domains, sufficient conditions for a set Σ to be an invariant region have been proven in [25, 123]. The sufficient conditions proposed by Taylor [125] for RDSs on stationary surfaces are analogous to the planar counterpart. To the best of the author's knowledge, the general case of RCDSs on stationary surfaces is not covered in the literature, although it is reasonable to think that the sufficient conditions given in [25] for RCDSs on planar domains still apply to the general case of stationary surfaces.

From a numerical point of view, the preservation of invariant regions has not been studied in depth. We summarise the state of the art on this topic in Table 1.1. To the best of the author's knowledge, the cases of RDSs on surfaces and RCDSs on planar domains or surfaces have not been considered in the literature. In this thesis we present, based on our recent

papers [55, 56] a LSFEM space discretisation and a LSFEM-IMEX Euler full discretisation of RDSs and RCDSs on general stationary surfaces, that preserve the invariant regions under discretisation.

As well as for the case of stationary surfaces, for scalar PDEs on evolving surfaces we consider the minimum-maximum- and maximum principles, whose definitions are analogous to (1.1)-(1.3), but since now the surface is time-dependent, a more precise formalism is needed, as discussed in detail in Chapter 6. Since the analysis and numerical approximation of PDEs on evolving surfaces are novel research areas, it is not surprising that the study of monotonicity properties for PDEs on evolving surfaces is almost completely unexplored, both at the continuous and discrete levels. The main challenge is to account for the impact of surface evolution on monotonicity properties. At the discrete level, an interesting insight in this direction is provided by the work in [15, 104], which study the impact of domain evolution on the *stability* of an Arbitrary Lagrangian Eulerian (ALE) FEM for parabolic PDEs on evolving planar domains. In order to face the open problem of discrete monotonicity properties we present, based on our recent paper [57] a lumped evolving surface finite element method (LESFEM) spatial discretisation and a LESFEM-IMEX Euler full discretisation for the linear heat equation and for RDSs on surfaces that evolve according to a prescribed material velocity. Moreover, to quantify the impact of surface evolution, we introduce indicators, called *dilation rates*, that measure the rate of expansion or contraction of the evolving surface. By exploiting these dilation rates we prove, at the spatially and fully discrete levels, sufficient conditions (i) for the minimum-maximum principle for the linear heat equation and (ii) for the existence of invariant regions for RDSs. To the best of the author's knowledge, these are the first examples of discrete monotonicity properties for PDEs on evolving surfaces presented in the literature. It is worth remarking that the continuous counterpart of our discrete monotonicity properties for PDEs on evolving surfaces remain an open problem in the field of pure analysis. As an application of our theory we prove, at the spatially discrete level, the existence of classes of invariant regions for four RD models on evolving surfaces existing in the literature: the Schnakenberg, Thomas, Hodgkin-Huxley models [100] and the morphochemical model for electrodeposition in [80].

Layout of the thesis

The present thesis is structured as follows.

In chapter 2 we set up the notations and definitions needed throughout the thesis. We state the classes of PDEs on stationary surfaces we are interested in: the Laplace-Beltrami equation, the semilinear heat equation, RDSs and RCDSs. We recall some analysis of the Laplace-Beltrami equation, alongside the SFEM for its numerical approximation. We survey some of the existing methods for the spatial approximation of the semilinear heat equation, RDSs and RCDSs.

In Chapter 3, based on our paper [58], we present the novel SVEM for the numerical approximation of the Laplace-Beltrami equation. We discuss the advantages and applications of polygonal meshes. We prove geometric error estimates for polygonal approximation of surfaces and analytical error estimates for the discrete bilinear forms involved in the method. We prove that the proposed method possesses a first order convergence in $H^1(\Gamma)$ norm, where Γ is the surface. We provide three numerical examples to show (i) the applications of polygonal

meshes and (ii) the convergence of the method.

In Chapter 4, based on our paper [56], we present the LSFEM for the spatial discretisation and the IMEX Euler-LSFEM for the full discretisation of the semilinear heat equation on a stationary surface Γ . We prove that our methods preserve the maximum principle under discretisation. We prove that the convergence of the proposed methods in $L^2([0, T]; H^1(\Gamma))$ norm is of second order in space and first order in time. In two numerical examples we show (i) the preservation of the maximum principle under discretisation and (ii) the convergence of the method.

In Chapter 5, based on our papers [55, 56], we present the LSFEM for the spatial discretisation and the IMEX Euler-LSFEM for the full discretisation of RDSs and RCDSs on a stationary surface Γ . We prove that the proposed methods preserve the invariant regions of the PDE system under discretisation. As well as for the semilinear heat equation considered in the previous chapter, we prove that the convergence of the methods in $L^2([0, T]; H^1(\Gamma))$ norm is of second order in space and first order in time. We provide four numerical examples to illustrate (i) in the first two examples, the preservation of an invariant region for a RDS and a RCDS, respectively, (ii) the convergence of the IMEX Euler-LSFEM and (iii) the application of the method to the simulation of biological pattern formation.

In Chapter 6, based on our paper [57], we consider the linear heat equation and RDSs on evolving surfaces. We present the LESFEM for the spatial discretisation and the IMEX Euler-LESFEM for the full discretisation of such PDEs. We introduce indicators called *dilation rates* that quantify the rate of expansion or contraction of smooth or triangulated surfaces. For the linear heat equation, we prove sufficient conditions under which the minimum-maximum principle holds at the spatially- and fully discrete levels. Likewise, for RDSs we prove sufficient conditions under which a region in the phase-space is invariant under spatial and full discretisation. In two numerical examples we experimentally show (i) the convergence of the IMEX Euler-LESFEM for the linear heat equation and (ii) the existence of an invariant region for a RDS at the fully discrete level.

In Chapter 7 we summarise the main findings of this thesis and we outline possible future extensions.

MAXIMUM PRINCIPLE FOR THE LINEAR HEAT EQUATION		
	Continuous level	Discrete level
Planar domains	Nirenberg (1953) ([103])	Nie & Thomée (1985) [101] Elliott & Stuart (1993) [47] Faragó et al. (2012) [49] Chatzipantelidis et al. (2015) [20]
Stationary surfaces	Calabi (1958) [18]	Frittelli et al. (2017) [56]
Evolving surfaces	-	Frittelli et al. (2018) [57]

INVARIANT REGIONS FOR RDSs		
	Continuous level	Discrete level
Planar domains	Chueh et al. (1977) [25]	Hoff (1978) [73] Garvie & Trenchea (2007) [60]
Stationary surfaces	Taylor (2013) [125]	Frittelli et al. (2017) [56]
Evolving surfaces	-	Frittelli et al. (2018) [57]

INVARIANT REGIONS FOR RCDSs		
	Continuous level	Discrete level
Planar domains	Chueh et al. (1977) [25]	-
Stationary surfaces	-	Frittelli et al. (2017) [55]
Evolving surfaces	-	-

Table 1.1: State of the art of (i) the maximum principle for the linear heat equation and (ii) invariant regions for RDSs and RCDSs. Our contribution is highlighted in bold. Concerning the linear heat equation, our work in [56] covers the more general semilinear heat equation.

Chapter 2

Partial differential equations on stationary surfaces

2.1 Introduction

This chapter introduces the necessary background to present and motivate the contributions of this thesis and is structured as follows. In Section 2.2 we recall the mathematical notions needed for the understanding and the analysis of surface PDEs at the continuous level. In Section 2.3 we summarise the classes of PDEs that will be addressed throughout the thesis. In Section 2.4 we introduce the Laplace-Beltrami equation in detail and recall the proof of existence and uniqueness of its weak solution, in order to make the reader familiar with the techniques that will be adopted throughout the remainder of this work. In Section 2.5 we recall from [40] the Surface Finite Element Method (SFEM) for the numerical approximation of the Laplace-Beltrami equation. All the novel numerical methods presented in this thesis will be extensions or modifications of the SFEM. In Section 2.6 we present the counterpart of SFEM for parabolic PDEs on stationary surfaces and we review some alternative existing methods for their spatial discretisation, thereby discussing some advantages and disadvantages with respect to the SFEM.

2.2 Preliminaries and notations

In this section we recall some fundamental notions concerning surface PDEs. If not explicitly stated, definitions and results are taken from [40].

Definition 1 (C^k surface, normal and conormal vectors). *Given $k \in \mathbb{N}$, a set $\Gamma \subset \mathbb{R}^3$ is said to be a C^k surface if, for every $\mathbf{x}_0 \in \Gamma$, there exist an open set $U_{\mathbf{x}_0} \subset \mathbb{R}^3$ containing \mathbf{x}_0 and a function $\phi \in C^k(U)$ such that*

$$U_{\mathbf{x}_0} \cap \Gamma = \{\mathbf{x} \in U_{\mathbf{x}_0} | \phi(\mathbf{x}) = 0\}.$$

The vector field

$$\boldsymbol{\nu} : \Gamma \rightarrow \mathbb{R}^3, \mathbf{x} \mapsto \frac{\nabla \phi(\mathbf{x})}{\|\nabla \phi(\mathbf{x})\|} \tag{2.1}$$

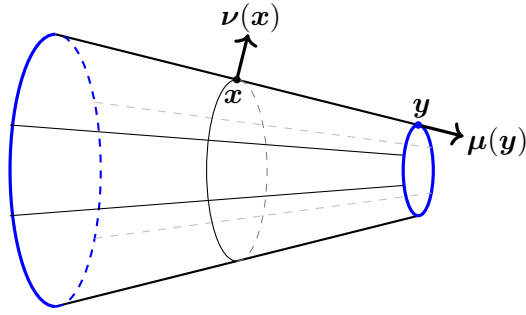


Figure 2.1: Illustration of normal vector field $\boldsymbol{\nu}$: defined in (2.1) and conormal vector field $\boldsymbol{\mu}$ defined in (2.2). The boundary $\partial\Gamma$ of the surface Γ is highlighted in blue.

is said to be the unit normal vector. We denote by $\partial\Gamma$ the one-dimensional boundary of Γ . If $\partial\Gamma$ has a well-defined tangent direction at each point, the unit vector field

$$\boldsymbol{\mu} : \partial\Gamma \rightarrow \mathbb{R}^3, \quad (2.2)$$

such that

- $\boldsymbol{\mu}(\mathbf{x}) \perp \boldsymbol{\nu}(\mathbf{x}), \quad \mathbf{x} \in \partial\Gamma;$
- $\boldsymbol{\mu}(\mathbf{x}) \perp \partial\Gamma, \quad \mathbf{x} \in \partial\Gamma;$
- $\boldsymbol{\mu}(\mathbf{x})$ points outward of $\Gamma,$

is called the conormal unit vector.

A representation of normal and conormal vectors is given in Figure 2.1.

Lemma 1 (Fermi coordinates, see [40]). *If Γ is a \mathcal{C}^2 surface, there exists an open neighbourhood $U \subset \mathbb{R}^3$ of Γ such that every $\mathbf{x} \in U$ admits a unique decomposition of the form*

$$\mathbf{x} = \mathbf{a}(\mathbf{x}) + d(\mathbf{x})\boldsymbol{\nu}(\mathbf{a}(\mathbf{x})), \quad \mathbf{a}(\mathbf{x}) \in \Gamma, \quad d(\mathbf{x}) \in \mathbb{R}. \quad (2.3)$$

The maximal open set U with this property is called the Fermi stripe of Γ , $\mathbf{a}(\mathbf{x})$ is called normal projection onto Γ , $d(\mathbf{x})$ is called oriented distance function and $(\mathbf{a}(\mathbf{x}), d(\mathbf{x}))$ are called the Fermi coordinates of \mathbf{x} . An example of Fermi stripe is depicted in Fig. 2.2.

Definition 2 (Tangential gradient, tangential divergence). *If Γ is a \mathcal{C}^1 surface, A is an open neighborhood of Γ and $f \in \mathcal{C}^1(A, \mathbb{R})$, the operator*

$$\nabla_{\Gamma} f : \Gamma \rightarrow \mathbb{R}^3, \quad \mathbf{x} \mapsto \nabla f(\mathbf{x}) - (\nabla f(\mathbf{x}) \cdot \boldsymbol{\nu}(\mathbf{x}))\boldsymbol{\nu}(\mathbf{x}) = P(\mathbf{x})\nabla f(\mathbf{x}), \quad (2.4)$$

where ∇ denotes the usual gradient in \mathbb{R}^3 and $P(\mathbf{x})_{ij} = \delta_{ij} - \nu_i(\mathbf{x})\nu_j(\mathbf{x})$, is called the tangential gradient of f . A pictorial representation is given in Figure 2.3. The components of the tangential gradient, i.e.

$$\underline{D}_i f : S \rightarrow \mathbb{R}, \quad \mathbf{x} \mapsto P_i(\mathbf{x})\nabla f(\mathbf{x}), \quad i \in \{1, 2, 3\}, \quad (2.5)$$

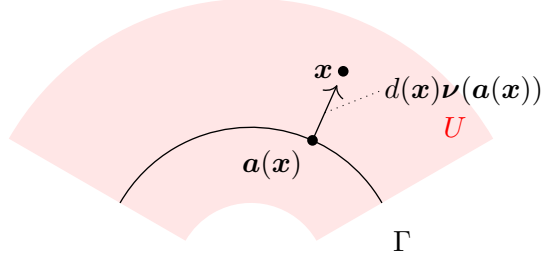


Figure 2.2: Schematic representation of the Fermi stripe U of a surface Γ , as defined in Lemma 1. According to (2.3), each point $\mathbf{x} \in U$ is obtained by moving its normal projection $\mathbf{a}(\mathbf{x}) \in \Gamma$ by a distance $d(\mathbf{x})$ in the normal direction $\boldsymbol{\nu}(\mathbf{a}(\mathbf{x}))$.

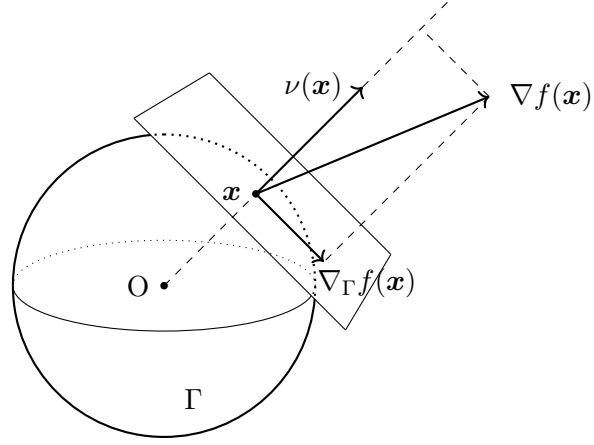


Figure 2.3: Schematic representation of tangential gradient, defined as the orthogonal projection of the standard gradient onto the tangent plane, according to (2.4).

where $P_i(\mathbf{x})$ is the i -th row of $P(\mathbf{x})$, are called the tangential derivatives of f . Given a vector field $F \in \mathcal{C}^1(A, \mathbb{R}^3)$, the operator

$$\nabla_{\Gamma} \cdot F : S \rightarrow \mathbb{R}, \quad \mathbf{x} \mapsto \sum_{i=1}^3 D_i F_i(\mathbf{x}) \quad (2.6)$$

is called the tangential divergence of F .

Theorem 1. Given $\Gamma \subset A$ a \mathcal{C}^1 surface, if f and g are $\mathcal{C}^1(A, \mathbb{R})$ functions such that $f|_{\Gamma} = g|_{\Gamma}$, then

$$\nabla_{\Gamma} f(\mathbf{x}) = \nabla_{\Gamma} g(\mathbf{x}), \quad \mathbf{x} \in \Gamma.$$

This means that the tangential derivatives of a function only depend on its restriction over Γ .

Thanks to Theorem 1, the following definition is well-posed.

Definition 3 ($C^k(\Gamma)$ functions). If Γ is a C^1 surface, a function $f : \Gamma \rightarrow \mathbb{R}$ is said to be $C^1(\Gamma)$ if it is differentiable at any point of Γ and its tangential derivatives are continuous over Γ . If $k \geq 2$ and Γ is a C^k surface, a function $f : \Gamma \rightarrow \mathbb{R}$ is said to be $C^k(\Gamma)$ if it is $C^1(\Gamma)$ and its tangential derivatives are $C^{k-1}(\Gamma)$ functions.

Definition 4 (Laplace-Beltrami operator). Given a C^2 surface Γ and $f \in C^2(\Gamma)$, the operator

$$\Delta_\Gamma f : \Gamma \rightarrow \mathbb{R}, \quad \mathbf{x} \mapsto \nabla_\Gamma \cdot \nabla_\Gamma f(\mathbf{x}) = \sum_{i=1}^3 \underline{D}_i \underline{D}_i f(\mathbf{x})$$

is called the Laplace-Beltrami operator of f .

We now recall the definitions of some remarkable Lebesgue and Sobolev spaces on surfaces. For further details, the reader is referred to [64], [70] or [125].

Definition 5 (Lebesgue and Sobolev spaces on surfaces). Let Γ be a C^1 surface and let $L^0(\Gamma)$ be the set of measurable functions on Γ with respect to the bidimensional Hausdorff measure on Γ . The Lebesgue spaces $L^2(\Gamma)$ and $L^\infty(\Gamma)$ are defined by

$$H^0(\Gamma) = L^2(\Gamma) = \left\{ f \in L^0(\Gamma) \mid \int_\Gamma |f|^2 d\sigma < +\infty \right\};$$

$$L^\infty(\Gamma) = \left\{ f \in L^0(\Gamma) \mid \operatorname{ess\,sup}_{\mathbf{x} \in \Gamma} |f(\mathbf{x})| < +\infty \right\},$$

respectively. Let now be $s \in \mathbb{N}$ and let Γ be a C^s surface. The Sobolev spaces on Γ are defined by

$$H^r(\Gamma) = \left\{ f \in L^2(\Gamma) \mid \underline{D}_i f \in H^{r-1}(\Gamma), \quad i \in \{1, 2, 3\} \right\}, \quad r = 1, \dots, s.$$

The space $L^\infty(\Gamma)$ is a Banach space with the following norm

$$\|f\|_\infty := \operatorname{ess\,sup}_{\mathbf{x} \in \Gamma} |f(\mathbf{x})|, \quad f \in L^\infty(\Gamma).$$

The space $H^0(\Gamma) = L^2(\Gamma)$ and $H^r(\Gamma)$, $r = 1, \dots, s$ are Hilbert spaces with the following inner products

$$\langle f, g \rangle_0 := \int_\Gamma fg d\sigma, \quad f, g \in L^2(\Gamma);$$

$$\langle f, g \rangle_r := \int_\Gamma \left(fg + \sum_{|\alpha| \leq r} \underline{D}_\alpha f \underline{D}_\alpha g \right) d\sigma, \quad f, g \in H^r(\Gamma),$$

respectively, which induce the following norms

$$\|f\|_0 := \left(\int_\Gamma f^2 d\sigma \right)^{\frac{1}{2}}, \quad f \in L^2(\Gamma);$$

$$\|f\|_r := \left(\int_\Gamma f^2 d\sigma + \sum_{|\alpha| \leq r} \int_\Gamma (\underline{D}_\alpha f)^2 d\sigma \right)^{\frac{1}{2}}, \quad f \in H^r(\Gamma),$$

where \underline{D}_α is the multi-index notation for partial derivatives ¹ and tangential derivatives are meant in a distributional sense ². On $H^r(\Gamma)$, $1 \leq r \leq s$, we consider the seminorm

$$|f|_r := \left(\sum_{|\alpha|=r} \int_{\Gamma} (\underline{D}_\alpha f)^2 d\sigma \right)^{\frac{1}{2}}, \quad f \in H^r(\Gamma).$$

The topological dual space of $H^r(\Gamma)$, $1 \leq r \leq s$, is denoted by $H^{-r}(\Gamma)$. The topological dual space of $L^2(\Gamma)$ is denoted by $L^{-2}(\Gamma)$.

Remark 1. if \tilde{T} is a compact subset of a C^s surface Γ , with $s \in \mathbb{N}$, the spaces $L^\infty(\tilde{T})$ and $H^r(\tilde{T})$, with $0 \leq r \leq s$ are defined similarly to Definition 5. The respective norms, seminorms and inner products will be denoted with an additional \tilde{T} subscript, e.g. $\|\cdot\|_{0,\tilde{T}}$, $|\cdot|_{2,\tilde{T}}$ and $\langle \cdot, \cdot \rangle_{1,\tilde{T}}$.

A basic result in surface calculus, taken from [39], is the following

Theorem 2 (Green's formula on surfaces, see [39]). *Given a C^2 surface Γ with a well-defined tangent vector field on the boundary $\partial\Gamma$, $f \in H^1(\Gamma)$ and $g \in H^2(\Gamma)$, it holds that*

$$\int_{\Gamma} f \Delta_{\Gamma} g d\sigma = - \int_{\Gamma} \nabla_{\Gamma} f \cdot \nabla_{\Gamma} g d\sigma + \int_{\partial\Gamma} f \frac{\partial g}{\partial \boldsymbol{\mu}} dl, \quad (2.7)$$

where $\boldsymbol{\mu}$ is the conormal vector (see Definition 1) and $\frac{\partial g}{\partial \boldsymbol{\mu}}(\mathbf{x}) := \nabla_{\Gamma} g(\mathbf{x}) \cdot \boldsymbol{\mu}(\mathbf{x})$ is the conormal derivative of g on $\partial\Gamma$. If Γ has no boundary, i.e. $\partial\Gamma = \emptyset$, then the boundary integral in (2.7) vanishes.

The analysis of elliptic problems requires suitable subspaces of the Lebesgue and Sobolev spaces, namely the *average-free* Lebesgue and Sobolev spaces.

Definition 6 (Average-free Lebesgue and Sobolev spaces). *Let $s \in \mathbb{N}$ and let Γ be a C^s surface. The zero-averaged Lebesgue and Sobolev spaces are defined by*

$$L_0^2(\Gamma) := \left\{ f \in L^2(\Gamma) \left| \int_{\Gamma} f = 0 \right. \right\};$$

$$H_0^r(\Gamma) := \left\{ f \in H^r(\Gamma) \left| \int_{\Gamma} f = 0 \right. \right\}, \quad 1 \leq r \leq s,$$

respectively. $L_0^2(\Gamma)$ and $H_0^r(\Gamma)$, $1 \leq r \leq s$, are Hilbert subspaces of $L^2(\Gamma)$ and $H^r(\Gamma)$ respectively.

Given a space B of space-dependent real functions endowed with a norm $\|\cdot\|_B$ and possibly with an inner product $\langle \cdot, \cdot \rangle_B$, the norm and the inner product are extended to \mathbb{R}^n -valued functions, with $n \in \mathbb{N}$, as follows

$$\|\mathbf{u}\|_B := \left(\sum_{i=1}^n \|u_i\|_B \right)^{\frac{1}{2}}, \quad \mathbf{u} = (u_1, \dots, u_n) \in B^n;$$

$$\langle \mathbf{u}, \mathbf{v} \rangle_B := \sum_{i=1}^n \langle u_i, v_i \rangle_B, \quad \mathbf{u} = (u_1, \dots, u_n), \mathbf{v} = (v_1, \dots, v_n) \in B^n.$$

¹See for instance [112].

²See [40] for a precise definition of distributional tangential derivatives.

As well as in the case of flat domains, the following Poincaré inequality holds in the zero-averaged space $H_0^1(\Gamma)$ on a smooth surface Γ , see [40].

Theorem 3 (Poincaré’s inequality on surfaces, see [40]). *Given a \mathcal{C}^2 surface Γ with a well-defined tangent vector field on the boundary $\partial\Gamma$, there exists $C > 0$ such that*

$$\|f\|_0 \leq C\|f\|_1 \quad \forall f \in H_0^1(\Gamma). \quad (2.8)$$

The analysis of time-dependent problems requires suitable spaces of time and space dependent functions defined on $\Gamma_T = \Gamma \times [0, T]$, namely the Bochner spaces, see for instance [112].

Definition 7 (Bochner spaces, see [112]). *Let B be a Banach space endowed with the norm $\|\cdot\|_B$. The Bochner spaces $L^2([0, T]; B)$ and $L^\infty([0, T]; B)$ are defined by*

$$L^2([0, T]; B) = \left\{ f : [0, T] \rightarrow B \mid \int_0^T \|f(t)\|_B^2 dt < +\infty \right\};$$

$$L^\infty([0, T]; B) = \left\{ f : [0, T] \rightarrow B \mid \operatorname{ess\,sup}_{t \in [0, T]} \|f(t)\|_B < +\infty \right\},$$

respectively, and are Banach spaces with the respective norms

$$\|f\|_{L^2([0, T]; B)} := \left(\int_0^T \|f(t)\|_B^2 dt \right)^{\frac{1}{2}}, \quad f \in L^2([0, T]; B);$$

$$\|f\|_{L^\infty([0, T]; B)} := \operatorname{ess\,sup}_{t \in [0, T]} \|f(t)\|_B, \quad f \in L^\infty([0, T]; B).$$

Finally, we set up the notation for transpose vectors and matrices, which we will adopt throughout the thesis.

Notation (Transpose vectors and matrices). *Let $m, n \in \mathbb{N}$ and let A be a $m \times n$ matrix with arbitrary entries (possibly a row- or column-vector when $m = 1$ or $n = 1$ respectively). Then, the $n \times m$ transpose of A is denoted by A^{tr} .*

2.3 Three model surface PDEs

In the present thesis we introduce novel extensions of the Surface Finite Element Method (see for instance [37, 40]) for the following three classes of surface PDEs. Let Γ be a \mathcal{C}^3 surface in \mathbb{R}^3 and let $f \in \mathcal{C}^0(\Gamma)$. The prototype of elliptic surface PDE is the *Laplace-Beltrami equation*

$$-\Delta_\Gamma u(\mathbf{x}) = f(\mathbf{x}), \quad \mathbf{x} \in \Gamma. \quad (2.9)$$

For time-dependent PDEs, it is enough to require that Γ is a \mathcal{C}^2 surface, as explained later. If $T > 0$ is the final time, $d > 0$ is a diffusion coefficient and $f \in \mathcal{C}^2(\Gamma \times [0, T])$ is a nonlinear source term, a time-dependent counterpart of (2.9) is the following semilinear *diffusion* or *heat equation* on Γ :

$$\frac{\partial u}{\partial t}(\mathbf{x}, t) - d\Delta_\Gamma u(\mathbf{x}, t) = f(\mathbf{x}, t), \quad (\mathbf{x}, t) \in \Gamma \times [0, T]. \quad (2.10)$$

If $r \in \mathbb{N}$, $D := (d_{ij}) \in \mathbb{R}^{r,r}$ is a positive definite matrix, $f_1, \dots, f_r \in \mathcal{C}^0(\mathbb{R}^r)$ are nonlinear reaction kinetics, a *reaction-cross-diffusion system* (RCDS) on Γ is given by

$$\begin{cases} \frac{\partial u_1}{\partial t}(\mathbf{x}, t) - \sum_{k=1}^r d_{1k} \Delta_\Gamma u_k(\mathbf{x}, t) = f_1(\mathbf{u}(\mathbf{x}, t)); \\ \vdots \\ \frac{\partial u_r}{\partial t}(\mathbf{x}, t) - \sum_{k=1}^r d_{rk} \Delta_\Gamma u_k(\mathbf{x}, t) = f_r(\mathbf{u}(\mathbf{x}, t)), \end{cases} \quad (\mathbf{x}, t) \in \Gamma \times [0, T], \quad (2.11)$$

where $u_1, \dots, u_r : \Gamma \times [0, T] \rightarrow \mathbb{R}$ are the components of the solution. When D is diagonal, i.e. $d_{ij} = 0$ for $i \neq j$, the system (2.11) is called a *reaction-diffusion system* (RDS). In vectorised form, system (2.11) can be written as

$$\frac{\partial \mathbf{u}}{\partial t}(\mathbf{x}, t) - D \Delta_\Gamma \mathbf{u}(\mathbf{x}, t) = \mathbf{f}(\mathbf{u}(\mathbf{x}, t)), \quad (\mathbf{x}, t) \in \Gamma \times [0, T], \quad (2.12)$$

where $\mathbf{u} := (u_1, \dots, u_r)^{tr}$, $\Delta_\Gamma \mathbf{u} := (\Delta_\Gamma u_1, \dots, \Delta_\Gamma u_r)^{tr}$ and $\mathbf{f} := (f_1, \dots, f_r)^{tr}$. In the two subsequent sections we recall some analysis of the Laplace-Beltrami equation (2.9) at the continuous level and the Surface Finite Element Method (SFEM) for its numerical approximation.

2.4 The Laplace-Beltrami equation

In this section we recall the derivation of the weak formulation of the Laplace-Beltrami equation (2.9) and the proof of existence and uniqueness of the weak solution in $H_0^1(\Gamma)$. These notions will provide the necessary background for (i) its SFEM discretisation recalled in the next section and (ii) the analysis of the time-dependent PDE problems (2.10) and (2.11) carried out in the following chapters.

Let Γ be a \mathcal{C}^3 surface without boundary. Let $f \in \mathcal{C}^0(\Gamma)$ such that $\int_\Gamma f = 0$. Observe that, if $u \in \mathcal{C}^2(\Gamma)$ is a solution of (2.9), then, for any $c \in \mathbb{R}$, $u + c$ is still a solution of (2.9). Hence, (2.9) does not have a unique solution. For this reason, we consider the following problem

$$\begin{cases} -\Delta_\Gamma u = f; \\ \int_\Gamma u = 0. \end{cases} \quad (2.13)$$

We now consider the weak formulation of (2.13). To this end, we define the bilinear form

$$a(u, v) := \int_\Gamma \nabla_\Gamma u \cdot \nabla_\Gamma v, \quad u, v \in H^1(\Gamma).$$

By multiplying both hands of the first equation in (2.13) by an arbitrary test function $\varphi \in H^1(\Gamma)$, integrating on Γ , and applying Green's formula (2.7), we have

$$a(u, \varphi) = \langle f, \varphi \rangle_0 \quad \forall \varphi \in H^1(\Gamma). \quad (2.14)$$

Notice that (2.14) is well-posed under the weaker regularity assumptions that $f \in L^2(\Gamma)$ and $u \in H^1(\Gamma)$. Hence, the weak formulation of (2.13) is:

$$\begin{aligned} & \text{find } u \in H^1(\Gamma) \text{ such that} \\ & \begin{cases} a(u, \varphi) = \langle f, \varphi \rangle_0 & \forall \varphi \in H^1(\Gamma); \\ \int_\Gamma u = 0. \end{cases} \end{aligned} \quad (2.15)$$

In order to show the existence and uniqueness of the solution of (2.15), it is useful to rephrase (2.15) in a different way. To this end, since $a(u, 1) = 0$ for all $u \in H^1(\Gamma)$ and $\langle f, 1 \rangle_0 = 0$, then (2.15) is equivalent to

$$\text{find } u \in H_0^1(\Gamma) \text{ such that } \quad a(u, \varphi) = \langle f, \varphi \rangle_0 \quad \forall \varphi \in H_0^1(\Gamma). \quad (2.16)$$

The following result of existence and uniqueness of the solution of (2.16) holds.

Theorem 4. *The weak Laplace-Beltrami equation (2.16) has a unique solution $u \in H^1(\Gamma)$.*

Proof. The bilinear form $a(\cdot, \cdot) : H_0^1(\Gamma) \times H_0^1(\Gamma) \rightarrow \mathbb{R}$ is:

- continuous since, from the Cauchy-Schwarz inequality, it holds that

$$|a(u, v)| \leq \|\nabla_{\Gamma} u\|_0 \|\nabla_{\Gamma} v\|_0 = |u|_1 |v|_1 \leq \|u\|_1 \|v\|_1, \quad u, v \in H_0^1(\Gamma);$$

- coercive since, from Poincaré's inequality (2.8), it holds that

$$a(u, u) = \|\nabla_{\Gamma} u\|_0^2 = |u|_1^2 \geq C \|u\|_1^2, \quad u \in H_0^1(\Gamma).$$

From Lax-Milgram's theorem follows that the weak Laplace-Beltrami equation (2.16) has a unique solution $u \in H_0^1(\Gamma)$.

□

Remark 2 (Surfaces with boundary). *The whole analysis carried out in the remainder of the chapter holds unchanged in the presence of a non-empty boundary, $\partial\Gamma \neq \emptyset$, and homogeneous Neumann boundary conditions. In the case of homogeneous Dirichlet boundary conditions, the analysis still holds if $H_0^1(\Gamma)$ is the space of $H^1(\Gamma)$ functions that vanish on $\partial\Gamma$ in the sense of traces, see [124, Chapter 4.5].*

2.5 The Surface Finite Element Method (SFEM) for the Laplace-Beltrami equation

This section is devoted to the (SFEM), introduced in [37] and further analysed in [40], for the discretisation of the weak Laplace-Beltrami equation (2.15). The SFEM will serve as a background to present and analyse novel extensions of the SFEM in the remainder of this thesis. In this chapter we (i) describe the SFEM discretisation of the weak Laplace-Beltrami equation (2.15), (ii) show the existence and uniqueness of the numerical solution and (iii) provide some numerical examples.

2.5.1 Approximation of the surface and definitions

Given a \mathcal{C}^2 surface in \mathbb{R}^3 and a number $h > 0$ called *meshsize*, a triangulation Γ_h of Γ is defined by

$$\Gamma_h = \bigcup_{T \in \mathcal{T}_h} T,$$

where

- \mathcal{T}_h is a set of finitely many non-degenerate triangles in \mathbb{R}^3 , whose diameters do not exceed h ;
- the $N \in \mathbb{N}$ vertices \mathbf{x}_i , $i = 1, \dots, N$, of Γ_h (called *nodes*) lie on Γ ;
- for any $T_1, T_2 \in \mathcal{T}_h$ with $T_1 \neq T_2$, the intersection $T_1 \cap T_2$ is either empty, or a common vertex, or a common edge of T_1 and T_2 ;
- Γ_h is contained in the Fermi stripe U associated to Γ , see Lemma 1;
- if $\mathbf{a} : U \rightarrow \Gamma$ is the normal projection defined in Lemma 1, the restriction $\mathbf{a}|_{\Gamma_h} : \Gamma_h \rightarrow \Gamma$ is one-to-one.

We now define a discrete function space on Γ_h . To this end, we need to define polynomials on (possibly slanted) planar regions in \mathbb{R}^3 . Let K be a (bounded or unbounded) planar region contained in \mathbb{R}^3 . Then, there exists a linear invertible mapping $J_K : \mathbb{R}^3 \rightarrow \mathbb{R}^3$ such that $J_K(\hat{K}) = K$, where \hat{K} is a planar region contained in the horizontal plane $\{(x, y, z) \in \mathbb{R}^3 | z = 0\}$. Clearly, given $K \in \mathcal{K}_h$, the couple (\hat{K}, J_K) is not unique. For $k \in \mathbb{N}$ the polynomial space $\mathbb{P}_k(K)$ on the planar region K is defined by

$$\mathbb{P}_k(K) := \{V : K \rightarrow \mathbb{R} | V \circ J_K \in \mathbb{P}_k(\hat{K})\}. \quad (2.17)$$

This definition is well-posed since it does not depend on the choice of the couple (\hat{K}, J_K) . The *finite element space* is defined by

$$\mathbb{V}_h := \{V \in \mathcal{C}^0(\Gamma_h) | V|_T \in \mathbb{P}_1(T), \forall T \in \mathcal{T}_h\}. \quad (2.18)$$

Central to the analysis of the SFEM method is the *average-free* subspace $\mathbb{V}_{h,0}$ of \mathbb{V}_h , defined by

$$\mathbb{V}_{h,0} := \left\{ V \in \mathbb{V}_h \left| \int_{\Gamma_h} V = 0 \right. \right\}.$$

For each $i = 1, \dots, N$, the i -th *Lagrange basis function* χ_i is the unique \mathbb{V}_h function such that

$$\chi_i(\mathbf{x}_j) = \delta_{ij}, \quad i, j = 1, \dots, N, \quad (2.19)$$

where δ_{ij} is the Kronecker symbol. The functions χ_i , $i = 1, \dots, N$, form a basis for \mathbb{V}_h . Given a function $v \in \mathcal{C}^0(\Gamma)$ or $v \in \mathcal{C}^0(\Gamma_h)$, the *Lagrange interpolant* $I_h(v)$ is the unique \mathbb{V}_h function such that

$$I_h(v)(\mathbf{x}_i) = v(\mathbf{x}_i), \quad i = 1, \dots, N. \quad (2.20)$$

The Lagrange interpolant $I_h(v)$ of v can be expressed as a linear combination of the Lagrange basis functions as follows

$$I_h(v)(\mathbf{x}) = \sum_{i=1}^N v(\mathbf{x}_i) \chi_i(\mathbf{x}), \quad \mathbf{x} \in \Gamma_h. \quad (2.21)$$

In order to compare functions defined on the continuous surface Γ with functions defined on the discrete surface Γ_h , we consider *lifts* following [40] and *unlifts* following [56]. Given $V : \Gamma_h \rightarrow \mathbb{R}$, its *lift* $V^\ell : \Gamma \rightarrow \mathbb{R}$ is defined by

$$V^\ell(\mathbf{a}(\mathbf{x})) := V(\mathbf{x}), \quad \mathbf{x} \in \Gamma_h. \quad (2.22)$$

Conversely, given $v : \Gamma \rightarrow \mathbb{R}$, its *unlift* $v^{-\ell} : \Gamma_h \rightarrow \mathbb{R}$ is defined by

$$v^{-\ell}(\mathbf{x}) := v(\mathbf{a}(\mathbf{x})), \quad \mathbf{x} \in \Gamma_h, \quad (2.23)$$

where $\mathbf{a} : \gamma_h \rightarrow \Gamma$ is the normal projection defined in Lemma 1. The analysis of the SFEM and of its extensions presented in this thesis requires Sobolev spaces on the discrete surface Γ_h . Particular attention must be paid in defining these spaces, as Γ_h is not smooth, which implies that the tangential derivatives are not defined globally on Γ_h .

Definition 8 (Discrete Sobolev spaces). *We define the following discrete Sobolev spaces*

$$\begin{aligned} L^\infty(\Gamma_h) &:= \left\{ U : \Gamma_h \rightarrow \mathbb{R} \mid \operatorname{ess\,sup}_{\mathbf{x} \in \Gamma_h} |U(\mathbf{x})| < +\infty \right\}; \\ H^0(\Gamma_h) &:= L^2(\Gamma_h) = \left\{ U : \Gamma_h \rightarrow \mathbb{R} \mid \int_{\Gamma_h} U^2 < +\infty \right\}; \\ H^1(\Gamma_h) &:= L^2(\Gamma_h) \cap \prod_{T \in \mathcal{T}_h} H^1(T); \\ H^2(\Gamma_h) &:= L^2(\Gamma_h) \cap \prod_{T \in \mathcal{T}_h} H^2(T). \end{aligned}$$

The above spaces are endowed with the following seminorms

$$\begin{aligned} |U|_{1,h} &:= \left(\sum_{T \in \mathcal{T}_h} |U|_{H^1(T)}^2 \right)^{\frac{1}{2}}, \quad U \in H^1(\Gamma_h); \\ |U|_{2,h} &:= \left(\sum_{T \in \mathcal{T}_h} |U|_{H^2(T)}^2 \right)^{\frac{1}{2}}, \quad U \in H^2(\Gamma_h), \end{aligned}$$

and the following norms

$$\begin{aligned} \|U\|_{\infty,h} &:= \operatorname{ess\,sup}_{\mathbf{x} \in \Gamma_h} |U(\mathbf{x})|, \quad U \in L^\infty(\Gamma_h); \\ \|U\|_{0,h} &:= \left(\int_{\Gamma_h} U^2 \right)^{\frac{1}{2}}, \quad U \in L^2(\Gamma_h); \\ \|U\|_{1,h} &:= \left(\|U\|_{0,h}^2 + |U|_{1,h}^2 \right)^{\frac{1}{2}}, \quad U \in H^1(\Gamma_h); \\ \|U\|_{2,h} &:= \left(\|U\|_{0,h}^2 + |U|_{1,h}^2 + |U|_{2,h}^2 \right)^{\frac{1}{2}}, \quad U \in H^2(\Gamma_h). \end{aligned}$$

The topological dual space of $L^2(\Gamma_h)$ will be denoted by $L^{-2}(\Gamma_h)$.

Remark 3. Notice that the seminorms and norms in Definition 8, are well-defined even for functions that are discontinuous across the edges of Γ_h . We will exploit this fact in the next chapter.

Remark 4. If $T \in \mathcal{T}_h$ is a face of Γ_h , the spaces $L^\infty(T)$ and $H^r(T)$, $r = 0, 1, 2$, are defined analogously to Definition 8. The respective norms and seminorms are denoted with a T subscript instead of h , e.g. $\|\cdot\|_{\infty,T}$ and $|\cdot|_{2,T}$.

As well as in the continuous case, we define the following discrete average-free Sobolev spaces.

Definition 9 (Average-free discrete Sobolev spaces). *The average-free Lebesgue and Sobolev spaces are defined by*

$$\begin{aligned} L_0^2(\Gamma_h) = H_0^0(\Gamma_h) &:= \left\{ U \in L^2(\Gamma_h) \left| \int_{\Gamma_h} U = 0 \right. \right\}; \\ H_0^r(\Gamma_h) &:= \left\{ U \in H^r(\Gamma_h) \left| \int_{\Gamma_h} U = 0 \right. \right\}, \quad r = 1, 2. \end{aligned}$$

We prove the following discrete Poincaré inequality in $H_0^1(\Gamma_h)$.

Lemma 2 (Discrete Poincaré inequality in $H_0^1(\Gamma_h)$). *Let Γ be a \mathcal{C}^3 surface without boundary. Then, there exists $h_0 > 0$ and $C > 0$ depending on Γ such that, for all $0 < h < h_0$ and for any triangulation Γ_h of Γ ,*

$$\|V\|_{0,h} \leq C|V|_{1,h}, \quad \forall V \in H_0^1(\Gamma_h). \quad (2.24)$$

Proof. This lemma is a special case of Theorem 8 in the next chapter. Hence, we omit the proof. \square

2.5.2 The SFEM space discretisation

In this section we recall from [37] and [40] the SFEM discretisation of the weak Laplace-Beltrami equation (2.15). Moreover, we present an implementation of the method as a square, sparse, full-rank linear system that accounts for the condition $\int_{\Gamma_h} U = 0$, where $U \in \mathbb{V}_h$ is the numerical solution.

Let Γ be a \mathcal{C}^3 surface without boundary, let Γ_h be a triangulation of Γ as defined in Section 2.5.1 and let $f \in H_0^2(\Gamma)$ be a load term.

Remark 5 (Regularity of f). *In contrast to the weak formulation (2.15) where $f \in L_0^2(\Gamma)$, we now require the stronger regularity assumption $f \in H_0^2(\Gamma)$. With this assumption, from Sobolev's embedding theorem on surfaces [4], the pointwise values of f (and thus the interpolant $I_h(f)$ of f) are well-defined. We remark that some alternative approximations of f are well-defined even if $f \in L_0^2(\Gamma)$, such as the Ritz projection [34, 44] or the unlift $f^{-\ell}$. However, on an arbitrary surface Γ , these alternative approximations of f are not computable in closed form.*

Notice that, if $\int_{\Gamma} f = 0$, it might not hold that $\int_{\Gamma_h} I_h(f) = 0$. For this reason, we consider the *average-free approximation* f_h of $I_h(f)$ defined as

$$f_h(\mathbf{x}) = I_h(f)(\mathbf{x}) - \frac{1}{|\Gamma_h|} \int_{\Gamma_h} I_h(f), \quad \mathbf{x} \in \Gamma_h, \quad (2.25)$$

where $|\Gamma_h|$ is the area of Γ_h . By construction, f_h fulfils $\int_{\Gamma_h} f_h = 0$, or equivalently

$$\langle f_h, 1 \rangle_{0,h} = 0. \quad (2.26)$$

We consider the bilinear form

$$a_h(U, V) := \int_{\Gamma_h} \nabla_{\Gamma_h} U \cdot \nabla_{\Gamma_h} V, \quad U, V \in \mathbb{V}_h.$$

The SFEM approximation of the weak Laplace-Beltrami equation (2.15) is:

$$\begin{aligned} & \text{find } U \in \mathbb{V}_h \text{ such that} \\ & \begin{cases} a_h(U, \phi) = \langle f_h, \phi \rangle_{0,h} & \forall \phi \in \mathbb{V}_h \\ \int_{\Gamma_h} U = 0 \end{cases} \end{aligned} \quad (2.27)$$

Since $\int_{\Gamma_h} \nabla_{\Gamma_h} V \cdot \nabla_{\Gamma_h} 1 = 0$ for all $V \in \mathbb{V}_h$ and $\langle f_h, 1 \rangle_{0,h} = 0$, then (2.27) is equivalent to

$$\text{find } U \in \mathbb{V}_{h,0} \text{ such that} \quad a_h(U, \phi) = \langle f_h, \phi \rangle_{0,h} \quad \forall \phi \in \mathbb{V}_{h,0} \quad (2.28)$$

Theorem 5. *For h sufficiently small, the SFEM spatially discrete Laplace-Beltrami equation (2.28) has a unique solution $U \in \mathbb{V}_{h,0}$.*

Proof. The bilinear form $a_h : \mathbb{V}_{h,0} \times \mathbb{V}_{h,0} \rightarrow \mathbb{R}$ is:

- continuous since, from the Cauchy-Schwarz inequality in $L^2(\Gamma_h)$, it holds that

$$|a_h(U, V)| \leq \|\nabla_{\Gamma_h} U\|_{0,h} \|\nabla_{\Gamma_h} V\|_{0,h} = |U|_{1,h} |V|_{1,h} \leq \|U\|_{1,h} \|V\|_{1,h}, \quad U, V \in \mathbb{V}_{h,0};$$

- coercive since, for h sufficiently small, we can apply the discrete Poincaré inequality (2.24), obtaining

$$a_h(U, U) = \|\nabla_{\Gamma_h} U\|_{0,h}^2 = |U|_{1,h}^2 \geq C \|U\|_1^2, \quad U \in \mathbb{V}_{h,0}.$$

From Lax-Milgram's theorem it follows that the SFEM discretisation (2.28) of the Laplace-Beltrami equation has a unique solution $U \in \mathbb{V}_{h,0}$. □

2.5.3 Implementation

We now present an implementation of the discrete Laplace-Beltrami equation (2.27) as an $N \times N$ sparse, full-rank algebraic linear system. To this end notice that, since the Lagrange functions χ_j , $j = 1, \dots, N$, form a basis for \mathbb{V}_h , problem (2.27) is equivalent to

$$\begin{aligned} & \text{find } U \in \mathbb{V}_h \text{ such that} \\ & \begin{cases} a_h(U, \chi_j) = \langle f_h, \chi_j \rangle_{0,h}, & j = 1, \dots, N, \\ \langle U, 1 \rangle_{0,h} = 0. \end{cases} \end{aligned} \quad (2.29)$$

Since $a_h(U, 1) = 0$ for all $U \in \mathbb{V}_h$ and

$$\sum_{i=1}^N \chi_i(\mathbf{x}) = 1, \quad \mathbf{x} \in \Gamma_h, \quad (2.30)$$

then the sum of the first N equations in (2.29) vanishes. This means that problem (2.29) can be rewritten equivalently by removing one of the first N equations. For instance, by removing the N -th equation in (2.29), we obtain

$$\begin{aligned} & \text{find } U \in \mathbb{V}_h \text{ such that} \\ & \begin{cases} a_h(U, \chi_j) = \langle f_h, \chi_j \rangle_{0,h}, & j = 1, \dots, N-1, \\ \langle U, 1 \rangle_{0,h} = 0. \end{cases} \end{aligned} \quad (2.31)$$

By expressing the numerical solution U and the load term f_h in the Lagrange basis, i.e.

$$U(\mathbf{x}) = \sum_{i=1}^N \xi_i \chi_i(\mathbf{x}), \quad f_h(\mathbf{x}) = \sum_{i=1}^N f_h(\mathbf{x}_i) \chi_i(\mathbf{x}), \quad \mathbf{x} \in \Gamma_h,$$

and using (2.30) in the last equation of (2.31), we rewrite problem (2.31) as

$$\begin{aligned} & \text{find } \boldsymbol{\xi} = (\xi_1, \dots, \xi_N) \in \mathbb{R}^N \text{ such that} \\ & \left\{ \begin{array}{l} \sum_{i=1}^N \xi_i a_h(\chi_i, \chi_j) = \sum_{i=1}^N f_h(\mathbf{x}_i) \langle \chi_i, \chi_j \rangle_{0,h}, \quad j = 1, \dots, N-1, \\ \sum_{i=1}^N \sum_{j=1}^N \xi_i \langle \chi_i, \chi_j \rangle_{0,h} = 0. \end{array} \right. \end{aligned} \quad (2.32)$$

By using the *mass matrix* $M = (m_{ij}) \in \mathbb{R}^{N,N}$ and the *stiffness matrix* $A = (a_{ij}) \in \mathbb{R}^{N,N}$, defined by

$$m_{ij} := \langle \chi_i, \chi_j \rangle_{0,h}, \quad i, j = 1, \dots, N; \quad (2.33)$$

$$a_{ij} := a_h(\chi_i, \chi_j), \quad i, j = 1, \dots, N, \quad (2.34)$$

respectively, we rewrite problem (2.32) as

$$\left\{ \begin{array}{l} \sum_{i=1}^N a_{ij} \xi_i = \sum_{i=1}^N m_{ij} f_h(\mathbf{x}_i), \quad j = 1, \dots, N-1; \\ \sum_{i=1}^N \left(\sum_{j=1}^N m_{ij} \right) \xi_i = 0, \end{array} \right. \quad (2.35)$$

which is an $N \times N$ linear algebraic system in the unknowns $\boldsymbol{\xi} = (\xi_1, \dots, \xi_N) \in \mathbb{R}^N$. It remains to show how to compute the nodal values $f_h(\mathbf{x}_i)$, $i = 1, \dots, N$, of the average-free load term f_h . From the definition (2.25) of f_h , using (2.21) and (2.30), it holds that

$$\begin{aligned} f_h(\mathbf{x}_i) &= I_h(f)(\mathbf{x}_i) - \frac{\langle I_h(f), 1 \rangle_{0,h}}{\langle 1, 1 \rangle_{0,h}} = f(\mathbf{x}_i) - \frac{\sum_{j=1}^N \sum_{k=1}^N f(\mathbf{x}_j) \langle \chi_j, \chi_k \rangle_{0,h}}{\sum_{j=1}^N \sum_{k=1}^N \langle \chi_j, \chi_k \rangle_{0,h}} \\ &= f(\mathbf{x}_i) - \frac{\sum_{j=1}^N \left(\sum_{k=1}^N m_{jk} \right) f(\mathbf{x}_j)}{\sum_{j=1}^N \sum_{k=1}^N m_{jk}}, \quad i = 1, \dots, N. \end{aligned}$$

In matrix form, we write system (2.35) as

$$B\boldsymbol{\xi} = \mathbf{c},$$

where $B = (b_{ij}) \in \mathbb{R}^{N,N}$ and $\mathbf{c} = (c_1, \dots, c_N)^{tr}$ are defined by

$$b_{ij} = \begin{cases} a_{ij} & \text{if } i = 1, \dots, N-1, j = 1, \dots, N; \\ \sum_{j=1}^N m_{Nj}, & \text{if } i = N; \end{cases}$$

$$c_i = \begin{cases} \sum_{j=1}^N m_{ij} f_h(\mathbf{x}_j) & \text{if } i = 1, \dots, N-1; \\ 0 & \text{if } i = N, \end{cases}$$

respectively. The matrix B is sparse, with only its last row being full, and unstructured. For a general review on numerical methods for sparse linear systems we refer the reader to [116].

2.6 Survey on numerical methods for the semilinear heat equation and RDSs on stationary surfaces

In this section we recall some of the existing numerical methods for the spatial discretisation of the semilinear heat equation (2.10) and RDSs (2.12) on stationary surfaces. For each of these methods, we point out their advantages and disadvantages.

2.6.1 Surface Finite Element Method

In Section 2.4 we have already recalled the SFEM for the Laplace-Beltrami equation introduced in [37]. Here we present the counterpart of the SFEM for parabolic problems introduced in [38]. In particular, we focus on the semilinear heat equation (2.10) and RCDSs of the form (2.11). As well as for the Laplace-Beltrami equation, the SFEM approximates the weak formulation of the problem.

Weak formulation

By multiplying both hands of the semilinear heat equation (2.10) by an arbitrary test function $\varphi \in H^1(\Gamma)$, integrating on Γ , and applying Green's formula (2.7), we obtain the following weak formulation: find $u \in L^2([0, T]; H^1(\Gamma))$ with $\dot{u} \in L^2([0, T]; H^{-1}(\Gamma))$ such that

$$\int_{\Gamma} \dot{u} \varphi + d \int_{\Gamma} \nabla_{\Gamma} u \cdot \nabla_{\Gamma} \varphi = -\beta \int_{\Gamma} u^{\alpha} \varphi, \quad (2.36)$$

for all $\varphi \in H^1(\Gamma)$, see for instance [56]. In a similar fashion, we obtain the weak formulation of the RCDS (2.11): find $u_1, \dots, u_r \in L^2([0, T]; H^1(\Gamma))$ with $\dot{u}_1, \dots, \dot{u}_r \in L^2([0, T]; H^{-1}(\Gamma))$ such that

$$\int_{\Gamma} \dot{u}_m \varphi_m + \sum_{k=1}^r d_{mk} \int_{\Gamma} \nabla_{\Gamma} u_k \cdot \nabla_{\Gamma} \varphi_m = \int_{\Gamma} f_m(\mathbf{u}) \varphi_m, \quad (2.37)$$

for all $\varphi_m \in L^2([0, T]; H^1(\Gamma))$ and $m = 1, \dots, r$, see for instance [55].

The SFEM space discretisation

We now use the notations introduced in Section 2.5.1. Let $h > 0$ and let Γ_h a triangulation of Γ with meshsize h . The SFEM spatial discretisation of the weak semilinear heat equation (2.36) is: find $U \in L^2([0, T]; \mathbb{V}_h)$ with $\dot{U} \in L^2([0, T]; \mathbb{V}_h)$ such that

$$\int_{\Gamma_h} \dot{U} \phi + d \int_{\Gamma_h} \nabla_{\Gamma_h} U \cdot \nabla_{\Gamma_h} \phi = -\beta \int_{\Gamma_h} U^\alpha \phi, \quad (2.38)$$

for all $\phi \in L^2([0, T], \mathbb{V}_h)$, where the initial condition $U_0 \in \mathbb{V}_h$ is the Lagrange interpolant of the exact initial condition $u_0 \in \mathcal{C}^2(\Gamma)$, namely $U_0 = I_h(u_0)$. Since the Lagrange functions χ_i , $i = 1, \dots, N$ defined in (2.19) are a basis of \mathbb{V}_h , the formulation (2.38) is equivalent to: find $U \in L^2([0, T]; \mathbb{V}_h)$ with $\dot{U} \in L^2([0, T]; \mathbb{V}_h)$ such that

$$\int_{\Gamma_h} \dot{U} \chi_j + d \int_{\Gamma_h} \nabla_{\Gamma_h} U \cdot \nabla_{\Gamma_h} \chi_j = -\beta \int_{\Gamma_h} U^\alpha \chi_j, \quad (2.39)$$

for all $j = 1, \dots, N$. For all $j = 1, \dots, N$, let $b_j(t)$ be an approximation of $\int_{\Gamma_h} U^\alpha \chi_j$ obtained through a sufficiently high order quadrature rule (see for instance [106] for a survey on quadrature rules in finite element methods) in order to preserve the convergence rate of the SFEM, which is quadratic in $L^\infty([0, T], L^2(\Gamma))$ norm and linear in $L^\infty([0, T], H^1(\Gamma))$ norm, see [38]. We obtain the following computable method: find $U \in L^2([0, T]; \mathbb{V}_h)$ with $\dot{U} \in L^2([0, T]; \mathbb{V}_h)$ such that

$$\int_{\Gamma_h} \dot{U} \chi_j + d \int_{\Gamma_h} \nabla_{\Gamma_h} U \cdot \nabla_{\Gamma_h} \chi_j = -\beta b_j, \quad (2.40)$$

for all $j = 1, \dots, N$, where the dependence of b_j on t is omitted for better readability. As shown in the following Chapters 4-5, the novel *Lumped Surface Finite Element Method* (LSFEM) provides a simpler spatially discrete formulation with an easily computable right-hand-side that requires no quadrature rule. By expressing the spatially discrete solution U in the Lagrange basis as

$$U(\mathbf{x}, t) = \sum_{i=1}^N \xi_i(t) \chi_i(\mathbf{x}), \quad (\mathbf{x}, t) \in \Gamma_h \times [0, T], \quad (2.41)$$

the formulation (2.40) becomes an ODE system in the N unknowns $\xi_1(t), \dots, \xi_N(t)$:

$$\sum_{i=1}^N \dot{\xi}_i(t) \int_{\Gamma_h} \chi_i \chi_j + d \sum_{i=1}^N \xi_i(t) \int_{\Gamma_h} \nabla_{\Gamma_h} \chi_i \cdot \nabla_{\Gamma_h} \chi_j = -\beta b_j(t), \quad (2.42)$$

for $j = 1, \dots, N$ and $t \in [0, T]$. By using the mass matrix M and the stiffness matrix A defined in (2.33)-(2.34) respectively, we can rewrite the ODE system (2.42) in vectorised form:

$$M \dot{\boldsymbol{\xi}}(t) + d A \boldsymbol{\xi}(t) = -\beta \mathbf{b}(t), \quad (2.43)$$

for all $t \in [0, T]$, where $\boldsymbol{\xi}(t) := (\xi_1(t), \dots, \xi_N(t))^{tr}$ and $\mathbf{b}(t) := (b_1(t), \dots, b_N(t))^{tr}$.

Analogously, the SFEM spatial discretisation of the weak RCDS (2.37) is: find $U_1, \dots, U_r \in L^2([0, T]; \mathbb{V}_h)$ with $\dot{U}_1, \dots, \dot{U}_r \in L^2([0, T]; \mathbb{V}_h)$ such that

$$\int_{\Gamma_h} \dot{U}_m \varphi_m + \sum_{k=1}^r d_{mk} \int_{\Gamma_h} \nabla_{\Gamma_h} U_k \cdot \nabla_{\Gamma_h} \varphi_m = \int_{\Gamma_h} f_m(\mathbf{U}) \varphi_m, \quad (2.44)$$

for all $\varphi_m \in L^2([0, T], \mathbb{V}_h)$, $m = 1, \dots, r$ and $t \in [0, T]$, where the initial condition $(U_{0,1}, \dots, U_{0,r}) \in \mathbb{V}_h^r$ is the Lagrange interpolant of the exact initial condition $(u_{0,1}, \dots, u_{0,r})$, namely $U_{0,m} = I_h(u_{0,m})$ for $m = 1, \dots, r$. By recalling that the Lagrange functions χ_i , $i = 1, \dots, N$ are a basis of \mathbb{V}_h and expressing the components of the numerical solution as

$$U_k(\mathbf{x}, t) = \sum_{i=1}^N \xi_{k,i}(t) \chi_i(\mathbf{x}), \quad (\mathbf{x}, t) \in \Gamma_h \times [0, T], \quad (2.45)$$

we rewrite (2.44) as follows

$$\sum_{i=1}^N \dot{\xi}_{k,i}(t) \int_{\Gamma_h} \chi_i \chi_j + \sum_{k=1}^r d_{mk} \sum_{i=1}^N \xi_{k,i}(t) \int_{\Gamma_h} \nabla_{\Gamma_h} \chi_i \cdot \nabla_{\Gamma_h} \chi_j = \int_{\Gamma_h} f_m(\mathbf{U}) \chi_j, \quad (2.46)$$

for $m = 1, \dots, r$, $j = 1, \dots, N$ and $t \in [0, T]$. As discussed above (2.40), for all $m = 1, \dots, r$ and $j = 1, \dots, N$ let $c_{m,j}(t)$ be an approximation of $\int_{\Gamma_h} f_m(\mathbf{U}) \chi_j$ obtained through quadrature. We obtain the following ODE system in the rN unknowns $\xi_{m,i}(t)$, $m = 1, \dots, r$, $i = 1, \dots, N$:

$$\sum_{i=1}^N \dot{\xi}_{m,i}(t) \int_{\Gamma_h} \chi_i \chi_j + \sum_{k=1}^r d_{mk} \sum_{i=1}^N \xi_{k,i}(t) \int_{\Gamma_h} \nabla_{\Gamma_h} \chi_i \cdot \nabla_{\Gamma_h} \chi_j = c_{m,j}(t), \quad (2.47)$$

for all $m = 1, \dots, r$, $j = 1, \dots, N$ and $t \in [0, T]$. By using the mass matrix M and the stiffness matrix A defined in (2.33) and (2.34) respectively, we can rewrite (2.47) in vectorised form:

$$M \dot{\boldsymbol{\xi}}_m(t) + \sum_{k=1}^r d_{mk} A \boldsymbol{\xi}_k(t) = \mathbf{c}_m(t), \quad (2.48)$$

for all $m = 1, \dots, r$ and $t \in [0, T]$, where for all $m = 1, \dots, r$, $\boldsymbol{\xi}_m(t) := (\xi_{m,1}(t), \dots, \xi_{m,N}(t))^{tr}$ and $\mathbf{c}_m(t) := (c_{m,1}(t), \dots, c_{m,N}(t))^{tr}$. The vectorised form (2.48) can be compacted as follows:

$$(I_r \otimes M) \dot{\boldsymbol{\xi}}(t) + (D \otimes A) \boldsymbol{\xi}(t) = \mathbf{c}(t), \quad (2.49)$$

for $t \in [0, T]$, where I_r is the $r \times r$ identity matrix, \otimes denotes the Kronecker product, see [83], while $\boldsymbol{\xi}(t)$ and $\mathbf{c}(t)$ are the column vectors defined by $\boldsymbol{\xi}(t) := (\boldsymbol{\xi}_1(t)^{tr}, \dots, \boldsymbol{\xi}_r(t)^{tr})^{tr}$ and $\mathbf{c}(t) := (\mathbf{c}_1(t)^{tr}, \dots, \mathbf{c}_r(t)^{tr})^{tr}$, respectively.

In the Chapters 4 and 5 next, we will mimic the approach followed in this section to derive spatially discrete formulations of the weak heat equation (2.36) and the weak RCDS (2.37) through the novel LSFEM.

Advantages and drawbacks

Advantages:

1. the method can cope with arbitrary surfaces;
2. since the method approximates the weak formulation, it provides meaningful solutions even when the right-hand-side of the considered PDE is $\mathcal{C}^1(\Gamma)$, only;

3. the mass- and stiffness matrices M and A involved in the method are sparse, which translates into computational efficiency;
4. the convergence rate of the method can be increased by considering *isoparametric elements* as shown in [32], i.e. by considering a piecewise polynomial function space \mathbb{V}_h^p of a given order $p \in \mathbb{N}$ on curved triangles of the same polynomial order p , see [32] for more details.

Drawbacks:

1. the exact surface Γ must be approximated with a triangulation Γ_h as shown in Section 2.5.1. Even if mesh generation is a well-studied topic and mesh-generating software is widely available, the computational cost related to mesh generation is not present in the so-called *meshless methods*, such as the *kernel methods* addressed in the next section.

2.6.2 Kernel Methods

The class of *kernel methods* has its origins in the pioneering work by Kansa [76], in which the method was introduced for some classes of elliptic, parabolic and hyperbolic equations on planar one- and two-dimensional domains. The method was then extended to solve PDEs on spherical surfaces, in particular: the Laplace-Beltrami equation, see [99], (ii) the heat equation, see [84], (iii) linear transport, see [53] and (iv) shallow water equation [52]. A further evolution allowed the method to solve parabolic PDEs, including RDSs, on arbitrary stationary surfaces, see [59]. For a more general overview on kernel methods we refer the interested reader to the survey paper [54]. In the remainder of this section we will describe the kernel method for RDSs on arbitrary surfaces presented in [59].

Kernel interpolation

We start from the notion of a *kernel interpolant* in \mathbb{R}^3 . Given a target function $v : \mathbb{R}^3 \rightarrow \mathbb{R}$ scattered at $N \in \mathbb{N}$ sample points $X := \{\mathbf{x}_j, j = 1, \dots, N\} \subset \mathbb{R}^3$ and a continuous function $\phi : \mathbb{R}^3 \times \mathbb{R}^3 \rightarrow \mathbb{R}$ called *kernel*, the *kernel interpolant* of v at the sample points X is defined by

$$I_\phi v(\mathbf{x}) := \sum_{j=1}^N c_j \phi(\mathbf{x}, \mathbf{x}_j), \quad \mathbf{x} \in \mathbb{R}^3, \quad (2.50)$$

where $c_j, j = 1, \dots, N$, are real coefficients to be determined by imposing the interpolation condition

$$I_\phi v(\mathbf{x}_j) = v(\mathbf{x}_j), \quad j = 1, \dots, N. \quad (2.51)$$

Using (2.50), the interpolation condition (2.51) can be written as a linear system as follows:

$$\sum_{j=1}^N c_j \phi(\mathbf{x}_i, \mathbf{x}_j) = v(\mathbf{x}_i), \quad i = 1, \dots, N. \quad (2.52)$$

Let now $\mathbf{c} := (c_1, \dots, c_N)^{tr}$ and consider the matrix $A_X = (a_{ij}) \in \mathbb{R}^{N,N}$ and the column vector $\mathbf{v}_X = (v_1, \dots, v_N)^{tr} \in \mathbb{R}^{N,1}$ defined respectively by

$$a_{ij} := \phi(\mathbf{x}_i, \mathbf{x}_j), \quad v_j := v(\mathbf{x}_j), \quad (2.53)$$

for all $i, j = 1, \dots, N$. The linear system (2.52) can be written in matrix form as

$$A_X \mathbf{c} = \mathbf{v}_X, \quad (2.54)$$

where $A = (a_{ij}) \in \mathbb{R}^{N,N}$, with $a_{ij} := \phi(\mathbf{x}_i, \mathbf{x}_j)$ for all $i, j = 1, \dots, N$ and $\mathbf{v}_X := (v(\mathbf{x}_1), \dots, v(\mathbf{x}_N))^{tr}$. The kernel ϕ is assumed to be *positive definite*, i.e.

$$\mathbf{b}^{tr} A_X \mathbf{b} > 0 \quad (2.55)$$

for all possible node sets $X := \{\mathbf{x}_j, j = 1, \dots, N\} \subset \mathbb{R}^3$ and for all nonzero column vectors $\mathbf{b} \in \mathbb{R}^{N,1}$. Assumption (2.55) ensures that the kernel interpolant (2.50) is uniquely defined. A positive definite kernel $\phi : \mathbb{R}^3 \times \mathbb{R}^3 \rightarrow \mathbb{R}$ is called a *radial basis function* (RBF) if there exists a function $\psi : [0, +\infty[\rightarrow \mathbb{R}$ such that

$$\phi(\mathbf{x}, \mathbf{y}) = \psi(\|\mathbf{x} - \mathbf{y}\|), \quad \mathbf{x}, \mathbf{y} \in \mathbb{R}^3, \quad (2.56)$$

where $\|\cdot\|$ is the Euclidean norm in \mathbb{R}^3 . Notice that, in contrast to ϕ , ψ is a function of one variable. Hence, in the remainder of this Section, we denote the derivative of ψ as ψ' if it exists. Here are three examples of RBFs:

1. Given $\varepsilon > 0$, the *Gaussian* RBF is given by

$$\phi(\mathbf{x}, \mathbf{y}) := e^{-(\varepsilon\|\mathbf{x} - \mathbf{y}\|)^2}, \quad \mathbf{x}, \mathbf{y} \in \mathbb{R}^3, \quad (2.57)$$

see for instance [50];

2. Given $\varepsilon > 0$, the *inverse multiquadric* (IMQ) RBF is given by

$$\phi(\mathbf{x}, \mathbf{y}) := \frac{1}{\sqrt{1 + (\varepsilon\|\mathbf{x} - \mathbf{y}\|)^2}}, \quad \mathbf{x}, \mathbf{y} \in \mathbb{R}^3, \quad (2.58)$$

see for instance [59];

3. Given $\varepsilon > 0$ and $\nu > \frac{3}{2}$, The *Matérn* RBF is given by

$$\phi(\mathbf{x}, \mathbf{y}) := \frac{2^{1-(\nu-3/2)}}{\Gamma_E(\nu-3/2)} (\varepsilon\|\mathbf{x} - \mathbf{y}\|)^{\nu-3/2} K_{\nu-3/2}(\varepsilon\|\mathbf{x} - \mathbf{y}\|), \quad \mathbf{x}, \mathbf{y} \in \mathbb{R}^3, \quad (2.59)$$

where $K_{\nu-3/2}$ is the modified second-kind Bessel function of order $\nu - 3/2$ and Γ_E is Euler's Gamma function, see for instance [59].

Exact surface differential operators of a radial kernel

Let $\phi : \mathbb{R}^3 \times \mathbb{R}^3 \rightarrow \mathbb{R}$ be a RBF, let $\psi : [0, +\infty[\rightarrow \mathbb{R}$ be defined by (2.56) and consider $N \in \mathbb{N}$ sample points $X := \{\mathbf{x}_j, j = 1, \dots, N\} \subset \mathbb{R}^3$. Let ∇ denote the gradient operator with respect to the variable $\mathbf{x} = (x, y, z)$. Using the chain rule, it holds that

$$\begin{aligned} \nabla \phi(\mathbf{x}, \mathbf{x}_j) &= \nabla \psi(\|\mathbf{x} - \mathbf{x}_j\|) = \begin{pmatrix} \frac{\partial}{\partial x} \psi(\|\mathbf{x} - \mathbf{x}_j\|) \\ \frac{\partial}{\partial y} \psi(\|\mathbf{x} - \mathbf{x}_j\|) \\ \frac{\partial}{\partial z} \psi(\|\mathbf{x} - \mathbf{x}_j\|) \end{pmatrix} \\ &= \begin{pmatrix} x - x_j \\ y - y_j \\ z - z_j \end{pmatrix} \frac{\psi'(\|\mathbf{x} - \mathbf{x}_j\|)}{\|\mathbf{x} - \mathbf{x}_j\|} = (\mathbf{x} - \mathbf{x}_j) \frac{\psi'(\|\mathbf{x} - \mathbf{x}_j\|)}{\|\mathbf{x} - \mathbf{x}_j\|}, \end{aligned} \quad (2.60)$$

for $\mathbf{x} \in \mathbb{R}^3$ and $j = 1, \dots, N$. Notice that, since $\phi(\cdot, \cdot)$ is smooth, (2.56) implies that $\lim_{r \rightarrow 0^+} \frac{\psi'(z)}{z}$ exists and is a finite number, see [59]. Hence, the apparent singularity in (2.60) cancels. Let now Γ be a \mathcal{C}^2 surface and let $\boldsymbol{\nu} = (\nu_x, \nu_y, \nu_z) : \Gamma \rightarrow \mathbb{R}^3$ be the outward unit normal vector as in Definition 1. By combining (2.4) and (2.60), we have the following expression for the tangential derivatives of ϕ :

$$\begin{aligned} \underline{D}_x \phi(\mathbf{x}, \mathbf{x}_j) = & \left((x - x_j)(1 - \nu_x^2(\mathbf{x})) - (y - y_j)\nu_x(\mathbf{x})\nu_y(\mathbf{y}) \right. \\ & \left. - (z - z_j)\nu_x(\mathbf{x})\nu_z(\mathbf{x}) \right) \frac{\psi'(\|\mathbf{x} - \mathbf{x}_j\|)}{\|\mathbf{x} - \mathbf{x}_j\|}; \end{aligned} \quad (2.61)$$

$$\begin{aligned} \underline{D}_y \phi(\mathbf{x}, \mathbf{x}_j) = & \left((y - y_j)(1 - \nu_y^2(\mathbf{x})) - (x - x_j)\nu_x(\mathbf{x})\nu_y(\mathbf{x}) \right. \\ & \left. - (z - z_j)\nu_y(\mathbf{x})\nu_z(\mathbf{x}) \right) \frac{\psi'(\|\mathbf{x} - \mathbf{x}_j\|)}{\|\mathbf{x} - \mathbf{x}_j\|}; \end{aligned} \quad (2.62)$$

$$\begin{aligned} \underline{D}_z \phi(\mathbf{x}, \mathbf{x}_j) = & \left((z - z_j)(1 - \nu_z^2(\mathbf{x})) - (x - x_j)\nu_x(\mathbf{x})\nu_z(\mathbf{x}) \right. \\ & \left. - (y - y_j)\nu_y(\mathbf{x})\nu_z(\mathbf{x}) \right) \frac{\psi'(\|\mathbf{x} - \mathbf{x}_j\|)}{\|\mathbf{x} - \mathbf{x}_j\|}, \end{aligned} \quad (2.63)$$

for all $\mathbf{x} \in \Gamma$ and $j = 1, \dots, N$.

Discrete surface differential operators of a sampled function

Given a function $v \in \mathcal{C}^2(\Gamma)$ known at the nodes $X = \{\mathbf{x}_i, i = 1, \dots, N\}$, consider its kernel interpolant $I_\phi v$ defined by (2.50). The *discrete tangential derivatives* of v are defined as the exact tangential derivatives of the interpolant $I_\phi v$. By using (2.50) and (2.61)-(2.63), these discrete tangential derivatives are given by

$$\begin{aligned} \underline{D}_x I_\phi v(\mathbf{x}) = & \sum_{j=1}^N c_j \underline{D}_x \phi(\mathbf{x}, \mathbf{x}_j) = \sum_{j=1}^N c_j \left((x - x_j)(1 - \nu_x^2(\mathbf{x})) \right. \\ & \left. - (y - y_j)\nu_x(\mathbf{x})\nu_y(\mathbf{y}) - (z - z_j)\nu_x(\mathbf{x})\nu_z(\mathbf{x}) \right) \frac{\psi'(\|\mathbf{x} - \mathbf{x}_j\|)}{\|\mathbf{x} - \mathbf{x}_j\|}; \end{aligned} \quad (2.64)$$

$$\begin{aligned} \underline{D}_y I_\phi v(\mathbf{x}) = & \sum_{j=1}^N c_j \underline{D}_y \phi(\mathbf{x}, \mathbf{x}_j) = \sum_{j=1}^N c_j \left((y - y_j)(1 - \nu_y^2(\mathbf{x})) \right. \\ & \left. - (x - x_j)\nu_x(\mathbf{x})\nu_y(\mathbf{x}) - (z - z_j)\nu_y(\mathbf{x})\nu_z(\mathbf{x}) \right) \frac{\psi'(\|\mathbf{x} - \mathbf{x}_j\|)}{\|\mathbf{x} - \mathbf{x}_j\|}; \end{aligned} \quad (2.65)$$

$$\begin{aligned} \underline{D}_z I_\phi v(\mathbf{x}) = & \sum_{j=1}^N c_j \underline{D}_z \phi(\mathbf{x}, \mathbf{x}_j) = \sum_{j=1}^N c_j \left((z - z_j)(1 - \nu_z^2(\mathbf{x})) \right. \\ & \left. - (x - x_j)\nu_x(\mathbf{x})\nu_z(\mathbf{x}) - (y - y_j)\nu_y(\mathbf{x})\nu_z(\mathbf{x}) \right) \frac{\psi'(\|\mathbf{x} - \mathbf{x}_j\|)}{\|\mathbf{x} - \mathbf{x}_j\|}, \end{aligned} \quad (2.66)$$

for $\mathbf{x} \in \Gamma$. The discrete derivative operators (2.64)-(2.66) are well-defined for all $\mathbf{x} \in \Gamma$. However, in order to carry out a numerical method for surface PDEs, we only need to evaluate these discrete tangential derivatives at the sample points $X = \{\mathbf{x}_i, i = 1, \dots, N\}$. To this

end, we introduce the matrices $B^x = (b_{ij}^x)$, $B^y = (b_{ij}^y)$, $B^z = (b_{ij}^z) \in \mathbb{R}^{N,N}$ defined respectively by

$$b_{ij}^x := \left((x_i - x_j)(1 - \nu_x^2(\mathbf{x}_i)) - (y_i - y_j)\nu_x(\mathbf{x}_i)\nu_y(\mathbf{x}_i) - (z_i - z_j)\nu_x(\mathbf{x}_i)\nu_z(\mathbf{x}_i) \right) \frac{\psi'(\|\mathbf{x}_i - \mathbf{x}_j\|)}{\|\mathbf{x}_i - \mathbf{x}_j\|}, \quad (2.67)$$

$$b_{ij}^y := \left((y_i - y_j)(1 - \nu_y^2(\mathbf{x}_i)) - (x_i - x_j)\nu_x(\mathbf{x}_i)\nu_y(\mathbf{x}_i) - (z_i - z_j)\nu_y(\mathbf{x}_i)\nu_z(\mathbf{x}_i) \right) \frac{\psi'(\|\mathbf{x}_i - \mathbf{x}_j\|)}{\|\mathbf{x}_i - \mathbf{x}_j\|}, \quad (2.68)$$

$$b_{ij}^z := \left((z_i - z_j)(1 - \nu_z^2(\mathbf{x}_i)) - (x_i - x_j)\nu_x(\mathbf{x}_i)\nu_z(\mathbf{x}_i) - (y_i - y_j)\nu_y(\mathbf{x}_i)\nu_z(\mathbf{x}_i) \right) \frac{\psi'(\|\mathbf{x}_i - \mathbf{x}_j\|)}{\|\mathbf{x}_i - \mathbf{x}_j\|}, \quad (2.69)$$

for all $i, j = 1, \dots, N$. By combining (2.64)-(2.66) with (2.67)-(2.69) we have the following expressions for discrete tangential derivatives evaluated at the sample points $X = \{\mathbf{x}_i, i = 1, \dots, N\}$:

$$\underline{D}_x I_\phi v(\mathbf{x}_i) = \sum_{j=1}^N b_{ij}^x c_j, \quad \underline{D}_y I_\phi v(\mathbf{x}_i) = \sum_{j=1}^N b_{ij}^y c_j, \quad \underline{D}_z I_\phi v(\mathbf{x}_i) = \sum_{j=1}^N b_{ij}^z c_j, \quad (2.70)$$

for all $i = 1, \dots, N$. By writing (2.70) in matrix form and using (2.54) we obtain

$$\underline{D}_x I_\phi v|_X = B^x \mathbf{c} = B^x A^{-1} \mathbf{v}_X; \quad (2.71)$$

$$\underline{D}_y I_\phi v|_X = B^y \mathbf{c} = B^y A^{-1} \mathbf{v}_X; \quad (2.72)$$

$$\underline{D}_z I_\phi v|_X = B^z \mathbf{c} = B^z A^{-1} \mathbf{v}_X, \quad (2.73)$$

The *discrete Laplace-Beltrami* operator $\Delta_{\Gamma, \phi}$ of $v \in \mathcal{C}^2(\Gamma)$ is defined as

$$\Delta_{\Gamma, \phi} v := \underline{D}_x I_\phi \underline{D}_x I_\phi v + \underline{D}_y I_\phi \underline{D}_y I_\phi v + \underline{D}_z I_\phi \underline{D}_z I_\phi v, \quad (2.74)$$

in analogy with its continuous counterpart, see Definition 4. Hence, using (2.71)-(2.73), the discrete Laplace-Beltrami operator of v at the sampling points X has the following matrix representation:

$$\Delta_{\Gamma, \phi} v|_X = L \mathbf{v}_X, \quad (2.75)$$

where $L := (B^x A^{-1})^2 + (B^y A^{-1})^2 + (B^z A^{-1})^2$. By reviewing the whole procedure, it is easy to see that L is a full matrix. The work in [52] introduces a *radial basis function-finite difference* (RBF-FD) method for the shallow water equation posed on a spherical surface, that produces a sparse discrete Laplace-Beltrami operator. The RBF-FD method was then extended to solve RDSs on *arbitrary* surfaces in [121]. However, the sparse structure of the RBF-FD method comes at the expense of the algorithmic complexity of the numerical method.

Spatially discretised problem

Consider the semilinear heat equation (2.10). With the notation introduced so far, its discrete formulation is given by

$$\frac{d}{dt}\mathbf{u}_X = dL\mathbf{u}_X - \beta\mathbf{u}_X^\alpha, \quad (2.76)$$

for $t \in [0, T]$, a nonlinear ODE system to be solved with a time integrator of choice. For instance, in [59] the 2-SBDF scheme is used to solve this system. Analogously, given the RDS (2.11), its discrete formulation is:

$$\frac{d}{dt}\mathbf{u}_{m,X} - \sum_{k=1}^r d_{mk}L\mathbf{u}_{k,X} = f_m(\mathbf{u}_{1,X}, \dots, \mathbf{u}_{r,X}), \quad (2.77)$$

for $m = 1, \dots, r$ and $t \in [0, T]$. In compact notation, system (2.77) becomes

$$\frac{d}{dt}\mathbf{u}_X - D \otimes A\mathbf{u}_X = \mathbf{b}_X, \quad (2.78)$$

for $t \in [0, T]$, where

$$\mathbf{u}_X := \begin{pmatrix} \mathbf{u}_{1,X} \\ \vdots \\ \mathbf{u}_{r,X} \end{pmatrix}, \quad \mathbf{b}_X := \begin{pmatrix} f_1(\mathbf{u}_{1,X}, \dots, \mathbf{u}_{r,X}) \\ \vdots \\ f_r(\mathbf{u}_{1,X}, \dots, \mathbf{u}_{r,X}) \end{pmatrix}.$$

Advantages and drawbacks

Advantages:

1. the method can cope with arbitrary surfaces;
2. the method only requires scattered points on the surface Γ , without any mesh or adjacency structure;
3. depending on the regularity of the chosen kernel ϕ , the method exhibits a high-order polynomial or even exponential convergence [59];

Drawbacks:

1. the discrete Laplace-Beltrami operator $\Delta_{\Gamma,\phi}$ defined in (2.75) is a full matrix;
2. the discrete Laplace-Beltrami operator $\Delta_{\Gamma,\phi}$ is typically ill-conditioned, see for instance [59].

2.6.3 Spectral Method of Lines based on Spherical Harmonics

This method, introduced by Chaplain, Ganesh and Graham in [19], is specifically devised to spatially discretise RDSs on the unit sphere, i.e. RDSs of the form (2.12) with $\Gamma = \mathcal{S}^2$. Even if the authors restrict their presentation to a RDS of two equations with Schnakenberg kinetics, their method is applicable to RDSs of arbitrarily many equations and with arbitrary kinetics. Hence, we present the spectral method of lines for an arbitrary RDS on the unit

sphere Γ . To this end, we recall from [19] some definitions. The *Associated Legendre Polynomials* are defined by

$$P_n^m(x) := \frac{(1-x^2)^{\frac{m}{2}}}{2^n n!} \frac{d^{m+n}}{dx^{m+n}}(x^2-1)^n, \quad (2.79)$$

where $x \in \mathbb{R}$, $n \in \mathbb{N} \cup \{0\}$ and $m = -n, \dots, n$. If $(\theta, \phi) \in [0, \pi] \times [0, 2\pi]$ are the spherical coordinates on \mathcal{S}^2 , the *spherical harmonics* are defined by

$$Y_n^m(\theta, \phi) := c_n^m P_n^{|m|}(\cos \theta) \exp(im\phi), \quad (2.80)$$

where

$$c_n^m = \sqrt{\frac{2n+1}{4\pi} \frac{(n-|m|)!}{(n+|m|)!}} \quad (2.81)$$

are normalization constants, $(\theta, \phi) \in [0, \pi] \times [0, 2\pi]$, $n \in \mathbb{N} \cup \{0\}$ and $m = -n, \dots, n$. The spherical harmonics are eigenfunctions for the Laplace-Beltrami operator Δ_Γ on the unit sphere Γ , i.e.

$$\Delta_\Gamma Y_n^m = -n(n+1)Y_n^m, \quad (2.82)$$

for all $n \in \mathbb{N} \cup \{0\}$ and $m = -n, \dots, n$. Moreover, the set of the spherical harmonics

$$\{Y_n^m | n \in \mathbb{N} \cup \{0\}, m = -n, \dots, n\} \quad (2.83)$$

is well-known to be a complete orthonormal set in $L^2(\Gamma)$. We recall that orthonormality means that

$$\int_\Gamma Y_n^m Y_{n'}^{m'} = \delta_{nn'} \delta_{mm'}, \quad (2.84)$$

for all $n, n' \in \mathbb{N} \cup \{0\}$, $m = -n, \dots, n$, $m' = -n', \dots, n'$ where δ_{ij} , $i, j \in \mathbb{Z}$ is the Kronecker symbol. *Complete* orthonormality implies that the exact solution \mathbf{u} of the RDS (2.11) of r equations may be uniquely expanded in the basis of spherical harmonics (2.83) as

$$\mathbf{u}(\mathbf{x}, t) = \sum_{n=0}^{+\infty} \sum_{m=-n}^n \boldsymbol{\xi}_n^m(t) Y_n^m(\mathbf{x}), \quad \mathbf{x} \in \Gamma, t \in [0, T], \quad (2.85)$$

where $\boldsymbol{\xi}_n^m(t) : [0, T] \rightarrow \mathbb{R}^r$, $n \in \mathbb{N} \cup \{0\}$, $m = -n, \dots, n$, are time-dependent coefficients.

Given $N \in \mathbb{N}$, consider an approximate solution $\mathbf{U}(\mathbf{x}, t)$ to the RDS (2.11) in the form of a *truncated* expansion in the same basis (2.83):

$$\mathbf{U}(\mathbf{x}) = \sum_{n=0}^{N-1} \sum_{m=-n}^n \boldsymbol{\eta}_n^m(t) Y_n^m(\mathbf{x}), \quad \mathbf{x} \in \Gamma, t \in [0, T], \quad (2.86)$$

where $\boldsymbol{\eta}_n^m(t) : [0, T] \rightarrow \mathbb{R}^r$, $n \in \mathbb{N} \cup \{0\}$ and $m = -n, \dots, n$ are time-dependent coefficients.

In order to introduce the numerical method, we first consider the following weak formulation³ of the RDS (2.12):

$$\int_\Gamma \frac{\partial \mathbf{u}}{\partial t} Y_n^m d\sigma + \int_\Gamma D \Delta_\Gamma \mathbf{u} Y_n^m d\sigma = \int_\Gamma \mathbf{f}(\mathbf{u}) Y_n^m d\sigma, \quad (2.87)$$

³This formulation differs from the usual weak formulation (2.37). This alternative weak formulation will allow for the derivation of a reasonably simple numerical method.

for all $n \in \mathbb{N} \cup \{0\}$, $m = -n, \dots, n$. The spectral method of lines seeks to find an approximate solution $\mathbf{U}(\mathbf{x}, t)$ by mimicking the weak formulation (2.87):

$$\int_{\Gamma} \frac{\partial \mathbf{U}}{\partial t} Y_n^m d\sigma + \int_{\Gamma} D\Delta_{\Gamma} \mathbf{U} Y_n^m d\sigma = \int_{\Gamma} \mathbf{f}(\mathbf{U}) Y_n^m d\sigma, \quad (2.88)$$

for all $n = 0, \dots, N$, $m = -n, \dots, n$. By choosing an approximate solution $U(\mathbf{x}, t)$ of the form (2.86) and using (2.82), the method (2.88) becomes

$$\sum_{n'=0}^{N-1} \sum_{m=-n'}^{n'} \left[\dot{\boldsymbol{\eta}}_{m'}^{n'}(t) \int_{\Gamma} Y_{n'}^{m'} Y_n^m d\sigma - n(n+1) D\boldsymbol{\eta}_{m'}^{n'}(t) \int_{\Gamma} Y_{n'}^{m'} Y_n^m d\sigma \right] = \int_{\Gamma} \mathbf{f}(\mathbf{U}) Y_n^m d\sigma, \quad (2.89)$$

for all $n = 0, \dots, N$, $m = -n, \dots, n$. By using the orthonormality property (2.84), the formulation (2.89) reduces to

$$\dot{\boldsymbol{\eta}}_n^m(t) - n(n+1) D\boldsymbol{\eta}_n^m(t) = \int_{\Gamma} \mathbf{f}(\mathbf{U}) Y_n^m d\sigma, \quad (2.90)$$

for all $n = 0, \dots, N-1$, $m = -n, \dots, n$, $t \in [0, T]$. By approximating the right-hand side of (2.90) with a Gauss-Legendre quadrature rule for the sphere (see [19] and reference therein), the formulation (2.90) becomes an ODE system in the N^2 vector-valued unknowns $\mathbf{U}_n^m(t)$, $n = 0, \dots, N-1$, $m = -n, \dots, n$, i.e. in rN^2 real-valued unknowns, where r is the number of equations in the RDS (2.12). Such quadrature rule should have a degree of accuracy $M \in \mathbb{N}$ with grows suitably with N in order to preserve the exponential convergence of the method. This relation between M and N depends on the nature of the kinetics and is discussed in [19].

Advantages and drawbacks

Advantages:

1. Since the method is based on a spectral decomposition of the solution, the convergence is exponential, see [19].

Drawbacks:

1. The method is limited to spherical surfaces;
2. The numerical approximation of the right-hand-side of (2.90) using quadrature formulas of suitable order is the bulk of the algorithmic complexity of the method.

2.6.4 Planar parametrisation through spherical coordinates

Another method specifically designed for RDSs on the unit sphere $\Gamma = \mathcal{S}^2$, presented by Varea, Aragón and Barrio [133], is based on the planar parametrisation of the sphere through spherical coordinates. The authors restrict the presentation to a particular RDS of two equations, but their method is applicable to arbitrary RDSs on the unit sphere. Hence, we present the method for general RDSs on the unit sphere.

Let $(\theta, \phi) \in [0, \pi] \times [0, 2\pi]$ be the spherical coordinates of the unit sphere Γ . We recall that the relation between the Cartesian coordinates (x, y, z) and the spherical coordinates (θ, ϕ) of any point of the unit sphere Γ is

$$\begin{cases} x = \sin \theta \cos \phi; \\ y = \sin \theta \sin \phi; \\ z = \cos \theta. \end{cases} \quad (\theta, \phi) \in [0, \pi] \times [0, 2\pi]. \quad (2.91)$$

Given any function $v(x, y, z)$ defined on the unit sphere Γ , we denote by $v(\theta, \phi)$ its planar parametrisation through spherical coordinates(2.91). If $v(x, y, z)$ is $\mathcal{C}^2(\Gamma)$, the planar parametrisation $\Delta_\Gamma v(\theta, \phi)$ of the surface Laplacian $\Delta_\Gamma v(x, y, z)$ has the following expression:

$$\Delta_\Gamma v(\theta, \phi) = \frac{1}{\sin \theta} \frac{\partial}{\partial \theta} \left(\sin \theta \frac{\partial v}{\partial \theta}(\theta, \phi) \right) + \frac{1}{\sin^2 \theta} \frac{\partial^2 v}{\partial \phi^2}(\theta, \phi), \quad (\theta, \phi) \in [0, \pi] \times [0, 2\pi], \quad (2.92)$$

see for instance [69, Appendix A]. Using (2.92), the planar parametrisation of the RDS system (2.12) is

$$\frac{\partial \mathbf{u}}{\partial t}(\theta, \phi, t) - D \frac{1}{\sin \theta} \frac{\partial}{\partial \theta} \left(\sin \theta \frac{\partial \mathbf{u}}{\partial \theta}(\theta, \phi, t) \right) + \frac{1}{\sin^2 \theta} \frac{\partial^2 \mathbf{u}}{\partial \phi^2}(\theta, \phi, t) = \mathbf{f}(\mathbf{u}(\theta, \phi, t)), \quad (2.93)$$

for $(\theta, \phi, t) \in [0, \pi] \times [0, 2\pi] \times [0, T]$, with additional boundary conditions

$$\mathbf{u}(\theta, 0, t) = \mathbf{u}(\theta, 2\pi, t), \quad \theta \in [0, \pi], \quad t \in [0, T], \quad (2.94)$$

$$\mathbf{u}(0, \phi, t) = \mathbf{u}(0, \phi + \pi, t), \quad \phi \in [0, \pi], \quad t \in [0, T], \quad (2.95)$$

$$\mathbf{u}(\pi, \phi, t) = \mathbf{u}(\pi, \phi + \pi, t), \quad \phi \in [0, \pi], \quad t \in [0, T]. \quad (2.96)$$

System (2.93)-(2.96) is a PDE system on the planar domain $[0, \pi] \times [0, 2\pi]$ that can be spatially discretised with any method of choice. For instance, Varea, Aragón and Barrio [133] choose finite differences on a grid constructed as follows. Given $M, N \in \mathbb{N}$ with N even, let

$$h_\theta := \frac{\pi}{M}, \quad h_\phi := \frac{2\pi}{N}. \quad (2.97)$$

The parameter space $[0, \pi] \times [0, 2\pi]$ is discretised with a rectangular grid constructed on the following $M \times N$ points:

$$\theta_m := \left(m + \frac{1}{2} \right) h_\theta, \quad m = 0, \dots, M-1, \quad (2.98)$$

$$\phi_n := n h_\phi, \quad n = 0, \dots, N-1. \quad (2.99)$$

On such grid, the boundary conditions (2.94)-(2.96) become

$$\mathbf{u}(\theta_m, \phi_0, t) = \mathbf{u}(\theta_m, \phi_{N-1}, t), \quad m = 0, \dots, M-1, \quad t \in [0, T]; \quad (2.100)$$

$$\mathbf{u}(\theta_0, \phi_n, t) = \mathbf{u}(\theta_0, \phi_{n+\frac{N}{2}}, t), \quad n = 0, \dots, \frac{N}{2} - 1, \quad t \in [0, T]; \quad (2.101)$$

$$\mathbf{u}(\theta_{M-1}, \phi_n, t) = \mathbf{u}(\theta_{M-1}, \phi_{n+\frac{N}{2}}, t), \quad n = 0, \dots, \frac{N}{2} - 1, \quad t \in [0, T], \quad (2.102)$$

From (2.92) we can see that the parametrised Laplace-Beltrami operator is singular when $\theta = 0$ or $\theta = \pi$, i.e. at the poles of the unit sphere. In order to avoid these singularities in the numerical method, the grid constructed by Varea, Aragón and Barrio avoids the points of $[0, \pi] \times [0, 2\pi]$ with $\theta = 0$ or $\theta = \pi$, as we can see in (2.98).

Advantages and drawbacks

Advantages:

1. Simplicity: the parametrisation through spherical coordinates reduces the problem to a PDE on a rectangle, which is easily solved by finite differences on a rectangular grid.

Drawbacks:

1. This approach is limited to surfaces that admit a global parametrisation, e.g. ellipsoids or spheres;
2. The presence of singularities in the spherical coordinates is a bottleneck in the convergence rate of the method, as discussed in [133].

2.6.5 Embedding methods and level set method

Consider a PDE on a surface $\Gamma \subset \mathbb{R}^3$ and let u be its solution. The paradigm of *embedding methods* is to consider a three-dimensional compact neighbourhood W of Γ and to derive an auxiliary PDE posed on W such that its solution, restricted to Γ , coincides with u or is a good approximation of u . The auxiliary PDE on W can be then discretised with any numerical method for PDEs on three-dimensional domains. There are different classes of embedding methods in the literature, such as *level set methods* [12, 67], *closest point methods* [90, 115] or finite elements in the embedding space [24]. However, for illustrative purposes, we present the level set method presented in [12] and improved in [67].

Level set methods are particular embedding methods that require the surface Γ to be represented as a level set of a function defined on a higher-dimensional domain. Precisely, let $U \subset \mathbb{R}^3$ be an open set and let $\phi : U \rightarrow \mathbb{R}$ be a \mathcal{C}^2 function, called the *level function*, such that $\nabla\phi(\mathbf{x}) \neq \mathbf{0}$ for all $x \in U$. Let Γ be the *zero level surface* defined by

$$\Gamma := \{\mathbf{x} \in U \mid \phi(\mathbf{x}) = 0\}. \quad (2.103)$$

Notice that this definition is stronger than Definition 1, as a zero level surface can be represented through one global level function. We present the method in [12], which can be considered the pioneering work in the field of level set methods. First, we have to make an appropriate choice for the compact neighbourhood W of Γ on which the auxiliary PDE will be posed, as clarified in the later paper [67]. To this end, let $\varepsilon > 0$ be a sufficiently small number such that the neighbourhood U_ε of Γ defined by

$$U_\varepsilon := \{\mathbf{x} \in \mathbb{R}^3 \mid |\phi(\mathbf{x})| \leq \varepsilon\}, \quad (2.104)$$

is contained in U . We choose $W = U_\varepsilon$. Second, the initial data $u_{0,W}$ of the auxiliary PDE on W is chosen as the constant extension of the initial data $u_0 : \Gamma \rightarrow \mathbb{R}$ in the normal direction to Γ , defined as follows:

$$\begin{cases} \nabla u_{0,W}(\mathbf{x}) \cdot \nabla\phi(\mathbf{x}) = 0, & \mathbf{x} \in W; \\ u_{0,W}(\mathbf{x}) = u_0(\mathbf{x}), & \mathbf{x} \in \Gamma, \end{cases} \quad (2.105)$$

see [12]. Finally, given a PDE on the zero level surface Γ , the corresponding auxiliary PDE on W must be determined. For instance, the authors of [12] prove that the homogeneous heat equation on Γ

$$\begin{cases} \frac{\partial u}{\partial t}(\mathbf{x}, t) - d\Delta_{\Gamma}u(\mathbf{x}, t) = 0, & (\mathbf{x}, t) \in \Gamma \times [0, T]; \\ u(\mathbf{x}, 0) = u_0(\mathbf{x}), & \mathbf{x} \in \Gamma, \end{cases} \quad (2.106)$$

where $d > 0$, is equivalent⁴ to the following PDE on W

$$\begin{cases} \frac{\partial u}{\partial t}(\mathbf{x}, t) - \frac{1}{\|\nabla\phi(\mathbf{x})\|} \nabla \cdot (P(\mathbf{x})\nabla u(\mathbf{x}, t)\|\nabla\phi(\mathbf{x})\|), & (\mathbf{x}, t) \in W \times [0, T]; \\ u(\mathbf{x}, 0) = u_{0,W}(\mathbf{x}), & \mathbf{x} \in W, \end{cases} \quad (2.107)$$

where \otimes denotes the Kronecker product, $u_{0,W}$ is defined in (2.106), $P(\mathbf{x})$ is the projection matrix onto the plane orthogonal to $\nabla\phi(\mathbf{x})$, defined by

$$P(\mathbf{x}) := I_3 - \frac{\nabla\phi(\mathbf{x})^{tr} \otimes \nabla\phi(\mathbf{x})}{\|\nabla\phi(\mathbf{x})\|^2}, \quad \mathbf{x} \in W, \quad (2.108)$$

where I_3 is the 3×3 identity matrix. As explained in [67, Section 2.3], even if W has a non-empty boundary, the PDE (2.107) does not need any boundary condition in order to be well-posed.

The authors of [12] numerically approximate (2.107) through finite differences in space. However, in contrast to the continuous formulation (2.107), its spatially discretised counterpart does need boundary conditions in order to be well-posed, but such appropriate boundary conditions cannot be determined exactly. The authors of [12] face this problem by frequently restarting the PDE with initial (and boundary) data defined by (2.106). The method was improved in [67] in order to overcome this limitation. Specifically, the author of [67] replaces the operator $P(\mathbf{x})$ defined in (2.108) with

$$\tilde{P}(\mathbf{x}) := (I_3 + \phi(\mathbf{x})\nabla^2\phi(\mathbf{x}))^{-1}P(\mathbf{x}), \quad \mathbf{x} \in W, \quad (2.109)$$

where $\nabla^2\phi(\mathbf{x})$ is the Hessian matrix of $\phi(\mathbf{x})$. With this choice, the solution $u(\mathbf{x}, t)$ of the following modified auxiliary PDE

$$\begin{cases} \frac{\partial u}{\partial t}(\mathbf{x}, t) - \frac{1}{\|\nabla\phi(\mathbf{x})\|} \nabla \cdot (\tilde{P}(\mathbf{x})\nabla u(\mathbf{x}, t)\|\nabla\phi(\mathbf{x})\|), & (\mathbf{x}, t) \in W \times [0, T]; \\ u(\mathbf{x}, 0) = u_{0,W}(\mathbf{x}), & \mathbf{x} \in W, \end{cases} \quad (2.110)$$

remains constant in the normal direction to Γ at all times, i.e.

$$\nabla u(\mathbf{x}, t) \cdot \nabla\phi(\mathbf{x}) = 0, \quad (\mathbf{x}, t) \in W \times [0, T]. \quad (2.111)$$

Since, from (2.104), the boundary of W is a level set of ϕ , the property (2.111) implies that $u(\mathbf{x}, t)$ fulfils homogeneous Neumann boundary conditions on the boundary of W , as shown in [67, Section 3.3]. Hence, the spatial discretisation of problem (2.110) must be complemented with homogeneous Neumann boundary conditions.

⁴meaning that the solution of (2.107), restricted to Γ , coincides with the solution of (2.106).

Advantages and drawbacks

Advantages:

- The method handles arbitrary surfaces without boundary;
- Since the auxiliary PDE is defined in a three-dimensional domain, it can be discretised with any existing method for PDEs in 3D. This avoids the difficulties of discretising surface differential operators on arbitrary surfaces.

Drawbacks:

- solving a PDE in a higher dimensional domain increases the computational complexity;
- in the original level set method [12] it is not clear which boundary conditions are to be enforced on the boundary of the narrow band W . This problem is removed in the improved method presented by Greer [67];
- the auxiliary PDE is much more complicated than the original surface PDE, especially in the improved method proposed by Greer [67].

2.7 Conclusions

In this chapter we have set the necessary notions to understand and motivate the novel results in the remainder of the thesis. In particular, we have recalled in detail the SFEM for elliptic and parabolic PDE problems on compact surfaces, introduced in [37] and [39], respectively. We have reviewed some of the existing methods for such PDE problems, thereby discussing some advantages and drawback of each method. In the next chapter we present a novel extension of the SFEM, called Surface Virtual Element Method (SVEM) for the numerical approximation of the Laplace-Beltrami equation.

Chapter 3

The Surface Virtual Element Method for the Laplace-Beltrami equation

The Surface Virtual Element Method (SVEM), introduced in the recent work [58] is a novel extension of the SFEM that allows for polygonal approximations Γ_h of the surface Γ in which each face of Γ_h is a polygon with arbitrarily many edges.

The Virtual Element Method (VEM) for PDEs on planar domains was first introduced in [8] for the Laplace equation and was then extended to several classes of partial differential equations on planar domains. A non exhaustive list is: linear elasticity [30], plate bending [17], fracture problems [10], eigenvalue problems [98], Cahn-Hilliard equation [3], heat [130] and wave equations [129].

The core idea of the virtual element paradigm is that, given a polynomial order $k \in \mathbb{N}$ and a polygonal element K , the local basis function space on K includes the polynomials of degree k (thus ensuring the optimal degree of accuracy) plus other basis functions that are not known in closed form [8]. The presence of these *virtual* functions motivates the name of the method. However, the knowledge of certain degrees of freedom attached to the basis functions is sufficient to compute the discrete bilinear forms with a degree of accuracy k . The aim of the present chapter is to consider the VEM in the case $k = 1$ and extend it to solve *surface PDEs*, i.e. PDEs having a two-dimensional smooth surface in \mathbb{R}^3 as spatial domain. Here we will focus on the Laplace-Beltrami equation (2.9), that is the prototypical second order elliptic PDE on smooth surfaces.

We will show that the novel SVEM has an improved geometric flexibility with respect to the triangular SFEM, as it handles *polygnal* and/or *nonconforming* meshes (see [5, 8] for the case of planar domains). This increased flexibility can be exploited in mesh pasting. In fact, nonconforming meshes naturally arise when pasting several meshes to obtain a polygonal approximation of the whole domain or surface [11, 22] and, in contrast to conforming pasting techniques [75, 122], there is no need to match the nodal points.

We prove, under minimal shape regularity assumptions on the polygonal mesh, some error estimates for the approximation of surfaces and for the projection operators and bilinear forms involved in the method. Furthermore, we prove the existence and uniqueness of the discrete solution and a first order (and thus optimal) H^1 error estimate.

Numerical examples are provided to show (i) the application of the SVEM to mesh pasting and (ii) that the experimental order of convergence in H^1 norm is linear as predicted by our analysis.

The structure of the chapter is as follows. In Section 3.1 we introduce polygonal approximation of surfaces and discrete function spaces involved in the method. In Section 3.2 we present the SVEM discretisation of the Laplace-Beltrami equation. In Section 3.3 we prove error estimates for the discrete bilinear forms and the approximation of geometry. In Section 3.4 we prove existence, uniqueness and first order H^1 convergence of the numerical solution. In Section 3.5 we face with the issues related to the implementation of the SVEM. In Section 3.6 we (i) discuss some advantages of the SVEM when applied to mesh pasting and (ii) present three numerical examples on a sphere, a torus and a cylinder, respectively.

3.1 Approximation of the surface and discrete function spaces

We now introduce polygonal approximations of surfaces (or *polygonations*) that generalise at once (i) the triangulations of the SFEM considered in Subsection 2.5.1 and (ii) the planar polygonal meshes of the VEM introduced in [8].

Given a \mathcal{C}^2 surface in \mathbb{R}^3 and a number $h > 0$ called *meshsize*, a polygonation Γ_h of Γ is defined by

$$\Gamma_h = \bigcup_{K \in \mathcal{K}_h} K, \quad (3.1)$$

where

- each $K \in \mathcal{K}_h$ is a *simple* polygon in \mathbb{R}^3 , i.e. without holes and with non self-intersecting boundary, such that the diameter h_K of K does not exceed h ;
- the $N \in \mathbb{N}$ vertices \mathbf{x}_i , $i = 1, \dots, N$ of Γ_h (called *nodes*) lie on Γ ;
- for any $K_1, K_2 \in \mathcal{K}_h$ with $K_1 \neq K_2$, the intersection $K_1 \cap K_2$ is either empty, or a common vertex, or a common edge of K_1 and K_2 ;
- Γ_h is contained in the Fermi stripe U associated to Γ , see Lemma 1;
- if $\mathbf{a} : U \rightarrow \Gamma$ is the normal projection defined in Lemma 1, the restriction $\mathbf{a}|_{\Gamma_h} : \Gamma_h \rightarrow \Gamma$ is one-to-one.

Different examples of polygonations are depicted in Figures 3.5(a), 3.6(a) and 3.7(a). Let $\boldsymbol{\nu}_h = (\nu_{h,1}, \nu_{h,2}, \nu_{h,3}) : \Gamma_h \rightarrow \mathbb{R}^3$ denote the outward unit normal vector field on Γ_h . Notice that $\boldsymbol{\nu}_h$ is piecewise constant as $\boldsymbol{\nu}_h$ is constant on every face $K \in \mathcal{K}_h$. Furthermore, we consider the following mesh regularity assumptions in the remainder of the chapter. There exist $\gamma_1, \gamma_2 > 0$ such that, for all $h > 0$, for any polygonation Γ_h of Γ and for any $K \in \mathcal{K}_h$,

(A1) K is star-shaped with respect to a ball of radius ρ_K such that

$$\rho_K \geq \gamma_1 h_K;$$

(A2) for every pair of nodes $P, Q \in K$, the distance $\|P - Q\|$ fulfils

$$\|P - Q\| \geq \gamma_2 h_K.$$

We now define a discrete function space on Γ_h . To this end, given $K \in \mathcal{K}_h$ we consider the space $\tilde{\mathbb{V}}_h(K)$ defined by

$$\tilde{\mathbb{V}}_h(K) := \{V \in H^1(K) \mid V|_e \in \mathbb{P}_1(e) \ \forall e \in \text{edges}(K), \Delta_K V \in \mathbb{P}_1(K)\}.$$

We remark that functions in $\tilde{\mathbb{V}}_h(K)$ are virtual, i.e. they are not known in closed form. For this reason, in order to formulate a computable numerical method, we consider the projection $\Pi_K^\nabla : \tilde{\mathbb{V}}_h(K) \rightarrow \mathbb{P}_1(K)$ defined by

$$\int_K \nabla_K \Pi_K^\nabla(V) \cdot \nabla_K q_1 = \int_K \nabla_K V \cdot \nabla_K q_1, \quad \forall q_1 \in \mathbb{P}_1(K); \quad (3.2)$$

$$\sum_{P \in \text{nodes}(K)} \Pi_K^\nabla V(P) = \sum_{P \in \text{nodes}(K)} V(P), \quad (3.3)$$

where (3.3) is needed to fix the free constant in (3.2). Exactly as in the case of planar domains considered in [8], this projection is computable. The *local virtual element space* is defined by

$$\mathbb{V}_h(K) := \left\{ V \in \tilde{\mathbb{V}}_h(K) \mid \int_K (V - \Pi_K^\nabla V) q_1 = 0 \ \forall q_1 \in \mathbb{P}_1(K) \right\}. \quad (3.4)$$

In [1] it has been proven, for the special case of planar domains, that the nodal values $\{V(P) \mid P \in \text{nodes}(K)\}$ are *unisolvent* for $\mathbb{V}_h(K)$, i.e. any specific choice of the nodal values uniquely identifies a function in $\mathbb{V}_h(K)$. Through a linear mapping argument it follows immediately that the same result holds when K is a polygon in \mathbb{R}^3 . Moreover, even if the functions in $\mathbb{V}_h(K)$ are still not known in closed form, we will be able to formulate a computable numerical method by using this function space. The *global virtual element space* \mathbb{V}_h is defined by

$$\mathbb{V}_h := \{V \in \mathcal{C}^0(\Gamma_h) \mid V|_K \in \mathbb{V}_h(K) \ \forall K \in \mathcal{K}_h\}. \quad (3.5)$$

For each $i = 1, \dots, N$, the i -th *virtual basis function* χ_i is the unique \mathbb{V}_h function such that

$$\chi_i(\mathbf{x}_j) = \delta_{ij}, \quad i, j = 1, \dots, N.$$

Since the nodal values $\{V(\mathbf{x}_i) \mid i = 1, \dots, N\}$ are unisolvent for \mathbb{V}_h , the set $\{\chi_i \mid i = 1, \dots, N\}$ is a basis for \mathbb{V}_h . In analogy with the Lagrange interpolant considered in Subsection 2.5.1 for the SFEM, we define the *virtual interpolant* $I_h(v)$ of a function $v \in \mathcal{C}^0(\Gamma)$ or $v \in \mathcal{C}^0(\Gamma_h)$ as the unique \mathbb{V}_h function such that

$$I_h(v)(\mathbf{x}_i) = v(\mathbf{x}_i), \quad i = 1, \dots, N. \quad (3.6)$$

Similarly to the expansion (2.21) considered for the SFEM case, $I_h(v)$ can be expressed in the virtual basis as

$$I_h(v)(\mathbf{x}) = \sum_{i=1}^N v(\mathbf{x}_i) \chi_i(\mathbf{x}), \quad \mathbf{x} \in \Gamma_h.$$

Furthermore, we define the *average-free virtual element space* as

$$\mathbb{V}_{h,0} := \left\{ V \in \mathbb{V}_h \mid \int_{\Gamma_h} V = 0 \right\}. \quad (3.7)$$

We observe that, from definition (3.5), the integral in (3.7) is computable even if the functions in \mathbb{V}_h are not known in closed form.

3.2 The SVEM space discretisation

In this section we introduce, following our recent work [58], the SVEM discretisation of the weak Laplace-Beltrami equation (2.15). Let Γ be a \mathcal{C}^3 surface without boundary and let Γ_h be a triangulation of Γ as defined in Section 2.5.1.

3.2.1 Approximation of the $a(\cdot, \cdot)$ form

Let $K \in \mathcal{K}_h$. Since the functions in $\mathbb{V}_h(K)$ cannot be expressed in closed form, the local bilinear form $a_{h,K} : \mathbb{V}_h(K) \times \mathbb{V}_h(K) \rightarrow \mathbb{R}$ defined by $a_{h,K}(U, V) := \int_K \nabla_K U \cdot \nabla_K V$ for all $U, V \in \mathbb{V}_h(K)$ is not computable. Hence, we need to define a computable bilinear form $b_{h,K} : \mathbb{V}_h(K) \times \mathbb{V}_h(K) \rightarrow \mathbb{R}$ that approximates $a_{h,K}$, defined by

$$b_{h,K}(U, V) := \int_K \nabla_K \Pi_K^\nabla U \cdot \nabla_K \Pi_K^\nabla V + S_K((Id - \Pi_K^\nabla)U, (Id - \Pi_K^\nabla)V), \quad (3.8)$$

for all $U, V \in \mathbb{V}_h(K)$, where $S_K : \mathbb{V}_h(K) \times \mathbb{V}_h(K) \rightarrow \mathbb{R}$ is the *stabilising form* defined by

$$S_K(U, V) := \sum_{P \in \text{nodes}(K)} U(P)V(P), \quad U, V \in \mathbb{V}_h(K). \quad (3.9)$$

Notice that, since $\Pi_K^\nabla q_1 = q_1$ for all $q_1 \in \mathbb{P}_1(K)$, the local form $b_{h,K}$ fulfils the consistency property

$$b_{h,K}(U, q_1) = a_{h,K}(U, q_1), \quad U \in \mathbb{V}_h(K), \quad q_1 \in \mathbb{P}_1(K). \quad (3.10)$$

Moreover, under the mesh regularity assumptions (A1)-(A2), S_K scales as $a_{h,K}$ on the kernel of Π_K^∇ , i.e. there exist $c^* > c_* > 0$ such that

$$c_* a_{h,K}(U, V) \leq S_K(U, V) \leq c^* a_{h,K}(U, V), \quad U, V \in \ker \Pi_K^\nabla, \quad (3.11)$$

see [8]. We can now define a global bilinear form $b_h : \mathbb{V}_h \times \mathbb{V}_h \rightarrow \mathbb{R}$ as follows

$$b_h(U, V) := \sum_{K \in \mathcal{K}_h} b_{h,K}(U|_K, V|_K), \quad U, V \in \mathbb{V}_h. \quad (3.12)$$

3.2.2 Approximation of the average-free condition

In order to impose the condition $\int_{\Gamma_h} U = 0$ to the numerical solution U , we need to define a computable approximate L^2 inner product on \mathbb{V}_h . To this end, let $K \in \mathcal{K}_h$. We consider the local projection $\Pi_K^0 : \mathbb{V}_h(K) \rightarrow \mathbb{P}_1(K)$ defined by

$$\int_K \Pi_K^0 U q_1 = \int_K U q_1, \quad q_1 \in \mathbb{P}_1(K). \quad (3.13)$$

We remark that $\Pi_K^0 = \Pi_K^\nabla$, see for instance [1]. Hence, Π_K^0 is computable. Following [8], we define the following local approximate $L^2(K)$ form

$$\langle U, V \rangle_{M,K} := \int_K \Pi_K^0 U \Pi_K^0 V + |K| S_K((Id - \Pi_K^0)U, (Id - \Pi_K^0)V), \quad U, V \in \mathbb{V}_h(K), \quad (3.14)$$

where S_K and Π_K^0 are defined in (3.9) and (3.13), respectively, and $|K|$ is the area of K . Notice that the bilinear form in (3.14) fulfils the following consistency property

$$\langle U, q_1 \rangle_{M,K} = \langle U, q_1 \rangle_{0,K}, \quad U \in \mathbb{V}_h(K), \quad q_1 \in \mathbb{P}_1(K). \quad (3.15)$$

A computable global approximate L^2 form is obtained by pasting the local ones:

$$\langle U, V \rangle_M := \sum_{K \in \mathcal{K}_h} \langle U|_K, V|_K \rangle_{M,K}, \quad U, V \in \mathbb{V}_h. \quad (3.16)$$

As a consequence of (3.15) and (3.16), we have that the integral of any function in \mathbb{V}_h can be computed exactly, i.e.

$$\langle U, 1 \rangle_M = \int_{\Gamma_h} U, \quad U \in \mathbb{V}_h. \quad (3.17)$$

Property (3.17) implies that the average-free virtual element space $\mathbb{V}_{h,0}$ can be represented as

$$\mathbb{V}_{h,0} := \{U \in \mathbb{V}_h \mid \langle U, 1 \rangle_M = 0\}. \quad (3.18)$$

Hence, the space $\mathbb{V}_{h,0}$ is computable. We will utilise the representation (3.18) of $\mathbb{V}_{h,0}$ for the implementation of the SVEM.

3.2.3 Approximation of the right-hand-side

Let $f \in H_0^2(\Gamma)$ be a load term (see Remark 5). Analogously to the SFEM, we consider an average-free approximation f_h of $I_h(f)$ defined as

$$f_h(\mathbf{x}) = I_h(f)(\mathbf{x}) - \frac{1}{|\Gamma_h|} \int_{\Gamma_h} I_h(f), \quad \mathbf{x} \in \Gamma_h, \quad (3.19)$$

By construction, f_h fulfils $\int_{\Gamma_h} f_h = 0$. To approximate the right hand side of the weak formulation (2.15), following [8], we consider the functional $\langle f_h, \cdot \rangle_R : \mathbb{V}_h \rightarrow \mathbb{R}$ defined by

$$\langle f_h, V \rangle_R := \sum_{K \in \mathcal{K}_h} \int_K f_h \sum_{P \in \text{nodes}(K)} \frac{V(P)}{n_K}, \quad V \in \mathbb{V}_h, \quad (3.20)$$

where n_K is the number of vertices of K . From (3.17) we have that $\langle f_h, V \rangle_R$ is computable, given the degrees of freedom of f_h and V . Furthermore, notice that

$$\langle f_h, 1 \rangle_R = \langle f_h, 1 \rangle_M = \int_{\Gamma_h} f_h = 0. \quad (3.21)$$

3.2.4 Discrete formulation

We may now ready to introduce the SVEM approximation of the Laplace-Beltrami equation (2.15):

$$\begin{aligned} & \text{find } U \in \mathbb{V}_h \text{ such that} \\ & \begin{cases} b_h(U, \phi) = \langle f_h, \phi \rangle_R & \forall \phi \in \mathbb{V}_h; \\ \langle U, 1 \rangle_M = 0, \end{cases} \end{aligned} \quad (3.22)$$

By using (3.18) and the consistency properties (3.10) and (3.15), the discrete Laplace-Beltrami problem (3.22) is equivalent to

$$\text{find } U \in \mathbb{V}_{h,0} \text{ such that } b_h(U, \phi) = \langle f_h, \phi \rangle_R \quad \forall \phi \in \mathbb{V}_{h,0}. \quad (3.23)$$

3.3 Interpolation, projection and geometric error estimates

In this subsection we recall and introduce some results that are crucial to analyse the SVEM in terms of existence, uniqueness and optimal convergence of the numerical solution. The following result taken from [16] addresses the projection error in $\mathbb{P}_1(K)$ for all $K \in \mathcal{K}_h$.

Theorem 6. *Under the mesh regularity assumptions (A1)-(A2), there exists $C > 0$ depending only on the constants γ_1, γ_2 defined (A1)-(A2) such that, for $s \in \{1, 2\}$ and for all $V \in H^s(K)$, there exists a $V_\pi \in \mathbb{P}_1(K)$ such that*

$$\|V - V_\pi\|_{0,K} + h_K |V - V_\pi|_{1,K} \leq Ch_K^s |V|_{s,K}. \quad (3.24)$$

The following theorem from [8] gives an interpolation error estimate in $\mathbb{V}_h(K)$ for all $K \in \mathcal{K}_h$.

Theorem 7. *Under the mesh regularity assumption (A1), there exists $C > 0$, depending only on the constant γ_1 defined in (A1), such that for all $V \in H^2(K)$, the interpolant $I_h(V) \in \mathbb{V}_h(K)$ fulfils*

$$\|V - I_h(V)\|_{0,K} + h_K |V - I_h(V)|_{1,K} \leq Ch_K^2 |V|_{2,K}. \quad (3.25)$$

To approximate integrals and bilinear forms under lifting, a geometric error must be taken into account. To this end, we recall some geometric quantities from [40]. For any $\mathbf{x} \in \Gamma_h$, let $B_\varepsilon(\mathbf{x})$ be an open ball (in the topology of Γ_h) centred in \mathbf{x} with radius ε . The quotient δ_h between the smooth and discrete surface measures is defined by

$$\delta_h(\mathbf{x}) = \lim_{\varepsilon \rightarrow 0} \frac{\text{meas}(\mathbf{a}(B_\varepsilon(\mathbf{x})))}{\text{meas}(B_\varepsilon(\mathbf{x}))}, \quad \mathbf{x} \in \Gamma_h, \quad (3.26)$$

where meas denotes the two-dimensional Hausdorff measure in \mathbb{R}^3 . Let $P_h : \Gamma_h \rightarrow \mathbb{R}^{3,3}$ be the matrix-valued function representing the projection onto Γ_h , defined by

$$P_{h,ij}(\mathbf{x}) := (\delta_{ij} - \nu_{h,i}(\mathbf{x})\nu_{h,j}(\mathbf{x})), \quad \mathbf{x} \in \Gamma_h, \quad i, j = 1, 2, 3. \quad (3.27)$$

This operator is the discrete counterpart of the projection P onto the continuous surface Γ , introduced in Definition 2. Let $\mathcal{H} : \Gamma \rightarrow \mathbb{R}^{3,3}$ be the Weingarten map of Γ defined by

$$\mathcal{H}_{ij}(\mathbf{x}) := \underline{D}_i \nu_j(\mathbf{x}), \quad \mathbf{x} \in \Gamma, \quad i, j = 1, 2, 3. \quad (3.28)$$

Let now $\mathcal{Q}_h : \Gamma_h \rightarrow \mathbb{R}^3$ be the matrix-valued function defined by

$$\mathcal{Q}_h(\mathbf{x}) := \frac{1}{\delta_h(\mathbf{x})} P(\mathbf{a}(\mathbf{x}))(I - d(\mathbf{x})\mathcal{H}(\mathbf{a}(\mathbf{x})))P_h(\mathbf{x})(I - d(\mathbf{x})\mathcal{H}(\mathbf{a}(\mathbf{x})))P(\mathbf{a}(\mathbf{x})), \quad \mathbf{x} \in \Gamma_h. \quad (3.29)$$

In the following lemma we provide geometric error estimates. The result extends [40, Lemma 4.1], devoted to triangulations, to the case when Γ_h is a polygonation of Γ as described in Subsection 3.1.

Lemma 3. *Let Γ_h be a polygonal approximation of Γ as in Subsection 3.1. The oriented distance function $d(\cdot)$ introduced in (2.3) fulfils*

$$\|d(\cdot)\|_{\infty,h} \leq Ch^2. \quad (3.30)$$

The surface measure quotient δ_h defined in (3.26) fulfils

$$\|1 - \delta_h\|_{\infty, h} \leq Ch^2. \quad (3.31)$$

The following estimate holds

$$\|P - Q_h\|_{\infty, h} \leq Ch^2. \quad (3.32)$$

In all of the claimed inequalities C depends only on the curvature of Γ .

Proof. Throughout this proof we denote by $d(\cdot)$ the oriented distance function defined in (2.3), in order to avoid confusion with the diffusion coefficient defined in (2.10). We start by recalling the definition of the $|\cdot|_{\mathcal{C}^2}$ seminorm on polygons, segments and bulks. Let U be an open set in \mathbb{R}^3 , let K be a polygon contained in U and let r be a segment contained in K . Without loss of generality, K and r may be assumed to lie in \mathbb{R}^2 and \mathbb{R} , respectively. Let $u \in \mathcal{C}^2(U)$. Then consider

$$\begin{aligned} |u|_{\mathcal{C}^2(r)} &:= \max_{x \in r} \left| \frac{\partial^2 u}{\partial x^2}(x) \right|; \\ |u|_{\mathcal{C}^2(K)} &:= \max_{\substack{\alpha \in (\mathbb{N} \cup 0)^2 \\ |\alpha|=2}} \max_{\mathbf{x} \in K} \left| \frac{\partial^2 u}{\partial \mathbf{x}^\alpha}(\mathbf{x}) \right|; \\ |u|_{\mathcal{C}^2(U)} &:= \max_{\substack{\alpha \in (\mathbb{N} \cup 0)^3 \\ |\alpha|=2}} \max_{\mathbf{x} \in U} \left| \frac{\partial^2 u}{\partial \mathbf{x}^\alpha}(\mathbf{x}) \right|, \end{aligned}$$

with the multi-index notation for partial derivatives. It is easy to prove that

$$|u|_{\mathcal{C}^2(r)} \leq |u|_{\mathcal{C}^2(K)} \leq |u|_{\mathcal{C}^2(U)}. \quad (3.33)$$

Furthermore, if u_r is the linear interpolant of u on r , i.e. the affine function on r that agrees with u at the endpoints of r , the following classical interpolation error estimate holds

$$\|u - u_r\|_{\infty, r} \leq C|r|^2 |u|_{\mathcal{C}^2(r)}, \quad (3.34)$$

where $|r|$ is the length of r , see [26]. Consider $K \in \mathcal{K}_h$, see Fig. 3.1(a). First of all we prove that

$$\|d(\cdot)\|_{\infty, \partial K} \leq Ch^2 |d(\cdot)|_{\mathcal{C}^2(K)}. \quad (3.35)$$

To this end, let $\mathbf{x}_B \in \partial K$ and let e be an edge of K such that $\mathbf{x}_B \in e$, see Fig. 3.1(b). Then, if $d_e(\cdot)$ is the linear interpolant of $d(\cdot)$ on e , then (i) $d_e(\mathbf{x}) = 0$ for all $\mathbf{x} \in e$ since $d(\cdot)$ vanishes at the endpoints of e and (ii) the interpolation error estimate (3.34) holds with $r = e$ and $u = d(\cdot)$. Using also (3.33), we have

$$|d(\mathbf{x}_B)| \leq \|d_e(\cdot)\|_{\infty, e} + \|d(\cdot) - d_e(\cdot)\|_{\infty, e} \leq C|e|^2 |d(\cdot)|_{\mathcal{C}^2(e)} \leq Ch^2 |d(\cdot)|_{\mathcal{C}^2(K)},$$

that proves (3.35). Now let $\mathbf{x} \in \overset{\circ}{K}$ and let s be any straight line contained in the plane of K and passing through \mathbf{x} , let $\mathbf{x}_1, \mathbf{x}_2 \in s \cap \partial K$ such that $[\mathbf{x}_1, \mathbf{x}_2] \subset K$, see Fig. 3.1(c), and let $d_s(\cdot)$ be the linear interpolant of $d(\cdot)$ on s . By choosing $r = s$ and $u = d$ in (3.34), using (3.33) and (3.35) we have that

$$\begin{aligned} |d(\mathbf{x})| &\leq \|d_s(\cdot)\|_{\infty, s} + \|d(\cdot) - d_s(\cdot)\|_{\infty, s} = \max(|d(\mathbf{x}_1)|, |d(\mathbf{x}_2)|) + \|d(\cdot) - d_s(\cdot)\|_{\infty, s} \\ &\leq \|d(\cdot)\|_{\infty, \partial K} + C|s|^2 |d(\cdot)|_{\mathcal{C}^2(s)} \leq Ch^2 |d(\cdot)|_{\mathcal{C}^2(K)} \leq Ch^2 |d(\cdot)|_{\mathcal{C}^2(U)}, \end{aligned} \quad (3.36)$$

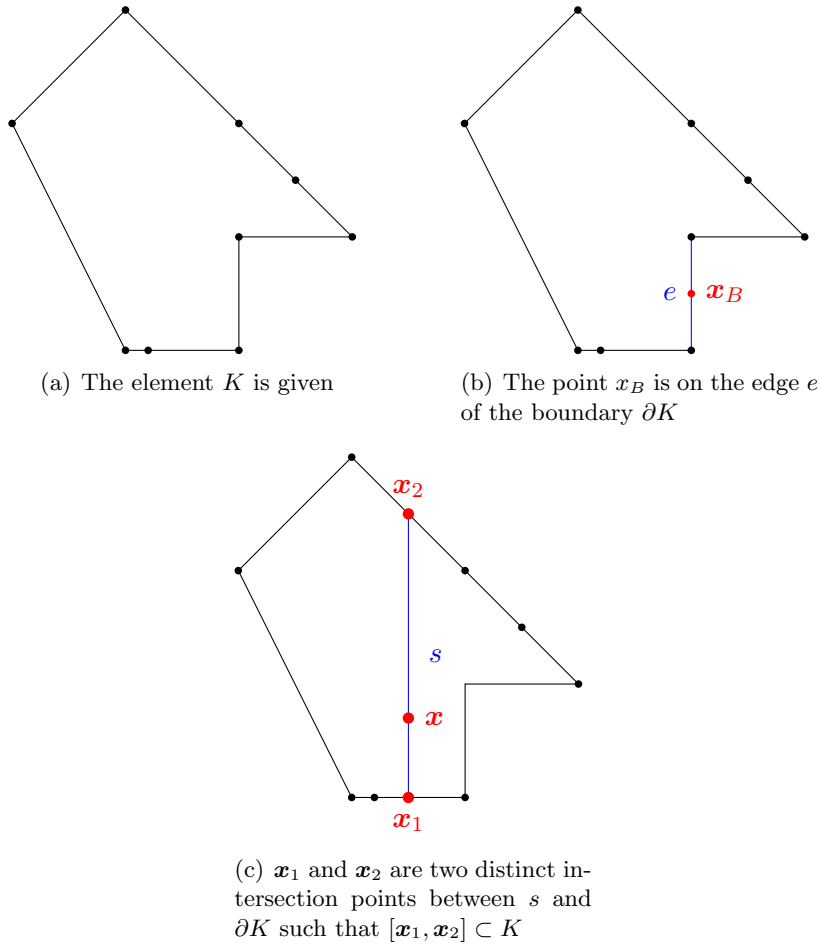


Figure 3.1: Graphical representation of the construction involved in the proof of Lemma 3.

where U is the Fermi stripe of Γ . Now, $|d(\cdot)|_{C^2(U)}$ depends only on the curvature of Γ , thus (3.36) proves (3.30). To prove (3.30), (3.31) and (3.32), we proceed as in [40, Lemma 4.1] using estimate (3.30) for polygonal meshes. \square

The remainder of our analysis relies on the following equalities borrowed from [40]:

$$\int_{\Gamma} U^\ell V^\ell - \int_{\Gamma_h} UV = \int_{\Gamma} \left(1 - \frac{1}{\delta_h^\ell}\right) U^\ell V^\ell; \quad (3.37)$$

$$\int_{\Gamma} \nabla_{\Gamma} U^\ell \cdot \nabla_{\Gamma} V^\ell - \int_{\Gamma_h} \nabla_{\Gamma_h} U \cdot \nabla_{\Gamma_h} V = \int_{\Gamma} (P - Q_h) \nabla_{\Gamma} U^\ell \cdot \nabla_{\Gamma} V^\ell, \quad (3.38)$$

for all $U, V : \Gamma_h \rightarrow \mathbb{R}$ such that the gradients and the integrals are well-defined. We remark that, even if the work in [40] is restricted to the case when Γ_h has triangular faces, the proof of equalities (3.37)-(3.38) does not utilise the assumption of triangular faces. Hence, the relations (3.37)-(3.38) still hold true in our polygonal setting. The following lemma generalizes Lemma

4.2 in [40] to our polygonal setting and provides lower and upper bounds for some norms of arbitrary functions when they are unlifted from Γ to Γ_h or lifted from Γ_h to Γ .

Lemma 4. *Let $V : \Gamma_h \rightarrow \mathbb{R}$ with lift $V^\ell : \Gamma \rightarrow \mathbb{R}$. Let $\mathbf{a} : \Gamma_h \rightarrow \Gamma$ be the projection onto Γ defined in (2.3) and, for every $K \in \mathcal{K}_h$, let $\tilde{K} := \mathbf{a}(K) \subset \Gamma$ be the curved element corresponding to $K \in \mathcal{K}_h$. Then*

$$\frac{1}{C} \|V\|_{0,K} \leq \|V^\ell\|_{0,\tilde{K}} \leq C \|V\|_{0,K}; \quad (3.39)$$

$$\frac{1}{C} \|\nabla_K V\|_{0,K} \leq \|\nabla_{\tilde{K}} V^\ell\|_{0,\tilde{K}} \leq C \|\nabla_K V\|_{0,K}; \quad (3.40)$$

$$\|\nabla_K^2 V\|_{0,K} \leq C \|\nabla_{\tilde{K}}^2 V^\ell\|_{0,\tilde{K}} + Ch_K \|\nabla_{\tilde{K}} V^\ell\|_{0,\tilde{K}}, \quad (3.41)$$

if the norms exist, where ∇_K^2 and $\nabla_{\tilde{K}}^2$ denote the tangential Hessian on K and \tilde{K} , respectively, and C depends only on the curvature of Γ .

Proof. We use the estimates of Lemma 3 for polygonal meshes into (3.37)-(3.38) and proceed exactly as in [40, Lemma 4.2]. \square

Notice that Eqs. (3.39) and (3.40) express the following equivalences under lifting: (3.39) between $L^2(\Gamma_h)$ and $L^2(\Gamma)$ norms and (3.40) between $H^1(\Gamma_h)$ and $H^1(\Gamma)$ seminorms. Eq. (3.41) can be interpreted as an h -perturbed dominance of the $H^2(\Gamma)$ seminorm over the $H^2(\Gamma_h)$ seminorm. The following result provides error estimates for the interpolation in \mathbb{V}_h^ℓ and the projection on $(\prod_K \mathbb{P}_1(K))^\ell$. The interpolation result extends to SVEM Lemma 4.3 in [40] for the triangular SFEM.

Lemma 5. *Given a C^2 surface Γ , there exists $C > 0$ such that, for all $v \in H^2(\Gamma)$ and $w \in H^s(\Gamma)$, $s \in \{1, 2\}$, and for all $h > 0$, then*

- the interpolant $I_h(v) \in \mathbb{V}_h$ fulfils

$$\|v - I_h(v)^\ell\|_0 + h|v - I_h(v)^\ell|_1 \leq Ch^2 (|v|_2 + h|v|_1); \quad (3.42)$$

- there exists a projection $w_\pi \in \prod_{K \in \mathcal{K}_h} \mathbb{P}_1(K)$ such that

$$\|w - w_\pi^\ell\|_0 + h|w - w_\pi^\ell|_{h,1} \leq Ch^s (|w|_{H^s(\Gamma)} + h|w|_1). \quad (3.43)$$

Proof. From Lemma 4, $w^{-\ell} \in L^2(\Gamma_h) \cap \prod_{K \in \mathcal{K}_h} H^s(K)$. Let w_π be the $\prod_{K \in \mathcal{K}_h} \mathbb{P}_1(K)$ projection of $w^{-\ell}$ defined piecewise by (3.24) and let $I_h(v)$ be the interpolant of $v^{-\ell}$ defined by (3.6). From Theorems 6 and 7, by summing piecewise contributions, we have

$$\|w^{-\ell} - w_\pi\|_{0,h} + h|w^{-\ell} - w_\pi|_{1,h} \leq Ch^s |w^{-\ell}|_{2,h}; \quad (3.44)$$

$$\|v^{-\ell} - I_h(v)\|_{0,h} + h|v^{-\ell} - I_h(v)|_{1,h} \leq Ch^2 |v^{-\ell}|_{2,h}. \quad (3.45)$$

From (3.44), (3.45) and Lemma 4 we have

$$\|w - w_\pi^\ell\|_0 + h|w - w_\pi^\ell|_{1,h} \leq Ch^s (|w|_{H^s(\Gamma)} + h|w|_1); \quad (3.46)$$

$$\|v - I_h(v)^\ell\|_0 + h|v - I_h(v)^\ell|_{1,h} \leq Ch^2 (|v|_2 + h|v|_1), \quad (3.47)$$

that are the desired estimates. \square

The following Lemma extends Lemma 4.7 in [40] to our polygonal/virtual setting and provides bounds for the geometric errors in the bilinear forms.

Lemma 6. *For any $(V, W) \in H^1(\Gamma_h) \times H^1(\Gamma_h)$, the following estimates hold:*

$$|\langle V^\ell, W^\ell \rangle_0 - \langle V, W \rangle_{0,h}| \leq Ch^2 \|V^\ell\|_0 \|W^\ell\|_0; \quad (3.48)$$

$$|a(V^\ell, W^\ell) - \bar{a}(V, W)| \leq Ch^2 \|\nabla_\Gamma V^\ell\|_0 \|\nabla_\Gamma W^\ell\|_0, \quad (3.49)$$

where C depends only on the geometry of Γ .

Proof. We proceed as in Lemma 4.7 of [40], but here using, into (3.37)-(3.38), the generalised estimates (3.30)-(3.32) given in the previous Lemma 3. \square

In the following theorem we prove a discrete Poincaré inequality in $H_0^1(\Gamma_h)$, i.e on polygonal surfaces Γ_h of the type (3.1).

Theorem 8 (Poincaré inequality in $H_0^1(\Gamma_h)$). *Let Γ be a closed C^3 surface in \mathbb{R}^3 . Then there exist $h_0 > 0$ and $C > 0$ depending on Γ such that, for all $0 < h < h_0$ and Γ_h as in (3.1),*

$$\|V\|_{0,h} \leq C|V|_{1,h} \quad \forall V \in L_0^2(\Gamma_h) \cap \prod_{K \in \mathcal{K}_h} H^1(K). \quad (3.50)$$

Proof. From (3.39) and the triangle inequality we have

$$\|V\|_{0,h} \leq C\|V^\ell\|_0 \leq C \left(\left\| V^\ell - \frac{1}{|\Gamma|} \int_\Gamma V^\ell \right\|_0 + \frac{1}{|\Gamma|^{\frac{1}{2}}} \int_\Gamma V^\ell \right). \quad (3.51)$$

Now, from (3.39) we have that $V^\ell - \frac{1}{|\Gamma|} \int_\Gamma V^\ell \in H_0^1(\Gamma)$. Then, from Poincaré's inequality (2.8) and (3.40) it follows that

$$\left\| V^\ell - \frac{1}{|\Gamma|} \int_\Gamma V^\ell \right\|_0 \leq C|V^\ell|_{1,h} \leq C|V|_{1,h}. \quad (3.52)$$

Furthermore, from (3.39), (3.48) and the fact that V is average-free on Γ_h , it follows that

$$\frac{1}{|\Gamma|^{\frac{1}{2}}} \int_\Gamma V^\ell \leq \frac{1}{|\Gamma|^{\frac{1}{2}}} \left(\left| \int_{\Gamma_h} V \right| + Ch^2 \|V^\ell\|_0 |\Gamma|^{\frac{1}{2}} \right) \leq Ch^2 \|V\|_{0,h}. \quad (3.53)$$

Combining (3.51), (3.52) and (3.53) we have

$$(1 - Ch^2) \|V\|_{0,h} \leq C|V|_{1,h}.$$

By choosing, for instance, $h_0 = \frac{1}{\sqrt{2C}}$, the result follows. \square

Concerning the convergence rates of the error estimates in Lemmas 5 and 6, we observe that:

- As shown in Lemma 6, in the approximation of the bilinear forms (3.48) and (3.49), the polygonal approximation of geometry yields a geometric error that is quadratic in L^2 norm and linear in H^1 norm. In fact, this Lemma is based on the geometric estimates of Lemma 3.

- The interpolation error on Γ , as shown by (3.42) in Lemma 5 (and its proof) arises from two sources. The first one is the interpolation error on flat polygons (cp. Theorem 7). The second one is given by the geometric estimates given in Lemma 3.

This implies that using higher-order virtual element spaces instead of (3.5) will not improve the convergence rate of the method, since geometric error would dominate over the interpolation one. The same drawback occurs with the standard SFEM [40] of higher order; in [32] it has been shown that a finite element space of degree $k \in \mathbb{N}$ defined on a suitable curvilinear triangulation of degree k (isoparametric elements) provides a SFEM with the same convergence rate as polynomial interpolation of degree k . This suggests that, to formulate a SVEM of order $k > 1$, a different approximation of the surface is needed.

We close this section proving an error estimate for the approximate right hand side $\langle f_h, \phi \rangle_h$ in the discrete formulation (3.22).

Theorem 9. *Let $f \in H_0^1(\Gamma)$. Under the regularity assumptions (A1)-(A2), there exists $C > 0$ depending on Γ , γ_1 and γ_2 such that*

$$|\langle f, V^\ell \rangle_0 - \langle f_h, V \rangle_R| \leq Ch(|f|_1 + h|f|_2) |V^\ell|_1, \quad V \in \mathbb{V}_{h,0}. \quad (3.54)$$

Proof. Let $I_h(f)$ be the piecewise linear interpolant of f and f_h be as in (3.7). We split the error as

$$\begin{aligned} |\langle f, V^\ell \rangle_0 - \langle f_h, V \rangle_R| &\leq |\langle f, V^\ell \rangle_0 - \langle I_h(f), V \rangle_{0,h}| + |\langle I_h(f), V \rangle_{0,h} - \langle f_h, V \rangle_{0,h}| \\ &\quad + |\langle f_h, V \rangle_{0,h} - \langle f_h, V \rangle_M|. \end{aligned} \quad (3.55)$$

From the Cauchy-Schwarz inequality and (3.48) we obtain

$$\begin{aligned} |\langle f, V^\ell \rangle_0 - \langle I_h(f), V \rangle_{0,h}| &\leq |\langle f - I_h(f)^\ell, V^\ell \rangle_0| + |\langle I_h(f)^\ell, V^\ell \rangle_0 - \langle I_h(f), V \rangle_{0,h}| \\ &\leq \|f - I_h(f)^\ell\|_0 \|V^\ell\|_0 + Ch^2 \|I_h(f)^\ell\|_0 \|V^\ell\|_0. \end{aligned} \quad (3.56)$$

From the Cauchy-Schwarz inequality, the definition of f_h and (3.48) we have

$$\begin{aligned} |\langle I_h(f), V \rangle_{0,h} - \langle f_h, V \rangle_{0,h}| &\leq |\Gamma_h|^{-\frac{1}{2}} |\langle I_h(f), 1 \rangle_{0,h}| \|V\|_{0,h} \\ &\leq |\Gamma_h|^{-\frac{1}{2}} \left(|\langle I_h(f)^\ell - f, 1 \rangle_0| + Ch^2 \|I_h(f)^\ell\|_0 \right) \|V\|_{0,h} \\ &\leq \left(\|I_h(f)^\ell - f\|_0 + Ch^2 \|I_h(f)^\ell\|_0 \right) \|V\|_{0,h}. \end{aligned} \quad (3.57)$$

Following [8], we know that

$$|\langle f_h, V \rangle_{0,h} - \langle f_h, V \rangle_R| \leq Ch |f_h|_{1,h} |V|_{1,h}, \quad (3.58)$$

but, from the definition of f_h and from (3.40) it follows that

$$|f_h|_{1,h} = |I_h(f)|_{1,h} \leq C |I_h(f)^\ell|_1. \quad (3.59)$$

Combining (3.55)-(3.59), using (3.39), (3.40), (3.42), the Poincaré inequalities (2.8), (3.50) and the triangle inequality we obtain

$$\begin{aligned} |\langle f, V^\ell \rangle_0 - \langle f_h, V \rangle_R| &\leq \left(\|f - I_h(f)^\ell\|_0 + Ch |I_h(f)^\ell|_1 + Ch^2 \|I_h(f)^\ell\|_0 \right) |V^\ell|_1 \\ &\leq \left((1 + Ch^2) \|f - I_h(f)^\ell\|_0 + Ch^2 \|f\|_0 + Ch |f - I_h(f)^\ell|_1 + Ch |f|_1 \right) |V^\ell|_1 \\ &\leq C \left((h^2 + h^4) |f|_2 + (h + h^3 + h^5) |f|_1 \right) |V^\ell|_1 \leq Ch (|f|_1 + h|f|_2) |V^\ell|_1, \end{aligned}$$

that is the desired estimate. \square

3.4 Existence, uniqueness and error analysis

The following theorem, that is the main result of this chapter, extends the error analysis in Theorem 3.1 in [8] for the case of planar domains to the Laplace-Beltrami equation on surfaces. In fact, it provides: (i) the existence and the uniqueness of the solution for the discrete problem (3.22) and (ii) an abstract convergence result. As a corollary, an optimal $H^1(\Gamma)$ error estimate for problem (3.22) will be given.

Theorem 10 (Abstract convergence theorem). *Let $a : H_0^1(\Gamma) \times H_0^1(\Gamma) \rightarrow \mathbb{R}$ be the bilinear form defined by*

$$a(u, v) = \int_{\Gamma} \nabla_{\Gamma} u \cdot \nabla_{\Gamma} v, \quad u, v \in H_0^1(\Gamma),$$

and let $b_h : \mathbb{V}_{h,0} \times \mathbb{V}_{h,0} \rightarrow \mathbb{R}$ be any symmetric bilinear form such that

$$b_h(U, V) = \sum_{K \in \mathcal{K}_h} b_{h,K}(U|_K, V|_K) \quad (3.60)$$

where, for all $K \in \mathcal{K}_h$, $b_{h,K}$ is a symmetric bilinear form on $\mathbb{V}_h(K) \times \mathbb{V}_h(K)$ such that

$$|b_{h,K}(p, V|_K) - a_{\tilde{K}}(p^\ell, V|_K^\ell)| \leq Ch^2 |p^\ell|_{1,\tilde{K}} |V|_K^\ell|_{1,\tilde{K}}, \quad V|_K \in \mathbb{V}_h(K), \quad p \in \mathbb{P}_1(K); \quad (3.61)$$

$$\alpha_* a_{\tilde{K}}(V|_K^\ell, V|_K^\ell) \leq b_{h,K}(V|_K, V|_K) \leq \alpha^* a_{\tilde{K}}(V|_K^\ell, V|_K^\ell), \quad V|_K \in \mathbb{V}_h(K), \quad (3.62)$$

where α_* and α^* are independent of h and $K \in \mathcal{K}_h$.

If $\mathbb{V}'_{h,0}$ is the topological dual space of $\mathbb{V}_{h,0}$, let $F \in L^{-2}(\Gamma)$ and $F_h \in \mathbb{V}'_{h,0}$ be linear continuous functionals. Consider the problems

$$\begin{cases} u \in H_0^1(\Gamma) \\ a(u, v) = F(v) \quad \forall v \in H_0^1(\Gamma) \end{cases} \quad (3.63)$$

$$\begin{cases} U \in \mathbb{V}_{h,0} \\ b_h(U, V) = F_h(V) \quad \forall V \in \mathbb{V}_{h,0} \end{cases} \quad (3.64)$$

Problem (3.64) has a unique solution and the following error estimate holds

$$|u - U^\ell|_1 \leq C \left(|u - u_\pi^\ell|_{h,1} + |u - u_I^\ell|_1 + \mathcal{F}_h + h \|F\|_{L^{-2}(\Gamma)} \right), \quad (3.65)$$

where \mathcal{F}_h is the smallest constant such that

$$|F(V^\ell) - F_h(V)| \leq \mathcal{F}_h |V^\ell|_1, \quad V \in \mathbb{V}_{h,0}. \quad (3.66)$$

Proof. Existence and uniqueness for (3.64) follows from Lax-Milgram's theorem. In fact the bilinear form b_h is

- coercive since

$$\begin{aligned} |b_h(V, V)| &\stackrel{(3.60)}{=} \left| \sum_{K \in \mathcal{K}_h} b_{h,K}(V|_K, V|_K) \right| \stackrel{(3.62)}{\geq} \alpha_* \sum_{K \in \mathcal{K}_h} |a_{\tilde{K}}(V|_K^\ell, V|_K^\ell)| = \alpha_* \sum_{K \in \mathcal{K}_h} |V|_{1,\tilde{K}}^{\ell 2} \\ &\stackrel{(3.40)}{\geq} C \sum_{K \in \mathcal{K}_h} |V|_{1,K}^2 = C |V|_{1,h}^2 \stackrel{(3.50)}{\geq} C \|V\|_{1,h}^2, \quad V \in \mathbb{V}_{h,0}; \end{aligned}$$

- continuous. In fact, since b_h is symmetric and coercive (i.e. it is an inner product on $\mathbb{V}_{h,0}$), then it fulfils the Cauchy-Schwarz inequality. Then we have

$$\begin{aligned}
|b_h(V, W)| &\leq (b_h(V, V)b_h(W, W))^{\frac{1}{2}} \stackrel{(3.60)}{\leq} \left(\sum_{K \in \mathcal{K}_h} \sum_{K' \in \mathcal{K}_h} b_{h,K}(V|_K, V|_K) a_{h,K'}(W|_{K'}, W|_{K'}) \right)^{\frac{1}{2}} \\
&\stackrel{(3.62)}{\leq} \alpha^* \left(\sum_{K \in \mathcal{K}_h} \sum_{K' \in \mathcal{K}_h} a_{\tilde{K}}(V|_K, V|_K) a_{\tilde{K}'}(W|_{K'}, W|_{K'}) \right)^{\frac{1}{2}} = \alpha^* (a(V^\ell, V^\ell) a(W^\ell, W^\ell))^{\frac{1}{2}} \\
&= \alpha^* |V^\ell|_1 |W^\ell|_1 \stackrel{(3.40)}{\leq} C |V|_{1,h} |W|_{1,h} \leq C \|V\|_{1,h} \|W\|_{1,h}, \quad V, W \in \mathbb{V}_{h,0}.
\end{aligned}$$

Hence, the discrete problem (3.64) meets the assumptions of Lax-Milgram's theorem.

Let us now prove the error estimate (3.65). Let $u_\pi \in \prod_{K \in \mathcal{K}_h} \mathbb{P}_1(K)$ be the projection of u defined in (3.43) and let $u_I \in \mathbb{V}_{h,0}$ be the interpolant of u defined in (3.42). From [40, Theorem 3.3], The solution of (3.63) fulfils $u \in H^2(\Gamma)$ and thus u_π and u_I are well-defined. Let $\delta_h = U - u_I$. It holds that

$$\begin{aligned}
\alpha_* |\delta_h^\ell|_W^2 &= \alpha_* a(\delta_h^\ell, \delta_h^\ell) \leq b_h(\delta_h, \delta_h) = b_h(U, \delta_h) - b_h(u_I, \delta_h) \\
&\stackrel{(3.60)}{=} F_h(\delta_h) - \sum_{K \in \mathcal{K}_h} b_{h,K}(u_I, \delta_h) = F_h(\delta_h) - \sum_{K \in \mathcal{K}_h} \left(b_{h,K}(u_I - u_\pi, \delta_h) + b_{h,K}(u_\pi, \delta_h) \right) \\
&\stackrel{(3.61)}{\leq} F_h(\delta_h) - \sum_{K \in \mathcal{K}_h} \left(b_{h,K}(u_I - u_\pi, \delta_h) + a_{\tilde{K}}(u_\pi^\ell, \delta_h^\ell) \right) + Ch^2 \sum_{K \in \mathcal{K}_h} |u_\pi^\ell|_{1,\tilde{K}} |\delta_h^\ell|_{1,\tilde{K}} \\
&= F_h(\delta_h) - \sum_{K \in \mathcal{K}_h} \left(b_{h,K}(u_I - u_\pi, \delta_h) + a_{\tilde{K}}(u_\pi^\ell - u, \delta_h^\ell) + a_{\tilde{K}}(u, \delta_h^\ell) \right) \tag{3.67} \\
&+ Ch^2 \left(|u_\pi^\ell|_{h,1}^2 + |\delta_h^\ell|_1^2 \right) = F_h(\delta_h) - a(u, \delta_h^\ell) + Ch^2 \left(|u_\pi^\ell|_{h,1}^2 + |\delta_h^\ell|_1^2 \right) \\
&- \sum_{K \in \mathcal{K}_h} \left(b_{h,K}(u_I - u_\pi, \delta_h) + a_{\tilde{K}}(u_\pi^\ell - u, \delta_h^\ell) \right) = F_h(\delta_h) - F(\delta_h^\ell) \\
&- \sum_{K \in \mathcal{K}_h} \left(b_{h,K}(u_I - u_\pi, \delta_h) + a_{\tilde{K}}(u_\pi^\ell - u, \delta_h^\ell) \right) + Ch^2 \left(|u_\pi^\ell|_{h,1}^2 + |\delta_h^\ell|_1^2 \right).
\end{aligned}$$

By using (3.62) and (3.66) into (3.67) and the continuity of a and b_h , we obtain

$$(\alpha_* - Ch^2) |\delta_h^\ell|_1^2 \leq \mathcal{F}_h |\delta_h^\ell|_1 + |u_I - u_\pi|_{h,1} |\delta_h|_{1,h} + |u_\pi^\ell - u|_{h,1} |\delta_h^\ell|_1 + Ch^2 |u_\pi^\ell|_{h,1}^2. \tag{3.68}$$

By using (3.40) and for h sufficiently small, (3.68) yields

$$|\delta_h^\ell|_1^2 \leq C(\mathcal{F}_h + |u_I - u_\pi^\ell|_{h,1} + |u_\pi^\ell - u|_{h,1}) |\delta_h^\ell|_1 + Ch^2 |u_\pi^\ell|_{h,1}^2. \tag{3.69}$$

By defining $A = \mathcal{F}_h + |u_I - u_\pi^\ell|_{h,1} + |u_\pi^\ell - u|_{h,1}$ and solving the second-degree-algebraic inequality (3.69) we have

$$|\delta_h^\ell|_1 \leq \frac{CA}{2} + \frac{1}{2} \sqrt{C^2 A^2 + 4Ch^2 |u_\pi^\ell|_{h,1}^2} \leq \frac{CA}{2} + \frac{1}{2} (CA + 2\sqrt{Ch} |u_\pi^\ell|_{h,1}) \leq CA + Ch |u_\pi^\ell|_{h,1}.$$

By recalling the definition of A and applying the triangle inequality, we get

$$|u - U^\ell|_1 \leq C(\mathcal{F}_h + |u - u_I^\ell|_1 + |u - u_\pi^\ell|_{h,1}) + Ch|u_\pi^\ell|_{h,1}.$$

By applying the triangle inequality to the last term, we obtain

$$|u - U^\ell|_1 \leq C \left(\mathcal{F}_h + |u - u_I^\ell|_1 + (1+h)|u - u_\pi^\ell|_{h,1} + h|u|_1 \right).$$

The obvious stability estimate $|u|_1 \leq C\|F\|_{L^{-2}(\Gamma)}$, where C is the constant in the Poincaré inequality (2.8), together with $h \leq h_0$, complete the proof. \square

From the abstract framework given in Theorem 10 we are now ready to derive the $H^1(\Gamma)$ error estimate between the continuous problem (2.15) and the discrete one (3.22).

Corollary 1 ($H^1(\Gamma)$ error estimate). *Problem (3.23) has a unique solution. Let u and U be the solutions of (2.16) and (3.23), respectively. Under the mesh regularity assumptions (A1)-(A2), if $f \in H_0^2(\Gamma)$, the following estimate holds:*

$$|u - U^\ell|_1 \leq Ch(|u|_2 + |f|_1) + Ch^2|f|_2. \quad (3.70)$$

Proof. In Theorem 10, we choose

$$\begin{aligned} F(v) &= \langle f, v \rangle_0, & v &\in H^1(\Gamma); \\ F_h(V) &= \langle f_h, V \rangle_R, & V &\in \mathbb{V}_{h,0}, \end{aligned}$$

with b_h defined in (3.8), (3.12). Under the mesh regularity assumptions (A1)-(A2),

1. Assumption (3.61) follows from (3.10) and (3.49);
2. Assumption (3.62) follows from (3.8), (3.11) and (3.40);
3. From [40, Theorem 3.3] we have $u \in H^2(\Gamma)$. Then, Lemma 5 provides

$$|u - u_\pi^\ell|_{h,1} + |u - u_I^\ell|_1 < Ch(|u|_2 + h|u|_1); \quad (3.71)$$

4. if $f \in H_0^1(\Gamma)$, the Poincaré inequality (2.8) provides

$$\|F\|_{L^{-2}(\Gamma)} = \|f\|_0 \leq C|f|_1, \quad (3.72)$$

and (3.54) yields

$$\mathcal{F}_h \leq Ch(|f|_1 + h|f|_2). \quad (3.73)$$

By substituting (3.71)-(3.73), into the abstract error bound (3.65), we obtain

$$|u - U^\ell|_1 \leq Ch(|u|_2 + |f|_1) + Ch^2(|u|_1 + |f|_2). \quad (3.74)$$

By using the Poincaré inequality (2.8), the stability estimate $|u|_1 \leq C\|F\|_{L^{-2}(\Gamma)}$ and (3.72) into (3.74), the result follows. \square

3.5 Implementation

In this section we will discuss how to implement the SVEM using only information on the mesh and the nodal values of the load term f . The major differences with respect to the planar case are:

1. construction of test problems on arbitrary surfaces, with the knowledge of the exact solution and construction of polygonal meshes;
2. computation of local matrices (mass, stiffness and load term);
3. formulation of the discrete problem as a square, full-rank linear system which also accounts for the zero-average condition on the solution.

3.5.1 Constructing test problems

To perform a convergence study of any numerical method for the Laplace-Beltrami equation, it is necessary to construct some *test problems*, where the exact solution is known in closed form. Constructing test problems, which is trivial in the planar case, is more involved on curved surfaces. For a generic surface, we proceed as follows:

- Represent Γ as a zero level set of a suitable function ϕ as in Definition 1;
- Compute the unit normal vector field ν according to (2.1);
- Choose the exact solution u such that u is well-defined and sufficiently smooth in an open neighbourhood of Γ ;
- By repeatedly computing the tangential derivatives of u as in (2.5), compute the Laplace-Beltrami of u according to (2.6), thus obtaining the right-hand side f of the Laplace-Beltrami equation (2.13). We remark that, if Γ has no boundary, then, by construction, f is average-free on Γ .

Though being merely algorithmic, this procedure can be particularly lengthy and tedious even on rather simple surfaces, nevertheless a symbolic calculus software could be used for this task. On very special surfaces, such as spheres and cylinders, some eigenfunctions of the Laplace-Beltrami operator are known in the literature [97]. Hence, if \bar{u} is an eigenfunction of $-\Delta_\Gamma$ with eigenvalue λ , a test problem is immediately obtained by choosing the load term as $f = \lambda\bar{u}$. This approach will be used in our numerical example provided in next Section 3.6 (Example 3.6.2).

Concerning the discretisation of generic surfaces for a Laplace-Beltrami equation, to the best of the author's knowledge, the problem of generating and refining arbitrary polygonal meshes is an open question and no general algorithm is available. More is known on the specific case of triangular meshes, see [31, 40, 107] and some codes are available [108, 119]. Here we suggest a possible way of constructing polygonal meshes in the following cases:

1. On spherical surfaces: polygonal meshes can be constructed starting from arbitrary triangulations by suitably subdividing the triangles and projecting the resulting nodes onto Γ , as explained in Figure 3.2 for a single triangle. In the caption of this figure we describe the steps required by this construction. We will apply this approach in Example 3.6.2, see Fig. 3.5(a).

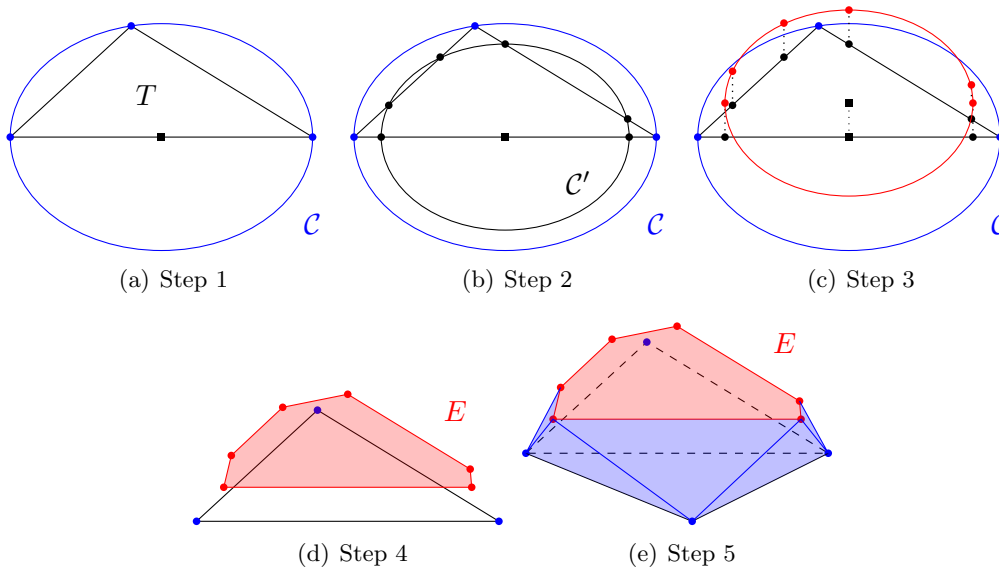


Figure 3.2: Algorithmic procedure, mentioned in Section 3.5.1, for the construction of polygonal meshes on the sphere. (a) Given a triangular element T , we consider the out-circle \mathcal{C} (which is contained in Γ). (b) We consider a circle \mathcal{C}' , concentric with \mathcal{C} , whose radius is such that \mathcal{C}' intersect each edge of T in two distinct points. (c) The resulting six points are moved, orthogonally to the plane of T , onto Γ . (d) By connecting these points, an hexagon K is created, whose vertices are on Γ . (e) New triangles are added to connect the nodes of K with the neighboring nodes of T .

2. For special surfaces, such as cylinders or tori: it is possible to trivially construct quadrilateral or trapezoidal meshes that significantly reduce the number of elements, on equal number of degrees of freedom. We will consider these meshes in Section 3.6.2 (Examples 2 and 3).

3.5.2 Constructing local matrices

In this section we explain how the construction of the stiffness and mass matrices on polygonal meshes in \mathbb{R}^3 differ from the planar case. For every element $K \in \mathcal{K}_h$, consider the local mass and stiffness matrices M_K and A_K defined respectively by

$$\begin{aligned}
 M_K &= (m_{ij}^K) := \langle \chi_i, \chi_j \rangle_{M,K}, & i, j : \mathbf{x}_i, \mathbf{x}_j \in \text{nodes}(K); \\
 A_K &= (a_{ij}^K) := b_{h,K}(\chi_i, \chi_j), & i, j : \mathbf{x}_i, \mathbf{x}_j \in \text{nodes}(K).
 \end{aligned}$$

For all $K \in \mathcal{K}_h$, we move K to the horizontal plane $\{z = 0\}$ and we use the algorithm described in [9] for the computation of the local matrices in the planar case.

To move K onto the horizontal plane, we proceed as follows. Let $n_K \in \mathbb{N}$ be the number of vertices of K , let $P_i, i = 1, \dots, n_K$ be the vertices of K and let $P'_i = (x'_i, y'_i), i = 1, \dots, n_K$, be the vertices of the transformed element. For the sake of simpleness, we fix the transformation by enforcing that

- the first vertex P_1 is moved to the origin, i.e. $P'_1 = O$;

- the second vertex P_2 is moved onto the x -axis, i.e. $y'_2 = 0$;
- if $j := \min\{i = 3, \dots, n_K \mid P_1, P_2 \text{ and } P_j \text{ are not aligned}\}$, then P_j is moved onto the positive y half-plane, i.e. $y'_j > 0$.

The vertices of the transformed element can be computed with the following rule:

$$\begin{aligned}
x'_1 &= 0, & x'_i &= \frac{(P_2 - P_1) \cdot (P_i - P_1)}{\|P_2 - P_1\|}, & i &= 2, \dots, n_K; \\
y'_1 &= y'_2 = 0, & |y'_i| &= \frac{\|(P_2 - P_1) \times (P_i - P_1)\|}{\|P_2 - P_1\|}, & i &= 3, \dots, n_K; \\
y'_j &> 0, & \text{sign } y'_i &= \text{sign} \left((P_2 - P_1) \times (P_j - P_1) \cdot \right. \\
& & & \left. \cdot (P_2 - P_1) \times (P_i - P_1) \right), & i &= j + 1, \dots, n_K,
\end{aligned}$$

where \times denotes the cross-product. Notice that the transformed elements are used in the computation of the local matrices, only. The numerical solution is then plotted on the original mesh in \mathbb{R}^3 .

3.5.3 Full-rank linear system associated to SVEM for the Laplace-Beltrami equation

As pointed out in Remark 2, the Laplace-Beltrami equation must be complemented with the zero-average condition when (i) Γ has no boundary or (ii) The boundary condition are of homogeneous Neumann type. In this subsection we explain how to write the discrete formulation as a square, full-rank linear system that accounts for the zero-average condition and whose dimension is minimal, i.e. equal to the number N of vertices. The implementation of the SFEM for the Laplace-Beltrami equation discussed in Section 3.5 is a special case of the procedure presented here. We express the numerical solution of (3.22) in the basis $\{\chi_i \mid i = 1, \dots, N\}$ as

$$U(\mathbf{x}) = \sum_{j=1}^N \xi_j \chi_j(\mathbf{x}), \quad \mathbf{x} \in \Gamma_h,$$

with $\xi_j \in \mathbb{R}$ for all $j = 1, \dots, N$. Problem (3.22) is then equivalent to

$$\sum_{j=1}^N b_h(\chi_i, \chi_j) \xi_j = \langle f_h, \chi_i \rangle_R, \quad i = 1, \dots, N; \quad (3.75)$$

$$\sum_{j=1}^N \langle 1, \chi_j \rangle_M \xi_j = 0. \quad (3.76)$$

Problem (3.75)-(3.76) is a rectangular $(N+1) \times N$ sparse linear system that has, from Corollary 1, a unique solution. We want to rephrase this problem as a square $N \times N$ sparse linear system. To this end, notice that the function $\bar{\chi} := \sum_{i=1}^N \chi_i$ fulfils $\bar{\chi}(\mathbf{x}_j) = 1$ for all $j = 1, \dots, N$ and thus, from the definition (3.5) of the virtual element space \mathbb{V}_h , we have

$$\sum_{i=1}^N \chi_i(\mathbf{x}) = 1, \quad \mathbf{x} \in \Gamma_h. \quad (3.77)$$

We show that the sum of all equations in (3.75) vanishes. In fact, for the left hand side of (3.75), using (3.10) and (3.77), we have that

$$\sum_{i=1}^N \sum_{j=1}^N b_h(\chi_i, \chi_j) \xi_j = \sum_{j=1}^N b_h \left(\sum_{i=1}^N \chi_i, \chi_j \right) \xi_j = \sum_{j=1}^N b_h(1, \chi_j) \xi_j = \sum_{j=1}^N \bar{a}(1, \chi_j) \xi_j = 0,$$

while for the right hand side of (3.75), from (3.21) and (3.77) we have $\sum_{i=1}^N \langle f_h, \chi_i \rangle_R = \langle f_h, 1 \rangle_R = 0$. We conclude that the sum of equations (3.75) vanishes. This implies that we can remove, for instance, the N -th equation in (3.75). System (3.75)-(3.76) is then equivalent to the $N \times N$ system

$$\begin{cases} \sum_{j=1}^N b_h(\chi_i, \chi_j) \xi_j = \langle f_h, \chi_i \rangle_R, & i = 1, \dots, N-1; \\ \sum_{j=1}^N \langle 1, \chi_j \rangle_M \xi_j = 0. \end{cases}$$

Consider the stiffness matrix A , the mass matrix M , and the load term \mathbf{b} defined by

$$\begin{aligned} A &= (a_{ij}) := b_h(\chi_i, \chi_j), & M &= (m_{ij}) := \langle \chi_i, \chi_j \rangle_M, & i, j &= 1, \dots, N; \\ \mathbf{b} &= (b_i) := \langle f_h, \chi_i \rangle_R, & i &= 1, \dots, N. \end{aligned}$$

The matrices A and M are assembled from the corresponding local matrices introduced in the previous section. To compute the load vector \mathbf{b} we observe that, from (3.20) and the definition of the basis functions, it holds that

$$b_i = \sum_{K: \mathbf{x}_i \in \text{nodes}(K)} \frac{1}{n_K} \int_K f_h, \quad i = 1, \dots, N. \quad (3.78)$$

Each integral in (3.78) is computed as follows. The nodal values of the load term f_h are computed by

$$f_h(\mathbf{x}_k) = I_h(f)(\mathbf{x}_k) - \frac{\langle f_h, 1 \rangle_M}{|\Gamma_h|} = f(\mathbf{x}_k) - \frac{\sum_{i=1}^N \langle \chi_i, 1 \rangle_M f(\mathbf{x}_i)}{\langle 1, 1 \rangle_M} = f(\mathbf{x}_k) - \frac{\sum_{i=1}^N (\sum_{j=1}^N m_{ij}) f(\mathbf{x}_i)}{\sum_{i=1}^N \sum_{j=1}^N m_{ij}},$$

for all $k = 1, \dots, N$. For every $K \in \mathcal{K}_h$, the integral of f_h on K is given by

$$\int_K f_h = \langle f_h, 1 \rangle_{L_h^2, K} = \sum_{i: \mathbf{x}_i \in \text{nodes}(K)} \langle \chi_i, 1 \rangle_{L_h^2, K} f_h(\mathbf{x}_i) = \sum_{i: \mathbf{x}_i \in \text{nodes}(K)} \left(\sum_{j: \mathbf{x}_j \in \text{nodes}(K)} m_{ij}^K \right) f_h(\mathbf{x}_i).$$

In conclusion, the discretisation of the Laplace-Beltrami equation (2.15) by SVEM is given by the following sparse, square, full-rank linear algebraic system

$$\begin{cases} \sum_{j=1}^N a_{ij} \xi_j = b_i, & i = 1, \dots, N-1; \\ \sum_{j=1}^N \left(\sum_{i=1}^N m_{ij} \right) \xi_j = 0. \end{cases} \quad (3.79)$$

In matrix form, we write system (3.79) as

$$B\xi = \mathbf{c}, \quad (3.80)$$

where $B = (b_{ij}) \in \mathbb{R}^{N,N}$ and $\mathbf{c} = (c_1, \dots, c_N)^{tr}$ are defined by

$$b_{ij} = \begin{cases} a_{ij} & \text{if } i = 1, \dots, N-1, j = 1, \dots, N; \\ \sum_{j=1}^N m_{Nj}, & \text{if } i = N; \end{cases}$$

$$c_i = \begin{cases} b_i & \text{if } i = 1, \dots, N-1; \\ 0 & \text{if } i = N. \end{cases}$$

The matrix B in (3.80) is sparse, with only its last row being full, and unstructured. For a general review on numerical methods for sparse linear systems we refer the reader to [116].

3.6 Applications and numerical examples

3.6.1 Mesh pasting

In this section we discuss a possible advantage of SVEM with respect to SFEM. Suppose that Γ is made up of two surfaces Γ_1 and Γ_2 , joining along a curve ℓ , i.e. $\Gamma = \Gamma_1 \cup \Gamma_2$ and $\Gamma_1 \cap \Gamma_2 = \ell$. Furthermore, suppose we are given two corresponding polygonal surfaces $\Gamma_{1,h}$, $\Gamma_{2,h}$. We want to construct a polygonal surface Γ_h by pasting $\Gamma_{h,1}$ and $\Gamma_{h,2}$. Such a process can lead to nonconforming and/or discontinuous meshes. For this reason, pasting algorithms for standard FEMs typically need additional steps to deform the meshes and match the nodes, see for instance [75, 122]. As illustrated below, mesh pasting becomes trivial in the framework of the SVEM. We distinguish two cases.

Pasting along a straight line

In the first case ℓ is a straight line. Suppose that $\Gamma_{1,h}$ and $\Gamma_{2,h}$ are triangulations that fit ℓ exactly, i.e. $\Gamma_{1,h} \cap \Gamma_{2,h} = \ell$. An example of pasting process is depicted in Fig. 3.3. As shown in Fig. 3.3(b) this can lead, in general, to a nonconforming overall triangulation, that is Γ_h is composed of three quadrilaterals and two triangles in this specific example. It is well-known that the triangular FEMs, including SFEM, are not applicable to nonconforming meshes, since the basis functions are not well-defined in the presence of arbitrarily many vertices per polygon.

Pasting along an arbitrary curve

The general case when ℓ is an arbitrary curve is more interesting. In this case it is not true that $\Gamma_{1,h} \cap \Gamma_{2,h} = \ell$. In general, only the vertices of $\Gamma_{1,h}$ and $\Gamma_{2,h}$ lie on ℓ . Hence, $\Gamma_{h,1} \cup \Gamma_{h,2}$ might be a discontinuous mesh, as depicted in Fig. 3.4(b).

In order to apply the SVEM in this case, we proceed as follows:

1. We sort the boundary nodes (i.e. that are on ℓ) of $\Gamma_{h,1} \cup \Gamma_{h,2}$ according to their curvilinear abscissa;

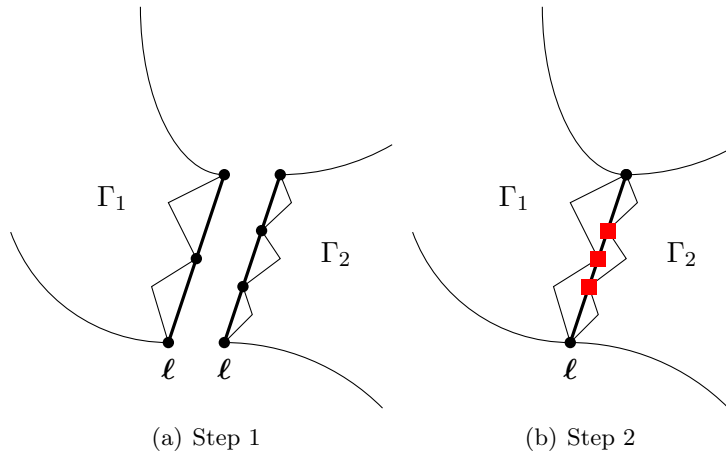


Figure 3.3: Graphical illustration of the algorithmic procedure, described in Section 3.6.1, for pasting two meshes along a straight line. Step 1: two surfaces Γ_1 and Γ_2 are given together with their approximations $\Gamma_{1,h}$ and $\Gamma_{2,h}$. The elements having an edge on ℓ are depicted and their nodes on ℓ are black-marked. Step 2: by pasting the polygonal surfaces, a nonconforming polygonation of $\Gamma = \Gamma_1 \cup \Gamma_2$ is formed, due to the presence of hanging nodes on ℓ , which are red-marked.

2. For each pair (P, R) of subsequent boundary nodes of $\Gamma_{h,1}$ and let T_1 be the element to which it belongs, see Fig. 3.4(a);
3. For any boundary node Q of the other polygonal surface $\Gamma_{h,2}$ that is between P and R , consider the orthogonal projection Q' of Q onto the edge \overline{PR} , as shown in Fig. 3.4(b);
4. Add Q' to the element T_1 as a hanging node;
5. Repeat steps (2)–(4) on the boundary nodes of the other mesh $\Gamma_{h,2}$;
6. For any pair (Q, Q') as above, enforce the *virtual continuity* condition $U(Q) = U(Q')$ on the numerical solution U .

Note that if $Q = Q'$, then of course the continuity condition is automatically fulfilled, but a new nonconforming element arises (see e.g. $R = R'$ in Fig. 3.4(b)). We remark that, when assembling the matrices involved in the method (mass, stiffness and load term), Q and Q' are associated to the same degree of freedom, hence *virtual continuity* does not affect the size of the linear system associated to the SVEM. Once again, this procedure strongly relies on the possibility of handling polygons with arbitrarily many vertices and hanging nodes, where standard FEMs are not well-defined. Furthermore, we point out that our convergence analysis in Section 3.4 does not cover this case of discontinuous meshes. However, without giving full details, our analysis can be extended to the present case in a straightforward way. In fact, based on interpolation estimates, it can be proven that the distance $\|Q - Q'\|$ decays quadratically with the meshsize (a similar result has been proven in [23] in the planar case). In Example 3 of the following Section 3.6.2 we experimentally show that this approach to mesh pasting does not affect the convergence rate of the method.

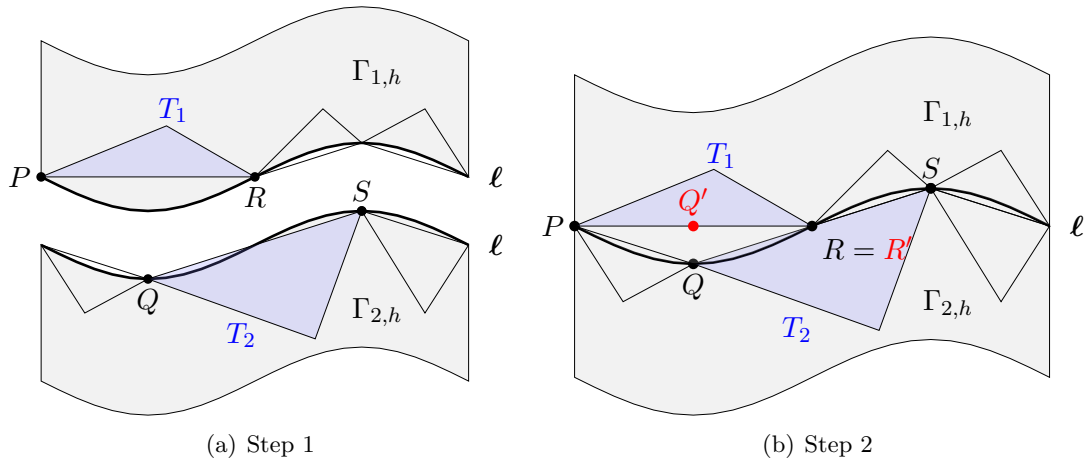


Figure 3.4: Graphical illustration of the algorithmic procedure, described in Section 3.6.1, for pasting two meshes along an arbitrary curve. (a) Step 1: two surfaces Γ_1 and Γ_2 are given together with their approximations $\Gamma_{1,h}$ and $\Gamma_{2,h}$. The elements having an edge on ℓ are depicted and some nodes on ℓ are black-marked. (b) Step 2: by pasting the polygonal surfaces, a discontinuous polygonation of $\Gamma = \Gamma_1 \cup \Gamma_2$ is formed. The new node Q' is obtained by projecting Q onto the edge \overline{PR} , so that the triangle T_1 becomes a quadrilateral with a hanging node, and the *virtual continuity* condition $U(Q) = U(Q')$ is enforced on the numerical solution. The node R coincides with its projection R' onto \overline{QS} and the triangle T_2 becomes a quadrilateral with a hanging node.

3.6.2 Numerical examples

In this section we will validate the theoretical findings through numerical examples.

In Example 1, a Laplace-Beltrami problem on the unit sphere, approximated with a polygonal mesh, is used to test the convergence rate in (3.70). The example also shows the robustness of the method with respect to “badly shaped” meshes, i.e with very tight polygons and of very different size, thus confirming the generality of assumptions (A1)-(A2). In Example 2, we solve the Laplace-Beltrami equation on a torus using the SVEM on trapezoidal meshes. In Example 3, to present an example of mesh pasting along a curve, we solve the Laplace-Beltrami equation on a cylindrical surface. We show that, even if discontinuous meshes are used, the theoretical convergence order of the SVEM is preserved.

All the simulations in the present thesis have been carried out using MATLAB. The linear systems have been solved with MATLAB direct solver in the “backslash” command. The codes are available on request.

Example 1 (Sphere)

In this example we solve the Laplace-Beltrami equation

$$\begin{cases} -\Delta_{\Gamma} u(x, y, z) = 6xy, & (x, y, z) \in \Gamma; \\ \int_{\Gamma} u(x, y, z) d\sigma = 0. \end{cases} \quad (3.81)$$

on the unit sphere $\Gamma := \mathcal{S}^2$, whose exact solution is given by $u(x, y, z) = xy$, $(x, y, z) \in \Gamma$. In this case, the Fermi stripe of Γ is $U = \mathbb{R}^3 \setminus \{\mathbf{0}\}$, the oriented distance function is given by $d(\mathbf{x}) = \|\mathbf{x}\| - 1$, $\mathbf{x} \in U$ and the outward unit normal vector field is given by $\boldsymbol{\nu}(\mathbf{x}) = \mathbf{x}$, $\mathbf{x} \in \Gamma$. Hence, the representation (2.4) of the tangential gradient of a function $f \in \mathcal{C}^1(\Gamma)$ becomes

$$\nabla_{\Gamma} f(\mathbf{x}) = \nabla f(\mathbf{x}) - (\nabla f(\mathbf{x}) \cdot \mathbf{x}) \mathbf{x} = \begin{bmatrix} 1 - x^2 & -xy & -xz \\ -xy & 1 - y^2 & -yz \\ -xz & -yz & 1 - z^2 \end{bmatrix} \nabla f(\mathbf{x}),$$

for all $\mathbf{x} = (x, y, z) \in \Gamma$. We solve the problem on a sequence of seven polygonal meshes, with decreasing meshsize h , made up with triangles and hexagons whose vertices lie on Γ . These polygonal meshes are constructed with an ad-hoc algorithm starting from a triangulation of the sphere obtained with the MATLAB library DistMesh [108]. Each polygonal mesh has been obtained by the algorithm explained in the previous Section 3.5.1. The sequence of polygonal meshes is such that in each mesh the ratio between the number of triangles and hexagons is approximately constant and for $h \rightarrow 0$, this ratio tends to 12 : 1. Furthermore, the sequence of polygonal meshes fulfils the regularity assumptions (A1)-(A2).

We test the convergence rate as follows. Let u_I be the interpolant, defined in (3.42), of the exact solution u and let $\delta_h := u_I - U$. We consider the following approximations of the L^2 , L^∞ and H^1 errors, respectively:

$$E_{L^2, h} := \langle \delta_h, \delta_h \rangle_M; \quad (3.82)$$

$$E_{L^\infty, h} := \max_{P \in \text{nodes}(\Gamma_h)} |\delta_h|; \quad (3.83)$$

$$E_{H^1, h} := b_h(\delta_h, \delta_h), \quad (3.84)$$

where the forms $b_h(\cdot, \cdot)$ and $\langle \cdot, \cdot \rangle_M$ are defined in (3.12) and (3.16), respectively. These approximations are $\mathcal{O}(h^2)$ -accurate, see for instance [130]. The need of defining these approximate norms and seminorms arise from the presence of the virtual basis functions that are not known in closed form. These norms are reminiscent of the approximate L^2 norm used for instance in [130, Equation 46], but also account for the fact that, in our case, the exact and the numerical solutions are defined on different surfaces. The convergence rate in the norms and seminorms defined in (3.82)-(3.84) is estimated by computing these errors as functions of h .

The coarsest of the polygonal meshes under consideration (meshsize $h = 0.6209$) is shown in Figure 3.5(a). The numerical solution obtained on the finest mesh (meshsize $h = 0.0798$) is shown in Figure 3.5(b). The convergence results are shown in Fig. 3.5(c). The convergence is linear in H^1 norm and, even if the method is not designed for optimal L^2 and L^∞ convergence, it appears to be quadratic in L^2 norm and almost quadratic in L^∞ norm. We remark that the considered meshes, like the one in Fig. 3.5(a), have polygons of very different size and shape, this means that the regularity assumptions (A1)-(A2) are quite weak and the method is thus robust with respect to badly shaped meshes.

Example 2 (Torus)

In this example we solve the Laplace-Beltrami equation

$$\begin{cases} -\Delta_\Gamma u(x, y, z) = \frac{100z}{9} \left(2 - \frac{7}{10}(x^2 + y^2)^{-\frac{1}{2}}\right), & (x, y, z) \in \Gamma; \\ \int_\Gamma u(x, y, z) d\sigma = 0. \end{cases} \quad (3.85)$$

on the torus

$$\Gamma := \left\{ (x, y, z) \in \mathbb{R}^3 \mid \left((x^2 + y^2)^{\frac{1}{2}} - \frac{7}{10} \right)^2 + z^2 = \frac{9}{100} \right\}, \quad (3.86)$$

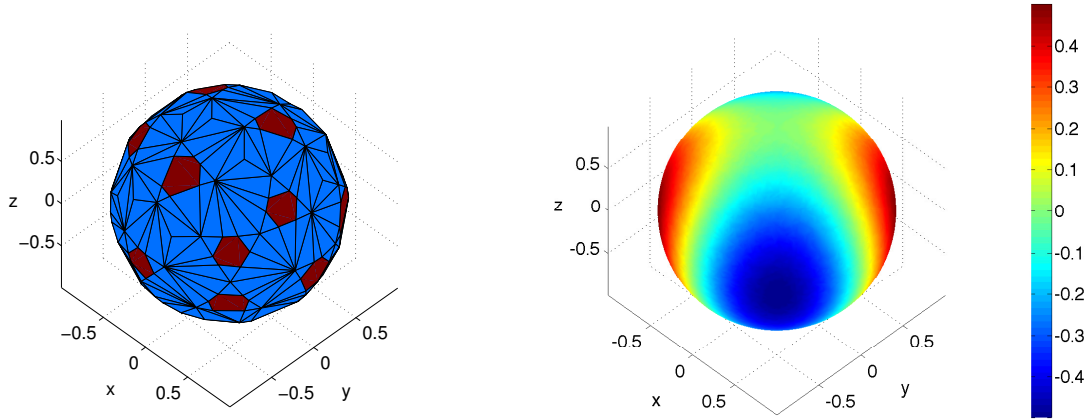
whose exact solution is given by $u(x, y, z) = z$, $(x, y, z) \in \Gamma$. A similar example has been considered in [33]. In this case, the Fermi stripe of Γ is $U = \{(x, y, z) \in \mathbb{R}^3 \mid (x, y) \neq (0, 0) \wedge (x^2 + y^2 \neq \frac{49}{100} \vee z \neq 0)\}$, that is the whole space deprived of a circle and the z -axis, the oriented distance function is given by $d(\mathbf{x}) = \left(\left((x^2 + y^2)^{\frac{1}{2}} - \frac{7}{10} \right)^2 + z^2 \right)^{\frac{1}{2}} - \frac{3}{10}$, $\mathbf{x} \in U$ and the outward unit normal vector field is given by $\boldsymbol{\nu}(x, y, z) = \frac{10}{3}(x, y, z) - \frac{35}{3(x^2 + y^2)^{\frac{1}{2}}}(x, y, 0)$, $(x, y, z) \in \Gamma$. Hence, the representation (2.4) of the tangential gradient of a function $f \in \mathcal{C}^1(\Gamma)$ becomes

$$\nabla_\Gamma f(\mathbf{x}) = \nabla f(\mathbf{x}) - (\nabla f(\mathbf{x}) \cdot \mathbf{x}) \mathbf{x} = \begin{bmatrix} 1 - \nu_1^2(\mathbf{x}) & -\nu_1(\mathbf{x})\nu_2(\mathbf{x}) & -\nu_1(\mathbf{x})\nu_3(\mathbf{x}) \\ -\nu_1(\mathbf{x})\nu_2(\mathbf{x}) & 1 - \nu_2^2(\mathbf{x}) & -\nu_2(\mathbf{x})\nu_3(\mathbf{x}) \\ -\nu_1(\mathbf{x})\nu_3(\mathbf{x}) & -\nu_2(\mathbf{x})\nu_3(\mathbf{x}) & 1 - \nu_3^2(\mathbf{x}) \end{bmatrix} \nabla f(\mathbf{x}),$$

for all $\mathbf{x} \in \Gamma$, with $\boldsymbol{\nu}(\mathbf{x}) = (\nu_1(\mathbf{x}), \nu_2(\mathbf{x}), \nu_3(\mathbf{x}))$ as defined above. We consider a family of meshes defined as follows. Given $m, n \in \mathbb{N}$, the approximation Γ_h of the torus Γ is the polytope having the following mn gridpoints as vertices

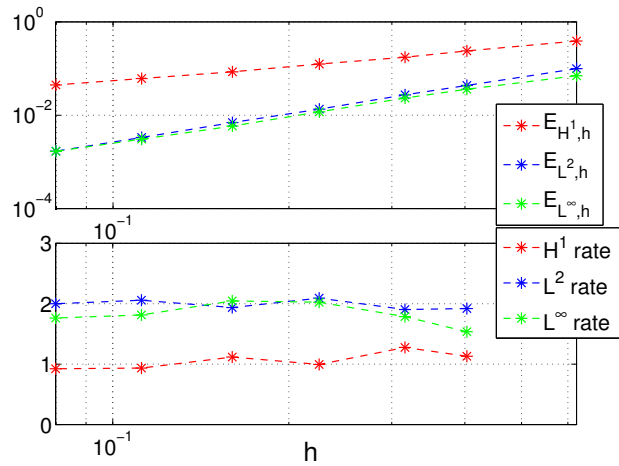
$$P_{ij} = \left(\left(\frac{7}{10} + \frac{3}{10} \cos \frac{2i\pi}{n} \right) \cos \frac{2j\pi}{m}, \left(\frac{7}{10} + \frac{3}{10} \cos \frac{2i\pi}{n} \right) \sin \frac{2j\pi}{m}, \frac{3}{10} \sin \frac{2i\pi}{n} \right),$$

for all $i = 1, \dots, n$ and $j = 1, \dots, m$, such that a trapezoidal mesh is obtained. To test the convergence, we consider a sequence of six trapezoidal meshes $\Gamma_h^{(k)}$ of the type described



(a) Polygonal approximation Γ_h of the unit sphere Γ , made up of triangles and hexagons, with meshsize $h = 0.6209$.

(b) Numerical solution obtained on Γ_h , for $h = 0.0798$.



(c) Convergence results in the $E_{L^2,h}$ and $E_{L^\infty,h}$ norms and in the $E_{H^1,h}$ seminorm defined in (3.82), (3.83) and (3.84), respectively.

Figure 3.5: *Example 1*. Laplace-Beltrami problem (3.81) on the unit sphere. The example (i) illustrates the usage of polygonal meshes on the sphere as described in Section (3.5.1), (ii) provides a convergence test and (iii) shows the robustness of the method with respect to meshes made of polygons with different shape and size.

above, obtained by increasing $n = 3 \cdot 2^k$ and $m = 8 \cdot 2^k$, $k = 0, \dots, 5$. The mesh $\Gamma_h^{(2)}$ is shown in Fig. 3.6(a), while the numerical solution obtained for $k = 5$ is shown in Fig. 3.6(b). For all $k = 0, \dots, 5$, the errors (3.82)-(3.84) are shown in Fig. 3.6(c) as functions of h . The experimental convergence rate is quadratic in the approximate L^2 , L^∞ norms and H^1 seminorm. This superconvergence is due to the symmetry of the mesh and of the solution.

Example 3 (Cylinder)

In this example we solve the Laplace-Beltrami equation and we address the problem of pasting two surfaces along a curve. We consider the cylinder

$$\Gamma := \{(x, y, z) \in \mathbb{R}^3 \mid x^2 + y^2 = 1 \wedge 0 \leq z \leq 2\} \quad (3.87)$$

and we split it into two parts $\Gamma_1 := \Gamma \cap \{z \leq 1\}$ and $\Gamma_2 := \Gamma \cap \{z \geq 1\}$.

We consider the following Laplace-Beltrami problem with Neumann boundary conditions

$$\begin{cases} -\Delta_\Gamma u = ((10 + \pi^2)x^2 - 6x^4 - 6x^2y^2 - 2) \cos(\pi z), & (x, y, z) \in \Gamma; \\ \frac{\partial u}{\partial \mathbf{n}} = 0, & (x, y, z) \in \partial\Gamma; \\ \int_\Gamma u d\sigma = 0, \end{cases} \quad (3.88)$$

whose exact solution is given by $x(x, y, z) = x^2 \cos(\pi z)$, $(x, y, z) \in \Gamma$.

In this case, the Fermi stripe of Γ is $U = \{(x, y, z) \in \mathbb{R}^3 \mid (x, y) \neq (0, 0)\}$, the oriented distance function is given by $d(x, y, z) = \sqrt{x^2 + y^2} - 1$, $(x, y, z) \in U$ and the outward unit normal vector field is given by $\boldsymbol{\nu}(x, y, z) = (x, y, 0)$, $(x, y, z) \in \Gamma$. Hence, the representation (2.4) of the tangential gradient of a function $f \in C^1(\Gamma)$ becomes

$$\nabla_\Gamma f(\mathbf{x}) = \nabla f(\mathbf{x}) - (\nabla f(\mathbf{x}) \cdot (x, y, 0))(x, y, 0) = \begin{bmatrix} 1 - x^2 & -xy & 0 \\ -xy & 1 - y^2 & 0 \\ 0 & 0 & 1 \end{bmatrix} \nabla f(\mathbf{x}),$$

for all $\mathbf{x} = (x, y, z) \in \Gamma$. We consider a family of meshes defined as follows. Let $n \in \mathbb{N}$. The half cylinder Γ_1 is approximated with $6n^2$ equal rectangular elements having the following $6n(n+1)$ gridpoints as vertices:

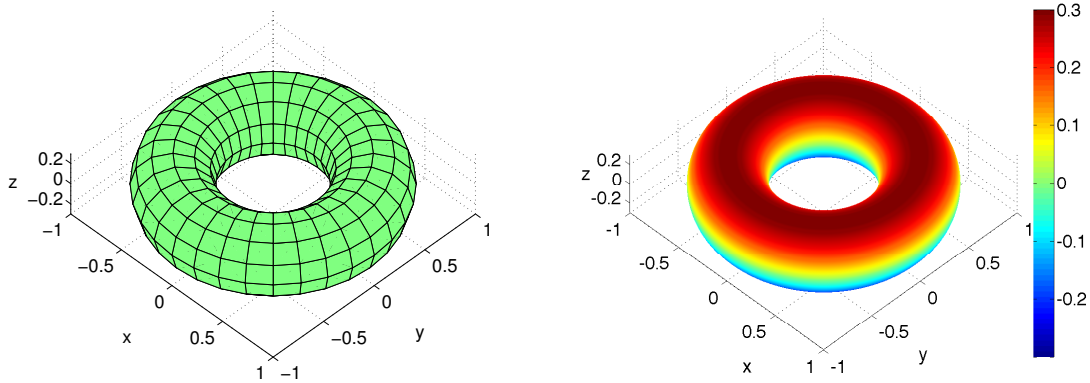
$$P_{ij} = \left(\cos \frac{i}{3n}\pi, \sin \frac{i}{3n}\pi, \frac{j}{n} \right), \quad i = 1, \dots, 6n, \quad j = 0, \dots, n,$$

while the half cylinder Γ_2 is approximated with $6n^2$ equal rectangular elements constructed on the following $6n(n+1)$ gridpoints:

$$P_{ij} = \left(\cos \frac{2i+1}{6n}\pi, \sin \frac{2i+1}{6n}\pi, \frac{j}{n} + 1 \right), \quad i = 1, \dots, 6n, \quad j = 0, \dots, n.$$

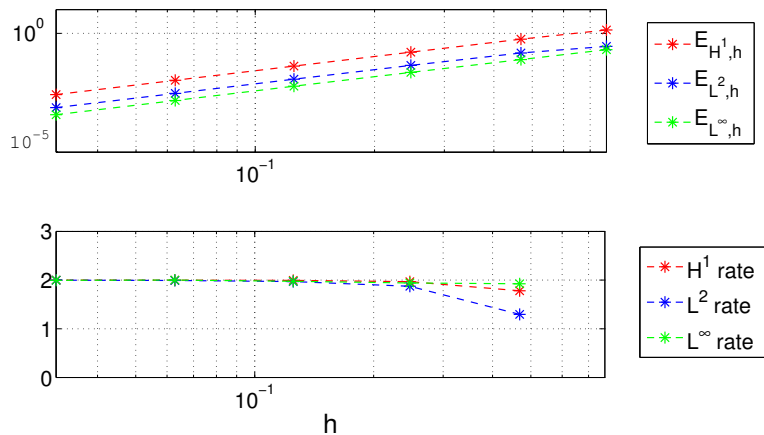
By pasting these meshes we end up with a nonconforming and discontinuous mesh Γ_h made up of $12n^2$ elements, of which $12n(n-1)$ rectangles and $12n$ degenerate pentagons with one hanging node each.

To test the convergence, we consider a sequence of six meshes $\Gamma_h^{(k)}$ of the type described above, by increasing $n = 2^k$, $k = 0, \dots, 5$. Notice that $h = \mathcal{O}(\frac{1}{n})$. For $n = 1$, the nonconforming



(a) Trapezoidal mesh $\Gamma_h^{(2)}$ for the torus Γ , with meshsize $h = 0.2470$.

(b) Numerical solution obtained on the finest mesh $\Gamma_h^{(5)}$, with meshsize $h = 0.0314$.



(c) Convergence results in the $E_{L^2,h}$ and $E_{L^\infty,h}$ norms and in the $E_{H^1,h}$ semi-norm defined in (3.82), (3.83) and (3.84), respectively.

Figure 3.6: *Example 2*. Laplace-Beltrami problem (3.85) on the torus (3.86). The example: (i) shows the usefulness of polygonal meshes in approximating particular surfaces as described in Section 3.5.1 and (ii) provides a convergence test.

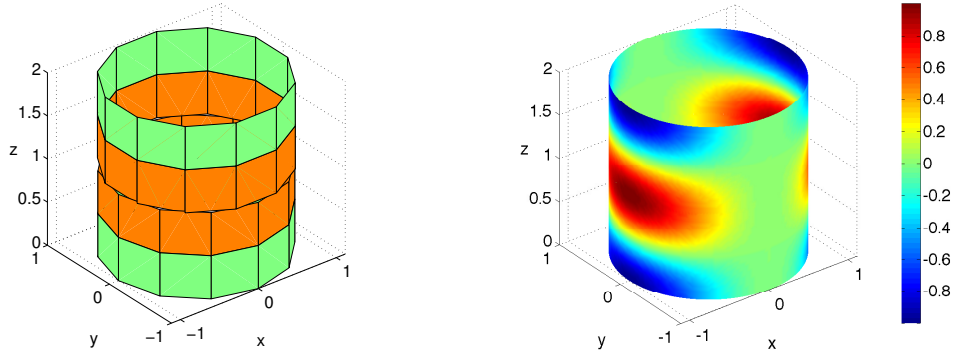
mesh $\Gamma_h^{(0)}$ is shown in Fig. 3.7(a), in which the rectangles are green and the pentagons are orange, while the corresponding numerical solution on the finest mesh is shown in Fig. 3.7(b).

For all $k = 0, \dots, 5$, the errors in the norms and seminorms (3.82)-(3.84) are shown in Fig. 3.7(c) as functions of h . The experimental convergence rate is quadratic in the approximate L^2 and L^∞ norms and superlinear in the approximate H^1 seminorm.

3.7 Conclusions

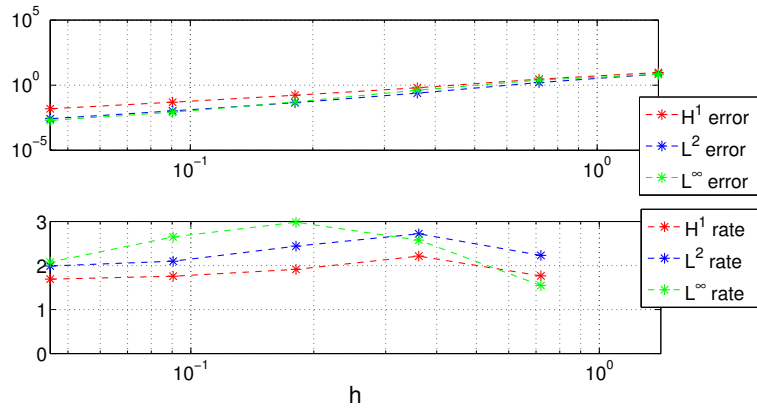
We have presented a Surface Virtual Element Method (SVEM) for the numerical approximation of the Laplace-Beltrami equation on smooth surfaces, by generalising the VEM on planar domains [8] and the SFEM [37]. The ability of the proposed method of handling non-conforming and/or discontinuous polygonal meshes can be easily exploited in mesh pasting. The SVEM retains the same (optimal) first-order convergence rate in H^1 norm exhibited by the SFEM [37, 40] and the planar VEM [8].

In the next two chapters we present another novel variation of the SFEM: the Lumped Surface Finite Element Method (LSFEM) for the numerical approximation of the semilinear heat equation (2.10) and RDSs (2.11), respectively. Even if the LSFEM can be equally applied to elliptic problems, we apply the LSFEM to time-dependent PDEs, only, because our analysis of the LSFEM is mainly concerned with (i) *discrete maximum principles* for the semilinear heat equation and (ii) *numerical preservation of invariant regions* of RDSs.



(a) Nonconforming polygonal approximation $\Gamma_h^{(1)}$ of Γ , with meshsize $h = 1.4142$, made up of rectangles and pentagons.

(b) Numerical solution obtained on the finest mesh $\Gamma_h^{(5)}$.



(c) Convergence results in the $E_{L^2,h}$ and $E_{L^\infty,h}$ norms and in the $E_{H^1,h}$ seminorm defined in (3.82), (3.83) and (3.84), respectively.

Figure 3.7: *Example 3*. Laplace-Beltrami problem (3.88) on the cylinder (3.87). The example (i) illustrates the possibility of pasting two meshes along a curve, as discussed in Section 3.6.1 and (ii) provides a convergence test.

Chapter 4

The heat equation on stationary surfaces

4.1 Introduction

This chapter is focused on a simple class of scalar parabolic surface PDEs, the semilinear heat equation (2.10). Our interest in the semilinear heat equation stems from the fact that (i) it models diffusion processes on a surface [39] and (ii) it constitutes a remarkable special case of the more general RDSs addressed in the next chapter.

An important property of the semilinear heat equation (2.10) is the *maximum principle*, that is

$$0 \leq u(\mathbf{x}, t) \leq \max_{\mathbf{y} \in \Gamma} u_0(\mathbf{y}), \quad (\mathbf{x}, t) \in \Gamma \times [0, T], \quad (4.1)$$

where $T > 0$ is the final time, $u : \Gamma \times [0, T] \rightarrow \mathbb{R}$ is the strong solution to (2.10), and $u_0 : \Gamma \rightarrow \mathbb{R}$ is the initial datum, see [18]. The maximum principle (4.1) (i) automatically provides a stability estimate for the solution and thus (ii) can be exploited in the convergence analysis of numerical methods. For the special case of the homogeneous heat equation on surfaces, i.e. when $\beta = 0$ in (4.2), it is known that the maximum principle is fulfilled at the continuous level, see [18].

The increasing interest from applications in PDEs on manifolds has stimulated the development of several numerical methods for such PDEs, and in particular for the semilinear heat equation (2.10). We have reviewed some of these methods in Section 2.6. Many of these methods are examples of the well-known Method of Lines (MOL) [118], i.e. the given PDE is approximated, through space discretisation, by a system of ordinary differential equations (ODEs). The ODE system obtained with the MOL must be then approximated through a numerical method for ODEs. Among the applications of the MOL to parabolic PDEs on manifolds -including the semilinear heat equation (2.10)- we mention the SFEM, see for instance [39, 40], whose success is mainly related to its geometric flexibility in coping with arbitrary surfaces.

In this chapter we present, following our recent work [56], a novel spatial and full discretisation of (2.10) that preserve the maximum principle (4.1) under discretisation, namely our methods fulfil *discrete maximum principles*. In particular:

- The spatial discretisation is obtained through a novel extension of the SFEM, the

Lumped Surface Finite Element Method (LSFEM). The method extends to surfaces the Lumped Finite Element Method (LFEM) analysed in [101, 126] for scalar parabolic equations on planar domains.

- The full discretisation is obtained by discretising the ODE system arising from space discretisation through the implicit-explicit (IMEX) Euler method, that approximates the linear diffusion part implicitly and the nonlinear reaction part explicitly. Fully discrete schemes based on the IMEX Euler time discretisation have been considered in the literature, for instance in [82, 91].

To the best of our knowledge, numerical methods for the semilinear heat equation (2.10) on surfaces that preserve the maximum principle have not yet been investigated. This motivates the contents of the present chapter. The main contributions of this chapter are the following:

1. For the semilinear heat equation (2.10), we prove that the LSFEM space discretisation and the IMEX Euler-LSFEM full discretisation preserve the invariant rectangles. A timestep restriction depending on the Lipschitz constants of the kinetics is needed at the fully discrete level. These preservation results require no space meshsize restriction or modified kinetics. A numerical example on the unit sphere confirms the result for the linear heat equation (Example 1).
2. By exploiting the discrete maximum principles, we prove optimal error bounds for the semi- and fully discrete schemes. These results are novel in that they account for errors arising from mass lumping and surface approximation, respectively. A numerical example on the unit sphere confirms the result for the homogeneous heat equation (Example 2).

The remainder of this chapter is structured as follows. In Section 4.2 we recall the semilinear heat equation on a compact surface in its strong and weak formulations and we recall the notion of maximum principle. In Section 4.3 we present the LSFEM space discretisation of the semilinear weak equation, while the LSFEM-IMEX Euler full discretisation is presented in Section 4.4. In Section 4.5 we prove the preservation of the maximum principle under spatial and full discretisation. In Section 4.6 we prove asymptotically optimal convergence results for the spatially and fully discrete methods. In Section 4.7 we present two numerical examples to confirm (i) the theoretical convergence rate of the LSFEM-IMEX Euler full discretisation of the linear heat equation on a sphere and (ii) the preservation of the maximum principle at the fully discrete level for the homogeneous heat equation on a sphere.

4.2 The semilinear heat equation at the continuous level

Let Γ be a \mathcal{C}^2 surface in \mathbb{R}^3 without boundary and let $T > 0$ be a final time. We consider the following semilinear heat equation

$$\begin{cases} \dot{u}(\mathbf{x}, t) - d\Delta_{\Gamma}u(\mathbf{x}, t) = -\beta u^{\alpha}(\mathbf{x}, t), & (\mathbf{x}, t) \in \Gamma \times [0, T]; \\ u(\mathbf{x}, 0) = u_0(\mathbf{x}), & \mathbf{x} \in \Gamma. \end{cases} \quad (4.2)$$

where $\beta \geq 0$, $\alpha \geq 1$, $d > 0$ is a diffusion coefficient and $u_0 \in \mathcal{C}^2(\Gamma)$ is a smooth initial datum, that we will omit in the remainder of this chapter.

Remark 6 (Regularity of Γ). *In Sections 2.4, 2.5 and Chapter 3, devoted to the Laplace-Beltrami equation, we had imposed the stronger assumption that $\Gamma \in \mathcal{C}^3$. In fact, the analysis of the Laplace-Beltrami equation relies on the Poincaré inequality in its continuous (2.8) and discrete (2.24) forms, which hold true when $\Gamma \in \mathcal{C}^3$. For the whole analysis carried out in this chapter, which does not rely on these Poincaré inequalities, it is sufficient to require that $\Gamma \in \mathcal{C}^2$, such that the Laplace-Beltrami operator Δ_Γ is well-defined.*

Remark 7 (Surfaces with boundary). *The following arguments still hold for systems on surfaces with boundaries, whose boundary conditions could be taken as homogeneous Neumann type, i.e. zero conormal derivative on $\partial\Gamma$ [40]. However, we will confine the present analysis to the case of compact surfaces without boundary to simplify the presentation.*

Definition 10 (Maximum principle). *Problem (4.2) is said to fulfil the maximum principle if $u_0(\mathbf{x}) \geq 0$ for all $\mathbf{x} \in \Gamma$ implies*

$$0 \leq u(\mathbf{x}, t) \leq \max_{\mathbf{y} \in \Gamma} u_0(\mathbf{y}), \quad (\mathbf{x}, t) \in \Gamma \times [0, T]. \quad (4.3)$$

Remark 8 (Minimum-maximum principle). *The nonlinear right-hand-side of the semilinear heat equation (4.2) is not defined for $u < 0$. However, for scalar PDEs that also admit negative solutions, one can consider the following minimum-maximum principle:*

$$\min \left\{ 0, \min_{\mathbf{y} \in \Gamma} u_0(\mathbf{y}) \right\} \leq u(\mathbf{x}, t) \leq \max \left\{ 0, \max_{\mathbf{y} \in \Gamma} u_0(\mathbf{y}) \right\}, \quad (\mathbf{x}, t) \in \Gamma \times [0, T]. \quad (4.4)$$

In the remainder of this chapter we present a semi- and a full-discretisation of (4.2), introduced in our recent work [56], that preserve the maximum principle (4.3) under discretisation.

4.3 The Lumped Surface Finite Element Method (LSFEM)

In the remainder of this chapter we utilise the same notations and definitions introduced in Section 2.5.1 for the SFEM. The LSFEM, that discretises the weak formulation (2.36) of the semilinear heat equation (4.2), seeks to find $U \in L^2([0, T]; \mathbb{V}_h)$ with $\dot{U} \in L^2([0, T]; \mathbb{V}_h)$ such that

$$\int_{\Gamma_h} I_h(\dot{U}\phi) + d \int_{\Gamma_h} \nabla_{\Gamma_h} U \cdot \nabla_{\Gamma_h} \phi = -\beta \int_{\Gamma_h} I_h(U^\alpha \phi), \quad \forall \phi \in \mathbb{V}_h, \quad (4.5)$$

where the initial condition $U_0 \in \mathbb{V}_h$ is the Lagrange interpolant of the exact initial condition $u_0 \in \mathcal{C}^2(\Gamma)$, namely $U_0 = I_h(u_0)$. Since $\{\chi_j | j = 1, \dots, N\}$ is a basis for \mathbb{V}_h , we can reformulate (4.5) as

$$\int_{\Gamma_h} I_h(\dot{U}\chi_j) + d \int_{\Gamma_h} \nabla_{\Gamma_h} U \cdot \nabla_{\Gamma_h} \chi_j = -\beta \int_{\Gamma_h} I_h(U^\alpha \chi_j), \quad j = 1, \dots, N. \quad (4.6)$$

Remark 9 (Standard finite elements). *The LSFEM discretisation (4.5) is obtained by adding the Lagrange interpolant I_h (mass lumping) to the standard SFEM discretisation (2.39). As we will see in the remainder of this chapter, mass lumping yields two advantages. In fact, the simplified structure of the ODE system associated to (4.5) (i) results in a computational advantage and (ii) allows us to prove a discrete maximum principle which does not hold in the absence of mass lumping.*

In order to formulate (4.5) as an ODE system, we express the spatially discrete solution U as a linear combination, with time-dependent coefficients, of the nodal basis functions $\{\chi_i | i = 1, \dots, N\}$ as follows

$$U(\mathbf{x}, t) = \sum_{i=1}^N \xi_i(t) \chi_i(\mathbf{x}) \quad (\mathbf{x}, t) \in \Gamma_h \times [0, T]. \quad (4.7)$$

By plugging the expansion (4.7) into (4.6) we obtain the following ODE system

$$\sum_{i=1}^N \dot{\xi}_i(t) \int_{\Gamma_h} I_h(\chi_i \chi_j) + d \sum_{i=1}^N \xi_i(t) \int_{\Gamma_h} \nabla_{\Gamma_h} \chi_i \cdot \nabla_{\Gamma_h} \chi_j = -\beta \int_{\Gamma_h} I_h \left(\left(\sum_{i=1}^N \xi_i(t) \chi_i \right)^\alpha \chi_j \right), \quad (4.8)$$

for all $j = 1, \dots, N$ and $t \in [0, T]$. From the definition (2.19) of the Lagrange basis functions and the definition (2.20) of the Lagrange interpolant, we can swap the integral with the sum in the right-hand-side of (4.8). Hence, (4.6) is equivalent to

$$\sum_{i=1}^N \dot{\xi}_i(t) \int_{\Gamma_h} I_h(\chi_i \chi_j) + d \sum_{i=1}^N \xi_i(t) a_h(\chi_i, \chi_j) = -\beta \sum_{i=1}^N \xi_i^\alpha(t) \int_{\Gamma_h} I_h(\chi_i \chi_j), \quad (4.9)$$

for all $j = 1, \dots, N$ and $t \in [0, T]$. In matrix form, the ODE system (4.9) can be written as

$$\bar{M} \dot{\boldsymbol{\xi}}(t) + dA \boldsymbol{\xi}(t) = -\beta \bar{M} \boldsymbol{\xi}^\alpha(t), \quad t \in [0, T], \quad (4.10)$$

where $\boldsymbol{\xi}(t) := (\xi_1(t), \dots, \xi_N(t))^{tr}$, $\boldsymbol{\xi}^\alpha(t) := (\xi_1^\alpha(t), \dots, \xi_N^\alpha(t))^{tr}$, $A \in \mathbb{R}^{N,N}$ is the stiffness matrix defined in (2.34) and $\bar{M} = (\bar{m}_{ij}) \in \mathbb{R}^{N,N}$ is the *lumped mass matrix* defined by

$$\bar{m}_{ij} := \int_{\Gamma_h} I_h(\chi_i, \chi_j) = \begin{cases} \int_{\Gamma_h} \chi_i & \text{if } i = j; \\ 0 & \text{if } i \neq j, \end{cases} \quad i, j = 1, \dots, N. \quad (4.11)$$

The lumped mass matrix (4.11) is positive definite and, in contrast to the standard mass matrix defined in (2.33), it is diagonal. Hence, the computation of its inverse \bar{M}^{-1} is trivial. This feature can be exploited in the implementation of the fully discrete scheme presented in the next section and results in a computational advantage. For the maximum principle analysis, we rewrite (4.10) as

$$\dot{\boldsymbol{\xi}}(t) = -d\bar{M}^{-1}A \boldsymbol{\xi}(t) - \beta \boldsymbol{\xi}^\alpha(t), \quad t \in [0, T]. \quad (4.12)$$

4.4 Time discretisation

To carry out a fully discrete scheme, we adopt the well-known Method of Lines, i.e. we regard the spatially discrete method as a system of ODEs, which we discretise through an ODE solver (timestepping scheme). The timestepping scheme that we choose for our purposes in the Implicit-Explicit (IMEX) Euler scheme, that approximates the diffusion terms implicitly and the reaction terms explicitly.

Let $\tau > 0$ be the timestep. By applying the IMEX Euler timestepping to the spatially discrete method (4.10), we obtain the fully-discrete scheme

$$\bar{M} \frac{\boldsymbol{\xi}^{n+1} - \boldsymbol{\xi}^n}{\tau} + dA \boldsymbol{\xi}^{n+1} = -\beta \bar{M} (\boldsymbol{\xi}^n)^\alpha, \quad n = 0, \dots, N_T, \quad (4.13)$$

with $\xi^0 = \xi(0)$, where $\xi(t)$ is defined in (4.7), and $N_T := \lfloor \frac{T}{\tau} \rfloor$ is the number of time steps. Equivalently, we write the scheme (4.13) as

$$\xi^{n+1} = (\bar{M} + d\tau A)^{-1} \bar{M} (\xi^n - \tau \beta (\xi^n)^\alpha), \quad n = 0, \dots, N_T. \quad (4.14)$$

We remark that, for $\beta = 0$ (for the case of the homogeneous heat equation), the timestepping scheme collapses to the standard implicit Euler method.

4.5 Semi- and fully-discrete maximum principles

In this section we show that, under suitable assumptions on the triangulation \mathcal{T}_h , the LSFEM space discretisation and the LSFEM-IMEX Euler full discretisation fulfil discrete maximum principles, i.e. discrete versions of (4.3). To this end we first introduce a regularity assumption for the triangulation on the mesh \mathcal{T}_h .

4.5.1 Mesh regularity assumption

We now introduce a regularity assumption for the triangulation on the mesh \mathcal{T}_h that mimicks the standard Delaunay condition on planar domains. We also show how this regularity assumption affects the properties of the matrices involved in the semi- and fully-discrete schemes.

Let e be an edge of the triangulation \mathcal{T}_h and let T_1 and T_2 be the triangles sharing the edge e . Let α_1 and α_2 be the angles in T_1 and T_2 opposite to e , respectively. For every edge e in \mathcal{T}_h we require that

$$\alpha_1 + \alpha_2 \leq \pi. \quad (4.15)$$

This condition is represented in Fig. 4.1.

Remark 10. *We remark that the construction of good quality meshes on arbitrary surfaces is well-studied in the literature and some theoretical works in this area are available (see for instance [31, 36, 107] and references therein). However the work in these references does not explicitly discuss the construction of surface meshes fulfilling the Delaunay property (4.15). To the best of our knowledge, algorithms for the construction of Delaunay triangulations on arbitrary smooth surfaces remain an open area of research.*

We provide the following result that extends to triangulated surfaces a characterization of (4.15) given in [126] for the planar case.

Lemma 7. *\mathcal{T}_h fulfils (4.15) if and only if*

$$(\nabla_{\Gamma_h} \chi_i, \nabla_{\Gamma_h} \chi_j) \leq 0 \quad \forall i \neq j. \quad (4.16)$$

Proof. Let \mathbf{x}_i and \mathbf{x}_j be two distinct nodes of \mathcal{T}_h . If \mathbf{x}_i and \mathbf{x}_j are not neighbours, then $(\nabla_{\Gamma_h} \chi_i, \nabla_{\Gamma_h} \chi_j) = 0$. Otherwise, let e be the edge connecting \mathbf{x}_i and \mathbf{x}_j . Since the intersection of the support of the pyramidal functions χ_i and χ_j is $T_1 \cup T_2$ (see Fig. 4.1) then we can write

$$(\nabla_{\Gamma_h} \chi_i, \nabla_{\Gamma_h} \chi_j) = (\nabla_{T_1} \chi_i, \nabla_{T_1} \chi_j) + (\nabla_{T_2} \chi_i, \nabla_{T_2} \chi_j). \quad (4.17)$$

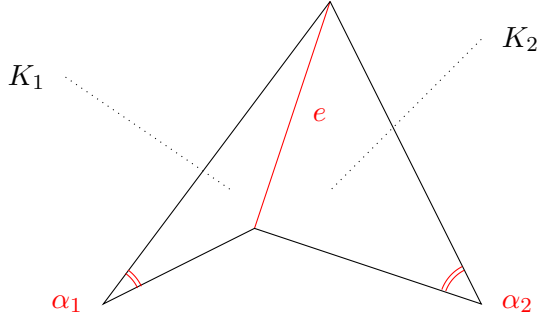


Figure 4.1: Schematic representation of Delaunay condition (4.15) for two triangles K_1 and K_2 .

Let F_1 and F_2 be two linear transformations that map T_1 and T_2 into two triangles T_1^0 and T_2^0 contained in the xy plane, respectively, and let J_1 and J_2 be the Jacobians of F_1 and F_2 , respectively. Then, expression (4.17) can be written equivalently as

$$\int_{T_1^0} \left(J_1 \nabla_{T_1^0}(\chi_i \circ F_1^{-1}) \right) \cdot \left(J_1 \nabla_{T_1^0}(\chi_j \circ F_1^{-1}) \right) \det(J_1) \\ + \int_{T_2^0} \left(J_2 \nabla_{T_2^0}(\chi_i \circ F_2^{-1}) \right) \cdot \left(J_2 \nabla_{T_2^0}(\chi_j \circ F_2^{-1}) \right) \det(J_2).$$

We choose F_1 and F_2 as direct isometries, that is $\det(J_1) = \det(J_2) = 1$. Since $\nabla_{T_1^0}$ and $\nabla_{T_2^0}$ both collapse to the standard gradient ∇ in \mathbb{R}^2 , the expression above becomes

$$\int_{T_1^0} \nabla(\chi_i \circ F_1^{-1}) \cdot \nabla(\chi_j \circ F_1^{-1}) + \int_{T_2^0} \nabla(\chi_i \circ F_2^{-1}) \cdot \nabla(\chi_j \circ F_2^{-1}).$$

It is known that (see [126]) this expression only depends on the transformed angles $\alpha_1^0 = \alpha_1$, $\alpha_2^0 = \alpha_2$ and is given by $-\frac{\sin(\alpha_1 + \alpha_2)}{4 \sin(\alpha_1) \sin(\alpha_2)}$, which is nonpositive if and only if $\alpha_1 + \alpha_2 \leq \pi$. This completes the proof. \square

Next, we proceed to state two key properties associated with the lumped mass and stiffness matrices to be used throughout the analysis. Let $\mathbf{1}$ and $\mathbf{0}$ be the vector of ones and the null vector in \mathbb{R}^N , respectively. As shown in [126, pages 272-273], the structure (4.16) of the stiffness matrix A , together with the diagonal structure of the lumped mass matrix \bar{M} , imply that, for every $s > 0$, $\bar{M} + sA$ is an M-matrix. It then follows that

$$(\bar{M} + sA)^{-1} \bar{M} \geq \mathbf{0}, \quad (4.18)$$

meaning that this matrix has nonnegative entries. If $\boldsymbol{\xi} = \mathbf{1}$, from (4.7) we have $U(\mathbf{x}, t) = 1$ for all $(\mathbf{x}, t) \in \Gamma_h \times [0, T]$, and thus $\nabla_{\Gamma_h} U(\mathbf{x}, t)$ vanishes, which yields $A\mathbf{1} = \mathbf{0}$. It therefore follows that

$$(\bar{M} + sA)^{-1} \bar{M} \mathbf{1} = \mathbf{1}. \quad (4.19)$$

We will show that (4.18) and (4.19) play a crucial role in the discrete maximum principle for the parabolic equation (4.2) and, in the next chapter, the preservation of invariant regions of reaction-diffusion systems.

4.5.2 Discrete maximum principles

It is known that the lumped FEM fulfils a discrete maximum principle for the homogeneous heat equation on planar domains (see [101, 126]). The purpose of this section is to extend this result to the semilinear heat equation on surfaces (4.2) which includes as a special case the homogeneous heat equation on surfaces.

Theorem 11 (Maximum principle for (4.12)). *Under the Delaunay condition (4.15), the semi-discrete solution $\boldsymbol{\xi}(t)$ of (4.12) fulfils the following discrete maximum principle*

$$0 \leq \xi_i(t) \leq \max_{\mathbb{R}^N} \{\boldsymbol{\xi}(0)\}, \quad i = 1, \dots, N, \quad t > 0. \quad (4.20)$$

Proof. Consider the auxiliary equation

$$\dot{\boldsymbol{\xi}} = -d\bar{M}^{-1}A\boldsymbol{\xi} - \beta|\boldsymbol{\xi}|^\alpha \text{sign}(\boldsymbol{\xi}), \quad (4.21)$$

where $|\boldsymbol{\xi}|$ and $\text{sign}(\boldsymbol{\xi})$ are the componentwise absolute value and the componentwise sign function of $\boldsymbol{\xi}$, respectively. If $\mu = \max_{\mathbb{R}^N} \{\boldsymbol{\xi}(0)\}$, it is sufficient to prove that the solution of the ODE system (4.12) does not escape the set $\Sigma = [0, \mu]^N$, i.e. we have to prove that, for every $\varepsilon > 0$, the solution of (4.21) does not leave the set $\bar{\Sigma} := [-\varepsilon, \mu]^N$. To this end, we have to prove that the vector field on the right-hand-side of (4.21), computed on every $(N-1)$ -dimensional face of $\bar{\Sigma}$, points toward the interior of $\bar{\Sigma}$. To this end, let $\boldsymbol{\xi}$ be a point on $\partial\bar{\Sigma}$. This means that there exists $i = 1, \dots, N$ such that $\xi_i \in \{-\varepsilon, \mu\}$. Suppose $\xi_i = \mu$; in the case $\xi_i = -\varepsilon$ the proof is analogous. Then

$$\xi_j \leq \xi_i, \quad j \neq i. \quad (4.22)$$

All we have to prove is that $\dot{\xi}_i$ is negative. Hence, we prove that:

1. $-|\xi_i|^\alpha \text{sign}(\xi_i) = -|\mu|^\alpha \text{sign}(\mu) < 0$ from (4.22);
2. The i^{th} component of the vector $-d\bar{M}^{-1}A\boldsymbol{\xi}$ is nonpositive. In fact, since \bar{M} is a diagonal matrix, this component is given by

$$-(d\bar{M}^{-1}A\boldsymbol{\xi})_i = -d\bar{m}_{ii}^{-1} \sum_{j=1}^N a_{ij} \xi_j. \quad (4.23)$$

We can split the sum on the right-hand-side by isolating the $a_{ii}\xi_i$ term:

$$d\bar{m}_{ii}^{-1} \left(-a_{ii}\xi_i + \sum_{j \in \{1, \dots, N\} \setminus \{i\}} (-a_{ij})\xi_j \right). \quad (4.24)$$

Since $a_{ij} \leq 0$ for $i \neq j$ from Lemma 7 and $\xi_j \leq \xi_i$ for $j \neq i$ from (4.22), expression (4.24) is less than or equal to

$$d\bar{m}_{ii}^{-1} \xi_i \left(-a_{ii} + \sum_{j \in \{1, \dots, N\} \setminus \{i\}} (-a_{ij}) \right) = -d\bar{m}_{ii}^{-1} \xi_i \sum_{j=1}^N a_{ij}. \quad (4.25)$$

From the definition of A , we have

$$-d\bar{m}_{ii}^{-1}\xi_i \sum_{j=1}^N a_{ij} = -d\bar{m}_{ii}^{-1}\xi_i \int_{\Gamma_h} \nabla_{\Gamma_h} \chi_i \cdot \nabla_{\Gamma_h} \sum_{j=1}^N \chi_j. \quad (4.26)$$

Since Γ_h has no boundary, $\sum_{j=1}^N \chi_j(\mathbf{x}) = 1$, $\mathbf{x} \in \Gamma_h$, and thus

$$\nabla_{\Gamma_h} \sum_{j=1}^N \chi_j(\mathbf{x}) = 0, \quad \mathbf{x} \in \Gamma_h. \quad (4.27)$$

By combining (4.23)-(4.27), we finally have

$$-(d\bar{M}^{-1}A\xi)_i \leq 0. \quad (4.28)$$

The above points 1. and 2. imply the desired result that $\dot{\xi}_i$ is negative. This completes the proof. \square

The following theorem is the fully-discrete counterpart of Theorem 11. In the specific case of the homogeneous heat equation on planar domains, the following theorem was proven in [126].

Theorem 12 (Maximum principle for (4.14)). *Under the Delaunay condition (4.15), the fully-discrete solution ξ^n with initial data ξ^0 of scheme (4.14) fulfils the following maximum principle*

$$0 \leq \xi_i^n \leq \max_{\mathbb{R}^N} \{\xi^0\}, \quad i = 1, \dots, N, \quad n \in \mathbb{N}, \quad (4.29)$$

if the timestep τ satisfies

$$\beta\tau \leq \left(\max_{\mathbf{y} \in \Gamma_h} \{U^0(\mathbf{y})\} \right)^{1-\alpha}. \quad (4.30)$$

In particular, for $\beta = 0$, (4.29) holds with no restriction on τ .

Proof. From the matrix properties (4.18) and (4.19) we have that, for every $\tau > 0$,

$$(\bar{M} + d\tau A)^{-1} \bar{M} \mathbf{1} = \mathbf{1}; \quad (4.31)$$

$$(\bar{M} + d\tau A)^{-1} \bar{M} \geq \mathbf{0}. \quad (4.32)$$

Let $n \in \mathbb{N} \cup \{0\}$. We assume by induction that $\xi^n \geq \mathbf{0}$. We have to prove that

$$\max_{\mathbb{R}^N} \xi^{n+1} \leq \max_{\mathbb{R}^N} \xi^n; \quad (4.33)$$

$$\xi^{n+1} \geq \mathbf{0}. \quad (4.34)$$

We first prove (4.33). Using (4.31) and (4.32) in the scheme (4.14), we observe that

$$\begin{aligned} \max_{\mathbb{R}^N} \xi^{n+1} &= \max_{\mathbb{R}^N} \left((\bar{M} + d\tau A)^{-1} \bar{M} (\xi^n - \tau\beta(\xi^n)^\alpha) \right) \\ &\leq (\bar{M} + d\tau A)^{-1} \bar{M} \left(\mathbf{1} \max_{\mathbb{R}^N} (\xi^n - \tau\beta(\xi^n)^\alpha) \right) = \max_{\mathbb{R}^N} (\xi^n - \tau\beta(\xi^n)^\alpha). \end{aligned} \quad (4.35)$$

Hence, (4.33) holds if

$$\max_{\mathbb{R}^N}(\boldsymbol{\xi}^n - \tau\beta(\boldsymbol{\xi}^n)^\alpha) \leq \max_{\mathbb{R}^N}(\boldsymbol{\xi}^n). \quad (4.36)$$

Since, from inductive hypothesis, $\boldsymbol{\xi}^n \geq \mathbf{0}$, then (4.36) holds. We are left to prove (4.34). Using (4.32) in the scheme (4.14), (4.34) holds if

$$\boldsymbol{\xi}^n - \tau\beta(\boldsymbol{\xi}^n)^\alpha \geq \mathbf{0}; \quad (4.37)$$

Condition (4.37) holds if

$$\tau\beta \leq \min_{\mathbb{R}^N}((\boldsymbol{\xi}^n)^{1-\alpha}) \leq \left(\max_{\mathbb{R}^N}(\boldsymbol{\xi}^n)\right)^{1-\alpha}. \quad (4.38)$$

We have proven that, for all $n \in \mathbb{N} \cup \{0\}$, (4.38) implies (4.33) and (4.34). From (4.33), the most severe of the timestep restrictions in (4.38) is

$$\tau\beta \leq \left(\max_{\mathbb{R}^N}(\boldsymbol{\xi}^0)\right)^{1-\alpha} = \left(\max_{\mathbf{y} \in \Gamma_h} \{U^0(\mathbf{y})\}\right)^{1-\alpha}, \quad (4.39)$$

which completes the proof. □

4.6 Convergence analysis

In this section we show optimal convergence results for the semi- and full-discretisations of the semilinear heat equation (4.2). These results are special cases of Theorems 18 and 19 in the forthcoming Section 5.3, devoted to general reaction-diffusion systems. Hence, we omit the proofs.

Theorem 13 (Error estimate for the semi-discrete solution (4.5)). *If the analytical solution u of (4.2) and its time derivative \dot{u} are $L^\infty([0, T]; H^2(\Gamma))$ and the approximate initial datum U_0 fulfils $\|u_0 - U_0^\ell\|_0 \leq ch^2$, then the following estimate holds*

$$\|u - U^\ell\|_0 \leq C(u, T)h^2, \quad (4.40)$$

where $C(u, T)$ is a constant depending on u and T .

Theorem 14 (Error estimate for the fully-discrete solution (4.14)). *If the analytical solution u of (4.2) and its time derivative \dot{u} are $L^\infty([0, T]; H^2(\Gamma))$, \ddot{u} is $L^\infty([0, T]; L^2(\Gamma))$ and the approximate initial datum U_0 fulfils $\|u_0 - U_0^\ell\|_0 \leq ch^2$, then the following estimate holds*

$$\|u^n - U^{\ell, n}\|_0 \leq C(u, T)(h^2 + \tau), \quad (4.41)$$

where u^n is the exact solution at time $t_n := n\tau$ and $C(u, T)$ is a constant depending on u and T .

4.7 Numerical examples

In this section we provide numerical validation of our theoretical results and show that the LSFEM combined with the IMEX Euler in time:

- fulfils the discrete maximum principle for the homogeneous heat equation as proven in Theorem 12, while the standard SFEM does not;
- exhibits the optimal convergence rate predicted in Theorem 14;

The meshes for our numerical examples have been constructed by using the MATLAB package DistMesh (see [108]). A-posteriori, we have verified that the generated meshes fulfil the Delaunay condition (4.15). The linear systems arising at each timestep have been solved with MATLAB direct solver in the “backslash” command.

Example 1: The homogeneous heat equation and the maximum principle

We solve the parabolic equation (4.2) for the homogeneous case $\beta = 0$ on the unit sphere Γ with $d = 0.1$ until the final time $T = 1$ and the nonnegative compactly supported $H^1(\Gamma)$ initial datum

$$u_0(x, y, z) = \begin{cases} \sqrt{1 - 25(x^2 + y^2)} & \text{if } 25(x^2 + y^2) \leq 1, z > 0; \\ 0 & \text{elsewhere on } \Gamma. \end{cases} \quad (4.42)$$

In this case, the invariant region is $\Sigma = [0, 1]$, then the solution must stay nonnegative at all times. Moreover, since $\beta = 0$, the IMEX Euler time discretisation reduces to Implicit Euler. In this example, as well as in the following example, the problem is solved on a sequence of eight meshes Γ_i , $i = 0, \dots, 7$ with corresponding meshsizes h_i with $h_0 = 4.013e-1$ and $h_i \approx \sqrt{2}^{-i} h_0$ for all $i = 1, \dots, 7$ and corresponding timesteps τ_i with $\tau_0 = 0.2$ and $\tau_i = 2^{-i} \tau_0$ for all $i = 1, \dots, 7$ (see parameter values in Tab. 4.2). Hence, τ_i is approximately proportional to h_i^2 in order to reveal the quadratic convergence, with respect to the mesh size, of the method. The minima of the computed numerical solution, obtained for every (h_i, τ_i) , $i = 0, \dots, 7$, are reported in Table 4.1. This example confirms our findings, as the LSFEM fulfils the discrete maximum principle, while the standard SFEM violates the maximum principle as illustrated in Table 4.1.

Example 2: The linear heat equation and convergence

In this example we solve the parabolic equation (4.2) in the linear case $\alpha = 1$ on the unit sphere $\Gamma = \{(x, y, z) \in \mathbb{R}^3 | x^2 + y^2 + z^2 = 1\}$:

$$\begin{cases} \dot{u} - d\Delta_{\Gamma}u = -\beta u; \\ u_0(x, y, z) = xyz, \quad (x, y, z) \in \Gamma, \end{cases} \quad (4.43)$$

with $d = \frac{1}{24}$ and $\beta = \frac{1}{2}$, to test the convergence rate of the LSFEM method. The exact solution of (4.43) is $u(x, y, z, t) = xyz e^{-t}$, $(x, y, z) \in \Gamma$, $t \geq 0$. We solve this problem on the same sequence of meshes Γ_i , $i = 0, \dots, 7$ and corresponding timesteps τ_i , $i = 0, \dots, 7$ considered in the previous example. For all $i = 0, \dots, 7$, τ_i fulfils the stability condition given in Theorem

i	N	h	$\min_{\Gamma_h \times [\tau, 1]} U$ SFEM	$\min_{\Gamma_h \times [\tau, 1]} U$ LSFEM
0	126	4.013e-01	-3.454e-04	7.016e-09
1	258	2.863e-01	-4.695e-06	4.812e-12
2	516	2.026e-01	-1.299e-03	1.213e-16
3	1062	1.414e-01	-2.123e-07	2.746e-23
4	2094	1.007e-01	-7.546e-04	3.142e-32
5	4242	7.082e-02	-1.037e-05	1.816e-45
6	8370	5.041e-02	-4.163e-04	5.324e-64
7	16962	3.542e-02	-1.254e-04	3.126e-90

Table 4.1: *Example 1*: homogeneous heat equation (4.2) on the unit sphere with $\beta = 0$, initial datum (4.42) and final time $T = 1$. Discrete maximum principle analysis on a sequence of eight Delaunay meshes Γ_i , $i = 0, \dots, 7$, and corresponding timesteps τ_i , $i = 0, \dots, 7$ as described in the text. The SFEM violates the discrete maximum principle for all $i = 0, \dots, 7$, while the LSFEM fulfils the discrete maximum principle for all $i = 0, \dots, 7$.

12. For every $i = 0, \dots, 7$ the $L^\infty([0, T], L^2(\Gamma_h))$ error between the numerical solution U and the interpolant $I_h(u)$ of the exact solution is reported in Table 4.2. The lumped solution at the final time $T = 1$ obtained on the finest mesh is shown in Figure 4.2 (left), as well as its planar projection through spherical coordinates

$$x = \cos \phi \cos \psi, \quad y = \cos \phi \sin \psi, \quad z = \sin \psi, \quad (\phi, \psi) \in [-\pi, \pi] \times \left[-\frac{\pi}{2}, \frac{\pi}{2}\right].$$

In this example the predicted second order convergence in space is attained. Furthermore, we observe that, for this specific example, the lumped SFEM exhibits a better accuracy than the standard SFEM. We believe that this phenomenon, which does not occur in general, is due to the particular symmetry of the considered problem.

4.8 Conclusions

We have introduced a surface finite element method with mass lumping (LSFEM) for the spatial discretisation of the semilinear heat equation (2.10) and we have carried out a fully discrete scheme by applying the IMEX Euler method to the semi-discrete formulation. Our spatial and full discretisations fulfil discrete maximum principles with no restriction on the mesh size. Only a timestep restriction is required for the fully discrete maximum principle. In the next chapter we extend the LSFEM space discretisation and the LSFEM-IMEX Euler full discretisation to general RDSs of arbitrarily many equations. The key feature of the proposed methods will be the *preservation of invariant rectangles* for such systems. For the special case of the semilinear heat equation (2.10), the preservation of invariant rectangles will imply the discrete maximum principles. Hence, the theory presented in the next chapter constitutes a generalisation of the present chapter.

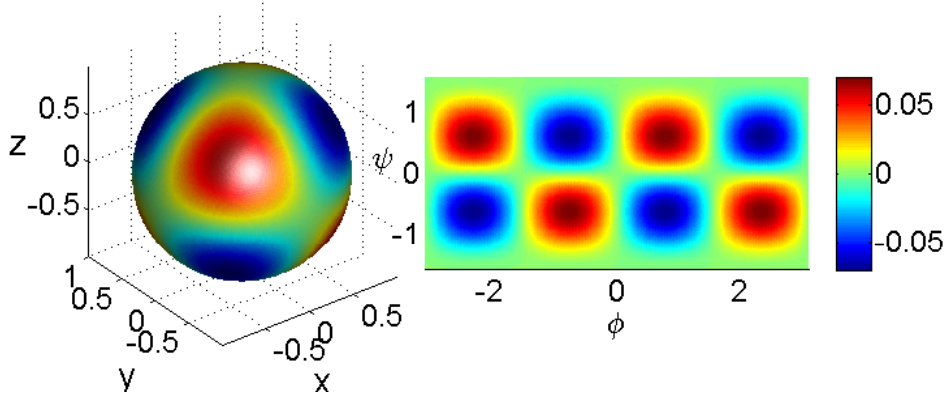


Figure 4.2: *Example 2*: Linear heat equation (4.43) on the unit sphere with $d = \frac{1}{24}$, $\beta = \frac{1}{2}$ and final time $T = 1$. LSFEM solution obtained on the Delaunay mesh Γ_7 with $N = 16962$ nodes, meshsize $h_7 = 3.542e-2$ and timestep $\tau_7 = 1.6e-3$ at $T = 1$ (left) and its planar projection through spherical coordinates (right).

i	N	h	SFEM		LSFEM	
			$L^\infty(L^2)$ error	rate	$L^\infty(L^2)$ error	rate
0	126	4.013e-01	6.100e-03	-	3.061e-03	-
1	258	2.863e-01	3.129e-03	1.977	1.846e-03	1.498
2	516	2.026e-01	1.594e-03	1.951	1.095e-03	1.510
3	1062	1.414e-01	7.899e-04	1.953	5.444e-04	1.945
4	2094	1.007e-01	3.966e-04	2.030	3.025e-04	1.731
5	4242	7.082e-02	2.013e-04	1.925	1.401e-04	2.184
6	8370	5.041e-02	1.003e-04	2.049	7.671e-05	1.773
7	16962	3.542e-02	5.063e-05	1.938	3.529e-05	2.200

Table 4.2: *Example 2*: Linear heat equation (4.43) on the unit sphere with $d = \frac{1}{24}$, $\beta = \frac{1}{2}$ and final time $T = 1$. Comparisons of the convergence analysis in $L^\infty([0, T], L^2(\Gamma_h))$ norm between the SFEM and the LSFEM.

Chapter 5

Reaction-cross-diffusion systems on stationary surfaces

In recent years, there has been a remarkable increase in the theoretical analysis of mathematical models of reaction-diffusion type with or without *cross-diffusion*, on planar domains or surfaces. Diffusion is a process in which the gradient in the concentration of one chemical or biological species induces a flux, either linearly or nonlinearly, of the species itself. Cross-diffusion, instead, is the process for which the gradient in the concentration of one species induces a flux of *another* species.

Reaction-diffusion systems (RDSs) have been extensively employed to model many different processes in a wide range of fields. On planar domains, we mention applications to biology ([51, 100, 102]), chemistry ([131]), electrochemistry ([13, 81]) and finance (e.g. [7]). On surfaces, RDSs have been applied to the study of biological patterning ([6]), tumour growth ([19]), metal dealloying ([43]), biomembrane modeling ([45]), electrochemistry ([79]) cell motility ([46]), just to mention a few examples.

We also mention some processes that have been modelled through reaction-cross-diffusion systems (RCDSs). For instance, in molecular biology, cross-diffusion processes appear in multicomponent systems containing at least two solute components [96, 135]. Multicomponent systems containing nanoparticles, surfactants, polymers and other macromolecules in solution play an important role in industrial applications and biological functions [96]. In developmental biology, recent experimental findings demonstrate that cross-diffusion can be quite significant in generating spatial structure [132]. The effects of cross-diffusion on models for pattern formation have been studied in many theoretical papers, such as [94]. Apart from pattern formation in developmental biology, other applications of reaction-cross-diffusion systems include cancer motility [61], finance [7] and biofilms [113]. The introduction of cross-diffusion in standard reaction-diffusion models has been shown to prevent blow-up phenomena that are associated with reaction-diffusion systems in the absence of cross-diffusion [71]. It must be noted that the concept of cross-diffusion includes well-known processes such as chemo- and haptotaxis [61].

In this chapter we consider reaction-cross-diffusion systems (RCDSs) of arbitrarily many equa-

tions on a compact surface of the form

$$\begin{cases} \frac{\partial u_i}{\partial t} - \sum_{j=1}^r d_{ij} \Delta_{\Gamma} u_j = f_i(u_1, \dots, u_r), & \text{in } \Gamma \times (0, T], \\ u_i(\mathbf{x}, 0) = u_{0,i}(\mathbf{x}), & \mathbf{x} \in \Gamma, \quad i = 1, \dots, r, \end{cases} \quad (5.1)$$

where Γ is a \mathcal{C}^2 surface in \mathbb{R}^3 without boundary, d_{ij} are any real diffusion and cross-diffusion coefficients such that the diffusion matrix $\mathbf{D} = (d_{ij})$ is positive definite, f_1, \dots, f_r are $\mathcal{C}^2(I; \mathbb{R})$ reaction kinetics defined on an open set $I \subset \mathbb{R}^r$ and an initial condition $(u_{0,1}, \dots, u_{0,r}) \in \mathcal{C}^2(\Gamma)$ is given.

For many RCDSs, an important property is the existence of *invariant regions*. From a modelling point of view, it is useful to know that a given model possesses an invariant region. For real applications, solutions for RCDSs are usually meaningful as long as they range within a limited set of values and an invariant region could provide an a-priori bound on the analytical solution which can be helpful, for instance, when studying the convergence of numerical methods. Sufficient conditions for a region to be invariant for a given RDS or RCDS were given (i) in [25, 123] for RCDSs on planar domains and (ii) in [125, p. 335-353] for the case of stationary surfaces. In the literature, preservation of invariant regions *under discretisation* has been addressed in the following special cases. In the scalar case, the existence of invariant regions corresponds to the maximum principle. On planar domains, works in this direction cover the homogeneous heat equation [20], RD scalar equations [47, 49, 101], anisotropic RD [87] and reaction-convection-diffusion scalar equations [88]. For RCDSs of many equations on planar domains, the problem is addressed in [73]. The aforementioned papers consider different spatial approximation approaches. Most of them require the discretisation to be sufficiently refined, in order to preserve invariant rectangles and maximum principles. A notable exception is the lumped finite element method (LFEM) [20, 47, 87, 88, 101].

In this chapter we present the results given in the recent works [55, 56] on RDSs and RCDSs, respectively. These results are organised as follows. In Section 5.1 we recall the weak formulation of the RCDS (5.1), we present its LSFEM space discretisation and its LSFEM-IMEX Euler time discretisation. In Section 5.2 we prove sufficient conditions for the existence of invariant regions of polytopal shape at the semi- and fully-discrete levels for semilinear RCDSs of the form (5.1). In Section 5.3 we prove (i) stability estimates at the continuous, spatially discrete and fully discrete levels and (ii) optimal asymptotic convergence rates for the spatially discrete and the fully discrete methods. In Section 5.4 we present four numerical examples to show:

- in the first two examples, the preservation of an invariant region for a RCDS with Rosenzweig-MacArthur kinetics on a sphere, without and with cross-diffusion respectively;
- in the third example, the convergence of the LSFEM-IMEX Euler full discretisation of a RDS with Schnakenberg kinetics on a sphere;
- in the fourth example, the comparison with an existing method for RCDSs on surfaces in terms of Turing pattern formation for the Schnakenberg model on a sphere.

5.1 Reaction-cross-diffusion systems on surfaces

Let Γ be a \mathcal{C}^2 surface in \mathbb{R}^3 without boundary (see Remarks 6 and 7 in the previous chapter). As shown in Section 2.6.1, the weak formulation of (5.1) is given by: find $u_1, \dots, u_r \in L^2([0, T]; H^1(\Gamma))$ with $\dot{u}_1, \dots, \dot{u}_r \in L^2([0, T]; H^{-1}(\Gamma))$ such that

$$\int_{\Gamma} \dot{u}_m \varphi_m + \sum_{k=1}^r d_{mk} \int_{\Gamma} \nabla_{\Gamma} u_k \cdot \nabla_{\Gamma} \varphi_m = \int_{\Gamma} f_m(\mathbf{u}) \varphi_m, \quad (5.2)$$

for all $\varphi_m \in L^2([0, T]; H^1(\Gamma))$ and $m = 1, \dots, r$.

5.1.1 Space discretisation

Let Γ_h be a triangulation of Γ as defined in Section 2.5.1 and let \mathbb{V}_h be the finite element space defined in (2.18). We define the following LSFEM space discretisation for the weak RCDS (5.2): find $U_1, \dots, U_r \in L^2([0, T]; \mathbb{V}_h)$ with $\dot{U}_1, \dots, \dot{U}_r \in L^2([0, T]; \mathbb{V}_h)$ such that

$$\int_{\Gamma_h} I_h(\dot{U}_m \varphi_m) + \sum_{k=1}^r d_{mk} \int_{\Gamma_h} \nabla_{\Gamma_h} U_k \cdot \nabla_{\Gamma_h} \varphi_m = \int_{\Gamma_h} I_h(f_m(\mathbf{U}) \varphi_m), \quad (5.3)$$

for all $\varphi_m \in L^2([0, T], \mathbb{V}_h)$ and $m = 1, \dots, r$, where the initial condition $(U_{0,1}, \dots, U_{0,r}) \in \mathbb{V}_h^r$ is the Lagrange interpolant of the initial condition $(u_{0,1}, \dots, u_{0,r})$ of the weak continuous system (5.2). Notice that (5.2) is analogous to the SFEM spatial discretisation (2.44), but differs for the presence of the interpolant operator I_h (mass lumping). By expressing each component U_k as

$$U_k(\mathbf{x}, t) = \sum_{i=1}^N \xi_{k,i}(t) \chi_i(\mathbf{x}), \quad \mathbf{x} \in \Gamma_h, t \in [0, T], \quad (5.4)$$

and choosing the test functions in (5.3) to be the nodal basis functions, we rewrite (5.3) as follows

$$\int_{\Gamma_h} I_h(\dot{U}_m \chi_j) + \sum_{k=1}^r d_{mk} \sum_{i=1}^N \xi_{k,i} \int_{\Gamma_h} \nabla_{\Gamma_h} \chi_i \cdot \nabla_{\Gamma_h} \chi_j = \int_{\Gamma_h} I_h(f_m(\mathbf{U}) \chi_j), \quad (5.5)$$

for all $m = 1, \dots, r$ and $j = 1, \dots, N$. If A and \bar{M} are the stiffness- and the lumped mass-matrices defined in (2.34) and (4.11), respectively, the matrix form of the LSFEM (5.5) is given by

$$\bar{M} \dot{\boldsymbol{\xi}}_m + \sum_{k=1}^r d_{mk} \mathbf{A} \boldsymbol{\xi}_k = \bar{M} f_m(\boldsymbol{\xi}_1, \dots, \boldsymbol{\xi}_r), \quad m = 1, \dots, r, \quad (5.6)$$

where, for all $k = 1, \dots, r$, $\boldsymbol{\xi}_k(t) := (\xi_{k,1}(t), \dots, \xi_{k,N}(t))^{tr}$ are the time-dependent coefficients of the nodal expansion (5.4) of U_k in the Lagrange basis $\{\chi_i | i = 1, \dots, N\}$. The system of ordinary differential equations (ODEs) (5.6) can also be rewritten as

$$\mathbf{I}_r \otimes \bar{M} \begin{pmatrix} \dot{\boldsymbol{\xi}}_1 \\ \vdots \\ \dot{\boldsymbol{\xi}}_r \end{pmatrix} + \mathbf{D} \otimes \mathbf{A} \begin{pmatrix} \boldsymbol{\xi}_1 \\ \vdots \\ \boldsymbol{\xi}_r \end{pmatrix} = \mathbf{I}_r \otimes \bar{M} \begin{pmatrix} f_1(\boldsymbol{\xi}_1, \dots, \boldsymbol{\xi}_r) \\ \vdots \\ f_r(\boldsymbol{\xi}_1, \dots, \boldsymbol{\xi}_r) \end{pmatrix}, \quad (5.7)$$

where $\mathbf{I}_r \in \mathbb{R}^{N,N}$ is the identity matrix and \otimes denotes the Kronecker product, see [83]. Since, from the properties of the Kronecker product [83], $(\mathbf{I}_r \otimes \bar{\mathbf{M}})^{-1}(\mathbf{D} \otimes \mathbf{A}) = (\mathbf{I}_r \otimes \bar{\mathbf{M}}^{-1})(\mathbf{D} \otimes \mathbf{A}) = (\mathbf{I}_r \mathbf{D}) \otimes (\bar{\mathbf{M}}^{-1} \mathbf{A}) = \mathbf{D} \otimes (\bar{\mathbf{M}}^{-1} \mathbf{A})$, we end up with the following ODE system of dimension rN :

$$\begin{pmatrix} \dot{\boldsymbol{\xi}}_1 \\ \vdots \\ \dot{\boldsymbol{\xi}}_r \end{pmatrix} = -\mathbf{D} \otimes (\bar{\mathbf{M}}^{-1} \mathbf{A}) \begin{pmatrix} \boldsymbol{\xi}_1 \\ \vdots \\ \boldsymbol{\xi}_r \end{pmatrix} + \begin{pmatrix} f_1(\boldsymbol{\xi}_1, \dots, \boldsymbol{\xi}_r) \\ \vdots \\ f_r(\boldsymbol{\xi}_1, \dots, \boldsymbol{\xi}_r) \end{pmatrix}, \quad (5.8)$$

with $\boldsymbol{\xi}_{k,i}(0) = U_{0,k}(\mathbf{x}_i)$ for $k = 1, \dots, r$ and $i = 1, \dots, N$. In the remainder of this chapter we assume that the mesh Γ_h meets the Delaunay property (4.15). We will show that the characterisation, given in Lemma 7, of the Delaunay property plays a crucial role in the existence of invariant regions of RCDSs at the discrete levels.

5.1.2 Time discretisation

As we did for the semilinear heat equation considered in the previous Chapter 4, we carry out a fully discrete scheme by applying the IMEX Euler timestepping to the semi-discrete scheme (5.3). If $\tau > 0$ is the timestep (hence, the total number of timesteps is given by $N_T := \lfloor \frac{T}{\tau} \rfloor$) the LSFEM-IMEX Euler fully-discrete method for (5.2) is: for all $n = 0, \dots, N_T$, for all $\varphi_1, \dots, \varphi_r \in \mathbb{V}_h$

$$\begin{cases} \int_{\Gamma} I_h \left(\frac{U_1^{n+1} - U_1^n}{\tau} \varphi_1 \right) + \sum_{k=1}^r d_{1k} \int_{\Gamma} \nabla_{\Gamma} U_k^{n+1} \cdot \nabla_{\Gamma} \varphi_1 = \int_{\Gamma} I_h(f_1(\mathbf{U}^n) \varphi_1); \\ \vdots \\ \int_{\Gamma} I_h \left(\frac{U_r^{n+1} - U_r^n}{\tau} \varphi_r \right) + \sum_{k=1}^r d_{rk} \int_{\Gamma} \nabla_{\Gamma} U_k^{n+1} \cdot \nabla_{\Gamma} \varphi_r = \int_{\Gamma} I_h(f_r(\mathbf{U}^n) \varphi_r), \end{cases} \quad (5.9)$$

where the initial condition (U_1^0, \dots, U_r^0) coincides with that of the semi-discrete method $(U_{0,1}, \dots, U_{0,r})$. We will utilise formulation (5.9) for stability and convergence analysis. In particular, the stability estimates for (5.9) will rely on an energy argument. For the implementation, we write system (5.9) as a system of rN algebraic linear equations, using the lumped mass- and stiffness-matrices $\bar{\mathbf{M}}$ and \mathbf{A} :

$$\begin{pmatrix} \boldsymbol{\xi}_1^{n+1} \\ \vdots \\ \boldsymbol{\xi}_r^{n+1} \end{pmatrix} = (\mathbf{I}_{Nr} + \tau \mathbf{D} \otimes (\bar{\mathbf{M}}^{-1} \mathbf{A}))^{-1} \begin{pmatrix} \boldsymbol{\xi}_1^n + \tau f_1(\boldsymbol{\xi}_1^n, \dots, \boldsymbol{\xi}_r^n) \\ \vdots \\ \boldsymbol{\xi}_r^n + \tau f_r(\boldsymbol{\xi}_1^n, \dots, \boldsymbol{\xi}_r^n) \end{pmatrix}, \quad (5.10)$$

to be solved at each timestep $t_n := n\tau$ for $n = 0, \dots, N_T$. Note that scheme (5.10) can be obtained equivalently by applying the IMEX Euler timestepping to the semi-discrete scheme (5.8). If the solutions of (5.8) and (5.10) are a-priori confined within any (possibly unbounded) set Σ contained in the domain of definition I of the kinetics and the kinetics are Lipschitz on Σ , then these solutions are well-defined at all positive times. This further motivates the study of invariant regions, addressed in the following section.

5.2 Invariant convex polytopes for the semi- and fully-discrete schemes

This section focuses on investigating an interesting property of the LSFEM discretisation of RCDSs which does not hold in the absence of lumping, that is the existence of invariant convex polytopes. For our purposes, we recall the following definition given in [123, 125].

Definition 11. *For the system (5.1), a region Σ in the phase-space \mathbb{R}^r is said to be positively invariant if, whenever the initial condition \mathbf{u}_0 is in Σ , \mathbf{u} stays in Σ as long as it exists and is unique.*

Let us now consider polytopal invariant regions. Let $s \in \mathbb{N}$, let $\mathbf{n}^l \in \mathbb{R}^r$, $l = 1, \dots, s$ be unit vectors and let $c^l \in \mathbb{R}$, $l = 1, \dots, s$ be real constants. Let Σ be the convex polytope in the phase-space defined as the intersection of s half-hyperspaces:

$$\Sigma = \{\mathbf{y} \in \mathbb{R}^r \mid \mathbf{n}^l \cdot \mathbf{y} \leq c^l, \quad l = 1, \dots, s\}, \quad (5.11)$$

and consider its hyperfaces $\Sigma^l := \{\mathbf{y} \in \Sigma \mid \mathbf{n}^l \cdot \mathbf{y} = c^l\}$, $l = 1, \dots, s$. Consider the following inward flux condition for the kinetics:

$$\mathbf{f}(\mathbf{y}) \cdot \mathbf{n}^l(\mathbf{y}) < 0, \quad \mathbf{y} \in \Sigma^l, \quad l = 1, \dots, s, \quad (5.12)$$

and the following compatibility condition between Σ and \mathbf{D}

$$\mathbf{n}^l \text{ is a left eigenvector of } \mathbf{D} \quad l = 1, \dots, s. \quad (5.13)$$

In order for the region Σ to be invariant, (i) condition (5.12) is sufficient in the absence of cross-diffusion when Γ is a Riemannian manifold without boundary [125], while (ii) the simultaneous conditions (5.12) and (5.13) are sufficient when Γ is a k -dimensional domain in \mathbb{R}^k , $k \in \mathbb{N}$ [123].

We remark that, on stationary domains, some systems are known to possess an invariant region which do not meet the strict inequalities (6.21)-(6.22). For instance, for many mass-action laws, the positive orthant is invariant [21, 56] even though the flux of \mathbf{f} is tangent to this region, instead of strictly inward.

Remark 11 (Invariant regions in the absence of cross-diffusion). *In the absence of cross-diffusion, i.e. when D is diagonal, the left eigenvectors of D are the standard basis vectors of \mathbb{R}^r . Consequently, the regions fulfilling the compatibility condition (5.13) are the hyper-rectangles of the form*

$$\Sigma = \prod_{k=1}^r [\underline{\sigma}_k, \bar{\sigma}_k], \quad (5.14)$$

where, for all $k = 1, \dots, r$, $\underline{\sigma}_k \in \mathbb{R} \cup \{-\infty\}$ and $\bar{\sigma}_k \in \mathbb{R} \cup \{+\infty\}$. We remark that hyper-rectangles of the form (5.14) can be bounded or unbounded. Some examples of unbounded hyper-rectangles are half-spaces, stripes and orthants.

Remark 12 (Maximum and minimum-maximum principles in terms of invariant regions). *In the case $r = 1$ of scalar equations, the maximum principle (4.3) considered in the previous chapter is equivalent to the invariance of the following family of regions:*

$$[0, M], \quad M > 0, \quad (5.15)$$

while the minimum-maximum principle (4.4) is equivalent to the invariance of the following family of regions:

$$[-M_1, M_2], \quad M_1, M_2 > 0. \quad (5.16)$$

In the following theorems we prove that, in the presence of cross-diffusion on a compact surface, under assumption (5.12), Σ is an invariant region for the semi- (5.8) and fully-discrete (5.10) systems conditionally on τ , as well.

Theorem 15 (Invariant convex polytopes for the semi-discrete system (5.8)). *Let the kinetics \mathbf{f} be Lipschitz on the polytope Σ in (5.11) and assume that (5.12)-(5.13) hold. Then Σ is an invariant region for the semi-discrete problem (5.8).*

Proof. It suffices to prove that the rN -dimensional polytope $\bar{\Sigma} = \Sigma^N$ is an invariant region for the ODE system (5.8), i.e. we have to prove that the vector field on the right-hand-side of (5.8), computed on the boundary of $\bar{\Sigma}$, points toward the interior of $\bar{\Sigma}$. To this end, let $(\xi_1, \dots, \xi_r)^{tr}$ be a point on $\partial\bar{\Sigma}$. This means that there exist $i = 1, \dots, N$ and $l = 1, \dots, s$ such that $\mathbf{n}^l \cdot \xi_{:,i} = c^l$. Then, $\mathbf{n}^l \cdot \xi_{:,j} \leq c^l$ for $j \neq i$, that implies

$$\xi_{:,j} \cdot \mathbf{n}^l \leq \xi_{:,i} \cdot \mathbf{n}^l, \quad j \neq i, \quad (5.17)$$

All we have to prove is that $\dot{\xi}_{:,i} \cdot \mathbf{n}^l$ is nonpositive. But since, from (5.12), $\mathbf{f}(\xi_{1,i}, \dots, \xi_{r,i}) \cdot \mathbf{n}^l < 0$, it remains to prove that

$$- \left(\mathbf{D} \otimes (\bar{\mathbf{M}}^{-1} \mathbf{A}) \begin{pmatrix} \xi_1 \\ \vdots \\ \xi_r \end{pmatrix} \right)_{:,i} \cdot \mathbf{n}^l \leq 0. \quad (5.18)$$

Since \mathbf{n}^l is a left eigenvector of \mathbf{D} (with eigenvalue $\lambda^l > 0$), the left-hand side of (5.18) is equal to

$$\begin{aligned} & -\lambda^l \left(\mathbf{I}_r \otimes (\bar{\mathbf{M}}^{-1} \mathbf{A}) \begin{pmatrix} \xi_1 \\ \vdots \\ \xi_r \end{pmatrix} \right)_{:,i} \cdot \mathbf{n}^l \\ &= -\lambda^l \sum_{k=1}^r n_k^l (\bar{\mathbf{M}}^{-1} \mathbf{A} \xi_k)_i = -\lambda^l \sum_{k=1}^r n_k^l \bar{m}_{ii}^{-1} \sum_{j=1}^N a_{ij} \xi_{k,j} \\ &= -\lambda^l \bar{m}_{ii}^{-1} \sum_{j=1}^N a_{ij} \sum_{k=1}^r n_k^l \xi_{k,j} = -\lambda^l \bar{m}_{ii}^{-1} \sum_{j=1}^N a_{ij} (\xi_{:,j} \cdot \mathbf{n}^l) \\ &= -\lambda^l \bar{m}_{ii}^{-1} \left(a_{ii} (\xi_{:,i} \cdot \mathbf{n}^l) + \sum_{j \in \{1, \dots, N\} \setminus \{i\}} a_{ij} (\xi_{:,j} \cdot \mathbf{n}^l) \right). \end{aligned} \quad (5.19)$$

From $a_{ij} \leq 0$, $i \neq j$ (Lemma 7) and (5.17), the right-hand side of (5.19) is less than or equal to

$$\lambda^l \bar{m}_{ii}^{-1} (\xi_{:,i} \cdot \mathbf{n}^l) \left(-a_{ii} + \sum_{j \in \{1, \dots, N\} \setminus \{i\}} (-a_{ij}) \right) = -\lambda^l \bar{m}_{ii}^{-1} (\xi_{:,i} \cdot \mathbf{n}^l) \sum_{j=1}^N a_{ij}. \quad (5.20)$$

From the definition of \mathbf{A} we have

$$\sum_{j=1}^N a_{ij} = \int_{\Gamma_h} \nabla_{\Gamma_h} \chi_i \cdot \nabla_{\Gamma_h} \sum_{j=1}^N \chi_j. \quad (5.21)$$

Since Γ_h has no boundary, $\sum_{j=1}^N \chi_j(\mathbf{x}) = 1$, $\mathbf{x} \in \Gamma_h$ and thus

$$\nabla_{\Gamma_h} \sum_{j=1}^N \chi_j(\mathbf{x}) = 0, \quad \mathbf{x} \in \Gamma_h. \quad (5.22)$$

By combining (5.19)-(5.22), we have proven (5.18), which completes the proof. \square

In order to prove the fully-discrete counterpart of Theorem 15, we need the two following original lemmas. In particular, Lemma 8 extends Lemma 15.5 in [126].

Lemma 8 (Preservation of linear constraints). *Given $r, N \in \mathbb{N}$, let $\mathbf{B} \in \mathbb{R}^{N,N}$ be a matrix with real nonnegative eigenvalues such that $b_{ij} \leq 0$ for $i \neq j$, let $\mathbf{H} \in \mathbb{R}^{r,r}$ be a (possibly non-symmetric) positive definite matrix, let \mathbf{n} be a left eigenvector of \mathbf{H} with real eigenvalue λ , let $\zeta_1, \dots, \zeta_r \in \mathbb{R}^N$ and let $\zeta = (\zeta_1, \dots, \zeta_r)^{tr} \in \mathbb{R}^{rN}$. If $(\mathbf{n}^{tr} \otimes \mathbf{I}_N)\zeta \geq \mathbf{0}$, then it holds that $(\mathbf{n}^{tr} \otimes \mathbf{I}_N)(\mathbf{I}_{rN} + \mathbf{H} \otimes \mathbf{B})^{-1}\zeta \geq \mathbf{0}$.*

Proof. For $\mu > 0$, we consider the matrix $K := \mu \mathbf{I}_{rN} - (\mathbf{I}_{rN} + \mathbf{H} \otimes \mathbf{B}) = (\mu - 1)\mathbf{I}_{rN} - \mathbf{H} \otimes \mathbf{B}$. Now, $\bar{\lambda}$ is an eigenvalue of $\mathbf{H} \otimes \mathbf{B}$ if and only if $\bar{\lambda} := \mu - 1 - \bar{\lambda}$ is an eigenvalue of K , in fact $\det(\bar{\lambda}\mathbf{I}_{rN} - \mathbf{H} \otimes \mathbf{B}) = \det((\mu - 1 - \bar{\lambda})\mathbf{I}_{rN} - \mathbf{H} \otimes \mathbf{B}) = \mathbf{0}$. Notice that

$$\operatorname{Re}(\bar{\lambda}) = \mu - 1 - \operatorname{Re}(\bar{\lambda}), \quad \operatorname{Im}(\bar{\lambda}) = -\operatorname{Im}(\bar{\lambda}). \quad (5.23)$$

Since, from the positive definiteness, the eigenvalues of \mathbf{H} have positive real part and, by assumption, \mathbf{B} has real nonnegative eigenvalues, then the eigenvalues of $\mathbf{H} \otimes \mathbf{B}$ have non-negative real part, namely $\operatorname{Re}(\bar{\lambda}) \geq 0$. Consequently, (5.23) implies $|\operatorname{Re}(\bar{\lambda})| \leq \mu - 1$, which, in combination with (5.23), yields $|\bar{\lambda}|^2 \leq (\mu - 1)^2 + (\operatorname{Im}(\bar{\lambda}))^2$. It follows that, by choosing $\mu > \max_{\bar{\lambda} \in \operatorname{eig}(\mathbf{H} \otimes \mathbf{B})} \frac{(\operatorname{Im}(\bar{\lambda}))^2 + 1}{2}$, the spectral radius of K is less than μ , then the spectral radius of $\mu^{-1}K$ is less than 1, and thus $\mu^{-1}K$ may be expressed as the sum of a geometric series. Assume now $(\mathbf{n}^{tr} \otimes \mathbf{I}_N)\zeta \geq \mathbf{0}$. Then

$$\begin{aligned} & (\mathbf{n}^{tr} \otimes \mathbf{I}_N)(\mathbf{I}_{rN} + \mathbf{H} \otimes \mathbf{B})^{-1}\zeta \\ &= (\mathbf{n}^{tr} \otimes \mathbf{I}_N)(\mu \mathbf{I}_{rN} - K)^{-1}\zeta = (\mathbf{n}^{tr} \otimes \mathbf{I}_N)\mu^{-1}(\mathbf{I}_{rN} - \mu^{-1}K)^{-1}\zeta \\ &= (\mathbf{n}^{tr} \otimes \mathbf{I}_N)\mu^{-1} \sum_{j=0}^{+\infty} \mu^{-j} K^j \zeta = \sum_{j=0}^{+\infty} \mu^{-1-j} (\mathbf{n}^{tr} \otimes \mathbf{I}_N)((\mu - 1)\mathbf{I}_{rN} - \mathbf{H} \otimes \mathbf{B})^j \zeta. \end{aligned}$$

We need to prove that, for all $j \in \mathbb{N}$, $(\mathbf{n}^{tr} \otimes \mathbf{I}_N)((\mu - 1)\mathbf{I}_{rN} - \mathbf{H} \otimes \mathbf{B})^j \zeta \geq \mathbf{0}$. However, by induction, it suffices to prove that

$$(\mathbf{n}^{tr} \otimes \mathbf{I}_N)((\mu - 1)\mathbf{I}_{rN} - \mathbf{H} \otimes \mathbf{B})\zeta \geq \mathbf{0}. \quad (5.24)$$

From the properties of the Kronecker product, the left-hand side in (5.24) can be rearranged as

$$[(\mu - 1)\mathbf{n}^{tr} \otimes \mathbf{I}_N - (\mathbf{n}^{tr} \mathbf{H}) \otimes (\mathbf{I}_N \mathbf{B})]\boldsymbol{\zeta} = [(\mu - 1)\mathbf{n}^{tr} \otimes \mathbf{I}_N - \lambda \mathbf{n}^{tr} \otimes \mathbf{B}]\boldsymbol{\zeta}. \quad (5.25)$$

Claim (5.24) can now be written componentwise as

$$(\mu - 1)((\mathbf{n}^{tr} \otimes \mathbf{I}_N)\boldsymbol{\zeta})_i \geq \lambda((\mathbf{n}^{tr} \otimes \mathbf{B})\boldsymbol{\zeta})_i, \quad i = 1, \dots, N. \quad (5.26)$$

We recast the left-hand side of (5.26) as

$$(\mu - 1) \sum_{k=1}^r n_k \zeta_{k,i}, \quad (5.27)$$

and the right-hand side of (5.26) as

$$\lambda \sum_{k=1}^r n_k (\mathbf{B}\boldsymbol{\zeta}_k)_i = \lambda \sum_{k=1}^r n_k \sum_{j=1}^N b_{ij} \zeta_{k,j} = \lambda \sum_{j=1}^N b_{ij} \sum_{k=1}^r n_k \zeta_{k,j} \leq \lambda b_{ii} \sum_{k=1}^r n_k \zeta_{k,i}, \quad (5.28)$$

where, in the inequality, we have exploited the the assumption that $b_{ij} \leq 0$ for $i \neq j$ and $(\mathbf{n}^{tr} \otimes \mathbf{I}_N)\boldsymbol{\zeta} \geq \mathbf{0}$. Now it suffices to prove that the right-hand side of (5.28) is less than or equal to (5.27) for all $i = 1, \dots, N$, which is true by enforcing $\mu \geq \lambda \max_{i=1, \dots, N} (b_{ii}) + 1$. \square

Lemma 9 (Zero discrete diffusion of spatially uniform states). *Let $\bar{\mathbf{M}}, \mathbf{A}, \mathbf{D}$ be the lumped mass matrix, the stiffness matrix and the diffusivity matrix introduced above, let $\tau > 0$ and let $\mathbf{v} \in \mathbb{R}^r$ be a column vector. Then $(\mathbf{I}_{rN} + \tau \mathbf{D} \otimes (\bar{\mathbf{M}}^{-1} \mathbf{A}))^{-1}(\mathbf{v} \otimes \mathbf{1}_N) = \mathbf{v} \otimes \mathbf{1}_N$.*

Proof. The claim follows from $\mathbf{A}\mathbf{1} = \mathbf{0}$. \square

Theorem 16 (Invariant convex polytopes for the fully-discrete scheme (5.10)). *Let the kinetics \mathbf{f} be Lipschitz on the polytope Σ in (5.11) and assume that (5.12)-(5.13) hold. Then Σ is an invariant region for the fully-discrete problem (5.10) if the timestep τ fulfils*

$$\tau \leq \bar{\tau} := \frac{1}{\max_{l=1, \dots, s} \sqrt{\sum_{k=1}^r (n_k^l L_k)^2}}, \quad (5.29)$$

where L_1, \dots, L_r are the Lipschitz constant of the kinetics f_1, \dots, f_r , respectively.

Proof. Given $n = 0, \dots, N_T$ and $\mathbf{U}^n \in \Sigma$, we must ensure that $\mathbf{U}^{n+1} \in \Sigma$, i.e., that it satisfies $\mathbf{n}^l \cdot \mathbf{U}^{n+1} \leq c^l$, $l = 1, \dots, s$. Since \mathbf{U}^{n+1} is an S_h function, it suffices to verify that \mathbf{U}^{n+1} satisfies the inequality at the gridpoints. Using the definition of the fully-discrete scheme (5.10) we wish to show that

$$\mathbf{n}^l \cdot \mathbf{U}^{n+1} = (\mathbf{n}^{l,T} \otimes \mathbf{I}_N) \mathcal{M}(\boldsymbol{\xi}^n + \tau \mathbf{f}^n) \leq c^l \mathbf{1}_N, \quad l = 1, \dots, s, \quad (5.30)$$

where $\mathcal{M} := (\mathbf{I}_{rN} + \tau \mathbf{D} \otimes \bar{\mathbf{M}}^{-1} \mathbf{A})^{-1}$ and $\mathbf{f}^n := \mathbf{f}(\boldsymbol{\xi}_1^n, \dots, \boldsymbol{\xi}_r^n)$. If $\mathbf{v} \in \mathbb{R}^r$ is such that $\mathbf{n}^l \cdot \mathbf{v} = c^l$, (5.30) becomes

$$(\mathbf{n}^{l,T} \otimes \mathbf{I}_N) \mathcal{M}(\boldsymbol{\xi}^n + \tau \mathbf{f}^n) \leq (\mathbf{n}^{l,T} \otimes \mathbf{I}_N)(\mathbf{v} \otimes \mathbf{I}_N), \quad l = 1, \dots, s, \quad (5.31)$$

By applying Lemma 9 in the Appendix to the right-hand side of (5.31), we end up with

$$(\mathbf{n}^{l,T} \otimes \mathbf{I}_N) \mathcal{M}(\boldsymbol{\xi}^n + \tau \mathbf{f}^n - \mathbf{v} \otimes \mathbf{1}_N) \leq \mathbf{0}, \quad l = 1, \dots, s. \quad (5.32)$$

From Lemma 8 in the Appendix, it suffices to prove that

$$(\mathbf{n}^{l,T} \otimes \mathbf{I}_N)(\boldsymbol{\xi}^n + \tau \mathbf{f}^n - \mathbf{v} \otimes \mathbf{1}_N) \leq \mathbf{0}, \quad l = 1, \dots, s, \quad (5.33)$$

but, recalling that $\mathbf{n}^l \cdot \mathbf{v} = c^l$, (5.33) is equivalent to

$$(\mathbf{n}^{l,T} \otimes \mathbf{I}_N)(\boldsymbol{\xi}^n + \tau \mathbf{f}^n) \leq c^l \mathbf{1}_N, \quad l = 1, \dots, s. \quad (5.34)$$

We now observe that $\mathbf{d}^{l,n} := c^l \mathbf{1}_N - (\mathbf{n}^{l,T} \otimes \mathbf{I}_N) \boldsymbol{\xi}^n$ is a vector in \mathbb{R}^N such that, for all $i = 1, \dots, N$, the i -th component $d_i^{l,n} = c^l - \mathbf{n}^l \cdot \boldsymbol{\xi}_{:,i}^n$ is the oriented distance between the solution $\boldsymbol{\xi}_{:,i}^n$ on the i -th nodal point and the hyperplane Σ^l . We then rewrite (5.34) as $\tau(\mathbf{n}^{l,T} \otimes \mathbf{I}_N) \mathbf{f}^n \leq \mathbf{d}^{l,n}$, $l = 1, \dots, s$. Componentwise, we have $\tau \mathbf{n}^l \cdot \mathbf{f}_{:,i}^n \leq d_i^{l,n}$, $i = 1, \dots, N$, $l = 1, \dots, s$. Now, since $\mathbf{U}^n \in \Sigma$, we can upper-bound this last inequality in terms of the oriented distances $\mathbf{d}^{l,n}$ and the directional Lipschitz constant \tilde{L}^l of the kinetics \mathbf{f} along the outward normal \mathbf{n}^l , obtaining $\tau \tilde{L}^l d_i^{l,n} \leq d_i^{l,n}$, $i = 1, \dots, N$, $l = 1, \dots, s$, but since $\tilde{L}^l \leq \sqrt{\sum_{k=1}^r (n_k^l)^2 L_k^2}$, the result follows. \square

Notice that, from Theorems 15 and 16, Remark 11 holds at the semi- and fully-discrete levels, as well.

Remark 13 (Timestep restriction in the absence of cross-diffusion). *In the absence of cross-diffusion, since the eigenvectors of D are the standard basis vectors of \mathbb{R}^r , the timestep restriction (5.29) becomes*

$$\tau \leq \bar{\tau} := \frac{1}{\max_{k=1, \dots, r} L_k}. \quad (5.35)$$

5.3 Stability and error analysis

Next we prove in this section stability estimates and optimal $L^\infty([0, T], L^2(\Gamma))$ error bounds for the semi-discrete (5.8) and the fully-discrete (5.10) solutions of the RCDS (5.1) of $r \in \mathbb{N}$ equations. First, we proceed to recall some preliminaries and basic notations.

The lumped L^2 product (see for instance [60, 101, 105, 126]) defined by $(U, V)_h := \int_{\Gamma_h} I_h(UV)$, $U, V \in L^2(\Gamma_h)$, where I_h is the piecewise linear interpolant defined in Section 5.1.1, induces the norm $\|U\|_h := \sqrt{(U, U)_h}$, $U \in \mathbb{V}_h$, which is equivalent to $\|\cdot\|_{0,h}$, uniformly with respect to h (see [114] for the proof):

$$\|U\|_{0,h} \leq \|U\|_h \leq C \|U\|_{0,h}, \quad U \in \mathbb{V}_h, \quad h > 0. \quad (5.36)$$

In [56] we proved the following estimate for the error $\varepsilon_h(U, V) := \int_{\Gamma_h} (UV - I_h(UV))$ in the lumped quadrature rule $(U, V)_h$, for all $U \in H^2(\Gamma_h)$ and $V \in \mathbb{V}_h$:

$$|\varepsilon_h(U, V)| \leq ch^2 \|U\|_{2,h} \|V\|_{1,h}. \quad (5.37)$$

We remark that inequalities (5.36) and (5.37) were proven on planar triangulations in [105] and [101], respectively. By using an affine map argument, we extended these inequalities to triangulated surfaces. From Lemma 4 we derive the following estimate for the broken H^2 norm of U .

Lemma 10 (Dominance of $H^2(\Gamma)$ norm over $H^2(\Gamma_h)$ norm). *If $u \in H^2(\Gamma)$, then $u^{-\ell} \in H^2(\Gamma_h)$ and*

$$\|u^{-\ell}\|_{2,h} \leq C\|u\|_2. \quad (5.38)$$

Proof. Let $K \in \mathcal{K}_h$. Then, from (3.39)-(3.41), we have

$$\begin{aligned} \|u^{-\ell}\|_{2,K}^2 &= \|u^{-\ell}\|_{0,K}^2 + \|\nabla_K u^{-\ell}\|_{0,K}^2 + \|\nabla_K^2 u^{-\ell}\|_{0,K}^2 \leq \frac{1}{c^2}\|u\|_{0,\tilde{K}}^2 + \frac{1}{c^2}\|\nabla_{\tilde{K}} u\|_{0,\tilde{K}}^2 \\ &\quad + c^2\|\nabla_{\tilde{K}}^2 u\|_{0,\tilde{K}}^2 + c^2 h^2 \|\nabla_{\tilde{K}} u\|_{0,\tilde{K}}^2 \leq C(1+h^2)\|u\|_{2,\tilde{K}}^2. \end{aligned} \quad (5.39)$$

Now, from (5.39), we have

$$\|u^{-\ell}\|_{2,h}^2 = \sum_{K \in \mathcal{K}_h} \|u^{-\ell}\|_{2,K}^2 \stackrel{(5.39)}{\leq} C(1+h^2) \sum_{K \in \mathcal{K}_h} \|u\|_{2,\tilde{K}}^2 = C(1+h^2)\|u\|_2^2. \quad (5.40)$$

This completes the proof. \square

For the following proofs we need to consider, for any positive definite matrix $\mathbf{B} \in \mathbb{R}^{r,r}$, the seminorms $|\cdot|_{\mathbf{B}}$ and $|\cdot|_{\mathbf{B},h}$ on $H^1(\Gamma)$ and $(H^1(\Gamma_h))^r$ respectively, defined by

$$|\mathbf{U}|_{\mathbf{B}}^2 := \int_{\Gamma} \mathbf{B} \nabla_{\Gamma} \mathbf{u} : \nabla_{\Gamma} \mathbf{u} = \int_{\Gamma} \mathbf{B}^s \nabla_{\Gamma} \mathbf{u} : \nabla_{\Gamma} \mathbf{u}, \quad \mathbf{u} \in H^1(\Gamma)^r; \quad (5.41)$$

$$|\mathbf{U}|_{\mathbf{B},h}^2 := \int_{\Gamma_h} \mathbf{B} \nabla_{\Gamma_h} \mathbf{U} : \nabla_{\Gamma_h} \mathbf{U} = \int_{\Gamma_h} \mathbf{B}^s \nabla_{\Gamma_h} \mathbf{U} : \nabla_{\Gamma_h} \mathbf{U}, \quad \mathbf{U} \in H^1(\Gamma_h)^r, \quad (5.42)$$

respectively where $\mathbf{B}^s := \frac{\mathbf{B} + \mathbf{B}^{tr}}{2}$ is the symmetric part of \mathbf{B} . It is well-known that a matrix is positive definite if and only if its symmetric part is positive definite. Then, the eigenvalues λ_i , $i = 1, \dots, r$, of \mathbf{B}^s are real and positive. It follows that

$$\min_{i=1,\dots,r} (\lambda_i) |\mathbf{u}|_1^2 \leq |\mathbf{u}|_{\mathbf{B}}^2 \leq \max_{i=1,\dots,r} (\lambda_i) |\mathbf{u}|_1^2, \quad \mathbf{u} \in (H^1(\Gamma))^r; \quad (5.43)$$

$$\min_{i=1,\dots,r} (\lambda_i) |\mathbf{U}|_{1,h}^2 \leq |\mathbf{U}|_{\mathbf{B},h}^2 \leq \max_{i=1,\dots,r} (\lambda_i) |\mathbf{U}|_{1,h}^2, \quad \mathbf{U} \in (H^1(\Gamma_h))^r, \quad (5.44)$$

i.e. the seminorms (5.41) and (5.42) are equivalent to $|\cdot|_1$ and $|\cdot|_{1,h}$, respectively.

We employ usual energy argument techniques to carry out the following stability estimates. Note that due to the existence of an invariant region, these estimates will not depend exponentially on time since they will not rely on Grönwall's lemma. The only requirement is that the reaction kinetics \mathbf{f} in (5.1) are Lipschitz locally in the invariant region and not globally Lipschitz. We recall that, given $n, m \in \mathbb{N}$ and any two matrices $\mathbf{A}, \mathbf{B} \in \mathbb{R}^{n,m}$, the Frobenius inner product of \mathbf{A} and \mathbf{B} is defined by $\mathbf{A} : \mathbf{B} := \sum_{i=1}^n \sum_{j=1}^m a_{ij} b_{ij}$.

Lemma 11 (Stability estimates for the weak formulation (5.2)). *If \mathbf{u} is the solution of (5.2), Σ as in (5.11) is a bounded invariant region for (5.2), \mathbf{f} is Lipschitz (and thus bounded) on Σ and $\mathbf{u}_0 \in \Sigma$, then the following estimates hold*

$$\sup_{t \in [0, T]} \|\mathbf{u}\|_0^2 + \int_0^T \|\nabla_{\Gamma} \mathbf{u}\|_0^2 \leq C (T + \|\mathbf{u}_0\|_0^2); \quad (5.45)$$

$$\int_0^T \|\dot{\mathbf{u}}\|_0^2 + \sup_{t \in [0, T]} \|\nabla_{\Gamma} \mathbf{u}\|_0^2 \leq C (T + \|\nabla_{\Gamma} \mathbf{u}_0\|_0^2), \quad (5.46)$$

for all $T > 0$, where C is a constant independent of T and \mathbf{u}_0 .

Proof. By summing over the equations in (2.37) and choosing $\varphi = \mathbf{u}$ we have

$$\frac{1}{2} \frac{d}{dt} \int_{\Gamma} |\mathbf{u}|^2 + |\mathbf{u}|_D^2 = \int_{\Gamma} \mathbf{f}(\mathbf{u}) : \mathbf{u}, \quad (5.47)$$

where $|\cdot|$ denotes the Euclidean norm of the vector \mathbf{u} . By combining (5.43) and (5.47) we have

$$\frac{d}{dt} \|\mathbf{u}\|_0^2 + |\mathbf{u}|_1^2 \leq C \int_{\Gamma} |\mathbf{f}(\mathbf{u}) : \mathbf{u}|.$$

Since $\mathbf{u} \in \Sigma$ at all times and \mathbf{f} is bounded on Σ , we obtain

$$\frac{d}{dt} \|\mathbf{u}\|_0^2 + |\mathbf{u}|_1^2 \leq C. \quad (5.48)$$

By integrating both sides of (5.48) over $[0, T]$, estimate (5.45) follows.

To prove the second estimate, we sum over the equations in (2.37) and we set $\varphi = \dot{\mathbf{u}}$, thereby obtaining:

$$\int_{\Gamma} |\dot{\mathbf{u}}|^2 + \frac{1}{2} \frac{d}{dt} \int_{\Gamma} D \nabla_{\Gamma} \mathbf{u} : \nabla_{\Gamma} \mathbf{u} \leq \int_{\Gamma} |\mathbf{f}(\mathbf{u})| |\dot{\mathbf{u}}|, \quad (5.49)$$

but, since \mathbf{f} is bounded on Σ , it holds that

$$\int_{\Gamma} |\mathbf{f}(\mathbf{u})| |\dot{\mathbf{u}}| \leq \frac{1}{2} \int_{\Gamma} |\mathbf{f}(\mathbf{u})|^2 + \frac{1}{2} \int_{\Gamma} |\dot{\mathbf{u}}|^2 \leq C + \frac{1}{2} \int_{\Gamma} |\dot{\mathbf{u}}|. \quad (5.50)$$

Combining (5.49) and (5.50) we have

$$\|\dot{\mathbf{u}}\|_0^2 + \frac{d}{dt} |\mathbf{u}|_D^2 \leq C, \quad (5.51)$$

from which, by integrating on $[0, T]$ we obtain

$$\int_0^T \|\dot{\mathbf{u}}\|_0^2 + |\mathbf{u}|_D^2 \leq CT + |\mathbf{u}_0|_D^2. \quad (5.52)$$

By using (5.43) into (5.52), we have

$$\int_0^T \|\dot{\mathbf{u}}\|_0^2 + |\mathbf{u}|_1^2 \leq C (T + |\mathbf{u}_0|_1^2),$$

from which estimate (5.46) immediately follows. \square

In the next lemmas we show analogous estimates for the semi- and fully-discrete problems.

Lemma 12 (Stability estimates for the semi-discrete system (5.3)). *If \mathbf{U} is the solution of (5.3), Σ is a bounded invariant region for (5.3), \mathbf{f} is Lipschitz on Σ and $\mathbf{U}_0 \in \Sigma$, then*

$$\sup_{t \in [0, T]} \|\mathbf{U}\|_{0,h}^2 + \int_0^T \|\nabla_{\Gamma} \mathbf{U}\|_{0,h}^2 \leq C (T + \|\mathbf{U}_0\|_{0,h}^2); \quad (5.53)$$

$$\int_0^T \|\dot{\mathbf{U}}\|_{0,h}^2 + \sup_{t \in [0, T]} \|\nabla_{\Gamma} \mathbf{U}\|_{0,h}^2 \leq C (T + \|\nabla_{\Gamma} \mathbf{U}_0\|_{0,h}^2), \quad (5.54)$$

for all $T > 0$, where C is a constant independent of T and \mathbf{U}_0 .

Proof. We use an energy argument as in the previous lemma and then use the equivalence (5.36) between the norms $\|\cdot\|_h$ and $\|\cdot\|_{0,h}$. \square

Lemma 13 (Stability estimates for the fully-discrete system (5.9)). *Let $\tau > 0$. If \mathbf{U}^n , $n = 0, \dots, N_T$, is the solution of (5.9), Σ is a bounded invariant region for (5.9), \mathbf{f} is Lipschitz on Σ and $\mathbf{U}^0 \in \Sigma$, then*

$$\|\mathbf{U}^{m+1}\|_{0,h}^2 + \tau \sum_{n=0}^m \|\nabla_{\Gamma_h} \mathbf{U}^{n+1}\|_{0,h}^2 \leq C(\|\mathbf{U}^0\|_{0,h} + T); \quad (5.55)$$

$$\frac{1}{\tau} \sum_{n=0}^m \|\mathbf{U}^{n+1} - \mathbf{U}^n\|_{0,h}^2 + \|\nabla_{\Gamma_h} \mathbf{U}^{m+1}\|_{0,h}^2 \leq C(\|\nabla_{\Gamma_h} \mathbf{U}^0\|_{0,h}^2 + T), \quad (5.56)$$

for all $n = 0, \dots, N_T$ and $T > 0$, where C is a constant independent of T and \mathbf{U}^0 .

Proof. By summing over the equations in (5.9) and choosing $\phi^n = \mathbf{U}^{n+1}$ we have

$$\frac{1}{\tau} \left(\|\mathbf{U}^{n+1}\|_h^2 - \int_{\Gamma_h} I_h(\mathbf{U}^n : \mathbf{U}^{n+1}) \right) + |\mathbf{U}^{n+1}|_{\mathbf{D},h}^2 = \int_{\Gamma_h} I_h(\mathbf{f}(\mathbf{U}^n) : \mathbf{U}^{n+1}).$$

After multiplying by τ , Cauchy-Schwarz inequality yields

$$\|\mathbf{U}^{n+1}\|_h^2 + \tau |\mathbf{U}^{n+1}|_{\mathbf{D},h} \leq \|\mathbf{U}^{n+1}\|_h \|\mathbf{U}^n\|_h + \tau \|\mathbf{f}(\mathbf{U}^n)\|_h \|\mathbf{U}^{n+1}\|_h.$$

Since \mathbf{U}^n and $\mathbf{U}^{n+1} \in \Sigma$ and \mathbf{f} is Lipschitz on Σ , the last term on the right-hand side is bounded by some constant $C > 0$: $\|\mathbf{U}^{n+1}\|_h^2 + \tau |\mathbf{U}^{n+1}|_{\mathbf{D},h} \leq \|\mathbf{U}^{n+1}\|_h \|\mathbf{U}^n\|_h + C\tau$. Young's inequality yields $\|\mathbf{U}^{n+1}\|_h^2 + \tau |\mathbf{U}^{n+1}|_{\mathbf{D},h}^2 \leq \|\mathbf{U}^n\|_h^2 + C\tau$. We sum for $n = 0, \dots, m$ to obtain

$$\|\mathbf{U}^{m+1}\|_h^2 + \tau \sum_{n=0}^m |\mathbf{U}^{n+1}|_{\mathbf{D},h}^2 \leq \|\mathbf{U}^0\|_h^2 + Cm\tau.$$

By using (5.36), (5.44) and $m \leq N_T$, (5.55) follows immediately. Summing over the equations in (5.9) and choosing $\phi^n = \mathbf{D}(\mathbf{U}^{n+1} - \mathbf{U}^n)$, since \mathbf{D} is constant and positive definite we have

$$\begin{aligned} \frac{1}{\tau} \|\mathbf{U}^{n+1} - \mathbf{U}^n\|_h^2 + \|\mathbf{D} \nabla_{\Gamma_h} \mathbf{U}^{n+1}\|_{0,h}^2 - \int_{\Gamma_h} \mathbf{D} \nabla_{\Gamma_h} \mathbf{U}^{n+1} : \mathbf{D} \nabla_{\Gamma_h} \mathbf{U}^n \\ \leq C \int_{\Gamma_h} I_h(\mathbf{f}(\mathbf{U}^n) : \mathbf{D}(\mathbf{U}^{n+1} - \mathbf{U}^n)). \end{aligned}$$

The Cauchy-Schwarz inequality yields

$$\begin{aligned} \frac{1}{\tau} \|\mathbf{U}^{n+1} - \mathbf{U}^n\|_h^2 + \|\mathbf{D}\nabla_{\Gamma_h} \mathbf{U}^{n+1}\|_{0,h}^2 \\ \leq \|\mathbf{D}\nabla_{\Gamma_h} \mathbf{U}^{n+1}\|_{0,h} \|\mathbf{D}\nabla_{\Gamma_h} \mathbf{U}^n\|_{0,h} + C \|\mathbf{f}(\mathbf{U}^n)\|_h \|\mathbf{D}(\mathbf{U}^{n+1} - \mathbf{U}^n)\|_h. \end{aligned}$$

Since \mathbf{f} is Lipschitz -and thus bounded- on Σ , say $\max_{\Sigma} |\mathbf{f}| = C$, we can bound the last term on the right-hand side as follows:

$$\frac{1}{\tau} \|\mathbf{U}^{n+1} - \mathbf{U}^n\|_h^2 + \|\mathbf{D}\nabla_{\Gamma_h} \mathbf{U}^{n+1}\|_{0,h}^2 \leq \|\mathbf{D}\nabla_{\Gamma_h} \mathbf{U}^{n+1}\|_{0,h} \|\mathbf{D}\nabla_{\Gamma_h} \mathbf{U}^n\|_{0,h} + C \|\mathbf{U}^{n+1} - \mathbf{U}^n\|_h.$$

Young's inequality yields

$$\begin{aligned} \frac{1}{\tau} \|\mathbf{U}^{n+1} - \mathbf{U}^n\|_h^2 + \|\mathbf{D}\nabla_{\Gamma_h} \mathbf{U}^{n+1}\|_{0,h}^2 \\ \leq \frac{1}{2} (\|\mathbf{D}\nabla_{\Gamma_h} \mathbf{U}^n\|_{0,h}^2 + \|\mathbf{D}\nabla_{\Gamma_h} \mathbf{U}^{n+1}\|_{0,h}^2) + C\tau + \frac{1}{2\tau} \|\mathbf{U}^{n+1} - \mathbf{U}^n\|_h^2. \end{aligned}$$

Rearranging terms and multiplying by 2 we have

$$\frac{1}{\tau} \|\mathbf{U}^{n+1} - \mathbf{U}^n\|_h^2 + \|\mathbf{D}\nabla_{\Gamma_h} \mathbf{U}^{n+1}\|_{0,h}^2 \leq \|\mathbf{D}\nabla_{\Gamma_h} \mathbf{U}^{n+1}\|_{0,h}^2 + C\tau. \quad (5.57)$$

By summing (5.57) for $n = 0, \dots, m$ we have

$$\frac{1}{\tau} \sum_{n=0}^m \|\mathbf{U}^{n+1} - \mathbf{U}^n\|_h^2 + \|\mathbf{D}\nabla_{\Gamma_h} \mathbf{U}^{m+1}\|_{0,h}^2 \leq \|\mathbf{D}\nabla_{\Gamma_h} \mathbf{U}^0\|_{0,h}^2 + Cm\tau.$$

Now, since \mathbf{D} is positive definite, by using (5.36) and $m \leq N_T$, (5.56) finally follows. \square

In what follows, we adopt the surface Ritz projection considered in [34, 44] to prove the convergence of the semi- and fully-discrete methods.

Definition 12 (Ritz projection). *Given $u : [0, T] \rightarrow H^1(\Gamma)$, the Ritz projection of u is the unique function $\bar{U} : [0, T] \rightarrow \mathbb{V}_h$ such that*

$$\int_{\Gamma_h} \nabla_{\Gamma_h} \bar{U} \cdot \nabla_{\Gamma_h} \varphi = \int_{\Gamma} \nabla_{\Gamma} u \cdot \nabla_{\Gamma} \varphi^\ell \quad \text{and} \quad \int_{\Gamma_h} \bar{U} = \int_{\Gamma} u \quad \forall \varphi \in \mathbb{V}_h. \quad (5.58)$$

It must be observed that this definition is different from the one considered in [41, 89]. The following error estimates for the Ritz projection can be found in [34, 44].

Theorem 17 (Error estimates for the Ritz projection). *Given $u : [0, T] \rightarrow H^2(\Gamma)$ such that $\dot{u} : [0, T] \rightarrow H^2(\Gamma)$, the error in the Ritz projection satisfies the following bounds*

$$\|u - \bar{U}^\ell\|_0 + h \|\nabla_{\Gamma}(u - \bar{U}^\ell)\|_0 \leq Ch^2 \|u\|_2; \quad (5.59)$$

$$\|\dot{u} - \dot{\bar{U}}^\ell\|_0 + h \|\nabla_{\Gamma}(\dot{u} - \dot{\bar{U}}^\ell)\|_0 \leq Ch^2 (\|u\|_2 + \|\dot{u}\|_2). \quad (5.60)$$

From here onwards, we will denote by $\bar{\mathbf{U}}$ the componentwise Ritz projection of a given vector function \mathbf{u} . This entails that the estimates (5.59)-(5.60) still hold in their respective tensor product norms.

In the following theorems, extracted from [55], we prove asymptotically optimal error bounds for the LSFEM space discretisation and for the LSFEM-IMEX Euler full discretisation.

Theorem 18 (Error estimate for the semi-discrete solution (5.3)). *Assume that Σ is an invariant region for (5.2) and (5.3), that $\mathbf{f} \in \mathcal{C}^2(\Sigma)$ and that $\mathbf{u}_0, \mathbf{U}_0 \in \Sigma$. If the solution \mathbf{u} of (5.2) and its time derivative $\dot{\mathbf{u}}$ are $L^\infty([0, T]; H^2(\Gamma))$ and $\|\mathbf{u}_0 - \mathbf{U}_0^\ell\|_0 \leq Ch^2$, then the following estimate holds*

$$\|\mathbf{u} - \mathbf{U}^\ell\|_0 \leq C(\mathbf{u}, T)h^2,$$

where $C(\mathbf{u}, T)$ is a constant depending on \mathbf{u} and T .

Proof. Following [56, Theorem 7], let us write the error as $\mathbf{U}^\ell - \mathbf{u} = (\mathbf{U}^\ell - \bar{\mathbf{U}}^\ell) + (\bar{\mathbf{U}}^\ell - \mathbf{u}) =: \boldsymbol{\theta}^\ell + \boldsymbol{\rho}^\ell$. Since \mathbf{u} and $\dot{\mathbf{u}}$ are $L^\infty([0, T], H^2(\Gamma))$, from the error estimates (5.59)-(5.60) for the Ritz projection and (3.39)-(3.40) we have that

$$\|\boldsymbol{\rho}\|_{0,h} \leq C\|\boldsymbol{\rho}^\ell\|_0 = C\|\bar{\mathbf{U}}^\ell - \mathbf{u}\|_0 \leq Ch^2\|\mathbf{u}\|_2; \quad (5.61)$$

$$\|\dot{\boldsymbol{\rho}}\|_{0,h} + h\|\nabla_{\Gamma_h}\dot{\boldsymbol{\rho}}\|_{0,h} \leq Ch^2(\|\mathbf{u}\|_2 + \|\dot{\mathbf{u}}\|_2). \quad (5.62)$$

It remains to show the convergence for $\boldsymbol{\theta}^\ell$. For the sake of simplicity, we derive an estimate for $\boldsymbol{\theta}$ in the norm $\|\cdot\|_h$ and then we will use (3.39) and (5.36) to estimate $\|\boldsymbol{\theta}^\ell\|_0$. In the weak and semi-discrete formulations (5.2) and (5.3) we choose the same test functions φ_m , $m = 1, \dots, r$, under lifting. By subtracting these two formulations and summing over $m = 1, \dots, r$, we have

$$\begin{aligned} & \left(\int_{\Gamma} \dot{\mathbf{u}} : \boldsymbol{\varphi}^\ell - \int_{\Gamma_h} I_h(\dot{\mathbf{U}} : \boldsymbol{\varphi}) \right) + \left(\int_{\Gamma} \mathbf{D}\nabla_{\Gamma}\mathbf{u} : \nabla_{\Gamma}\boldsymbol{\varphi}^\ell - \int_{\Gamma_h} \mathbf{D}\nabla_{\Gamma_h}\mathbf{U} : \nabla_{\Gamma_h}\boldsymbol{\varphi} \right) \\ &= \left(\int_{\Gamma} \mathbf{f}(\mathbf{u}) : \boldsymbol{\varphi}^\ell - \int_{\Gamma_h} I_h(\mathbf{f}(\mathbf{U}) : \boldsymbol{\varphi}) \right), \end{aligned} \quad (5.63)$$

Using (3.37) and (5.58) we rearrange the three terms between brackets in (5.63) as follows

$$\begin{aligned} 1) \quad & \int_{\Gamma} \dot{\mathbf{u}} : \boldsymbol{\varphi}^\ell - \int_{\Gamma_h} I_h(\dot{\mathbf{U}} : \boldsymbol{\varphi}) \\ &= \int_{\Gamma} \left(1 - \frac{1}{\delta_h^\ell} \right) \dot{\mathbf{u}} : \boldsymbol{\varphi}^\ell - \int_{\Gamma_h} \dot{\boldsymbol{\rho}} : \boldsymbol{\varphi} + \varepsilon_h(\dot{\mathbf{U}}, \boldsymbol{\varphi}) - \int_{\Gamma_h} I_h(\dot{\boldsymbol{\theta}} : \boldsymbol{\varphi}); \\ 2) \quad & \int_{\Gamma} \mathbf{D}\nabla_{\Gamma}\mathbf{u} : \nabla_{\Gamma}\boldsymbol{\varphi}^\ell - \int_{\Gamma_h} \mathbf{D}\nabla_{\Gamma_h}\mathbf{U} : \nabla_{\Gamma_h}\boldsymbol{\varphi} \\ &= \int_{\Gamma_h} \mathbf{D}\nabla_{\Gamma_h}\bar{\mathbf{U}} : \nabla_{\Gamma_h}\boldsymbol{\varphi} - \int_{\Gamma_h} \mathbf{D}\nabla_{\Gamma_h}\mathbf{U} : \nabla_{\Gamma_h}\boldsymbol{\varphi} = - \int_{\Gamma_h} \mathbf{D}\nabla_{\Gamma_h}\boldsymbol{\theta} : \nabla_{\Gamma_h}\boldsymbol{\varphi}; \\ 3) \quad & \int_{\Gamma} \mathbf{f}(\mathbf{u}) : \boldsymbol{\varphi}^\ell - \int_{\Gamma_h} I_h(\mathbf{f}(\mathbf{U}) : \boldsymbol{\varphi}) = \int_{\Gamma} \mathbf{f}(\mathbf{u}) : \boldsymbol{\varphi}^\ell - \int_{\Gamma_h} \mathbf{f}(\mathbf{u}^{-\ell}) : \boldsymbol{\varphi} + \int_{\Gamma_h} \mathbf{f}(\mathbf{u}^{-\ell}) : \boldsymbol{\varphi} \\ & - \int_{\Gamma_h} I_h(\mathbf{f}(\mathbf{u}^{-\ell}) : \boldsymbol{\varphi}) + \int_{\Gamma_h} I_h((\mathbf{f}(\mathbf{u}^{-\ell}) - \mathbf{f}(\mathbf{U})) : \boldsymbol{\varphi}) \\ &= \int_{\Gamma} \left(1 - \frac{1}{\delta_h^\ell} \right) \mathbf{f}(\mathbf{u}) : \boldsymbol{\varphi}^\ell + \varepsilon_h(\mathbf{f}(\mathbf{u}^{-\ell}), \boldsymbol{\varphi}) + \int_{\Gamma_h} I_h((\mathbf{f}(\mathbf{u}^{-\ell}) - \mathbf{f}(\mathbf{U})) : \boldsymbol{\varphi}). \end{aligned}$$

By using these relations in (5.63) we obtain

$$\begin{aligned}
& \int_{\Gamma_h} I_h(\dot{\boldsymbol{\theta}} : \boldsymbol{\varphi}) + \int_{\Gamma_h} \mathbf{D} \nabla_{\Gamma_h} \boldsymbol{\theta} : \nabla_{\Gamma_h} \boldsymbol{\varphi} = \int_{\Gamma_h} I_h((\mathbf{f}(\mathbf{U}) - \mathbf{f}(\mathbf{u}^{-\ell})) : \boldsymbol{\varphi}) \\
& - \varepsilon_h(\mathbf{f}(\mathbf{u}^{-\ell}), \boldsymbol{\varphi}) - \int_{\Gamma} \left(1 - \frac{1}{\delta_h^\ell}\right) \mathbf{f}(\mathbf{u}) : \boldsymbol{\varphi}^\ell - \int_{\Gamma_h} \dot{\boldsymbol{\rho}} : \boldsymbol{\varphi} \\
& + \varepsilon_h(\dot{\mathbf{U}}, \boldsymbol{\varphi}) + \int_{\Gamma} \left(1 - \frac{1}{\delta_h^\ell}\right) \dot{\mathbf{u}} : \boldsymbol{\varphi}^\ell.
\end{aligned} \tag{5.64}$$

In (5.64) we choose $\boldsymbol{\varphi} = \boldsymbol{\theta}$. For the first term of (5.64) we observe that

$$\int_{\Gamma_h} I_h(\dot{\boldsymbol{\theta}} : \boldsymbol{\theta}) = \frac{1}{2} \frac{d}{dt} \|\boldsymbol{\theta}\|_h^2. \tag{5.65}$$

We estimate the single terms on the right-hand side of (5.64) in turn. By using the Cauchy-Schwarz inequality, the Lipschitz continuity of \mathbf{f} , the definition of $\boldsymbol{\theta}$, (3.39), (5.36) and (5.61), we have that

$$\begin{aligned}
& \left| \int_{\Gamma_h} I_h((\mathbf{f}(\mathbf{U}) - \mathbf{f}(\mathbf{u}^{-\ell})) : \boldsymbol{\theta}) \right| \leq C \|\mathbf{U} - \mathbf{u}^{-\ell}\|_h \|\boldsymbol{\theta}\|_h \\
& \leq C (\|\boldsymbol{\rho}\|_0 + \|\boldsymbol{\theta}\|_h) \|\boldsymbol{\theta}\|_h = C(\mathbf{u})(h^2 + \|\boldsymbol{\theta}\|_h) \|\boldsymbol{\theta}\|_h.
\end{aligned} \tag{5.66}$$

By using the estimate (5.37) for ε_h , (5.38), the regularity assumptions $\mathbf{u} \in L^\infty([0, T], H^2(\Gamma))$ and $\mathbf{f} \in \mathcal{C}^2(\Sigma)$, and by applying the chain rule to the composite function $\mathbf{f}(\mathbf{u})$ it follows that

$$\begin{aligned}
& |\varepsilon_h(\mathbf{f}(\mathbf{u}^{-\ell}), \boldsymbol{\theta})| \leq Ch^2 \|\mathbf{f}(\mathbf{u}^{-\ell})\|_{2,h} \|\boldsymbol{\theta}\|_{1,h} \leq Ch^2 \|\mathbf{f}(\mathbf{u})\|_2 \|\boldsymbol{\theta}\|_{1,h} \\
& \leq Ch^2 \|\mathbf{f}\|_{\mathcal{C}^2(\Sigma)} \|\mathbf{u}\|_2 \|\boldsymbol{\theta}\|_1 \leq Ch^2 \|\boldsymbol{\theta}\|_{1,h}.
\end{aligned} \tag{5.67}$$

Since \mathbf{f} is Lipschitz over the compact region Σ , then $\mathbf{f} \in L^\infty(\Sigma)$. Hence, by using the Cauchy-Schwarz inequality, (3.39) and the geometric estimate (3.31) we have

$$\left| \int_{\Gamma} \left(1 - \frac{1}{\delta_h^\ell}\right) \mathbf{f}(\mathbf{u}) : \boldsymbol{\theta}^\ell \right| \leq \left\| 1 - \frac{1}{\delta_h^\ell} \right\|_\infty \|\mathbf{f}(\mathbf{u})\|_0 \|\boldsymbol{\theta}^\ell\|_0 \leq Ch^2 \|\boldsymbol{\theta}\|_{0,h}. \tag{5.68}$$

From the Cauchy-Schwarz inequality, the error estimate (5.62) for $\dot{\boldsymbol{\rho}}$ and (3.39) we have

$$\left| \int_{\Gamma_h} \dot{\boldsymbol{\rho}} : \boldsymbol{\theta} \right| \leq C \|\dot{\boldsymbol{\rho}}\|_{0,h} \|\boldsymbol{\theta}\|_{0,h} \leq C(\mathbf{u}) h^2 \|\boldsymbol{\theta}\|_{0,h}. \tag{5.69}$$

From the estimate (5.37) for ε_h , the estimate (5.62) for $\dot{\boldsymbol{\rho}}$, (3.39), (3.40), the triangle inequality and $\dot{\mathbf{U}}, \boldsymbol{\theta} \in \mathbb{V}_h$ we have

$$\begin{aligned}
& |\varepsilon_h(\dot{\mathbf{U}}, \boldsymbol{\theta})| \leq Ch^2 \|\dot{\mathbf{U}}\|_{1,h} \|\boldsymbol{\theta}\|_{1,h} \leq Ch^2 \left(\|\dot{\boldsymbol{\rho}}\|_{1,h} + \|\dot{\mathbf{u}}^{-\ell}\|_{1,h} \right) \|\boldsymbol{\theta}\|_{1,h} \\
& \leq Ch^2 (C(\mathbf{u})h + C \|\dot{\mathbf{u}}\|_1) \|\boldsymbol{\theta}\|_{1,h} \leq C(\mathbf{u}) h^2 \|\boldsymbol{\theta}\|_{1,h}.
\end{aligned} \tag{5.70}$$

The Cauchy-Schwarz inequality, (3.39), the geometric estimate (3.31) and the stability bound (5.45) yield

$$\left| \int_{\Gamma} \left(1 - \frac{1}{\delta_h^\ell}\right) \dot{\mathbf{u}} : \boldsymbol{\theta}^\ell \right| \leq \left\| 1 - \frac{1}{\delta_h^\ell} \right\|_\infty \|\dot{\mathbf{u}}\|_0 \|\boldsymbol{\theta}\|_{0,h} \leq C(\mathbf{u}) h^2 \|\boldsymbol{\theta}\|_{0,h}. \tag{5.71}$$

Combining (5.64)–(5.71), using (3.39), (3.40), (5.36) and (5.44), we have

$$\frac{1}{2} \frac{d}{dt} \|\boldsymbol{\theta}\|_h^2 + m \|\nabla_{\Gamma_h} \boldsymbol{\theta}\|_{0,h}^2 \leq C(\mathbf{u}) (h^2 + \|\boldsymbol{\theta}\|_h) \|\boldsymbol{\theta}\|_{1,h} \leq C(\mathbf{u}, m) (h^4 + \|\boldsymbol{\theta}\|_h^2) + m \|\boldsymbol{\theta}\|_{1,h}^2,$$

where $m = \min(\text{eig}(\mathbf{D}^s))$. Canceling $m \|\nabla_{\Gamma_h} \boldsymbol{\theta}\|_{0,h}^2$ on both sides and using (5.36), we have that $\frac{d}{dt} \|\boldsymbol{\theta}\|_h^2 \leq C(\mathbf{u}) h^4 + C(\mathbf{u}) \|\boldsymbol{\theta}\|_h^2$. Using Grönwall's lemma, the assumption $\|\boldsymbol{\theta}_0^\ell\|_0 \leq Ch^2$, (5.36) and (3.39), we obtain $\|\boldsymbol{\theta}^\ell\|_0^2 \leq C(\mathbf{u}, T) h^4$, which yields the desired result. \square

Similarly to the approach employed in [101] and [82], one obtains the following $L^\infty([0, T], L^2(\Gamma))$ error estimate for the fully-discrete solution (5.9) as follows.

Theorem 19 (Error estimate for the fully-discrete solution (5.9)). *Assume that Σ is an invariant region for (5.2) and (5.9), $\mathbf{f} \in C^2(\Sigma)$ and $\mathbf{u}_0, \mathbf{U}_0 \in \Sigma$. If the solution \mathbf{u} of (5.2) and its time derivative $\dot{\mathbf{u}}$ are $L^\infty([0, T]; H^2(\Gamma))$, $\ddot{\mathbf{u}}$ is $L^\infty([0, T]; L^2(\Gamma))$ and $\|\mathbf{u}_0 - \mathbf{U}_0^\ell\|_0 \leq ch^2$, then the following estimate holds*

$$\|\mathbf{u}^n - \mathbf{U}^{\ell,n}\|_0 \leq C(\mathbf{u}, T)(h^2 + \tau), \quad n = 0, \dots, N_T,$$

where \mathbf{u}^n is the exact solution at time $t_n := n\tau$ and $C(\mathbf{u}, T)$ is a constant depending on \mathbf{u} and T .

Proof. Following [56, Theorem 8], let us write the error as $\mathbf{U}^{\ell,n} - \mathbf{u}^n = (\mathbf{U}^{\ell,n} - \bar{\mathbf{U}}^{\ell,n}) + (\bar{\mathbf{U}}^{\ell,n} - \mathbf{u}^n) =: \boldsymbol{\theta}^{\ell,n} + \boldsymbol{\rho}^{\ell,n}$ and the discrete time derivative of any function $\phi : \Gamma_h \times [0, T] \rightarrow \mathbb{R}^r$ as $\bar{\partial}\phi^n := \frac{\phi^n - \phi^{n-1}}{\tau}$. Since \mathbf{u} and $\dot{\mathbf{u}}$ are $L^\infty([0, T], H^2(\Gamma))$, from (3.39), (3.40), (5.59) and (5.60), we have that

$$\|\boldsymbol{\rho}^n\|_{0,h} \leq C \|\boldsymbol{\rho}^{\ell,n}\|_0 = C \|\bar{\mathbf{U}}^{\ell,n} - \mathbf{u}^n\|_0 \leq ch^2 \|\mathbf{u}^n\|_2; \quad (5.72)$$

$$\|\dot{\boldsymbol{\rho}}^n\|_{0,h} + h \|\nabla_{\Gamma_h} \dot{\boldsymbol{\rho}}^n\|_{0,h} \leq ch^2 (\|\mathbf{u}^n\|_2 + \|\dot{\mathbf{u}}^n\|_2). \quad (5.73)$$

It remains to show the convergence for $\boldsymbol{\theta}^{\ell,n}$. To this end, we derive an estimate for $\boldsymbol{\theta}^n$ in the $L^2(\Gamma_h)$ norm and then use (3.39) and (5.36) to estimate $\|\boldsymbol{\theta}^{\ell,n}\|_0$. The continuous problem (5.2) and the fully-discrete formulation (5.9), the definition of Ritz projection (5.58), and the relation (3.37), imply that

$$\begin{aligned} & \int_{\Gamma_h} I_h(\bar{\partial}\boldsymbol{\theta}^n : \boldsymbol{\varphi}^n) + \int_{\Gamma_h} \mathbf{D}\nabla_{\Gamma_h} \boldsymbol{\theta}^n : \nabla_{\Gamma_h} \boldsymbol{\varphi}^n = -\varepsilon_h(\mathbf{f}(\mathbf{u}^{-\ell,n-1}), \boldsymbol{\varphi}^n) \\ & - \int_{\Gamma} \left(1 - \frac{1}{\delta_h^\ell}\right) \mathbf{f}(\mathbf{u}^{n-1}) : \boldsymbol{\varphi}^{\ell,n} + \int_{\Gamma_h} I_h((\mathbf{f}(\mathbf{U}^{n-1}) - \mathbf{f}(\mathbf{u}^{-\ell,n-1})) : \boldsymbol{\varphi}^n) \\ & + \int_{\Gamma} (\mathbf{f}(\mathbf{u}^{n-1}) - \mathbf{f}(\mathbf{u}^n)) : \boldsymbol{\varphi}^{\ell,n} - \int_{\Gamma_h} \bar{\partial}\boldsymbol{\rho}^n : \boldsymbol{\varphi}^n + \varepsilon_h(\bar{\partial}\bar{\mathbf{U}}^n, \boldsymbol{\varphi}^n) \\ & - \int_{\Gamma_h} (\bar{\partial} - \partial_t)\mathbf{u}^{-\ell,n} : \boldsymbol{\varphi}^n + \int_{\Gamma} \left(1 - \frac{1}{\delta_h^\ell}\right) \dot{\mathbf{u}}^n : \boldsymbol{\varphi}^{\ell,n}. \end{aligned} \quad (5.74)$$

In (5.74) we choose $\boldsymbol{\varphi}^n = \boldsymbol{\theta}^n$. For the first term in (5.74) we observe that, from Young's inequality,

$$\int_{\Gamma_h} I_h(\bar{\partial}\boldsymbol{\theta}^n : \boldsymbol{\theta}^n) \geq \frac{1}{2\tau} (\|\boldsymbol{\theta}^n\|_h^2 - \|\boldsymbol{\theta}^{n-1}\|_h^2). \quad (5.75)$$

We estimate the single terms on the right-hand side of (5.74) in turn. From the Cauchy-Schwarz inequality, the Lipschitz continuity of \mathbf{f} , the definition of $\boldsymbol{\theta}^n$, (5.36) and (5.72), it follows that

$$\begin{aligned} \left| \int_{\Gamma_h} I_h((\mathbf{f}(\mathbf{U}^{n-1}) - \mathbf{f}(\mathbf{u}^{-\ell, n-1})) : \boldsymbol{\theta}^n) \right| &\leq C \|\mathbf{U}^{n-1} - \mathbf{u}^{-\ell, n-1}\|_h \|\boldsymbol{\theta}^n\|_h \\ &\leq C(\|\boldsymbol{\rho}^{n-1}\|_0 + \|\boldsymbol{\theta}^{n-1}\|_h) \|\boldsymbol{\theta}^n\|_h \leq C(\mathbf{u})(h^2 + \|\boldsymbol{\theta}^{n-1}\|_h) \|\boldsymbol{\theta}^n\|_h. \end{aligned} \quad (5.76)$$

From the estimate (5.37) for ε_h and (5.38), we obtain that

$$\begin{aligned} |\varepsilon_h(\mathbf{f}(\mathbf{u}^{-\ell, n-1}), \boldsymbol{\theta}^n)| &\leq Ch^2 \|\mathbf{f}(\mathbf{u}^{-\ell, n-1})\|_{2,h} \|\boldsymbol{\theta}^n\|_{1,h} \\ &\leq Ch^2 \|\mathbf{f}(\mathbf{u}^{n-1})\|_2 \|\boldsymbol{\theta}^n\|_{1,h} \leq Ch^2 \|\mathbf{f}\|_{\mathcal{C}^2(\Sigma)} \|\mathbf{u}^{n-1}\|_2 \|\boldsymbol{\theta}^n\|_{1,h} \leq Ch^2 \|\boldsymbol{\theta}^n\|_{1,h}, \end{aligned} \quad (5.77)$$

where we have exploited the regularity assumptions $\mathbf{f} \in \mathcal{C}^2(\Sigma)$ and $\mathbf{u} \in L^\infty([0, T], H^2(\Gamma))$. Since \mathbf{f} is Lipschitz over the compact region Σ then $\mathbf{f} \in L^\infty(\Sigma)$. This fact, together with Cauchy-Schwarz inequality, (3.39) and the geometric estimate (3.31), yields

$$\left| \int_{\Gamma} \left(1 - \frac{1}{\delta_h^\ell}\right) \mathbf{f}(\mathbf{u}^{n-1}) : \boldsymbol{\theta}^{\ell, n} \right| \leq \left\| 1 - \frac{1}{\delta_h^\ell} \right\|_\infty \|\mathbf{f}(\mathbf{u}^{n-1})\|_{0,h} \|\boldsymbol{\theta}^n\|_0 \leq Ch^2 \|\boldsymbol{\theta}^n\|_{0,h}. \quad (5.78)$$

The Cauchy-Schwarz inequality yields, together with (3.39) and the stability estimate (5.46),

$$\begin{aligned} \left| \int_{\Gamma} (\mathbf{f}(\mathbf{u}^{n-1}) - \mathbf{f}(\mathbf{u}^n)) : \boldsymbol{\theta}^{\ell, n} \right| &\leq C \|\mathbf{u}^n - \mathbf{u}^{n-1}\|_0 \|\boldsymbol{\theta}^n\|_{0,h} = \left\| \int_{t_{n-1}}^{t_n} \dot{\mathbf{u}} \right\|_0 \|\boldsymbol{\theta}^n\|_{0,h} \\ &\leq \|\boldsymbol{\theta}^n\|_{0,h} \int_{t_{n-1}}^{t_n} \|\dot{\mathbf{u}}\|_0 \leq \tau \|\dot{\mathbf{u}}\|_{L^\infty([0, T], L^2(\Gamma))} \|\boldsymbol{\theta}^n\|_{0,h} = C(\mathbf{u})\tau \|\boldsymbol{\theta}^n\|_{0,h}. \end{aligned} \quad (5.79)$$

The Cauchy-Schwarz inequality and the estimate (5.73) for $\dot{\boldsymbol{\rho}}$ yield

$$\begin{aligned} \left| \int_{\Gamma_h} \bar{\delta} \boldsymbol{\rho}^n : \boldsymbol{\theta}^n \right| &\leq C \|\bar{\delta} \boldsymbol{\rho}^n\|_{0,h} \|\boldsymbol{\theta}^n\|_{0,h} = \frac{C}{\tau} \left\| \int_{t_{n-1}}^{t_n} \dot{\boldsymbol{\rho}} \right\|_{0,h} \|\boldsymbol{\theta}^n\|_{0,h} \\ &\leq \frac{C}{\tau} \|\boldsymbol{\theta}^n\|_{0,h} \int_{t_{n-1}}^{t_n} \|\dot{\boldsymbol{\rho}}\|_{0,h} \leq C \|\dot{\boldsymbol{\rho}}\|_{L^\infty([0, T], L^2(\Gamma_h))} \|\boldsymbol{\theta}^n\|_{0,h} \leq C(\mathbf{u})h^2 \|\boldsymbol{\theta}^n\|_{0,h}. \end{aligned} \quad (5.80)$$

From the estimate (5.37) for ε_h , the estimate (5.73) for $\dot{\boldsymbol{\rho}}$, the equivalences (3.39), (3.40), the triangle inequality and $\bar{\delta} \bar{\mathbf{U}}^n, \boldsymbol{\theta}^n \in \mathbb{V}_h$ we obtain

$$\begin{aligned} |\varepsilon_h(\bar{\delta} \bar{\mathbf{U}}^n, \boldsymbol{\theta}^n)| &\leq Ch^2 \|\bar{\delta} \bar{\mathbf{U}}^n\|_{1,h} \|\boldsymbol{\theta}^n\|_{1,h} \leq \frac{Ch^2}{\tau} \|\boldsymbol{\theta}^n\|_{1,h} \int_{t_{n-1}}^{t_n} \|\dot{\bar{\mathbf{U}}}\|_{1,h} \\ &\leq Ch^2 \|\dot{\bar{\mathbf{U}}}\|_{L^\infty([0, T], H^1(\Gamma_h))} \|\boldsymbol{\theta}^n\|_{1,h} \end{aligned} \quad (5.81)$$

$$\begin{aligned} &\leq Ch^2 \left(\|\dot{\boldsymbol{\rho}}\|_{L^\infty([0, T], H^1(\Gamma_h))} + \|\dot{\mathbf{u}}^{-\ell}\|_{L^\infty([0, T], H^1(\Gamma_h))} \right) \|\boldsymbol{\theta}^n\|_{1,h} \\ &\leq Ch^2 (C(\mathbf{u})h + C \|\dot{\mathbf{u}}\|_{L^\infty([0, T], H^1(\Gamma))}) \|\boldsymbol{\theta}^n\|_{1,h} \leq C(\mathbf{u})h^2 \|\boldsymbol{\theta}^n\|_{1,h}. \end{aligned} \quad (5.82)$$

The Cauchy-Schwarz inequality and (3.39) give rise to the following inequalities

$$\begin{aligned} \left| \int_{\Gamma_h} (\bar{\delta} - \partial_t) \mathbf{u}^{-\ell, n} : \boldsymbol{\theta}^n \right| &\leq C \|(\bar{\delta} - \partial_t) \mathbf{u}^n\|_0 \|\boldsymbol{\theta}^n\|_{0,h} \leq \frac{C}{\tau} \|\boldsymbol{\theta}^n\|_{0,h} \int_{t_{n-1}}^{t_n} \|\dot{\mathbf{u}}(t) - \dot{\mathbf{u}}(t_n)\|_0 dt \\ &\leq \frac{C}{\tau} \|\boldsymbol{\theta}^n\|_{0,h} \int_{t_{n-1}}^{t_n} \int_t^{t_n} \|\ddot{\mathbf{u}}(s)\| ds dt \leq C\tau \|\ddot{\mathbf{u}}\|_{L^\infty([0, T], L^2(\Gamma))} \|\boldsymbol{\theta}^n\|_{0,h} = C(\mathbf{u})\tau \|\boldsymbol{\theta}^n\|_{0,h}, \end{aligned} \quad (5.83)$$

where we have exploited the assumption that $\dot{\mathbf{u}} \in L^\infty([0, T], L^2(\Gamma))$. The Cauchy-Schwarz inequality, (3.39), the geometric estimate (3.31) and the stability bound (5.45) yield

$$\left| \int_{\Gamma} \left(1 - \frac{1}{\delta_h^\ell}\right) \dot{\mathbf{u}}^n : \boldsymbol{\theta}^{\ell, n} \right| \leq \left\| 1 - \frac{1}{\delta_h^\ell} \right\|_{\infty} \|\dot{\mathbf{u}}^n\|_0 \|\boldsymbol{\theta}^n\|_{0, h} \leq C(\mathbf{u}) h^2 \|\boldsymbol{\theta}^n\|_{0, h}. \quad (5.84)$$

Combining (5.74)-(5.84), using (5.36), (5.44) and Young's inequality we get

$$\begin{aligned} \frac{1}{2\tau} (\|\boldsymbol{\theta}^n\|_h^2 - \|\boldsymbol{\theta}^{n-1}\|_h^2) + m \|\nabla_{\Gamma_h} \boldsymbol{\theta}^n\|_{0, h}^2 &\leq C(\mathbf{u}) (h^2 + \tau + \|\boldsymbol{\theta}^{n-1}\|_h) \|\boldsymbol{\theta}^n\|_{1, h} \\ &\leq C(\mathbf{u}, m) (h^4 + \tau^2 + \|\boldsymbol{\theta}^{n-1}\|_h^2) + m \|\boldsymbol{\theta}^n\|_{1, h}^2, \end{aligned} \quad (5.85)$$

where $m = \min(\text{eig}(\mathbf{D}^s))$, from which, canceling $\|\nabla_{\Gamma_h} \boldsymbol{\theta}^n\|_{0, h}$ on both sides of (5.85), and using (5.36), we have that

$$\|\boldsymbol{\theta}^n\|_h^2 \leq (1 + C(\mathbf{u})\tau) \|\boldsymbol{\theta}^{n-1}\|_h^2 + C(\mathbf{u})\tau(h^4 + \tau^2). \quad (5.86)$$

By recursively applying (5.86), taking into account the assumption that $\|\boldsymbol{\theta}^0\|_0 \leq Ch^2$, and then using (3.39) and (5.36), we obtain $\|\boldsymbol{\theta}^{\ell, n}\|_0^2 \leq C(\mathbf{u})(h^4 + \tau^2)$, which yields the desired result. \square

In summary, the previous theorems entail that our semi- and fully-discrete schemes exhibit optimal convergence rates that are quadratic in the mesh size and linear in the timestep.

5.4 Numerical examples

In this section we provide numerical validation of our theoretical results and show that the LSFEM combined with the IMEX Euler in time:

- preserves the invariant rectangles of RDSs, while the standard SFEM does not (see Example 1);
- preserves the invariant polytopes of RCDSs, while the standard SFEM does not (see Example 2);
- exhibits the optimal convergence rate predicted in Theorem 14 (see Example 3);
- the LSFEM can be applied for the approximation of Turing patterns on surfaces, in good agreement with the results obtained with another method in [62] (see Example 4);

The meshes for our numerical examples have been constructed by using the MATLAB package DistMesh (see [108]). A-posteriori, we have verified that the generated meshes fulfil the Delaunay condition (4.15). The linear systems arising at each timestep have been solved with MATLAB direct solver in the “backslash” command.

Example 1: preservation of an invariant rectangle of a RDS

In this example we consider the reaction-diffusion system with Rosenzweig-MacArthur kinetics (see [60, 65])

$$\begin{cases} u_t - d_1 \Delta_\Gamma u = au(1-u) - b \frac{uv}{u+\alpha}; \\ v_t - d_2 \Delta_\Gamma v = c \frac{uv}{u+\alpha} - dv, \end{cases} \quad (5.87)$$

where α, a, b, c and d are positive constants. The surface considered is the *Dupin ring cyclide*

$$\Gamma := \left\{ (x, y, z) \in \mathbb{R}^3 : \left(x^2 + y^2 + z^2 + \frac{261}{100} \right)^2 - 4 \left(2x - \frac{\sqrt{39}}{10} \right)^2 - \frac{361}{25} y^2 = 0 \right\}, \quad (5.88)$$

(see [59]). This system has been numerically solved in [60] on a planar domain with LFEM in combination with an implicit Euler time discretisation. However, since the theory developed in [60] addresses a problem on domains of more general dimension ($n \leq 3$) there is no discrete maximum principle and the authors consider modified kinetics to ensure the positivity of the numerical solution. The present example shows that, on two dimensional manifolds, lumping guarantees the preservation of the invariant region without the need of modifying the kinetics.

When $c = d$ and $0 < \alpha < \frac{1}{\sqrt{2}}$ for every $0 < \varepsilon < 1 - 2\sqrt{a}$, the rectangle

$$\Sigma := \left[\varepsilon, 1 \right] \times \left[0, \frac{a\alpha}{2b} \right] \quad (5.89)$$

is an invariant region for (5.87), see for instance the analysis in [65]. An easy way to see this is to observe that, for every $\varepsilon, \varepsilon' > 0$, the rectangle

$$\Sigma_1 := \left[\varepsilon, 1 + \frac{\varepsilon' a \alpha}{b} \right] \times \left[-\varepsilon', \frac{a\alpha}{2b} \right]$$

fulfils condition (5.12). Since the intersection of invariant regions is still invariant, hence Σ is invariant for (5.87). The $H^1(\Gamma)$ initial datum

$$u_0(x, y, z) = \begin{cases} \varepsilon + (1 - \varepsilon) \sqrt{1 - \frac{y^2}{0.16}} & \text{if } y^2 \leq 0.16; \\ 0 & \text{elsewhere on } \Gamma; \end{cases}$$

$$v_0(x, y, z) = \frac{a\alpha}{2b}, \quad (x, y, z) \in \Gamma,$$

is contained in the invariant region Σ . Furthermore, for $0 < \alpha < 1$, it is easy to verify that, in Σ , the Lipschitz constants L_1 and L_2 of the kinetics in (5.87) fulfil

$$L_1 < \sqrt{2} \left(3a + \frac{b}{2\alpha} \right), \quad \text{and} \quad L_2 < \sqrt{2} \left(\frac{c}{2\alpha} + \frac{d}{2} \right).$$

In the following we choose $\varepsilon = 1\text{e-}7$ while, for the diffusion coefficients and reaction parameters we set

$$d_1 = d_2 = 1\text{e-}2, \quad \alpha = 1\text{e-}3, \quad a = 10, \quad b = 1\text{e-}2, \quad c = d = 1. \quad (5.90)$$

With these settings the invariant region (5.89) becomes

$$\Sigma = [1e-7, 1] \times \left[0, \frac{1}{2}\right], \quad (5.91)$$

and the stability condition (5.35) on the timestep is fulfilled if we choose

$$\tau \leq \bar{\tau} := \frac{1}{\sqrt{2} \max \left\{ \left(3a + \frac{b}{2\alpha}\right), \left(\frac{c}{2\alpha} + \frac{d}{2}\right) \right\}} \approx 1.4e-3. \quad (5.92)$$

We thus solve the problem on a sequence of seven spatial meshes Γ_i , $i = 0, \dots, 6$ with corresponding meshsizes h_i with $h_0 = 1.190$ and $h_i \approx \sqrt{2}^{-i} h_0$ for all $i = 1, \dots, 6$, with a fixed timestep $\bar{\tau} = 1e-3$ and final time $T = 5$. In Tables 5.1-5.2 we show the minima and the maxima of the components of the computed numerical solution: we observe that the LSFEM solution preserves Σ , whilst the SFEM one blows-up on all meshes. In Figure 5.1 we show, for the v component, the SFEM (left) and LSFEM (right) solutions, computed on mesh $i = 6$, at the time $\bar{t} := 0.4770$ in which the SFEM solution attains its absolute minimum (-5.529). In Figure 5.1 we set the bounds of the colormap to the endpoints of the invariant region ($[0, 0.5]$) to highlight the points on the surface in which the SFEM solution violates the region.

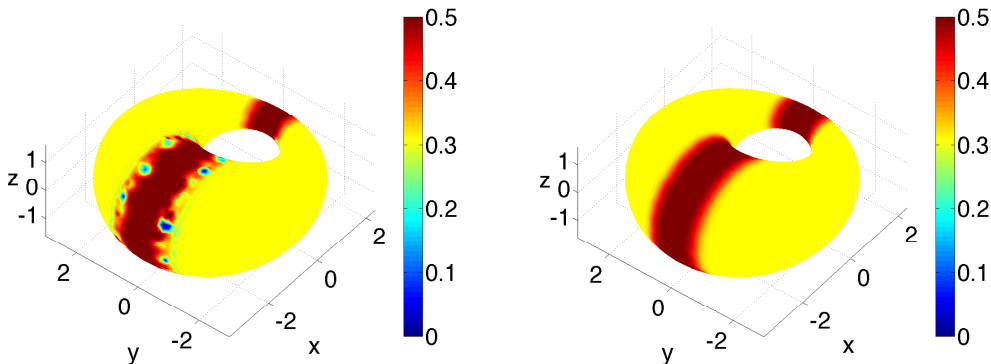


Figure 5.1: *Example 1*: Rosenzweig-MacArthur RDS (5.87) on the Dupin ring cyclide (5.88) with diffusion coefficients and reaction parameters as in (5.90) and final time $T = 5$. Component v of the numerical solution obtained by SFEM (left) and LSFEM (right) on a mesh with $N = 15552$ gridpoints, meshsize $h = 0.1531$, at the time $\bar{t} = 0.477$. The bounds of the colormap are set to $[0, 0.5]$ to highlight the areas in which the SFEM solution violates the invariant region (5.91).

Example 2: preservation of an invariant parallelogram of a RCDS

In this example we consider the RCD system with non-dimensional Rosenzweig-MacArthur kinetics [60, 65] and linear cross-diffusion given by

$$\begin{cases} u_t - d_{uu}\Delta_{\Gamma}u - d_{uv}\Delta_{\Gamma}v = au(1-u) - b\frac{uv}{u+\alpha}; \\ v_t - d_{vu}\Delta_{\Gamma}u - d_{vv}\Delta_{\Gamma}v = c\frac{uv}{u+\alpha} - dv, \end{cases} \quad (5.93)$$

on the unit sphere Γ , where α , a , b , c and d are positive constants.

i	N	h	$\min_{\Gamma_h \times [\tau, 5]} U$	$\max_{\Gamma_h \times [\tau, 5]} U$	$\min_{\Gamma_h \times [\tau, 5]} V$	$\max_{\Gamma_h \times [\tau, 5]} V$
0	242	1.190e+00	-2.199e+173	1.670e+169	-1.157e-01	5.159e-01
1	486	8.537e-01	-1.654e+161	2.663e+157	-1.629e+00	7.239e-01
2	986	5.898e-01	-2.788e+254	5.341e+250	-5.002e-01	2.170e+00
3	1950	4.273e-01	-4.164e+174	7.136e+170	-2.448e+00	3.394e+00
4	3866	3.011e-01	-5.784e+215	8.624e+211	-2.816e+00	7.301e+00
5	7766	2.114e-01	-1.961e+158	5.002e+154	-2.472e+01	2.114e+01
6	15552	1.531e-01	-2.891e+178	1.688e+175	-5.529e+01	1.085e+01

Table 5.1: *Example 1*: Rosenzweig-MacArthur RDS (5.87) on the Dupin ring cyclide (5.88) with diffusion coefficients and reaction parameters as in (5.90) and final time $T = 5$. Invariance analysis for the SFEM solution: the solution blows up on all meshes, hence the SFEM does not preserve the bounded invariant region (5.91).

i	$\min_{\Gamma_h \times [\tau, 5]} U$	$\max_{\Gamma_h \times [\tau, 5]} U$	$\min_{\Gamma_h \times [\tau, 5]} V$	$\max_{\Gamma_h \times [\tau, 5]} V$
0	1.005e-07	0.999919049314999	0.140403459482026	0.499999499006500
1	1.005e-07	0.999859791592458	0.140314932710790	0.499999500147031
2	1.005e-07	0.999928903829794	0.140311706814337	0.499999500464241
3	1.005e-07	0.999882762800890	0.140311624718897	0.499999500411808
4	1.005e-07	0.999929620790774	0.140311624053878	0.499999500465688
5	1.005e-07	0.999932927703920	0.140311624044096	0.499999500467816
6	1.005e-07	0.999934143729114	0.140311624043996	0.499999500468662

Table 5.2: *Example 1*: Rosenzweig-MacArthur RDS (5.87) on the Dupin ring cyclide (5.88) with diffusion coefficients and reaction parameters as in (5.90) and final time $T = 5$. Invariance analysis for LSFEM: the numerical solution stays in the invariant rectangle (5.91) for all meshes. The minima of U coincide up to machine precision.

In the absence of cross-diffusion, this model has been solved in [60] on a planar domain. To the best of the authors' knowledge, until now there is no discussion about the existence of an invariant region at the discrete level. In the present example we show that the IMEX-LSFEM full discretisation of system (5.93) possesses an invariant parallelogram in the presence of linear cross-diffusion with no modifications of the kinetics. For the reaction kinetics, we choose the following parameters

$$\alpha = 1e-3, a = 10, b = 1e-2, c = 1, d = 2.2. \quad (5.94)$$

For the diffusion coefficients, we choose

$$\begin{pmatrix} d_{uu} & d_{uv} \\ d_{vu} & d_{vv} \end{pmatrix} = \begin{pmatrix} 6e-2 & 0 \\ 1e-2 & 1.2e-1 \end{pmatrix}. \quad (5.95)$$

It is possible to verify that the parallelogram Σ defined by

$$\Sigma = \{(u, v) \in \mathbb{R}^2 \mid \sigma_l(u, v) \geq 0, l = 1, \dots, 4\}, \quad (5.96)$$

where the affine functions σ_l , $l = 1, \dots, 4$ are given by

$$\sigma_1(u, v) = u - \varepsilon; \quad (5.97)$$

$$\sigma_2(u, v) = 6 - 5\alpha + \sqrt{(6 - 5\alpha)^2 + 24\alpha(6 - \varepsilon)} - 12u; \quad (5.98)$$

$$\sigma_3(u, v) = u + 6v - \varepsilon; \quad (5.99)$$

$$\sigma_4(u, v) = 3 + \varepsilon - u - 6v, \quad (5.100)$$

with $\varepsilon = 1e-7$, is an invariant region for system (5.93). Σ is depicted in Fig. 5.2. The

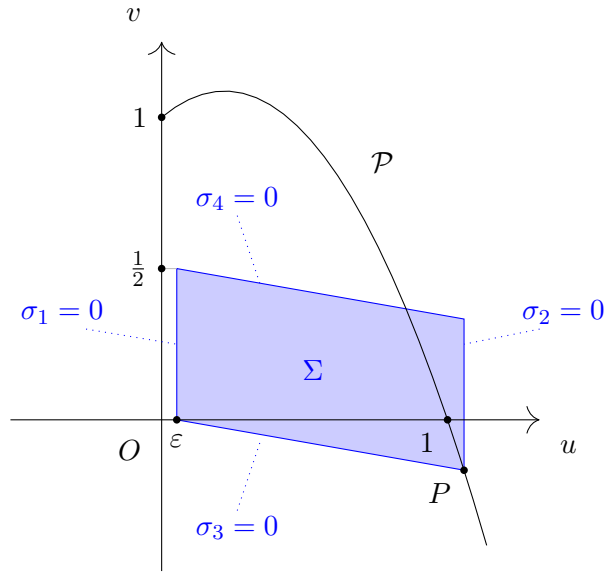


Figure 5.2: *Example 2*: Rosenzweig-MacArthur RCDS (5.93) on the unit sphere, with reaction parameters and diffusion coefficients as defined in (5.94) and (5.95), respectively. Pictorial representation of the invariant parallelogram Σ defined in (5.96). The edges are represented as the zero-level sets of the functions σ_i , $i = 1, \dots, 4$ defined in (5.97)-(5.100), in which we set $\varepsilon = 1e-7$. The slope of the slanting edges is $-\frac{1}{6}$. The corner P lies on the nullcline \mathcal{P} of the kinetic for u .

invariance of Σ means that σ_l , $l = 1, \dots, 4$, defined above, are positive for all times after discretisation. The $H^1(\Gamma)$ initial datum

$$u_0(x, y, z) = \begin{cases} \varepsilon + (1 - \varepsilon)\sqrt{1 - \frac{x^2+y^2}{r^2}} & \text{if } x^2 + y^2 \leq r^2, z > 0; \\ \varepsilon & \text{elsewhere on } \Gamma; \end{cases} \quad (5.101)$$

$$v_0(x, y, z) = \frac{a\alpha}{3b}, \quad (x, y, z) \in \Gamma, \quad (5.102)$$

i	N	h	$\min_{\Gamma_h \times [\tau, 5]} \sigma_1(U)$	$\min_{\Gamma_h \times [\tau, 5]} \sigma_2(U)$	$\min_{\Gamma_h \times [\tau, 5]} \sigma_3(U, V)$	$\min_{\Gamma_h \times [\tau, 5]} \sigma_4(U, V)$
0	126	4.013e-01	-7.503e+271	-4.733e+269	-7.460e+271	-7.730e+268
1	258	2.863e-01	-1.538e+305	-1.935e+303	-1.521e+305	-3.086e+302
2	516	2.026e-01	-1.871e-02	2.198e-02	-4.275e+00	-1.707e+00
3	1062	1.414e-01	-1.704e-02	-1.901e-01	-2.756e-01	-1.588e+00
4	2094	1.007e-01	-1.424e-02	2.198e-02	-8.777e+00	1.613e-02
5	4242	7.082e-02	-1.288e-02	2.198e-02	1.553e-01	-5.531e+00
6	8370	5.041e-02	-9.164e-03	2.198e-02	1.553e-01	-2.390e+00
7	16962	3.542e-02	-6.391e-03	2.198e-02	1.553e-01	7.946e-03

Table 5.3: *Example 2*: Rosenzweig-MacArthur RCDS (5.93) on the unit sphere, with reaction parameters and diffusion coefficients as defined in (5.94) and (5.95), respectively, with final time $T = 5$. Invariance analysis for the SFEM solution. By solving the problem on a sequence of eight meshes Γ_i , $i = 0, \dots, 7$ with fixed timestep $\tau = 1e-3$, the solution blows up on the five coarsest meshes. On the three finest meshes the numerical solution stays bounded, though still violating the invariant parallelogram Σ defined in (5.96) and depicted in Fig. 5.2.

with $r = 0.2$, is contained in the invariant region Σ . It is easy to verify that, on Σ , the Lipschitz constants L_1 and L_2 of the kinetics in (5.93) satisfy

$$L_1 < \tilde{L}_1 := \sqrt{2} \left(3a + \frac{b}{2\alpha} \right) \approx 49.4975, \text{ and } L_2 < \tilde{L}_2 := \sqrt{2} \left(\frac{c}{2\alpha} + \frac{d}{2} \right) \approx 708.6624.$$

The stability condition (5.29) on the timestep is fulfilled if we choose

$$\tau \leq \bar{\tau} := \frac{1}{\max \left(\tilde{L}_1, \sqrt{\frac{1}{37} \tilde{L}_1^2 + \frac{36}{37} \tilde{L}_2^2} \right)} \approx 1.43e-3. \quad (5.103)$$

We solve the problem with a fixed timestep $\tau = 1e-3$ until the final time $T = 5$, on a sequence of eight meshes Γ_i , $i = 0, \dots, 7$ with decreasing meshsizes $h_i \approx \frac{h_0}{(\sqrt{2})^i}$, $h_0 = 4.013e-1$, so that, for all $i = 0, \dots, 6$, the number of nodal points of Γ_{i+1} is approximately double that of Γ_i . For all $i = 0, \dots, 7$, the minima of σ_l , $l = 1, \dots, 4$, defined above are shown in Table 5.3 for SFEM and in Table 5.4 for LSFEM. We observe that the LSFEM solution is in Σ at all times, whilst the SFEM solution without lumping escapes Σ on all considered meshes. Furthermore, the SFEM exhibits a stability threshold: the numerical solution blows up on meshes Γ_i , $i = 0, 1$, while it appears to stay bounded on the finer meshes Γ_i , $i = 2, \dots, 7$. It is worth noting that the timestep restriction (5.103) is only a sufficient condition for the IMEX-LSFEM scheme to possess an invariant region. In fact, we have carried out the above invariance test with larger timesteps and we have observed that the IMEX-LSFEM admits Σ as an invariant region on all meshes Γ_i also for larger values of τ , that is $1e-3 \leq \tau \leq 1e-1$, while for $\tau = 0.2$, the method violates Σ on all meshes Γ_i .

Example 3: RDS and convergence

In this example, we test the convergence rate of the method on the unit sphere Γ for the well-studied *activator-depleted* substrate kinetics (see [63, 100, 110, 120]) with an additional forcing term:

$$\begin{cases} u_t - d_1 \Delta_\Gamma u = a - u + u^2 v + f_1(x, y, z, t); \\ v_t - d_2 \Delta_\Gamma v = b - u^2 v + f_2(x, y, z, t), \end{cases} \quad (5.104)$$

i	N	h	$\min_{\Gamma_h \times [\tau, 5]} \sigma_1(U)$	$\min_{\Gamma_h \times [\tau, 5]} \sigma_2(U)$	$\min_{\Gamma_h \times [\tau, 5]} \sigma_3(U, V)$	$\min_{\Gamma_h \times [\tau, 5]} \sigma_4(U, V)$
0	126	4.013e-01	6.667e-10	2.198e-02	1.619e-01	2.033e-02
1	258	2.863e-01	6.667e-10	2.198e-02	1.568e-01	7.509e-02
2	516	2.026e-01	6.667e-10	2.198e-02	1.556e-01	1.158e-01
3	1062	1.414e-01	6.667e-10	2.198e-02	1.553e-01	8.724e-03
4	2094	1.007e-01	6.667e-10	2.198e-02	1.553e-01	1.496e-02
5	4242	7.082e-02	6.667e-10	2.198e-02	1.553e-01	8.220e-03
6	8370	5.041e-02	6.667e-10	2.198e-02	1.553e-01	1.326e-02
7	16962	3.542e-02	6.667e-10	2.198e-02	1.553e-01	8.201e-03

Table 5.4: *Example 2*: Rosenzweig-MacArthur RCDS (5.93) on the unit sphere, with reaction parameters and diffusion coefficients as defined in (5.94) and (5.95), respectively, with final time $T = 5$. Invariance analysis for the LSFEM solution. By solving the problem on a sequence of eight meshes Γ_i , $i = 0, \dots, 7$ with fixed timestep $\tau = 1e-3$, the solution stays in the invariant parallelogram Σ defined in (5.96) and depicted in Fig. 5.2 on all considered meshes.

where the functions $f_1(\mathbf{x}, t)$ and $f_2(\mathbf{x}, t)$ are chosen in such a way that the exact solution is known at all times. Although this example is beyond the scope of the present work, due to the space and time dependence of the reaction terms, we include it merely as a numerical test. For the reaction parameters and the diffusion coefficients, we choose

$$a = 1, \quad b = 1, \quad d_1 = \frac{1}{6}, \quad d_2 = \frac{1}{12}. \quad (5.105)$$

Moreover, we choose the following forcing terms

$$f_1(x, y, z, t) = xye^{-t}(1 + x^2y^2e^{-2t}) - 1, \quad f_2(x, y, z, t) = -x^3y^3ze^{-t} - 1; \quad (5.106)$$

and the following initial condition

$$u_0(x, y, z) = xy, \quad v_0(x, y, z) = -xyz, \quad (x, y, z) \in \Gamma; \quad (5.107)$$

such that the exact solution is given by

$$u(x, y, z, t) = xye^{-t}, \quad v(x, y, z, t) = -xyze^{-t}, \quad (x, y, z) \in \Gamma, \quad t \geq 0. \quad (5.108)$$

We solve the problem on the same sequence of meshes and timesteps considered in Example 1, with final time $T = 1$, for both the SFEM and the LSFEM, where the contributions due to the forcing terms f_k , $k = 1, 2$ are approximated with the standard and the lumped quadrature rule given by

$$\int_{\Gamma_h} I_h(f_k)\chi_i, \quad \text{and} \quad \int_{\Gamma_h} I_h(f_k\chi_i), \quad i = 1, \dots, N,$$

respectively. We observe that the standard quadrature rule is exact for piecewise linear functions, whilst the lumped one is only exact when the product of the functions is piecewise linear. For this reason, the LSFEM is expected to produce larger errors than the SFEM. The L^2 errors and experimental convergence rates are plotted in Figure 5.3 together with the LSFEM solution obtained on the finest mesh at the final time $T = 1$. As expected, the LSFEM exhibits slightly larger errors than the SFEM. Nonetheless, they have the same convergence rate, in agreement with our theoretical findings.

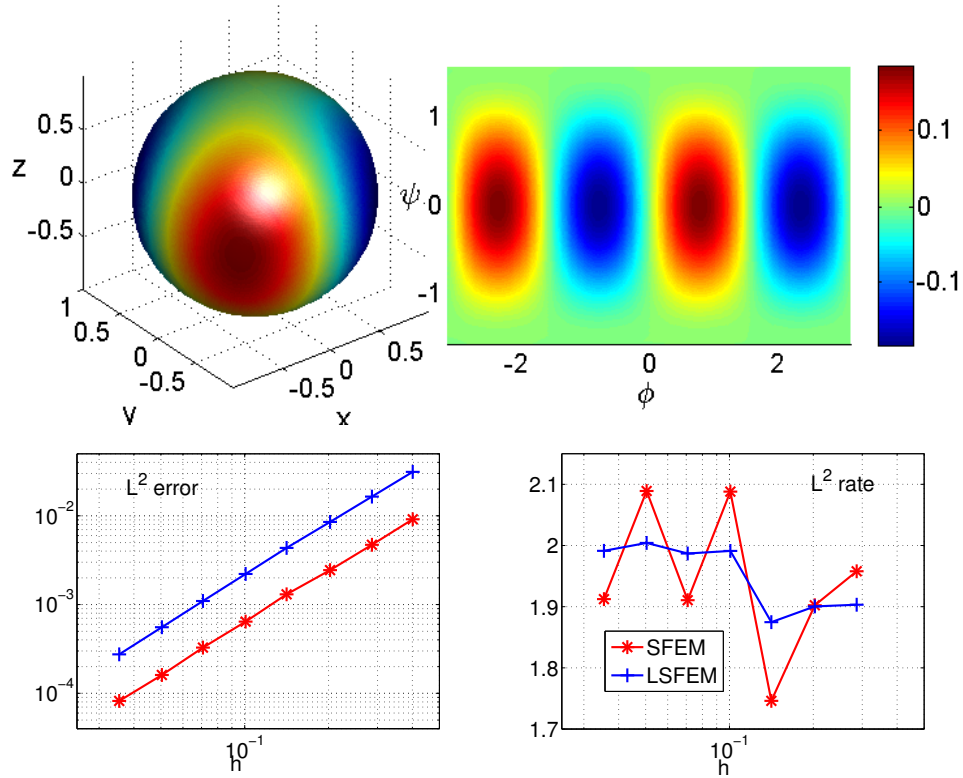


Figure 5.3: *Example 3*: RDS with *activator-depleted* kinetics (5.104) on the unit sphere with reaction parameters and diffusion coefficients as in (5.105), forcing terms (5.106), initial datum (5.107) and final time $T = 1$, solved on a mesh with $N = 16962$ nodes and timestep $\tau = 1.6e-3$. Top row: the u -component of the LSFEM solution at the final time $T = 1$ and its corresponding planar projection through spherical coordinates. Bottom row: convergence analysis of the SFEM and LSFEM. As predicted, the LSFEM retains the quadratic convergence rate of the SFEM.

Example 4: RCDS and pattern formation

In this example, we solve the RCDS with Rosenzweig-MacArthur kinetics in (5.93) with the following diffusion coefficients

$$\begin{pmatrix} d_{uu} & d_{uv} \\ d_{vu} & d_{vv} \end{pmatrix} = \begin{pmatrix} 100 & 100 \\ 400 & 500 \end{pmatrix}; \quad (5.109)$$

and the following reaction parameters

$$\alpha = \frac{11}{15}, \quad a = 1, \quad b = \frac{2}{3}, \quad c = \frac{2}{30}, \quad d = \frac{11}{1000}. \quad (5.110)$$

The final time is $T = 50$. This choice is equivalent, by rescaling time, to the parameter choice in Fig. 4A of [62] and leads to Turing instability, as proven therein. The initial condition is a spatially random perturbation, of amplitude $1e-5$, of the homogeneous steady

state $(u^*, v^*) := \left(\frac{d\alpha}{c-d}, \frac{a}{b} \left(1 - \frac{d\alpha}{c-d} \right) \left(\alpha + \frac{d\alpha}{c-d} \right) \right) = (0.1935, 1.0406)$. Since, in [62], the problem is solved on the square $[0, 200]^2$, we consider a sphere of the same area, thus with radius $R = \frac{100}{\sqrt{\pi}}$. We solve the system with SFEM and LSFEM on a mesh with $N = 16962$ gridpoints and timestep $\tau = 1e-2$. The solutions at the final time $T = 50$ are shown in Fig. 5.4(a) for SFEM and in Fig. 5.4(b) for LSFEM, respectively. We observe that (i) starting from the same initial datum, SFEM and LSFEM exhibit almost the same final pattern and (ii) with SFEM and LSFEM, we obtain the same kind of patterns obtained in [62] by using finite differences in space (on the planar domain).

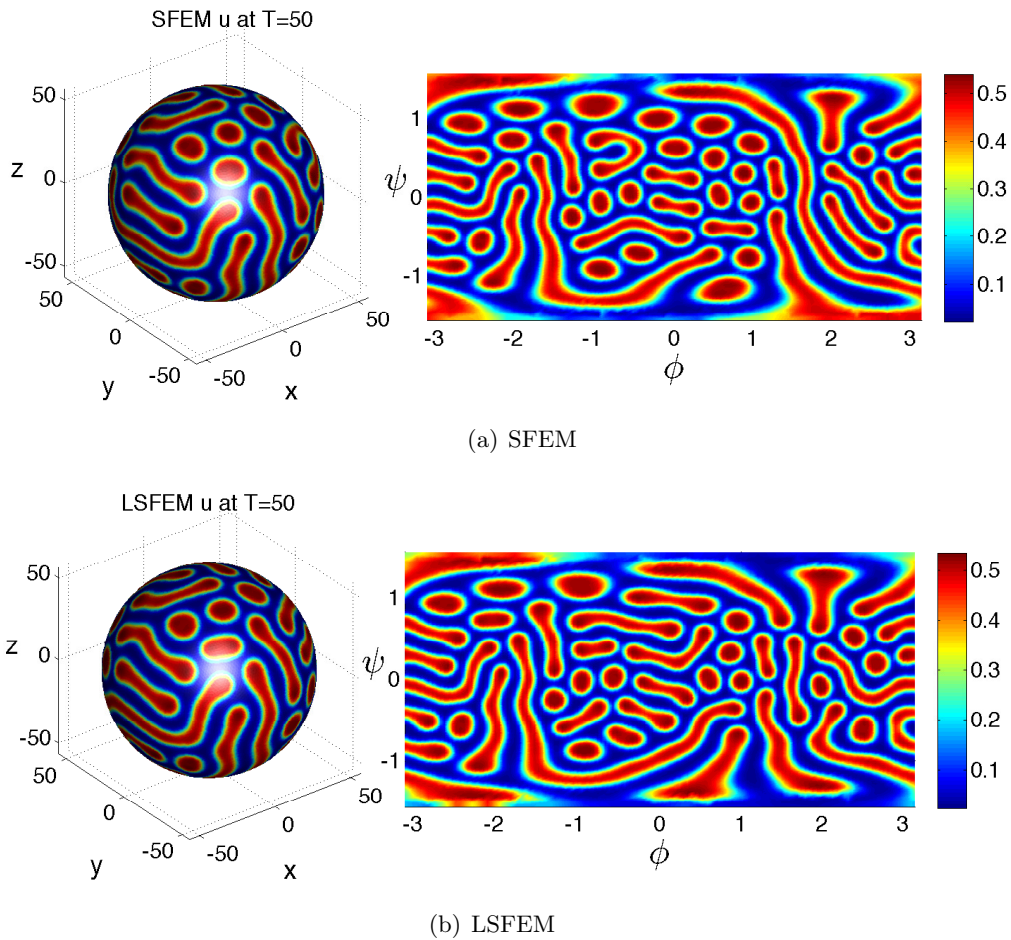


Figure 5.4: *Example 4*: Rosenzweig-MacArthur RCDS (5.93) on a sphere with radius $R = \frac{100}{\sqrt{\pi}}$ with diffusion coefficients (5.109), reaction parameters (5.110) and final time $T = 50$, solved on a triangular mesh of $N = 16962$ gridpoints, with timestep $\tau = 1e-2$. The picture shows the u -component of the SFEM (top row) and LSFEM (bottom row) numerical solutions at the final time $T = 50$. The planar deployments of the numerical solutions, through spherical coordinates (ϕ, ψ) , are shown on the right side of each panel.

5.5 Conclusions

We have presented a LSFEM spatial discretisation and a LSFEM-IMEX Euler full discretisation of RCDSs on \mathcal{C}^2 surfaces without boundary. Both discretisations preserve the invariant regions of the continuous PDE problem at the spatially- and fully discrete levels with no restriction on the meshsize. A timestep restriction depending on the Lipschitz constants of the kinetics is required at the fully discrete level, only.

In the next chapter we extend the LSFEM to solve RDSs on *evolving surfaces* and we prove sufficient conditions, that account for surface evolution, for the existence of invariant regions at the spatially and fully discrete levels.

Chapter 6

Linear heat equation and reaction-diffusion systems on evolving surfaces

6.1 Introduction

In this chapter we consider RDSs on surfaces which may be time-dependent, namely RDSs on *evolving surfaces*. RDSs on evolving surfaces arise from the mathematical modelling of numerous phenomena, among which we mention brain growth [85], cell migration [14], chemotaxis [46], developmental biology [92], and phase field modeling [136]. The growing interest toward PDEs on evolving surfaces has stimulated the development of several numerical methods for such problems, among which we mention embedding methods [12], kernel methods [59], surface finite element methods (SFEM) [40] and some of their recent variations and extensions [48, 56, 58, 66, 78, 127].

As well as for the case of RDSs on stationary surfaces, we care about existence of invariant regions. Once again, for scalar equations, the well-known notion of maximum principle is equivalent to the invariance of all the regions of the form $[0, M]$, $M > 0$. As mentioned in the previous chapter, for RDSs on a stationary surface, sufficient conditions have been found for a region to be invariant at the continuous level, see [125]. To the best of the authors' knowledge, the extension of these results to RDSs on evolving surfaces has not been considered in the literature. In this chapter we will focus on surfaces that evolve according to a prescribed *material velocity* field.

From a numerical point of view, it is interesting to understand if the invariant regions of the continuous problem are preserved under discretisation. In the previous chapter, based on our recent publications [55, 56] we proved that, for RDSs and RCDSs on stationary surfaces, the LSFEM, combined with the IMEX Euler method, preserves the invariant regions of the continuous problem. The purpose of the present chapter, based on an unpublished manuscript, is to extend these results to the case of evolving surfaces, in particular (i) we prove a semi- and a fully-discrete maximum principle for the heat equation with a linear source term and (ii) we provide sufficient conditions under which a region is invariant at the semi- and fully-discrete levels when a lumped evolving surface finite element method (LESFEM) and an IMEX Euler timestepping are considered. In particular we quantify the impact of surface evolution

(measured through the *dilation rate*) on the existence of invariant regions and we find that surface growth or contraction respectively fosters or inhibits the invariance of a given region in the phase-space.

Crucial in our analysis is the assumption that the mesh preserves the Delaunay property under evolution, which is not true for an arbitrary surface evolution law. A class of surface evolution laws for which the Delaunay property is automatically preserved is that of isotropic growth [93], which has biological applications [27, 86, 111, 117]. To the best of the authors' knowledge, an adaptive strategy for the preservation of the Delaunay property under a generic evolution law is still an open problem. An attempt in this direction is the work in [77]. For the special case of isotropic growth, we provide fully practical sufficient conditions for the existence of invariant regions at the semi- and fully-discrete levels. As an application of our general theory, we classify some classes of invariant regions, depending on the *growth rate* of the evolving surface, for two well-known RD models in the literature: the *activator-depleted* (or Schnakenberg, also known as the Brusselator model) and the Thomas models. Finally, we provide two numerical examples. In the first example we experimentally show that the LESFEM-IMEX Euler method, applied to the heat equation with a linear source term on a linearly growing sphere, exhibits optimal convergence rates in space and time. In the second example we consider the Thomas RDS on an exponentially growing Dupin ring cyclide thereby showing (i) the existence of invariant regions for the fully discretised model and (ii) the violation of this region in the absence of mass lumping.

The chapter is structured as follows. First, in Section 6.2 we recall (i) the derivation of RDSs on evolving surfaces and (ii) some basic notions about invariant regions and we introduce the notion of dilation rate, which is crucial in our analysis. In Section 6.3 we introduce the LESFEM for the space discretisation of RDSs on evolving surfaces and we carry out a fully-discrete scheme using the IMEX Euler timestepping. Section 6.4 deals with the characterisation of the dilation rate in terms of the material velocity. In particular, we compute exactly the dilation rate for the class of isotropic growth laws. In Section 6.5 we prove a semi- and a fully-discrete maximum principle for the linear heat equation on evolving surfaces with a linear source term. We prove, in Section 6.6, sufficient conditions for the existence of invariant regions for RDSs of arbitrarily many equations on evolving surfaces at the semi- and fully discrete levels. Section 6.7 presents some classes of invariant regions for the *activator-depleted*, the Thomas, the DIB and the Hodgkin-Huxley RD models on evolving surfaces, respectively. Numerical examples are presented in Section 6.8. Finally, in Section 6.9 we conclude and discuss our findings with an eye for future extensions of the present work.

6.2 Reaction-diffusion equations on an evolving surface

6.2.1 Preliminaries and basic results

In analogy with Definition 1 in Chapter 2 -with the bare addition of time dependence- let $T > 0$ be the final time and, for $t \in [0, T]$, let $\Gamma(t)$ be a \mathcal{C}^2 orientable surface in \mathbb{R}^3 , represented as the zero-level set of a signed distance function $d \in \mathcal{C}^1([0, T], \mathcal{C}^2(\mathbb{R}^3))$, i.e. $\Gamma(t) = \{\mathbf{x} \in \mathbb{R}^3 \mid d(\mathbf{x}, t) = 0\}$, with $\nabla d(\mathbf{x}, t) \neq 0$ for $t \in [0, T]$ and $\mathbf{x} \in \Gamma(t)$. Hence, the outward unit normal vector field on $\Gamma(t)$ is given by

$$\mathbf{n}(\mathbf{x}, t) := \frac{\nabla d(\mathbf{x}, t)}{\|\nabla d(\mathbf{x}, t)\|}, \quad t \in [0, T], \quad \mathbf{x} \in \Gamma(t), \quad (6.1)$$

where $\|\cdot\|$ denotes the Euclidean norm in \mathbb{R}^3 . Following [40, Section 5], we assume that there exists a mapping $G : \Gamma(0) \times [0, T] \rightarrow \mathbb{R}^3$, $G \in \mathcal{C}^1([0, T], \mathcal{C}^2(\Gamma(0)))$, such that for all $t \in [0, T]$, $G(\Gamma(0), t) = \Gamma(t)$ and $G(\cdot, t)$ is a diffeomorphism between $\Gamma(0)$ and $\Gamma(t)$. The space-time surface \mathcal{G}_T is defined by $\mathcal{G}_T := \bigcup_{t \in [0, T]} \Gamma(t) \times \{t\}$. The material velocity $\mathbf{v} : \mathcal{G}_T \rightarrow \mathbb{R}^3$ of $\Gamma(t)$ is defined by

$$\mathbf{v}(G(\mathbf{x}_0, t), t) = \frac{\partial G}{\partial t}(\mathbf{x}_0, t), \quad \mathbf{x}_0 \in \Gamma(0), \quad t \in [0, T]. \quad (6.2)$$

Vice-versa, if $\tilde{\mathbf{v}} \in \mathcal{C}^1([0, T], \mathcal{C}^2(\mathbb{R}^3))$ is an extension of \mathbf{v} , i.e. $\tilde{\mathbf{v}}(G(\mathbf{x}_0, t), t) = \mathbf{v}(G(\mathbf{x}_0, t), t)$ for $\mathbf{x}_0 \in \Gamma(0)$ and $t \in [0, T]$, the mapping G (and thus the time-dependent surface $\Gamma(t)$) is recovered by solving, for each $\mathbf{x}_0 \in \Gamma(0)$, the Cauchy problem

$$\begin{cases} \frac{\partial G}{\partial t}(\mathbf{x}_0, t) = \tilde{\mathbf{v}}(G(\mathbf{x}_0, t), t), & t \in [0, T]; \\ G(\mathbf{x}_0, 0) = \mathbf{x}_0. \end{cases} \quad (6.3)$$

For $t \in [0, T]$ and $\delta > 0$, let $U_\delta(t)$ be the open neighbourhood of $\Gamma(t)$ defined by

$$U_\delta(t) := \{(\mathbf{x}, t) \in \mathbb{R}^3 \times [0, T] : |d(\mathbf{x}, t)| < \delta\}. \quad (6.4)$$

In the following, we will write Γ instead of $\Gamma(t)$ to simplify the notation. Furthermore, let $\partial^\bullet g$ denote the material derivative of g defined by

$$\partial^\bullet g := \frac{\partial \tilde{g}}{\partial t} + \mathbf{v} \cdot \nabla \tilde{g}, \quad (6.5)$$

where ∇ is the standard gradient in \mathbb{R}^3 and \tilde{g} is any differentiable extension of g defined on a neighborhood of \mathcal{G}_T . Definition (6.5) is *intrinsic*, i.e. it does not depend on the choice of the extension \tilde{g} (see [41] for further details). The analysis of RDSs on evolving surfaces requires suitable function spaces, the *evolving Bochner spaces*, introduced in [2].

Definition 13 (Bochner spaces on evolving surfaces, see [2]). *Let $\Gamma(t)$, $t \in [0, T]$, be an evolving surface as defined in Section 6.2.1. For $t \in [0, T]$, let $B(t)$ be either $H^1(\Gamma(t))$ or $H^{-1}(\Gamma(t))$. The evolving Bochner spaces $L^2([0, T]; B(t))$ and $L^\infty([0, T]; B(t))$ are defined by*

$$L^2([0, T]; B(t)) = \left\{ f : [0, T] \rightarrow B(t) \mid \int_0^T \|f(t)\|_{B(t)}^2 dt < +\infty \right\};$$

$$L^\infty([0, T]; B(t)) = \left\{ f : [0, T] \rightarrow B(t) \mid \operatorname{ess\,sup}_{t \in [0, T]} \|f(t)\|_{B(t)} < +\infty \right\},$$

respectively. These spaces are Banach spaces with the respective norms

$$\|f\|_{L^2([0, T]; B(t))} := \left(\int_0^T \|f(t)\|_{B(t)}^2 dt \right)^{\frac{1}{2}}, \quad f \in L^2([0, T]; B(t));$$

$$\|f\|_{L^\infty([0, T]; B(t))} := \operatorname{ess\,sup}_{t \in [0, T]} \|f(t)\|_{B(t)}, \quad f \in L^\infty([0, T]; B(t)).$$

Let us recall some basic results from [40].

Lemma 14 (Integration by parts). *If $\mathbf{g} \in L^2([0, T]; H^1(\Gamma(t)))$, it holds that*

$$\int_{\partial\Gamma(t)} \mathbf{g} \cdot \boldsymbol{\mu} = \int_{\Gamma(t)} \nabla_{\Gamma} \cdot \mathbf{g} - \int_{\Gamma(t)} (\mathbf{g} \cdot \mathbf{n})(\nabla_{\Gamma} \cdot \mathbf{n}), \quad t \in [0, T], \quad (6.6)$$

where $\boldsymbol{\mu} : \partial\mathcal{R}(t) \rightarrow \mathbb{R}^3$ is the outward conormal unit vector on $\partial\mathcal{R}(t)$, i.e. normal to $\partial\mathcal{R}(t)$ and tangent to $\mathcal{R}(t)$. Specifically, if \mathbf{g} is tangent to Γ , i.e. $\mathbf{g} \cdot \mathbf{n} = 0$, it holds that

$$\int_{\partial\Gamma(t)} \mathbf{g} \cdot \boldsymbol{\mu} = \int_{\Gamma(t)} \nabla_{\Gamma} \cdot \mathbf{g}, \quad t \in [0, T]. \quad (6.7)$$

□

Lemma 15 (Transport formula). *If $g \in L^2([0, T]; H^1(\Gamma(t)))$ is such that $\partial^{\bullet}g \in L^2([0, T]; H^{-1}(\Gamma(t)))$, then it holds that*

$$\frac{d}{dt} \int_{\Gamma(t)} g = \int_{\Gamma(t)} (\partial^{\bullet}g + g \nabla_{\Gamma} \cdot \mathbf{v}), \quad t \in [0, T]. \quad (6.8)$$

□

Remark 14 (Surfaces without boundary). *Lemma 14 holds on surfaces with or without boundary, i.e. $\partial\Gamma(t) \neq \emptyset$ or $\partial\Gamma(t) = \emptyset$, respectively. Specifically, if $\partial\Gamma(t) = \emptyset$, then the boundary integral in (6.7), vanishes.*

6.2.2 Derivation of the reaction-diffusion model in strong form

Suppose we are given $r \in \mathbb{N}$ species $u_k : \Gamma(t) \rightarrow \mathbb{R}$, $k = 1, \dots, r$, and let $\mathbf{q}_k : \Gamma(t) \rightarrow \mathbb{R}^3$, $k = 1, \dots, r$, be their fluxes tangent to $\Gamma(t)$. We recall from [6] the derivation of a system of r equations for $\mathbf{u} := (u_1, \dots, u_r)$ that accounts for (i) the diffusion on the surface, (ii) the flux across the boundary (if non-empty) and (iii) the (possibly nonlinear) production rates $f_k(\mathbf{u})$, $k = 1, \dots, r$, of the given species. To this end, let $\mathcal{R}(0)$ be a portion of $\Gamma(0)$ and let $\mathcal{R}(t) = G(\mathcal{R}(0), t)$ be the portion of $\Gamma(t)$ corresponding to the initial portion $\mathcal{R}(0)$. We consider a mass balance on $\mathcal{R}(t)$ of the form

$$\frac{d}{dt} \int_{\mathcal{R}(t)} u_k = - \int_{\partial\mathcal{R}(t)} \mathbf{q}_k \cdot \boldsymbol{\mu} + \int_{\mathcal{R}(t)} f_k(\mathbf{u}), \quad k = 1, \dots, r, \quad t \in [0, T]. \quad (6.9)$$

Since the fluxes \mathbf{q}_k , $k = 1, \dots, r$, are tangent to $\Gamma(t)$, we can apply the integration-by-parts formula (6.7) to the first term on the right hand side of (6.9). Then (6.9) becomes

$$\frac{d}{dt} \int_{\mathcal{R}(t)} u_k = - \int_{\mathcal{R}(t)} \nabla_{\Gamma} \cdot \mathbf{q}_k + \int_{\mathcal{R}(t)} f_k(\mathbf{u}), \quad k = 1, \dots, r, \quad t \in [0, T]. \quad (6.10)$$

By applying the transport formula (6.8) to the left hand side of (6.10), we obtain

$$\int_{\mathcal{R}(t)} (\partial^{\bullet}u_k + u_k \nabla_{\Gamma} \cdot \mathbf{v} + \nabla_{\Gamma} \cdot \mathbf{q}_k) = \int_{\mathcal{R}(t)} f_k(\mathbf{u}), \quad k = 1, \dots, r, \quad t \in [0, T], \quad (6.11)$$

where \mathbf{v} is the material velocity defined in Section 6.2.1. Since $\mathcal{R}(t)$ is an arbitrary portion, we conclude that

$$\partial^{\bullet}u_k + u_k \nabla_{\Gamma} \cdot \mathbf{v} + \nabla_{\Gamma} \cdot \mathbf{q}_k = f_k(\mathbf{u}), \quad k = 1, \dots, r, \quad t \in [0, T]. \quad (6.12)$$

We assume \mathbf{q}_k corresponds to a diffusive flux according to Fick's law as follows:

$$\mathbf{q}_k = -d_k \nabla_{\Gamma} u_k, \quad k = 1, \dots, r, \quad (6.13)$$

where d_k , $k = 1, \dots, r$, are positive diffusivity constants. By inserting (6.13) into (6.12), we end up with the reaction-diffusion system of the form

$$\partial^{\bullet} u_k + u_k \nabla_{\Gamma} \cdot \mathbf{v} = d_k \Delta_{\Gamma} u_k + f_k(\mathbf{u}), \quad k = 1, \dots, r, \quad t \in [0, T]. \quad (6.14)$$

6.2.3 Invariant regions and maximum principle

In this section we recall basic notions concerning invariant regions for systems of the form (6.14) and conjecture a sufficient condition under which system (6.14) possesses an invariant region. To this end, we give the following definitions.

Definition 14 (Dilation rates). *The minimum and maximum instantaneous dilation rates are defined by*

$$H_{min}^*(t) := \min_{\mathbf{x} \in \Gamma(t)} \nabla_{\Gamma} \cdot \mathbf{v}(\mathbf{x}, t) \quad \text{and} \quad H_{max}^*(t) := \max_{\mathbf{x} \in \Gamma(t)} \nabla_{\Gamma} \cdot \mathbf{v}(\mathbf{x}, t), \quad t \in [0, T], \quad (6.15)$$

respectively. When the minimum and maximum instantaneous dilation rates coincide, we call $H^*(t) := H_{min}^*(t) = H_{max}^*(t)$ the instantaneous dilation rate. The minimum and maximum global dilation rates are defined by

$$\mu_{min}^* := \min_{t \in [0, T]} H_{min}^*(t) \quad \text{and} \quad \mu_{max}^* := \max_{t \in [0, T]} H_{max}^*(t), \quad (6.16)$$

respectively. When the minimum and maximum global dilation rates coincide, we call $\mu^* := \mu_{min}^* = \mu_{max}^*$ the global dilation rate.

As in the previous chapter, we are interested in invariant regions for the RDS (6.14). The definition 11 of invariant regions holds unchanged in the case of evolving surfaces considered here. For scalar RDSs ($r = 1$), we consider the following notions of maximum and minimum-maximum principles.

Definition 15 (Maximum and minimum-maximum principles). *Consider the scalar case $r = 1$ in the RDS (6.14) in strong formulation, let $u(\mathbf{x}, t)$ be its solution. The minimum-maximum principle holds if, for any initial condition $u(\cdot, 0)$, the solution fulfils*

$$\min \left\{ 0, \min_{\mathbf{y} \in \Gamma(0)} u(\mathbf{y}, 0) \right\} \leq u(\mathbf{x}, t) \leq \max \left\{ 0, \max_{\mathbf{y} \in \Gamma(0)} u(\mathbf{y}, 0) \right\}, \quad (\mathbf{x}, t) \in \mathcal{G}_T. \quad (6.17)$$

For nonnegative initial conditions $u(\cdot, 0) \geq 0$, the minimum-maximum principle reduces to the following: maximum principle:

$$0 \leq u(\mathbf{x}, t) \leq \max_{\mathbf{y} \in \Gamma(0)} u(\mathbf{y}, 0), \quad (\mathbf{x}, t) \in \mathcal{G}_T. \quad (6.18)$$

The above definition of maximum and minimum-maximum principles is analogous to the one considered in the case of stationary surfaces (see Definition 10 and Remark 8), but includes the time-dependence of Γ . As well as in the case of stationary surfaces, the maximum and minimum-maximum principles can be regarded in terms of invariant regions, see Remark 12. We focus our attention on regions $\Sigma \subset \mathbb{R}^r$ of hyper rectangular shape, that is to say of the form

$$\Sigma := \prod_{k=1}^r [\underline{\sigma}_k, \bar{\sigma}_k], \quad (6.19)$$

where $\underline{\sigma}_k \in \mathbb{R} \cup \{-\infty\}$ and $\bar{\sigma}_k \in \mathbb{R} \cup \{+\infty\}$ for all $k = 1, \dots, r$. For instance, if $\underline{\sigma}_k = 0$ and $\bar{\sigma}_k = +\infty$ for all $k = 1, \dots, r$, then Σ is the positive orthant in \mathbb{R}^r , which means that the solution of the RDS stays positive at all times. Consider the $(r - 1)$ -dimensional hyperfaces

$$\underline{\Sigma}_k := \Sigma \cap \{u_k = \underline{\sigma}_k\}, \quad \bar{\Sigma}_k := \Sigma \cap \{u_k = \bar{\sigma}_k\}, \quad k = 1, \dots, r.$$

For $k = 1, \dots, r$, we define the constants

$$\bar{\mu}_k^* := \begin{cases} \mu_{min}^* & \text{if } \bar{\sigma}_k \geq 0; \\ \mu_{max}^* & \text{if } \bar{\sigma}_k < 0, \end{cases} \quad \underline{\mu}_k^* := \begin{cases} \mu_{max}^* & \text{if } \underline{\sigma}_k \geq 0; \\ \mu_{min}^* & \text{if } \underline{\sigma}_k < 0, \end{cases} \quad (6.20)$$

where μ_{min}^* and μ_{max}^* are defined in (6.16).

Next, we conjecture a criterion under which a hyper-rectangle is invariant for system (6.14). This criterion holds true in the stationary cases (when $\mu^* = 0$): (i) when Γ is a stationary monodimensional domain in \mathbb{R} (see [123]), (ii) when Γ is a stationary k -dimensional domain in \mathbb{R}^k , $k \in \mathbb{N}$ (see [25]) and (iii) when Γ is a stationary Riemannian manifold without boundary (see [125]). In the case of isotropically evolving flat domains, the invariance of the positive orthant was studied in [134]. To the best of the author's knowledge, the case of evolving surfaces has not been studied at the continuous level. Hence, we introduce at the continuous level the following conjecture.

Conjecture 1. *Let Σ be a hyper-rectangle as in (6.19) in the phase space of (6.14) and let \mathbf{f} be Lipschitz on Σ . If*

$$f_k(\mathbf{u}) < \bar{\mu}_k^* \bar{\sigma}_k, \quad \mathbf{u} \in \bar{\Sigma}_k \cap \mathbb{R}^r, \quad k = 1, \dots, r; \quad (6.21)$$

$$f_k(\mathbf{u}) > \underline{\mu}_k^* \underline{\sigma}_k, \quad \mathbf{u} \in \underline{\Sigma}_k \cap \mathbb{R}^r, \quad k = 1, \dots, r, \quad (6.22)$$

then Σ is an invariant region for (6.14). In particular, when $\bar{\sigma}_k = +\infty$ and $\underline{\sigma}_k = -\infty$, then $\bar{\Sigma}_k \cap \mathbb{R}^r$ and $\underline{\Sigma}_k \cap \mathbb{R}^r$ are respectively empty, and so (6.21) and (6.22) are automatically fulfilled, respectively.

Notice that on stationary surfaces, since $\bar{\mu}_k^* = \underline{\mu}_k^* = 0$, then conditions (6.21)-(6.22) reduce to the inward flux condition considered in [125, Chapter 4]. In the next Section 4, we will prove the discrete counterpart of Conjecture 1 obtained by discretising the RDS in space with the lumped version of the ESFEM method [40] and IMEX Euler in time.

6.2.4 Derivation of the variational formulation

Following [6], we derive the variational formulation of system (6.14). To this end, for each $t \in [0, T]$ we multiply the equations of (6.14) by respective test functions $\varphi_1, \dots, \varphi_r \in L^2([0, T]; H^1(\Gamma(t)))$ with $\partial^\bullet \varphi_1, \dots, \partial^\bullet \varphi_r \in L^2([0, T]; H^{-1}(\Gamma(t)))$ and integrate over $\Gamma(t)$:

$$\int_{\Gamma(t)} (\varphi_k \partial^\bullet u_k + \varphi_k u_k \nabla_\Gamma \cdot \mathbf{v} - \varphi_k f_k(\mathbf{u})) = d_k \int_{\Gamma(t)} \varphi_k \Delta_\Gamma u_k, \quad (6.23)$$

for all $k = 1, \dots, r$. By applying the Green formula (2.7) to the right hand side of (6.23) we obtain

$$\int_{\Gamma(t)} (\varphi_k \partial^\bullet u_k + \varphi_k u_k \nabla_\Gamma \cdot \mathbf{v} - \varphi_k f_k(\mathbf{u})) + d_k \int_{\Gamma(t)} \nabla_\Gamma \varphi_k \cdot \nabla_\Gamma u_k = d_k \int_{\partial\Gamma(t)} \varphi_k \nabla_\Gamma u_k \cdot \boldsymbol{\mu}, \quad (6.24)$$

for all $k = 1, \dots, r$. We assume that either $\Gamma(t)$ has no boundary, i.e. $\partial\Gamma(t) = \emptyset$, or homogeneous Neumann boundary condition are enforced, i.e. $\nabla_\Gamma u_k \cdot \boldsymbol{\mu} = 0$ on $\partial\Gamma(t)$, so that the last term in (6.24) vanishes (see Remark 14). Furthermore, by observing that $\partial^\bullet(\varphi_k u_k) = \varphi_k \partial^\bullet u_k + u_k \partial^\bullet \varphi_k$, (6.24) becomes

$$\int_{\Gamma(t)} \partial^\bullet(\varphi_k u_k) = \int_{\Gamma(t)} (u_k \partial^\bullet \varphi_k - \varphi_k u_k \nabla_\Gamma \cdot \mathbf{v} + \varphi_k f_k(\mathbf{u})) - d_k \int_{\Gamma(t)} \nabla_\Gamma \varphi_k \cdot \nabla_\Gamma u_k, \quad (6.25)$$

for all $k = 1, \dots, r$. By applying the transport property to the first term on the left hand side of (6.25), we have

$$\frac{d}{dt} \int_{\Gamma(t)} \varphi_k u_k - \int_{\Gamma(t)} u_k \partial^\bullet \varphi_k = \int_{\Gamma(t)} \varphi_k f_k(\mathbf{u}) - d_k \int_{\Gamma(t)} \nabla_\Gamma \varphi_k \cdot \nabla_\Gamma u_k, \quad (6.26)$$

for all $k = 1, \dots, r$. Therefore, the variational formulation seeks to find $u_1, \dots, u_r \in L^2([0, T]; H^1(\Gamma(t)))$ with $\partial^\bullet u_1, \dots, \partial^\bullet u_r \in L^2([0, T]; H^{-1}(\Gamma(t)))$ such that, for each $t \in [0, T]$,

$$\frac{d}{dt} \int_{\Gamma(t)} u_k \varphi_k - \int_{\Gamma(t)} u_k \partial^\bullet \varphi_k + d_k \int_{\Gamma(t)} \nabla_\Gamma u_k \cdot \nabla_\Gamma \varphi_k = \int_{\Gamma(t)} f_k(\mathbf{u}) \varphi_k, \quad (6.27)$$

for all $\varphi_1, \dots, \varphi_r \in L^2([0, T]; H^1(\Gamma(t)))$ with $\partial^\bullet \varphi_1, \dots, \partial^\bullet \varphi_r \in L^2([0, T]; H^{-1}(\Gamma(t)))$.

6.3 Lumped evolving surface finite element method

Following the evolving surface finite element method (ESFEM) studied in [6] for the approximation of the variational problem (6.27), and extending to evolving surfaces the LSFEM presented in the previous chapter, we present a lumped evolving surface finite element method (LESFEM).

6.3.1 Surface triangulation and some definitions

Following [38], given $h > 0$, called *meshsize*, a triangulation $\Gamma_h(t)$ of the evolving surface $\Gamma(t)$ is defined by

$$\Gamma_h(t) = \bigcup_{Z(t) \in \mathcal{Z}_h(t)} Z(t),$$

where $\mathcal{Z}_h(t)$ is a set of evolving triangles, with $\mathbf{x}_i(t), i = 1, \dots, N \in \mathbb{N}$, being the overall evolving nodes, such that

- The nodes evolve with the exact material velocity, i.e. $\dot{\mathbf{x}}_i(t) = \mathbf{v}(\mathbf{x}_i(t), t)$ for $t \in [0, T]$ and $i = 1, \dots, N$;
- For all $t \in [0, T]$ and for any two distinct triangles $Z_1(t)$ and $Z_2(t)$ in $\mathcal{Z}_h(t)$, the intersection $Z_1(t) \cap Z_2(t)$ is either empty, or a node, or a complete edge;
- For all $t \in [0, T]$ and $Z(t) \in \mathcal{Z}_h(t)$, $Z(t) \subset U(t)$, where $U(t)$ is the Fermi stripe of $\Gamma(t)$ as defined in Lemma 1;
- For all $t \in [0, T]$, the normal projection $\mathbf{a}(\cdot, t) : U_\delta(t) \rightarrow \Gamma(t)$ defined in Lemma 1 is a one-to-one mapping between $\Gamma_h(t)$ and $\Gamma(t)$, i.e. $\mathbf{a}(\Gamma_h(t), t) = \Gamma(t)$.

Notice that, for the special case of stationary surfaces, i.e. $\mathbf{v}(\mathbf{x}, t) = 0$ for all $(\mathbf{x}, t) \in \mathbb{R}^3 \times [0, T]$, the above definition of evolving triangulations reduces to the definition of stationary triangulations given in Section 2.5.1. We assume that, for each $t \in [0, T]$, $\Gamma_h(t)$ meets the Delaunay condition (4.15). This assumption does not hold true for arbitrary evolution laws, but it does for any isotropic growth law, as we will show in a later section. The space-time triangulated surface $\mathcal{G}_{h,T}$ is defined by

$$\mathcal{G}_{h,T} := \bigcup_{t \in [0, T]} \Gamma_h(t) \times \{t\}.$$

Since $\Gamma_h(t)$ is piecewise planar, there exists a time-differentiable mapping $G_h : \Gamma_h(0) \times [0, T] \rightarrow \mathbb{R}^3$ such that, for all $t \in [0, T]$, $G_h(\Gamma_h(0), t) = \Gamma_h(t)$ and, for every facet $Z \in \mathcal{Z}_h$, $G_h(\cdot, t)$ is a diffeomorphism between $Z(0)$ and $Z(t)$.

For a fixed time $t \in [0, T]$, let $\mathbb{V}_h(t)$ be the space of piecewise linear functions on $\Gamma_h(t)$ defined by

$$\mathbb{V}_h(t) := \{\varphi \in \mathcal{C}^0(\Gamma_h(t)) \mid \varphi|_Z \text{ is linear affine for each } Z \in \mathcal{Z}_h\}. \quad (6.28)$$

Let \mathbb{V}_h be the space of time-dependent, spatially piecewise linear functions defined by

$$\mathbb{V}_h := \{\varphi : \mathcal{G}_{h,T} \rightarrow \mathbb{R} \mid \varphi(\cdot, t) \in \mathbb{V}_h(t) \text{ for each } t \in [0, T]\}. \quad (6.29)$$

Given $t \in [0, T]$ and a function $\eta \in \mathcal{C}^0(\Gamma_h(t))$, its linear interpolant $I_h\eta$ is the unique function in $\mathbb{V}_h(t)$ such that

$$I_h\eta(\mathbf{x}_i(t)) = \eta(\mathbf{x}_i(t)), \quad i = 1, \dots, N.$$

The discrete material derivative of a sufficiently smooth function $U \in \mathbb{V}_h$ is defined by

$$\partial_h^\bullet U := \frac{\partial U}{\partial t} + I_h(\mathbf{v}) \cdot \nabla U, \quad (\mathbf{x}, t) \in \mathcal{G}_{h,T},$$

where \mathbf{v} is the material velocity. For our purposes, we define the discrete counterpart of the dilation rates introduced in Definition 14.

Definition 16 (Discrete dilation rates). *The minimum and maximum discrete instantaneous dilation rates are defined by*

$$H_{min}(t) := \operatorname{ess\,inf}_{\mathbf{x} \in \Gamma_h(t)} \nabla_{\Gamma_h} \cdot I_h(\mathbf{v})(\mathbf{x}, t), \quad t \in [0, T]; \quad (6.30)$$

$$H_{max}(t) := \operatorname{ess\,sup}_{\mathbf{x} \in \Gamma_h(t)} \nabla_{\Gamma_h} \cdot I_h(\mathbf{v})(\mathbf{x}, t), \quad t \in [0, T], \quad (6.31)$$

respectively. When the minimum and maximum discrete instantaneous dilation rates coincide, we call $H(t) := H_{min}(t) = H_{max}(t)$ the discrete instantaneous dilation rate. The minimum and maximum discrete global dilation rates are defined by

$$\mu_{min} := \min_{t \in [0, T]} H_{min}(t), \quad \mu_{max} := \max_{t \in [0, T]} H_{max}(t), \quad (6.32)$$

respectively. When the minimum and maximum discrete global dilation rates coincide, we call $\mu := \mu_{min} = \mu_{max}$ the discrete global dilation rate.

For every $i = 1, \dots, N$, the i -th Lagrange basis function χ_i is the unique \mathbb{V}_h function such that

$$\chi_i(\mathbf{x}_j(t), t) = \delta_{ij}, \quad t \in [0, T], \quad i, j = 1, \dots, N, \quad (6.33)$$

where δ_{ij} is the usual Kronecker symbol. The components $U_1, \dots, U_r \in \mathbb{V}_h$ of the spatially discrete solution may be expressed in the Lagrange basis as

$$U_k(\mathbf{x}, t) = \sum_{i=1}^N \xi_{k,i}(t) \chi_i(\mathbf{x}, t), \quad (\mathbf{x}, t) \in \mathcal{G}_{h,T}, \quad k = 1, \dots, r. \quad (6.34)$$

6.3.2 Preliminary results on triangulated surfaces

We recall from [38] the following property of the basis functions.

Lemma 16 (Transport property of the basis functions). *The basis functions χ_i , $i = 1, \dots, N$, defined in (6.33) fulfil*

$$\partial_h^\bullet \chi_i = 0, \quad i = 1, \dots, N. \quad (6.35)$$

Hence, for the functions U_k , $k = 1, \dots, r$ defined in (6.34) it holds that

$$\partial_h^\bullet U_k(\mathbf{x}, t) = \sum_{i=1}^N \dot{\xi}_{k,i}(t) \chi_i(\mathbf{x}, t), \quad (\mathbf{x}, t) \in \mathcal{G}_{h,T}, \quad k = 1, \dots, r. \quad (6.36)$$

□

We recall from [40, Lemma 5.6 and Remark 5.7] the following preliminary result.

Lemma 17 (Leibniz formula on triangulated surfaces). *For any time-differentiable $U, V \in \mathbb{V}_h$, it holds that*

$$\frac{d}{dt} \int_{\Gamma_h(t)} UV = \int_{\Gamma_h(t)} \partial^\bullet UV + \int_{\Gamma_h(t)} U \partial^\bullet V + \int_{\Gamma_h(t)} UV \nabla_{\Gamma_h} \cdot I_h(\mathbf{v}). \quad (6.37)$$

□

6.3.3 Lumped evolving surface finite element method

The lumped evolving surface finite element method (LESFEM), applied to the variational formulation (6.27), seeks to find $U_1, \dots, U_r \in \mathbb{V}_h$ such that

$$\frac{d}{dt} \int_{\Gamma_h(t)} I_h(U_k \chi_i) - \int_{\Gamma_h(t)} U_k \partial_h^\bullet \chi_i + d_k \int_{\Gamma_h(t)} \nabla_{\Gamma_h} U_k \cdot \nabla_{\Gamma_h} \chi_i = \int_{\Gamma_h(t)} I_h(f_k(\mathbf{U}) \chi_i), \quad (6.38)$$

for all $k = 1, \dots, r$ and $i = 1, \dots, N$. Thanks to the transport property (6.35) of the basis functions, formulation (6.38) is equivalent to: find $U_1, \dots, U_r \in \mathbb{V}_h$ such that

$$\frac{d}{dt} \int_{\Gamma_h(t)} I_h(U_k \chi_i) + d_k \int_{\Gamma_h(t)} \nabla_{\Gamma_h} U_k \cdot \nabla_{\Gamma_h} \chi_i = \int_{\Gamma_h(t)} I_h(f_k(\mathbf{U}) \chi_i), \quad (6.39)$$

for all $k = 1, \dots, r$ and $i = 1, \dots, N$. The LESFEM method (6.39) differs from the evolving surface finite element method (ESFEM) in [6] due to the presence of the interpolant operator on the first and the last terms in (6.39). By expressing U_1, \dots, U_r according to (6.34), the matrix form of (6.39) is

$$\frac{d}{dt} (M \boldsymbol{\xi}_k) + d_k A \boldsymbol{\xi}_k = M f_k(\boldsymbol{\xi}_1, \dots, \boldsymbol{\xi}_r), \quad k = 1, \dots, r, \quad (6.40)$$

where A and M are the (time-dependent) stiffness and lumped mass matrices defined by

$$A_{ij}(t) = \int_{\Gamma_h(t)} \nabla_{\Gamma_h} \chi_i \cdot \nabla_{\Gamma_h} \chi_j, \quad i, j = 1, \dots, N;$$

$$M_{ij}(t) = \int_{\Gamma_h(t)} I_h(\chi_i \chi_j) = \begin{cases} \int_{\Gamma_h(t)} \chi_i & \text{if } i = j; \\ 0 & \text{if } i \neq j, \end{cases} \quad i, j = 1, \dots, N,$$

for $t \in [0, T]$, respectively. Notice that the lumped mass matrix $M(t)$ is diagonal. The Delaunay condition (4.15) holds iff

$$A_{ij}(t) \leq 0, \quad i \neq j, \quad t \in [0, T]. \quad (6.41)$$

Since, for all $t \in [0, T]$, $M(t)$ is diagonal, we obtain the following time-dependent counterparts of relations (4.18)-(4.19):

$$(M + sA)^{-1} M(t) \geq \mathbf{0}, \quad s \geq 0, \quad t \in [0, T]; \quad (6.42)$$

$$(M + sA)^{-1} M(t) \mathbf{1} = \mathbf{1}, \quad s \geq 0, \quad t \in [0, T], \quad (6.43)$$

see Section 4.5.1 for the derivation.

6.3.4 Time discretisation

We are now concerned with the time discretisation of the spatially discrete system (6.40) arising from the LESFEM. We discretise system (6.40) by means of the IMEX Euler method, i.e by treating diffusion implicitly and reaction terms explicitly. To this end, let $\tau > 0$ be a timestep, let $t_n := n\tau$ for all $n = 0, \dots, N_T$ with $N_T = \lfloor \frac{T}{\tau} \rfloor$, let A^n and M^n be the stiffness and lumped mass matrices at time t_n , respectively, let $(\boldsymbol{\xi}_1^n, \dots, \boldsymbol{\xi}_r^n)$ be the coefficients of the

numerical solution at time t_n , and let $\mathbf{f}_k^n := f_k(\boldsymbol{\xi}_1^n, \dots, \boldsymbol{\xi}_n^n)$ for each $k = 1, \dots, r$. If $(\boldsymbol{\xi}_1^0, \dots, \boldsymbol{\xi}_r^0)$ are the coefficients of the spatially discrete initial datum, the IMEX Euler time discretisation of (6.40) is

$$\frac{M^{n+1}\boldsymbol{\xi}_k^{n+1} - M^n\boldsymbol{\xi}_k^n}{\tau} + d_k A^{n+1}\boldsymbol{\xi}_k^{n+1} = M^n \mathbf{f}_k^n, \quad k = 1, \dots, r, \quad n = 0, \dots, N_T, \quad (6.44)$$

or equivalently

$$\boldsymbol{\xi}_k^{n+1} = (M^{n+1} + \tau d_k A^{n+1})^{-1} M^n (\boldsymbol{\xi}_k^n + \tau \mathbf{f}_k^n), \quad k = 1, \dots, r, \quad n = 0, \dots, N_T. \quad (6.45)$$

6.4 Characterisation of surface growth

The purpose of this section is to characterise surface growth in terms of the material velocity \mathbf{v} , with specific regard to isotropic growth. In fact, the lumped mass $M(t)$ and stiffness $A(t)$ matrices depend on \mathbf{v} . In particular:

1. For an arbitrary triangulated surface that evolves with an arbitrary material velocity, we bound the time derivative $\frac{dM}{dt}$ of the lumped mass matrix in terms of the constants μ_{min} and μ_{max} defined in (6.32), i.e. in terms of the divergence $\nabla_{\Gamma_h} \cdot I_h(\mathbf{v})$ of the discrete material velocity. We will need this result to prove a sufficient condition for the existence of invariant regions for the semi- and fully-discrete schemes;
2. For an arbitrary smooth or triangulated surface that evolves with an arbitrary material velocity, we characterise the velocity flows $\nabla_{\Gamma} \cdot \mathbf{v}$ and $\nabla_{\Gamma_h} \cdot I_h(\mathbf{v})$ in terms of the mappings G and G_h introduced in Sections 6.2.1 and 6.3.1, respectively;
3. For an arbitrary smooth or triangulated surface that evolves *isotropically* in space, that is

$$\mathbf{v}(\mathbf{x}, t) = S(t)\mathbf{x}, \quad (\mathbf{x}, t) \in \mathbb{R}^3 \times [0, T], \quad (6.46)$$

where $S : [0, T] \rightarrow \mathbb{R}$ is an arbitrary smooth function, we compute exactly $\nabla_{\Gamma} \cdot \mathbf{v}$ and $\nabla_{\Gamma_h} \cdot I_h(\mathbf{v})$ in terms of \mathbf{v} . This result will yield a fully practical criterion to detect the invariant regions of a given RDS in the case of isotropic surface evolution.

6.4.1 Bounding the rate of change of the mass matrix in terms of the dilation rates

In this section we bound the time derivative $\frac{dM}{dt}$ of M in terms of the discrete dilation rates defined in (6.32). To this end, we prove the following characterisation of $\frac{dM}{dt}$.

Lemma 18 (Transport formula for the lumped mass matrix M). *The entries of the lumped mass matrix M fulfil the following property*

$$\frac{d}{dt} \int_{\Gamma_h(t)} I_h(\chi_i \chi_j) = \int_{\Gamma_h(t)} I_h(\chi_i \chi_j) \nabla_{\Gamma_h} \cdot I_h(\mathbf{v}), \quad i = 1, \dots, N. \quad (6.47)$$

Proof. By choosing $U = I_h(\chi_i \chi_j)$ for any $i, j = 1, \dots, N$ and $V = 1$ in the Leibniz formula (6.37) we have

$$\frac{d}{dt} \int_{\Gamma_h(t)} I_h(\chi_i \chi_j) = \int_{\Gamma_h(t)} \partial^\bullet I_h(\chi_i \chi_j) + \int_{\Gamma_h(t)} I_h(\chi_i \chi_j) \nabla_{\Gamma_h} \cdot I_h(\mathbf{v}). \quad (6.48)$$

Now, if $i = j$, then $I_h(\chi_i \chi_j) = \chi_i$, otherwise, if $i \neq j$, $I_h(\chi_i \chi_j) = 0$. Then, from the transport property (6.35) we have $\partial^\bullet I_h(\chi_i \chi_j) = 0$ for all $i, j = 1, \dots, N$. Equation (6.48) thus implies the desired result (6.47). \square

In some proofs we will need the following corollary of Lemma 18.

Corollary 2 (Consequence of the transport formula for the lumped mass matrix M). *The diagonal matrix $\frac{dM}{dt}$ fulfils the estimates*

$$\mu_{min} m_{ii}(t) \leq \frac{dm_{ii}}{dt}(t) \leq \mu_{max} m_{ii}(t), \quad i = 1, \dots, N, \quad t \in [0, T], \quad (6.49)$$

where μ_{min} and μ_{max} are defined in (6.32). \square

6.4.2 Characterising velocity flows in terms of the mappings G and G_h

We wish to characterise the continuous and discrete velocity flows $\nabla_\Gamma \cdot \mathbf{v}$ and $\nabla_{\Gamma_h} \cdot I_h(\mathbf{v})$ in terms of the mappings G and G_h introduced in Sections 6.2.1 and 6.3.1, respectively, for arbitrary smooth or triangulated surfaces that evolve under an arbitrary material velocity. To this end, let $\Gamma(t)$ be an arbitrary evolving smooth surface and let (A, X) be any local parametrisation of $\Gamma(0)$, where $A \subset \mathbb{R}^2$ is an open connected set and $X : A \rightarrow \Gamma(0)$ is a differentiable map such that its Jacobian J is full-rank on A . Let B be a measurable subset of A . For all t , the portion $X(B)$ of $\Gamma(0)$ evolves into $G(X(B), t) \subset \Gamma(t)$.

By choosing $f(\mathbf{x}, t) = 1$ for each $(\mathbf{x}, t) \in \mathcal{G}_T$ in the transport formula (6.8), we have

$$\frac{d}{dt} \int_{G(X(B), t)} 1 = \int_{G(X(B), t)} \nabla_\Gamma \cdot \mathbf{v}. \quad (6.50)$$

Let \hat{e}_i , $i = 1, 2, 3$, be the standard basis vectors in \mathbb{R}^3 . For $(\boldsymbol{\theta}, t) \in B \times [0, T]$, let $J(\mathbf{x}, t) \in \mathbb{R}^{2,3}$ be the (spatial) Jacobian of the function $G(X(\boldsymbol{\theta}), t)$ and let

$$\tilde{J}(\boldsymbol{\theta}, t) := \det \begin{bmatrix} \hat{e}_1 & \hat{e}_2 & \hat{e}_3 \\ \vdots & \vdots & \vdots \\ J(\boldsymbol{\theta}, t) \end{bmatrix} \in \mathbb{R}^3. \quad (6.51)$$

The surface integrals in (6.50) can be written as integrals on the planar domain B by using the parametrisation $G(X(\cdot), t) : B \rightarrow G(X(B), t)$. Hence, (6.50) becomes

$$\frac{d}{dt} \int_B \|\tilde{J}(\boldsymbol{\theta}, t)\| d\boldsymbol{\theta} = \int_B \nabla_\Gamma \cdot \mathbf{v}(G(X(\boldsymbol{\theta}), t)) \|\tilde{J}(\boldsymbol{\theta}, t)\| d\boldsymbol{\theta}, \quad (6.52)$$

where $\|\cdot\|$ denotes the Euclidean norm in \mathbb{R}^3 , or equivalently,

$$\int_B \frac{d}{dt} \|\tilde{J}(\boldsymbol{\theta}, t)\| d\boldsymbol{\theta} = \int_B \nabla_\Gamma \cdot \mathbf{v}(G(X(\boldsymbol{\theta}), t)) \|\tilde{J}(\boldsymbol{\theta}, t)\| d\boldsymbol{\theta}. \quad (6.53)$$

Since (6.53) holds for any measurable subset B of A , then it holds that

$$\frac{d}{dt} \|\tilde{J}(\boldsymbol{\theta}, t)\| = \nabla_{\Gamma} \cdot \mathbf{v}(G(X(\boldsymbol{\theta}), t)) \|\tilde{J}(\boldsymbol{\theta}, t)\|. \quad (6.54)$$

By applying the chain rule, (6.54) is equivalent to

$$\nabla_{\Gamma} \cdot \mathbf{v}(G(X(\boldsymbol{\theta}), t)) = \frac{d}{dt} \ln \|\tilde{J}(\boldsymbol{\theta}, t)\|. \quad (6.55)$$

Given any triangulated surface $\Gamma_h(t)$ (which evolves under the discrete velocity field $I_h(\mathbf{v})$), we notice that every facet $Z(t) \in \mathcal{Z}_h(t)$ is smooth and thus parametrisable. For any facet of the initial triangulated surface, $Z(0) \in \mathcal{Z}_h(0)$, let (A, X) be a parametrisation of $Z(0)$, as described above. For $(\boldsymbol{\theta}, t) \in A \times [0, T]$, let $J_h(\boldsymbol{\theta}, t) \in \mathbb{R}^{2,3}$ be the Jacobian of the function $G_h(X(\boldsymbol{\theta}), t)$ and let

$$\tilde{J}_h(\boldsymbol{\theta}, t) := \det \begin{bmatrix} \hat{e}_1 & \hat{e}_2 & \hat{e}_3 \\ J_h(\boldsymbol{\theta}, t) \end{bmatrix} \in \mathbb{R}^3. \quad (6.56)$$

By reasoning as above we obtain the following discrete counterpart of (6.55).

$$\nabla_{\Gamma_h} \cdot I_h \mathbf{v}(G_h(X(\boldsymbol{\theta}), t)) = \frac{d}{dt} \ln \|\tilde{J}_h(\boldsymbol{\theta}, t)\|. \quad (6.57)$$

Relations (6.55) and (6.57) are useful in that they (i) express the velocity flow without tangential derivatives and (ii) can be computed exactly when G and G_h are known explicitly, e.g. for the isotropic growth as discussed in the next subsection.

6.4.3 Computing the dilation rates for the isotropic growth

In this section we compute the dilation rates defined in (6.16) and (6.32), respectively, for arbitrary surfaces that evolve with the material velocity (6.46). The velocity field (6.46) corresponds to the specific case of isotropic evolution, see for instance [28, 93] for the case of evolving planar domains and [6, 109] for the general case. In particular, for suitable choices of the function $S(t)$, the growth law (6.46) admits some specific cases such as uniform, exponential, logistic and periodic growth, see [6, 28, 93, 109]. From (6.3), it is easy to show that, with the velocity field (6.46), each $\mathbf{x}_0 \in \Gamma_0$ evolves to the point

$$G(\mathbf{x}_0, t) = \exp \left(\int_0^t S(\tau) d\tau \right) \mathbf{x}_0, \quad t \in [0, T], \quad (6.58)$$

therefore the evolution induced by an isotropic growth is a time-dependent dilation of the initial surface. The function

$$\phi(t) := \exp \left(\int_0^t S(\tau) d\tau \right), \quad t \in [0, T], \quad (6.59)$$

that appears in (6.58) is known as the *growth function*, see for instance [93].

Remark 15 (Properties of isotropic growth). *Isotropic growth preserves the angles of triangulated surfaces. This has two consequences:*

1. if $\Gamma_h(0)$ meets the Delaunay condition, then $\Gamma_h(t)$ retains the Delaunay condition for all $t \in [0, T]$;
2. if $A(0)$ and $M(0)$ are the stiffness and the mass matrices at $t = 0$, then

$$A(t) = A(0), \quad M(t) = \phi^2(t)M(0), \quad t \in [0, T]. \quad (6.60)$$

Hence, in implementations, $A(t)$ and $M(t)$ need not be computed at each time step.

In the following result we compute the dilation rates μ_{min} , μ_{max} , μ_{min}^* and μ_{max}^* on an arbitrary smooth or triangulated surface that evolves with the material velocity (6.46), in terms of $S(t)$.

Theorem 20 (Velocity flow on isotropically growing smooth or triangulated surfaces). *Let $\Gamma(t)$ be a smooth surface that evolves with the velocity field (6.46) and let $\Gamma_h(t)$ be the corresponding triangulated surface. Then, the instantaneous dilation rates satisfy*

$$H(t) = 2S(t) = H^*(t), \quad t \in [0, T]. \quad (6.61)$$

Hence, it follows that

$$\mu_{min} = \mu_{min}^* = 2 \min_{t \in [0, T]} S(t), \quad \text{and} \quad \mu_{max} = \mu_{max}^* = 2 \max_{t \in [0, T]} S(t). \quad (6.62)$$

Proof. Let $\Gamma_h(t)$ be an evolving smooth surface and let (A, X) , $J(\boldsymbol{\theta}, t)$ and $\tilde{J}(\boldsymbol{\theta}, t)$ as defined in Section 6.4.2. From (6.58) and (6.59), $J(\boldsymbol{\theta}, t)$ fulfils

$$J(\boldsymbol{\theta}, t) = \phi(t)J_X(\boldsymbol{\theta}), \quad (\boldsymbol{\theta}, t) \in A \times [0, T], \quad (6.63)$$

where $J_X : A \rightarrow \mathbb{R}^{2,3}$ is the Jacobian of X . It follows that

$$\|\det \tilde{J}(\boldsymbol{\theta}, t)\| = \phi^2(t) \|\det \tilde{J}(\boldsymbol{\theta}, 0)\|, \quad (\boldsymbol{\theta}, t) \in A \times [0, T], \quad (6.64)$$

which implies that

$$\ln \|\det \tilde{J}(\boldsymbol{\theta}, t)\| - \ln \|\det \tilde{J}(\boldsymbol{\theta}, 0)\| = 2 \ln \phi(t) = 2 \int_0^t S(\tau) d\tau, \quad (\boldsymbol{\theta}, t) \in A \times [0, T]. \quad (6.65)$$

By differentiating (6.65), we have

$$\frac{d}{dt} \ln \|\det \tilde{J}(\boldsymbol{\theta}, t)\| = 2S(t), \quad (\boldsymbol{\theta}, t) \in A \times [0, T]. \quad (6.66)$$

By combining (6.55), (6.66) and dropping the parametric coordinates $\boldsymbol{\theta}$, we have

$$\nabla_{\Gamma} \cdot \mathbf{v}(\mathbf{x}, t) = 2S(t), \quad (\mathbf{x}, t) \in \mathcal{G}_T, \quad (6.67)$$

which proves the first equality in (6.61). Analogously, we prove the second equality in (6.61) by using (6.57). This completes the proof. \square

For the uniform, exponential, logistic and periodic growths, the functions $\phi(t)$, $S(t)$ and the dilation rates μ_{min} , μ_{min}^* , μ_{max} and μ_{max}^* are detailed in Table 6.1, see also [93, Table 1] for the case of evolving planar domains, while the corresponding plots are depicted in Figure 6.1.

Type of growth	Growth function $\phi(t)$	$S(t)$	$\mu_{min} = \mu_{min}^*$	$\mu_{max} = \mu_{max}^*$
Linear	$rt + 1$	$\frac{r}{rt + 1}$	$\frac{2r}{rT + 1}$	$2r$
Exponential	$\exp(rt)$	$\frac{r}{K - 1 + \exp(Krt)}$	$\frac{2r}{K - 1 + \exp(KrT)}$	$2r(K - 1)$
Logistic	$\frac{K \exp(Krt)}{K - 1 + \exp(Krt)}$	$\frac{r \sin(rt)}{2 - \cos(rt)}$	$-\frac{2r\sqrt{3}}{3}$	$\frac{2r\sqrt{3}}{3}$

Table 6.1: Particular types of isotropic growth with their respective growth functions $\phi(t)$, $S(t)$ functions and constants μ_{min} , μ_{max} , μ_{min}^* , and μ_{max}^* . The constant $r > 0$ is the growth rate. For the logistic growth, $K > 1$ is the *carrying capacity*, i.e. the square root of the asymptotical ratio between the final and the initial area of the surface, see [93].

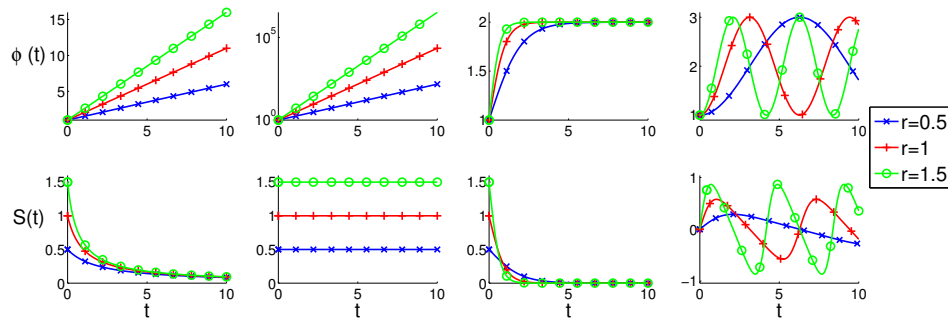


Figure 6.1: Plots of the growth functions $\phi(t)$ (top row) and the corresponding $S(t)$ functions (bottom row) listed in Table 6.1 for $K = 2$ and $r = 0.5, 1, 1.5$. From left to right: linear, exponential, logistic and periodic growth profiles.

6.5 Linear heat equation and discrete maximum principles

We consider, for $k = 1$, the specific case of linear heat equation on an evolving surface $\Gamma(t)$:

$$\partial^\bullet u + u \nabla_\Gamma \cdot \mathbf{v} = d \Delta_\Gamma u - \beta u, \quad \beta \in \mathbb{R}, \quad (6.68)$$

and we prove the semi- and fully-discrete maximum principles for the case when $\mu_{min} + \beta \geq 0$. Equation (6.68) is a special case of the general system (6.14) that we are interested in. However, we start with this specific case as (i) it provides more insights on the effect of growth on stability, (ii) we are able to prove a better timestep stability condition and (iii) to make the reader familiar with the demonstrative techniques.

The following result, that we proved in [56, Theorem 2.1] for the special case of stationary surfaces, addresses the maximum principle at the semi-discrete level.

Theorem 21 (Semi-discrete maximum principle for the linear heat equation (6.68)).

If the velocity field \mathbf{v} fulfils

$$\mu_{min} + \beta \geq 0, \quad (6.69)$$

with μ_{min} as defined in (6.32), and the triangulation $\Gamma_h(t)$ meets the Delaunay condition for all $t \in [0, T]$, then the LESFEM solution of (6.68) fulfils the following discrete maximum

principle

$$\min \left\{ 0, \min_{j=1, \dots, N} \xi_j(0) \right\} \leq \xi_i(t) \leq \max \left\{ 0, \max_{j=1, \dots, N} \xi_j(0) \right\}, \quad (6.70)$$

for $i = 1, \dots, N$ and $t \in [0, T]$.

Proof. From (6.40), the LESFEM spatial discretisation of (6.68) is

$$\frac{d}{dt}(M\xi) + dA\xi = -\beta M\xi. \quad (6.71)$$

By applying the chain rule, (6.71) becomes

$$M\dot{\xi} + \frac{dM}{dt}\xi + dA\xi = -\beta M\xi. \quad (6.72)$$

By multiplying (6.72) on the left by M^{-1} , we have

$$\dot{\xi} = -dM^{-1}A\xi - M^{-1}\frac{dM}{dt}\xi - \beta\xi. \quad (6.73)$$

All we have to prove is that the ODE (6.73) is dissipative, i.e. $-dM^{-1}A|\xi| - M^{-1}\frac{dM}{dt}|\xi| - \beta|\xi| \leq \mathbf{0}$. For every $t \in [0, T]$, M is diagonal with positive diagonal entries and A fulfils (6.41) from the Delaunay condition. Then, it follows that $-dM^{-1}A|\xi| \leq \mathbf{0}$. Hence, it suffices to prove that $-(M^{-1}\frac{dM}{dt} + \beta I)|\xi| \leq \mathbf{0}$, which is true provided

$$M^{-1}\frac{dM}{dt} + \beta I \geq \mathbf{0}. \quad (6.74)$$

By using (6.49), condition (6.74) is true if

$$(\mu_{min} + \beta)I \geq \mathbf{0}, \quad (6.75)$$

which holds true from assumption (6.69). This completes the proof. \square

The next theorem shows the same result for the LESFEM-IMEX Euler full-discretisation of (6.68), under a timestep restriction. This result holds true for the special case of stationary surfaces (see [56, Theorem 2.2]).

Theorem 22 (Fully-discrete maximum principle for the linear heat equation (6.68)).

If the velocity field \mathbf{v} fulfils

$$\mu_{min} + \beta \geq 0, \quad t \geq 0, \quad (6.76)$$

with μ_{min} as defined in (6.32), and the triangulation Γ_h meets the Delaunay condition for all $t > 0$, then the LESFEM-IMEX Euler solution of (6.68) fulfils the following minimum-maximum principle

$$\min \left\{ 0, \min_{j=1, \dots, N} \xi_j^0 \right\} \leq \xi_i^n \leq \max \left\{ 0, \max_{j=1, \dots, N} \xi_j^0 \right\}, \quad (6.77)$$

for $i = 1, \dots, N$ and $n = 0, \dots, N_T$, if the timestep satisfies

$$\tau\beta \leq 1. \quad (6.78)$$

In particular, there is no timestep restriction if $\beta \leq 0$.

Proof. The full-discretisation (6.45) of the heat equation (6.68) can be written as

$$\boldsymbol{\xi}^{n+1} = (M^{n+1} + \tau dA^{n+1})^{-1} M^{n+1} (M^{n+1})^{-1} M^n (1 - \tau\beta) \boldsymbol{\xi}^n, \quad n = 0, \dots, N_T. \quad (6.79)$$

From (6.42)-(6.43) we have

$$(M^{n+1} + \tau dA^{n+1})^{-1} M^{n+1} \geq \mathbf{0}, \quad n = 0, \dots, N_T; \quad (6.80)$$

$$(M^{n+1} + \tau dA^{n+1})^{-1} M^{n+1} \mathbf{1} = \mathbf{1}, \quad n = 0, \dots, N_T. \quad (6.81)$$

Then, the scheme (6.79) fulfils the discrete maximum principle if

$$(M^{n+1})^{-1} M^n (1 - \tau\beta) \boldsymbol{\xi}^n \geq \min\{\mathbf{0}, \boldsymbol{\xi}^n\}, \quad n = 0, \dots, N_T; \quad (6.82)$$

$$(M^{n+1})^{-1} M^n (1 - \tau\beta) \boldsymbol{\xi}^n \leq \max\{\mathbf{0}, \boldsymbol{\xi}^n\}, \quad n = 0, \dots, N_T. \quad (6.83)$$

Since $(M^{n+1})^{-1} M^n$ is diagonal with strictly positive diagonal entries, conditions (6.82)-(6.83) are true provided

$$1 - \tau\beta \geq 0; \quad (6.84)$$

$$(1 - \tau\beta)I \leq (M^n)^{-1} M^{n+1}, \quad n = 0, \dots, N_T. \quad (6.85)$$

Condition (6.84) is true under assumption (6.78). In order to prove (6.85), we need to estimate M^{n+1} as a function of M^n . To this end, by applying Gronwall's lemma to the first inequality in (6.49), we have

$$M^{n+1} \geq M^n e^{\tau\mu_{min}}, \quad n = 0, \dots, N_T. \quad (6.86)$$

By using (6.86), condition (6.85) is true if

$$1 - \tau\beta \leq e^{\tau\mu_{min}}. \quad (6.87)$$

Let us now define $f(\tau) := 1 - \tau\beta$ and $g(\tau) = e^{\tau\mu_{min}}$. These functions fulfil $f(0) = g(0) = 1$, f is linear and g is non-concave for all $\mu_{min} \in \mathbb{R}$. Then

- if $f'(0) > g'(0)$, then condition (6.87) is not fulfilled for any sufficiently small τ .
- if $f'(0) \leq g'(0)$, then condition (6.87) is fulfilled for every $\tau > 0$.

Now, condition $f'(0) \leq g'(0)$ means $-\beta \leq \mu_{min}$, which is true from assumption (6.76). This completes the proof. \square

Remark 16 (Interplay between material velocity and source term). *Relation (6.69) implies that*

- *domain growth* ($\mu_{min} > 0$) can enable the discrete maximum principle even for $\beta < 0$;
- *local domain contraction* ($\mu_{min} < 0$) can prevent the discrete maximum principle even for $\beta \geq 0$.

This interplay is justified by observing that domain evolution implies a dilution effect, explained as follows. By choosing $\varphi = 1$ in the variational formulation (6.27) with $k = 1$ and $f_1(u) = -\beta u$, we obtain

$$\frac{d}{dt} \int_{\Gamma(t)} u = -\beta \int_{\Gamma(t)} u, \quad t \in [0, T]. \quad (6.88)$$

If $|\Gamma(t)|$ denotes the surface area of $\Gamma(t)$ and $\langle u(t) \rangle := \frac{1}{|\Gamma(t)|} \int_{\Gamma(t)} u$ denotes the mean value of u , (6.88) becomes

$$\frac{d}{dt} (|\Gamma(t)| \langle u(t) \rangle) = -\beta |\Gamma(t)| \langle u(t) \rangle, \quad t \in [0, T]. \quad (6.89)$$

By solving (6.89) for $\frac{d}{dt} \langle u(t) \rangle$, we obtain

$$\frac{d}{dt} \langle u(t) \rangle = -\frac{\beta |\Gamma(t)| + \frac{d}{dt} |\Gamma(t)|}{|\Gamma(t)|} \langle u(t) \rangle, \quad t \in [0, T]. \quad (6.90)$$

By choosing $g = 1$ in the transport formula (6.8), we have

$$\frac{d}{dt} |\Gamma(t)| = \int_{\Gamma(t)} \nabla_{\Gamma} \cdot \mathbf{v} \geq |\Gamma(t)| \mu_{min}^*, \quad t \in [0, T]. \quad (6.91)$$

By combining (6.90) and (6.91) we have

$$\frac{d}{dt} \langle u(t) \rangle \leq -(\beta + \mu_{min}^*) \langle u(t) \rangle, \quad t \in [0, T]. \quad (6.92)$$

From (6.92), the dilution effect arising from surface growth can be interpreted as the dampening or uplifting effect of μ_{min}^* on $\langle u(t) \rangle$. The estimate (6.92) implies that $\langle u(t) \rangle$ is non-increasing if

$$\beta + \mu_{min}^* \geq 0, \quad (6.93)$$

which is the continuous counterpart of (6.69). We conclude that condition (6.69) is consistent with the interpretation of surface growth in terms of dilution effect.

Remark 17 (Interplay between timestep restriction and source term). *Relation (6.78) implies that the timestep restriction needed for guaranteeing the discrete maximum principle is independent of the material velocity and it only depends on the stiffness parameter β of the source term. In particular, when the source term is nonnegative (i.e. when $\beta \leq 0$), the LESFEM - IMEX Euler fully-discrete scheme unconditionally fulfils the discrete maximum principle.*

6.6 Reaction-diffusion systems and invariant regions

In this section we prove, for the semi- and full-discretisations of RDSs of the form (6.14), a criterion to test if a hyper-rectangle in the phase-space is invariant. In the case $k = 1$ of scalar equations, the notion of invariant region collapses to that of minimum-maximum principle, considered in the previous section for the special case of the linear heat equation. We assume

that the Delaunay regularity of the mesh is preserved under evolution. For $k = 1, \dots, r$, we define the constants

$$\bar{\mu}_k := \begin{cases} \mu_{min} & \text{if } \bar{\sigma}_k \geq 0; \\ \mu_{max} & \text{if } \bar{\sigma}_k < 0, \end{cases} \quad \underline{\mu}_k := \begin{cases} \mu_{max} & \text{if } \underline{\sigma}_k \geq 0; \\ \mu_{min} & \text{if } \underline{\sigma}_k < 0, \end{cases} \quad (6.94)$$

where μ_{min} and μ_{max} are the dilation rates defined in (6.32). In the following theorem we prove that, under similar assumptions of Conjecture 1, Σ is an invariant region for the solution obtained from the semi-discrete scheme (6.40). Hence, in the following theorem we extend [56, Theorem 3.3] to the case of evolving surfaces.

Theorem 23 (Invariant rectangles for (6.40)). *Let Σ be a hyper-rectangle as in (6.19) in the phase space of (6.40), let \mathbf{f} be Lipschitz on Σ . If the triangulation $\Gamma_h(t)$ satisfies the Delaunay condition for all $t \geq 0$ and*

$$f_k(\mathbf{U}) < \bar{\mu}_k \bar{\sigma}_k, \quad \mathbf{U} \in \bar{\Sigma}_k \cap \mathbb{R}^r, \quad k = 1, \dots, r; \quad (6.95)$$

$$f_k(\mathbf{U}) > \underline{\mu}_k \underline{\sigma}_k, \quad \mathbf{U} \in \underline{\Sigma}_k \cap \mathbb{R}^r, \quad k = 1, \dots, r, \quad (6.96)$$

then Σ is an invariant region for (6.40).

Proof. The semidiscrete method (6.40) can be written, after applying the chain rule to the term $\frac{d}{dt}(M\xi_k)$ and multiplying on the left by M^{-1} as

$$\dot{\xi}_k = -d_k \bar{M}^{-1} A \xi_k + f_k(\xi_1, \dots, \xi_r) - \bar{M}^{-1} \frac{dM}{dt} \xi_k, \quad k = 1, \dots, r. \quad (6.97)$$

Since M is diagonal with positive diagonal entries and $A_{ij} \leq 0$ for $i \neq j$ from the assumption of Delaunay regularity, proceeding as in the proof of [56, Theorem 3.3], it suffices to verify that, for all $(U_1, \dots, U_r) \in \Sigma$, $k = 1, \dots, r$, and $i = 1, \dots, N$,

$$f_k(U_1, \dots, \bar{\sigma}_k, \dots, U_r) - m_{ii}^{-1} \frac{dm_{ii}}{dt} \bar{\sigma}_k < 0; \quad (6.98)$$

$$f_k(U_1, \dots, \underline{\sigma}_k, \dots, U_r) - m_{ii}^{-1} \frac{dm_{ii}}{dt} \underline{\sigma}_k > 0, \quad (6.99)$$

where $\underline{\sigma}_k$ and $\bar{\sigma}_k$ are as in (6.19). Using relation (6.49), conditions (6.98)-(6.99) hold if, for all $k = 1, \dots, r$,

$$f_k(U_1, \dots, \bar{\sigma}_k, \dots, U_r) - \bar{\mu}_k \bar{\sigma}_k < 0; \quad (6.100)$$

$$f_k(U_1, \dots, \underline{\sigma}_k, \dots, U_r) - \underline{\mu}_k \underline{\sigma}_k > 0, \quad (6.101)$$

with $\underline{\mu}_k$ and $\bar{\mu}_k$ as in (6.94), that is true from assumptions (6.95)-(6.96). This completes the proof. \square

The following theorem provides a sufficient condition for regions to be invariant for the LESFEM-IMEX Euler scheme (6.45) and extends [56, Theorem 3.4]. In contrast to the semi-discrete case, we relax the strict inequalities (6.21)-(6.22) with conditions (6.103)-(6.104), in which we use the perturbed dilation rates $\tilde{\mu}_k$ and μ_k given by

$$\tilde{\mu}_k := \begin{cases} \mu_{min} & \text{if } \bar{\sigma}_k \geq 0; \\ \frac{e^{\tau \mu_{max}} - 1}{\tau} & \text{if } \bar{\sigma}_k < 0, \end{cases} \quad \mu_k := \begin{cases} \frac{e^{\tau \mu_{max}} - 1}{\tau} & \text{if } \underline{\sigma}_k > 0; \\ \mu_{min} & \text{if } \underline{\sigma}_k \leq 0, \end{cases} \quad (6.102)$$

respectively, and μ_{min} and μ_{max} are defined in (6.32). Observe that $\tilde{\mu}_k \rightarrow \bar{\mu}_k$ and $\mu_k \rightarrow \underline{\mu}_k$ as $\tau \rightarrow 0$.

Theorem 24 (Invariant rectangles for (6.45)). *Let Σ be a hyper-rectangle as in (6.19) in the phase space of (6.40), let \mathbf{f} be Lipschitz on Σ . If the triangulation $\Gamma_h(t)$ meets the Delaunay condition for all $t \geq 0$ and*

$$f_k(\mathbf{U}) \leq \bar{\sigma}_k \tilde{\mu}_k, \quad \mathbf{U} \in \bar{\Sigma}_k \cap \mathbb{R}^r, \quad k = 1, \dots, r; \quad (6.103)$$

$$f_k(\mathbf{U}) \geq \underline{\sigma}_k \underline{\mu}_k, \quad \mathbf{U} \in \underline{\Sigma}_k \cap \mathbb{R}^r, \quad k = 1, \dots, r, \quad (6.104)$$

then Σ is an invariant region for (6.45) if the timestep τ fulfils

$$\tau L_k \leq 1, \quad k = 1, \dots, r, \quad (6.105)$$

where, for all $k = 1, \dots, r$, L_k is the Lipschitz constant of f_k .

Proof. The fully-discrete scheme (6.45) can be written as

$$\boldsymbol{\xi}_k^{n+1} = (M^{n+1} + \tau dA^{n+1})^{-1} M^{n+1} (M^{n+1})^{-1} M^n (\boldsymbol{\xi}_k^n + \tau \mathbf{f}_k^n), \quad (6.106)$$

$n \in \mathbb{N} \cup \{0\}$, $k = 1, \dots, r$. Since the mesh meets the Delaunay assumption at all times, the matrix properties (6.80)-(6.81) hold. Then, it suffices to prove that

$$\underline{\sigma}_k \mathbf{1} \leq (M^{n+1})^{-1} M^n (\boldsymbol{\xi}_k^n + \tau \mathbf{f}_k^n) \leq \bar{\sigma}_k \mathbf{1}, \quad k = 1, \dots, r, \quad (6.107)$$

where $\mathbf{1}$ is the column vector of ones. We will prove the two inequalities in (6.107) in turn. From (6.49), the inequality on the right-hand-side of (6.107) holds true if

$$\boldsymbol{\xi}_k^n + \tau \mathbf{f}_k^n \leq \bar{\sigma}_k e^{\tau \bar{\mu}_k} \mathbf{1}, \quad k = 1, \dots, r, \quad (6.108)$$

with $\bar{\mu}_k$ as defined in (6.94). Suppose $\bar{\sigma}_k \geq 0$. From assumption (6.103) we can estimate \mathbf{f}_k^n as follows

$$\mathbf{f}_k^n \leq \bar{\sigma}_k \bar{\mu}_k + L_k (\bar{\sigma}_k \mathbf{1} - \boldsymbol{\xi}_k^n), \quad k = 1, \dots, r. \quad (6.109)$$

From (6.109), condition (6.108) holds true provided

$$\boldsymbol{\xi}_k^n (1 - \tau L_k) + \tau \bar{\mu}_k \bar{\sigma}_k + \tau L_k \bar{\sigma}_k \mathbf{1} \leq \bar{\sigma}_k e^{\tau \bar{\mu}_k} \mathbf{1}, \quad k = 1, \dots, r. \quad (6.110)$$

From assumption (6.105), since $\boldsymbol{\xi}_k^n \leq \bar{\sigma}_k \mathbf{1}$, then (6.110) holds true if

$$\bar{\sigma}_k (1 - \tau L_k) + \tau \bar{\mu}_k \bar{\sigma}_k + \tau \tilde{L}_k \bar{\sigma}_k \leq \bar{\sigma}_k e^{\tau \bar{\mu}_k}, \quad k = 1, \dots, r, \quad (6.111)$$

that is to say

$$1 + \tau \bar{\mu}_k \leq e^{\tau \bar{\mu}_k}, \quad k = 1, \dots, r, \quad (6.112)$$

which holds true for each $\tau \in \mathbb{R}$. Suppose, instead, $\bar{\sigma}_k < 0$. From assumption (6.103) we can estimate \mathbf{f}_k^n as follows

$$\mathbf{f}_k^n \leq \frac{e^{\tau \bar{\mu}_k} - 1}{\tau} \bar{\sigma}_k + L_k (\bar{\sigma}_k \mathbf{1} - \boldsymbol{\xi}_k^n), \quad k = 1, \dots, r. \quad (6.113)$$

From (6.113), condition (6.108) holds true provided

$$\xi_k^n(1 - \tau L_k) + \bar{\sigma}_k(e^{\tau \bar{\mu}_k} - 1 + \tau L_k)\mathbf{1} \leq \bar{\sigma}_k e^{\tau \bar{\mu}_k} \mathbf{1}, \quad k = 1, \dots, r. \quad (6.114)$$

From assumption (6.105), since $\xi_k^n \leq \bar{\sigma}_k \mathbf{1}$, then (6.114) holds true if

$$\bar{\sigma}_k(1 - \tau L_k)\mathbf{1} + \bar{\sigma}_k(e^{\tau \bar{\mu}_k} - 1 + \tau L_k)\mathbf{1} \leq \bar{\sigma}_k e^{\tau \bar{\mu}_k} \mathbf{1}, \quad k = 1, \dots, r. \quad (6.115)$$

As (6.115) always holds with the equality, we conclude that the second inequality in (6.107) is true under assumptions (6.103) and (6.105). Similarly, the inequality on the left side of (6.107) holds under assumptions (6.104) and (6.105). This completes the proof. \square

Remark 18 (Sharper timestep restriction). *In the specific case of the linear heat equation (6.68), estimate (6.78) in Theorem 22 is sharper than estimate (6.105) in Theorem 24. In fact, since the Lipschitz constant of the source term is $L = |\beta|$, the timestep restriction (6.105) is fulfilled for $\tau|\beta| \leq 1$, which is more restrictive than condition (6.78).*

6.7 Velocity-induced invariant regions for RD models

Now, we consider four different RDSs that are well-known in the literature and prove, at the discrete level, the existence of discrete invariant hyper-rectangles for these RDSs, depending on the global discrete dilation rates μ_{min} and μ_{max} defined in (6.16). The results in this section are confined to the spatially discrete level, but from Conjecture 1, we claim that the same results holds at the continuous level. In the special case of stationary surfaces (i.e. when $\mu_{min} = \mu_{max} = 0$), we obtain invariant hyper-rectangles that have been studied in the literature (see [21, 25, 65]). It is worth remarking that, even though we consider four RD models for illustrative purposes, the following analysis can be easily extended to other types of RDSs.

6.7.1 RDS with *activator-depleted* kinetics

Let us consider an RDS with the well-known non-dimensional *activator-depleted* kinetics, also known as Schnakenberg or Brusselator kinetics (see for instance [6, 120]), on evolving surfaces

$$\begin{cases} \partial^\bullet u_1 + u_1 \nabla_\Gamma \cdot \mathbf{v} - \Delta_\Gamma u_1 = f_1(u_1, u_2) := \gamma(a - u_1 + u_1^2 u_2); \\ \partial^\bullet u_2 + u_2 \nabla_\Gamma \cdot \mathbf{v} - d \Delta_\Gamma u_2 = f_2(u_1, u_2) := \gamma(b - u_1^2 u_2), \end{cases} \quad (6.116)$$

where a , b and γ are positive parameters and d is a positive diffusion rate. The model describes a system of two interacting chemicals, in which $u_1 \geq 0$ and $u_2 \geq 0$ are the respective concentrations. For this reason, we focus our attention on invariant regions contained in the positive orthant. In the following theorem we prove that: (i) the positive orthant is invariant for (6.116) regardless of μ_{min} and μ_{max} . At the continuous level, the result holds in the specific case of stationary planar domains, see [21]. (ii) when $\mu_{min} > 0$, the model possesses unbounded invariant stripes (depending on μ_{min}) in the positive orthant.

Theorem 25 (Velocity-induced invariant regions for the activator-depleted model (6.116)). *For the LESFEM spatial discretisation of (6.116), the following statements hold:*

1. For any value of the constants μ_{min} , and μ_{max} defined in (6.32), the positive orthant $\Sigma^+ := [0, +\infty[^2$ is invariant.
2. If $\mu_{min} > 0$ and $\bar{\sigma}_2$ is a constant such that

$$\bar{\sigma}_2 \geq \frac{\gamma b}{\mu_{min}}, \quad (6.117)$$

then the stripe $\Sigma = [0, +\infty[\times [0, \bar{\sigma}_2]$ is invariant.

Proof. In order to prove Statements 1 and 2 we have to verify conditions (6.21)-(6.22). For Statement 1, we observe that

- a) $\underline{\Sigma}_1 := \{0\} \times [0, \bar{\sigma}_2] \subset \underline{\Sigma}_1^+ := \{0\} \times [0, +\infty[$ and, for $(u_1, u_2) \in \underline{\Sigma}_1^+$, we have $\underline{f}_1(u_1, u_2) = f_1(u_1, u_2) = \gamma a > 0$;
- b) $\underline{\Sigma}_2 := [0, \bar{\sigma}_1] \times \{0\} \subset \underline{\Sigma}_2^+ := [0, +\infty[\times \{0\}$ and, for $(u_1, u_2) \in \underline{\Sigma}_2^+$, we have $\underline{f}_2(u_1, u_2) = f_2(u_1, u_2) = \gamma b > 0$.

This proves Statement 1. For Statement 2, let $\mu_{min} > 0$ and we assume for the moment that the strict inequality holds in (6.117). Then the set $\bar{\Sigma}_1 := [0, +\infty[\times \{\bar{\sigma}_2\}$ is contained in the region

$$\left\{ (u, v) \in \mathbb{R}^2 \left| u > 0, v > \frac{\gamma a - (\gamma + \mu_{min})u}{\gamma u^2} \right. \right\},$$

in which $\bar{f}_1(u_1, u_2) := f_1(u_1, u_2) - \mu_{min}u_1 < 0$. This proves Statement 2 when the strict inequality holds in (6.117). Otherwise, observe that

$$\Sigma = [0, +\infty[\times [0, \bar{\sigma}_2] = \bigcap_{\varepsilon > 0} [0, +\infty[\times [0, \bar{\sigma}_2 + \varepsilon], \quad (6.118)$$

i.e. Σ is the intersection of invariant regions and is thus invariant. This completes the proof of Statement 2. \square

6.7.2 RDS with Thomas kinetics

Let us consider an RDS with the non-dimensional Thomas kinetics (see for instance [100, p. 78]), on evolving surfaces

$$\begin{cases} \partial^\bullet u_1 + u_1 \nabla_\Gamma \cdot \mathbf{v} - \Delta_\Gamma u_1 = f_1(u_1, u_2) := \gamma \left(a - u_1 - \rho \frac{u_1 u_2}{1 + u_1 + K u_1^2} \right); \\ \partial^\bullet u_2 + u_2 \nabla_\Gamma \cdot \mathbf{v} - d \Delta_\Gamma u_2 = f_2(u_1, u_2) := \gamma \left(\alpha (b - u_2) - \rho \frac{u_1 u_2}{1 + u_1 + K u_1^2} \right), \end{cases} \quad (6.119)$$

where α, a, b, γ, K and ρ are positive constants and d is a positive diffusion rate. The model describes a system of two interacting chemicals, in which $u_1 \geq 0$ and $u_2 \geq 0$ are the respective concentrations. For this reason, we focus our attention on invariant regions contained in the positive orthant.

Theorem 26 (Velocity-induced invariant regions for the Thomas model (6.119)). *For the LESFEM spatial discretisation of (6.119), the following statements hold:*

1. For any value of the constants μ_{min} , and μ_{max} defined in (6.32), the positive orthant $\Sigma^+ := [0, +\infty]^2$ is invariant.

2. If $\mu_{min} > -\gamma \min(1, \alpha)$ and $\bar{\sigma}_1$ and $\bar{\sigma}_2$ are two constants such that

$$\bar{\sigma}_1 \geq \frac{\gamma a}{\gamma + \mu_{min}}, \quad \bar{\sigma}_2 \geq \frac{\gamma \alpha b}{\gamma \alpha + \mu_{min}}, \quad (6.120)$$

then the region $\Sigma = [0, \bar{\sigma}_1] \times [0, \bar{\sigma}_2]$ is invariant.

Proof. To prove Statements 1 and 2, we have to verify conditions (6.21)-(6.22). For Statement 1), observe that

a) for $(u_1, u_2) \in \underline{\Sigma}_1 := \{0\} \times [0, \bar{\sigma}_2]$, we have $\underline{f}_1(u_1, u_2) = f_1(u_1, u_2) = a > 0$;

b) for $(u_1, u_2) \in \underline{\Sigma}_2 := [0, \bar{\sigma}_1] \times \{0\}$, we have $\underline{f}_2(u_1, u_2) = f_2(u_1, u_2) = \alpha b > 0$.

Items a) and b) prove Statement 1. For Statement 2, let $\mu_{min} > -\gamma \min(1, \alpha)$ and we assume for the moment that the strict inequalities hold in (6.120). Then, observe that

c) the set $\bar{\Sigma}_1 := \{\bar{\sigma}_1\} \times [0, \bar{\sigma}_2]$ is contained in the region

$$\left\{ (u, v) \in \mathbb{R}^2 \mid u > 0, v > (\gamma a - (\mu_{min} + \gamma)u) \frac{1 + u + Ku^2}{\gamma \rho u} \right\},$$

in which $\bar{f}_1(u_1, u_2) := f_1(u_1, u_2) - \mu_{min}u_1 < 0$;

d) the set $\bar{\Sigma}_2 := [0, \bar{\sigma}_1] \times \{\bar{\sigma}_2\}$ is contained in the region

$$\left\{ (u, v) \in \mathbb{R}^2 \mid u > 0, v > \frac{\gamma \alpha b (1 + u + Ku^2)}{\gamma \rho u + (\gamma \alpha + \mu_{min})(1 + u + Ku^2)} \right\},$$

in which $\bar{f}_2(u_1, u_2) := f_2(u_1, u_2) - \mu_{min}u_2 < 0$.

Items a) through d) prove Statement 2 when the strict inequalities hold in (6.120). Otherwise, we have that

$$\Sigma = [0, \bar{\sigma}_1] \times [0, \bar{\sigma}_2] = \bigcap_{\varepsilon > 0} [0, \bar{\sigma}_1 + \varepsilon] \times [0, \bar{\sigma}_2 + \varepsilon], \quad (6.121)$$

i.e. Σ is the intersection of invariant regions and is thus invariant. \square

6.7.3 Morphochemical RDS model for electrodeposition

Let us consider a RDS on an arbitrary evolving surface $\Gamma(t)$, given by

$$\begin{cases} \partial^\bullet u_1 + u_1 \nabla_\Gamma \cdot \mathbf{v} - \Delta_\Gamma u_1 = f_1(u_1, u_2); \\ \partial^\bullet u_2 + u_2 \nabla_\Gamma \cdot \mathbf{v} - d \Delta_\Gamma u_2 = f_2(u_1, u_2), \end{cases} \quad (6.122)$$

where $f_1(u_1, u_2)$ and $f_2(u_1, u_2)$ are the kinetics considered in [79, 80, 81], given by

$$f_1(u_1, u_2) := A_1(1 - u_2)u_1 - A_2u_1^3 - B(u_2 - \alpha); \quad (6.123)$$

$$f_2(u_1, u_2) := C(1 + k_2u_1)(1 - u_2)(1 - \gamma + \gamma u_2) - Du_2(1 + \gamma u_2)(1 + k_3u_1), \quad (6.124)$$

respectively, and $A_1, A_2, B, C, D, \alpha, \gamma, k_2, k_3$ are positive constants. Following [80], we fix the following constraints on the parameters:

$$\alpha = 0.5, \gamma = 0.2, k_2 = 2.5, k_3 = 1.5; \quad (6.125)$$

$$\chi := \frac{D}{C} = \frac{(1-\alpha)(1-\gamma+\gamma\alpha)}{\alpha(1+\gamma\alpha)} \approx 0.8182. \quad (6.126)$$

Hence, we choose A_1, A_2, B, C as free parameters. The above model (called DIB model after the authors) describes electrodeposition processes as discussed in detail in [80]. In particular, we recall that the unknowns have the following interpretation:

- $u_1(\mathbf{x}, t)$ is the *morphology*. A positive value of $u_1(\mathbf{x}, t)$ corresponds to metal deposition, while a negative value of $u_1(\mathbf{x}, t)$ corresponds to corrosion;
- $u_2(\mathbf{x}, t)$ is the *surface chemistry* and ranges in $[0, 1]$.

To summarize, the solutions of the DIB model should be confined in the region $\mathbb{R} \times [0, 1]$ of the phase space. Even if this property has not been proven in the literature, our invariant region analysis gives a partial answer to the problem. In fact, a consequence of the next theorem is that, when the parameters fulfil (6.125)-(6.126), and $\Gamma(t)$ is not contracting too quickly, then the $u_2(\mathbf{x}, t)$ component of the solution fulfils $u_2(\mathbf{x}, t) \leq 1$. A rigorous proof of the positivity of $u_2(\mathbf{x}, t)$ remains an open problem. It is worth remarking that this RD model has been studied in the literature on stationary planar domains in [80, 81] and on stationary surfaces in [79]. However, in this section we pose the model on evolving surfaces and we carry out an invariant region study. Hence, in the special case $\mu_{min} = \mu_{max} = 0$ our invariant region analysis covers the case of stationary domains and surfaces.

Theorem 27 (Velocity-induced invariant regions for the DIB model (6.122)-(6.124)). *Let conditions (6.125)-(6.126) hold. Let*

$$\underline{\sigma}_2 := \frac{(2\gamma - 1)k_2 - \chi k_3 - \sqrt{((2\gamma - 1)k_2 - \chi k_3)^2 + 4(1 - \gamma)k_2\gamma(k_2 + \chi k_3)}}{2\gamma(k_2 + \chi k_3)} \approx -4.2847; \quad (6.127)$$

$$\bar{\sigma}_2 := \frac{(2\gamma - 1)k_2 - \chi k_3 + \sqrt{((2\gamma - 1)k_2 - \chi k_3)^2 + 4(1 - \gamma)k_2\gamma(k_2 + \chi k_3)}}{2\gamma(k_2 + \chi k_3)} \approx 0.6262, \quad (6.128)$$

and let $\underline{\Lambda}, \bar{\Lambda}$ be defined by

$$\underline{\Lambda} := (1 - \underline{\sigma}_2)(1 - \gamma + \gamma\underline{\sigma}_2) - \chi\underline{\sigma}_2(1 + \gamma\underline{\sigma}_2) \approx 0.2006; \quad (6.129)$$

$$\bar{\Lambda} := (1 - \bar{\sigma}_2)(1 - \gamma + \gamma\bar{\sigma}_2) - \chi\bar{\sigma}_2(1 + \gamma\bar{\sigma}_2) \approx -0.2306, \quad (6.130)$$

If the minimum dilation rate μ_{min} fulfils

$$\frac{\mu_{min}}{C} > \max \left\{ \frac{\underline{\Lambda}}{\underline{\sigma}_2}, \frac{\bar{\Lambda}}{\bar{\sigma}_2} \right\} \approx -0.04682, \quad (6.131)$$

then there exist $\underline{\sigma}_1 < 0$ and $\bar{\sigma}_2 > 0$ (depending only on A_1, A_2 and B) such that the region $\Sigma := [\underline{\sigma}_1, \bar{\sigma}_1] \times [\underline{\sigma}_2, \bar{\sigma}_2]$ is invariant for the LESFEM spatial discretisation of the DIB model (6.122)-(6.124).

Proof. To prove the theorem, we have to verify conditions (6.21)-(6.22). To this end observe that, since $\underline{\sigma}_2 < 0$ and $\bar{\sigma}_2 > 0$, then $\underline{f}_2(u_1, u_2) = \bar{f}_2(u_1, u_2) = f_2(u_1, u_2) - \mu_{min}u_2$ for all $(u_1, u_2) \in \mathbb{R}^2$. Now notice that $\bar{f}_2(u_1, u_2)$ can be rearranged as

$$\begin{aligned} \bar{f}_2(u_1, u_2) = C \left\{ u_1 [k_2(1 - u_2)(1 - \gamma + \gamma u_2) - \chi k_3(1 + \gamma u_2)u_2] \right. \\ \left. + [(1 - u_2)(1 - \gamma + \gamma u_2) - \chi(1 + \gamma u_2)u_2] - \frac{\mu_{min}}{C}u_2 \right\}. \end{aligned} \quad (6.132)$$

Hence, $\bar{f}_2(u_1, u_2)$ does not depend on u_1 when

$$k_2(1 - u_2)(1 - \gamma + \gamma u_2) - \chi k_3(1 + \gamma u_2)u_2 = 0, \quad (6.133)$$

i.e. when u_2 takes one of the two values $\underline{\sigma}_2$ or $\bar{\sigma}_2$ defined in (6.127)-(6.128). In particular, for all $u_1 \in \mathbb{R}$, it holds that

$$\bar{f}_2(u_1, \bar{\sigma}_2) = C\bar{\Lambda} - \mu_{min}\bar{\sigma}_2; \quad (6.134)$$

$$\underline{f}_2(u_1, \underline{\sigma}_2) = C\underline{\Lambda} - \mu_{min}\underline{\sigma}_2, \quad (6.135)$$

with $\bar{\Lambda}$ and $\underline{\Lambda}$ as defined in (6.129) and (6.130). Now, in order to verify conditions (6.21)-(6.22) for $f_2(u_1, u_2)$ we require that

$$C\bar{\Lambda} - \mu_{min}\bar{\sigma}_2 < 0; \quad (6.136)$$

$$C\underline{\Lambda} - \mu_{min}\underline{\sigma}_2 > 0, \quad (6.137)$$

i.e. we require that (6.131) holds. To complete the proof we need to prove the existence of $\underline{\sigma}_1 < 0$ and $\bar{\sigma}_1 > 0$ such that

$$f_1(\underline{\sigma}_1, u_2) - \mu_{min}\underline{\sigma}_1 > 0; \quad (6.138)$$

$$f_1(\bar{\sigma}_1, u_2) - \mu_{min}\bar{\sigma}_1 < 0, \quad (6.139)$$

for all $u_2 \in [\underline{\sigma}_2, \bar{\sigma}_2]$. But since the dominating term in $f_1(u_1, u_2)$ is $-A_2u_1^3$, it suffices to choose $\underline{\sigma}_1$ and $\bar{\sigma}_1$ sufficiently large in modulus in order to fulfil conditions (6.138)-(6.139). This completes the proof. \square

We remark that the dilation rate restriction (6.131) means that the evolving surface $\Gamma(t)$ is allowed to grow arbitrarily quickly, but if $\Gamma(t)$ is contracting, then the contraction must be sufficiently slow in comparison to C .

6.7.4 RDS with Hodgkin-Huxley kinetics

Let us now consider a RDS on arbitrary evolving surfaces with the well-known non-dimensional Hodgkin-Huxley kinetics (see [29, 72] and [123, Chapter 14]), given by

$$\begin{cases} \partial^\bullet u_1 + u_1 \nabla_\Gamma \cdot \mathbf{v} - \Delta_\Gamma u_1 = f_1(u_1, u_2, u_3, u_4) := k_1 u_2^3 u_3 (c_1 - u_1) + k_2 u_4^4 (c_2 - u_1) + k_3 (c_3 - u_1); \\ \partial^\bullet u_2 + u_2 \nabla_\Gamma \cdot \mathbf{v} - d_1 \Delta_\Gamma u_2 = f_2(u_1, u_2) := g_1(u_1)(h_1(u_1) - u_2); \\ \partial^\bullet u_3 + u_3 \nabla_\Gamma \cdot \mathbf{v} - d_2 \Delta_\Gamma u_3 = f_3(u_1, u_3) := g_2(u_1)(h_2(u_1) - u_3); \\ \partial^\bullet u_4 + u_4 \nabla_\Gamma \cdot \mathbf{v} - d_3 \Delta_\Gamma u_4 = f_4(u_1, u_4) := g_3(u_1)(h_3(u_1) - u_4), \end{cases} \quad (6.140)$$

where $c_1 > c_3 > 0 > c_2$, $d_i > 0$, $0 < h_i(u) < 1$ and $g_i(u) > 0$ for $i \in \{1, 2, 3\}$ and $u \in \mathbb{R}$. On stationary planar domains, this model has been used to model the propagation of neuronal impulses, see [29]. In particular, the variable u_1 represent a current (which can be positive or negative), while the variables $u_k \geq 0$, $k = 2, 3, 4$, represent chemical concentrations. For this reason, we focus our attention on invariant regions contained in the stripe $S := \mathbb{R} \times [0, +\infty[^3$. In the following theorem we prove that: (i) the stripe $S := \mathbb{R} \times [0, +\infty[^3$ is invariant for (6.140) regardless of μ_{min} and μ_{max} ; (ii) if $\mu_{min} \geq 0$, bounded invariant rectangles arise in S . At the continuous level, the result holds in the specific case of stationary planar domains, see [25].

Theorem 28 (Velocity-induced invariant regions for the Hodgkin-Huxley model (6.140)).
For the LESFEM spatial discretisation of (6.140), the following statements hold:

1. For every value of the constants μ_{min} and μ_{max} defined in (6.16), the stripe $S = \mathbb{R} \times [0, +\infty[^3$ is invariant for system (6.140);
2. If $\mu_{min} \geq 0$, $\underline{\sigma}_1 \leq c_2$, $\bar{\sigma}_1 \geq c_1$ and

$$\bar{\sigma}_{i+1} \geq \left(1 + \frac{\mu_{min}}{\max_{u \in [\underline{\sigma}_1, \bar{\sigma}_1]} g_i(u)} \right)^{-1}, \quad i \in \{1, 2, 3\}, \quad (6.141)$$

then any region of the form $\Sigma := [\underline{\sigma}_1, \bar{\sigma}_1] \times \prod_{i=2}^4 [0, \bar{\sigma}_i]$ (and thus $\Sigma \subset S$) is invariant for system (6.140).

Proof. In order to prove Statement 1 we have to verify condition (6.22). To this end, we observe that

- a) For $(u_1, \dots, u_4) \in \underline{\Sigma}_2 := \mathbb{R} \times \{0\} \times [0, +\infty[^2$, we have $\underline{f}_2(u_1, u_2) = f_2(u_1, u_2) = g_1(u_1)h_1(u_1) > 0$;
- b) For $(u_1, \dots, u_4) \in \underline{\Sigma}_3 := \mathbb{R} \times [0, +\infty[\times \{0\} \times [0, +\infty[$, we have $\underline{f}_3(u_1, u_3) = f_3(u_1, u_3) = g_2(u_1)h_2(u_1) > 0$;
- c) For $(u_1, \dots, u_4) \in \underline{\Sigma}_4 := \mathbb{R} \times [0, +\infty[^2 \times \{0\}$, we have $\underline{f}_4(u_1, u_4) = f_4(u_1, u_4) = g_3(u_1)h_3(u_1) > 0$.

Then, condition (6.22) is fulfilled. This proves Statements 1. To prove Statement 2 we have to verify conditions (6.21)-(6.22). Let us assume for the moment that the strict inequality holds in (6.141). We complement the first part of the proof by observing that

- d) For $(u_1, \dots, u_4) \in \underline{\Sigma}_1 := \{\underline{\sigma}_1\} \times \prod_{i=2}^4 [0, \bar{\sigma}_i]$, we have $f_1(u_1, \dots, u_4) - \mu_{min}u_1 = k_1u_2^3u_3(c_1 - \underline{\sigma}_1) + k_2u_4^4(c_2 - \underline{\sigma}_1) + k_3 \left(c_3 - \underline{\sigma}_1 \left(1 + \frac{\mu_{min}}{k_3} \right) \right) > 0$;
- e) For $(u_1, \dots, u_4) \in \bar{\Sigma}_1 := \{\bar{\sigma}_1\} \times \prod_{i=2}^4 [0, \bar{\sigma}_i]$, we have $f_1(u_1, \dots, u_4) - \mu_{min}u_1 = k_1u_2^3u_3(c_1 - \bar{\sigma}_1) + k_2u_4^4(c_2 - \bar{\sigma}_1) + k_3 \left(c_3 - \bar{\sigma}_1 \left(1 + \frac{\mu_{min}}{k_3} \right) \right) < 0$;
- f) For $(u_1, \dots, u_4) \in \bar{\Sigma}_2 := [\underline{\sigma}_1, \bar{\sigma}_1] \times \{\bar{\sigma}_2\} \times \prod_{i=3}^4 [0, \bar{\sigma}_i]$, we have $f_2(u_1, u_2) - \mu_{min}u_2 = g_1(u_1) \left(h_1(u_1) - \bar{\sigma}_2 \left(1 + \frac{\mu_{min}}{g_1(u_1)} \right) \right) < g_1(u_1) \left(1 - \bar{\sigma}_2 \left(1 + \frac{\mu_{min}}{\max_{u \in [\underline{\sigma}_1, \bar{\sigma}_1]} g_1(u)} \right) \right) < 0$;

- g) Analogously, for $(u_1, \dots, u_4) \in \bar{\Sigma}_3 := [\underline{\sigma}_1, \bar{\sigma}_1] \times [0, \bar{\sigma}_2] \times \{\bar{\sigma}_3\} \times [0, \bar{\sigma}_4]$, we have $f_3(u_1, u_3) - \mu_{min}u_3 < 0$;
- h) Analogously, for $(u_1, \dots, u_4) \in \bar{\Sigma}_4 := [\underline{\sigma}_1, \bar{\sigma}_1] \times \prod_{i=2}^3 [0, \bar{\sigma}_i] \times \{\bar{\sigma}_4\}$, we have $f_4(u_1, u_4) - \mu_{min}u_4 < 0$.

Items a) through h) imply that conditions (6.21)-(6.22) are fulfilled. This proves Statements 2) when the strict inequality holds in (6.141). Let us now suppose that $\bar{\sigma}_k$, $k = 2, 3, 4$, fulfil the equalities in (6.141). Then it holds that

$$\Sigma = [\underline{\sigma}_1, \bar{\sigma}_1] \times \prod_{k=2}^4 [0, \bar{\sigma}_k] = \bigcap_{\varepsilon_2, \varepsilon_3, \varepsilon_4 > 0} \left([\underline{\sigma}_1, \bar{\sigma}_1] \times \prod_{k=2}^4 [0, \bar{\sigma}_k + \varepsilon_k] \right), \quad (6.142)$$

i.e. Σ is the intersection of invariant regions and is thus invariant. This completes the proof. \square

6.8 Numerical examples

The purpose of this section is to provide two numerical examples in which we (i) estimate the experimental order of convergence of the LESFEM and (ii) experimentally show the ability of Theorem 24 to find invariant regions of RDSs on evolving surfaces at the discrete level.

Example 1: Linear heat equation on an evolving sphere

In this example, we wish to estimate the experimental order of convergence of the LESFEM. As a test problem, we consider the linear heat equation given by

$$\partial^\bullet u + u \nabla_\Gamma \cdot \mathbf{v} - \frac{1}{12} \Delta_\Gamma u = u. \quad (6.143)$$

We choose $T = 1$ to be the final time. The initial domain $\Gamma(0)$ is the unit sphere \mathcal{S}^2 , that evolves under the velocity field

$$\mathbf{v}(\mathbf{x}, t) := \frac{\mathbf{x}}{t+1}, \quad (\mathbf{x}, t) \in \mathbb{R}^3 \times [0, 1], \quad (6.144)$$

and undergoes linear growth for $r = 1$, see Table 6.1. In particular, the domain $\Gamma(t)$ at time $t \in [0, T]$ is a sphere whose radius is given by the growth function $\phi(t) = t + 1$ and the minimum dilation rate fulfils $\mu_{min} = \frac{2r}{rT+1} = 1$ (see Table 6.1).

In order to determine the experimental order of convergence, we consider the analytical solution to (6.143) given by

$$u(x, y, z, t) = \frac{xyz}{(t+1)^3} \exp\left(t - 2 \log(t+1) - \frac{t}{t+1}\right), \quad (x, y, z, t) \in \mathbb{R}^3 \times [0, 1]. \quad (6.145)$$

Hence, for the initial condition we choose the solution (6.145) at $t = 0$:

$$u_0(x, y, z) = xyz, \quad (x, y, z) \in \mathcal{S}^2. \quad (6.146)$$

See Appendix for the derivation of the analytical solution (6.145).

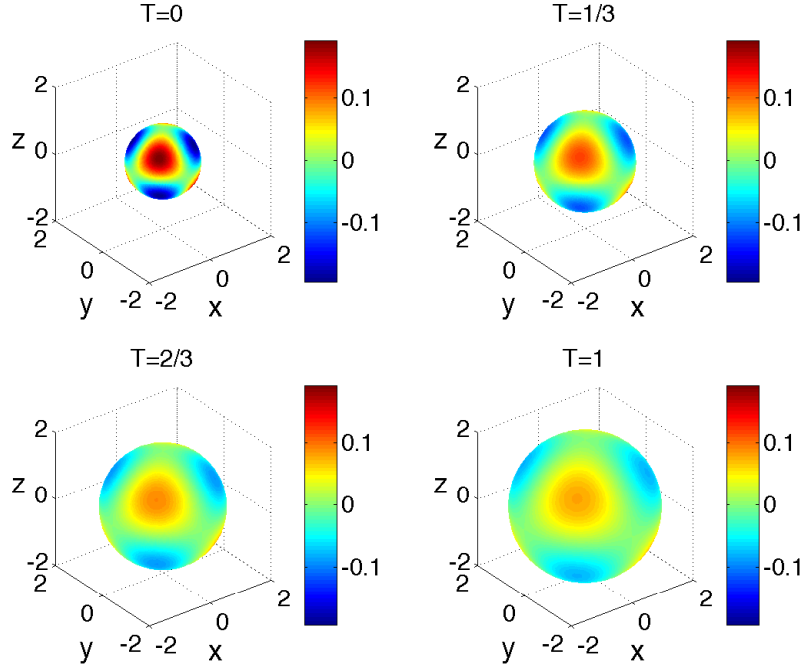


Figure 6.2: *Example 1*: Linear heat equation (6.143) on a sphere that evolves linearly with the material velocity field (6.144) with initial datum (6.146) and final time $T = 1$. Plots at different times of the numerical solution obtained on the finest mesh Γ_8 (see text) with $N = 16962$ gridpoints, initial meshsize $h_8(0) = 3.542e-2$ and timestep $\tau = 3.116e-4$. Plotted values range from -0.1924 (blue) to 0.1924 (red).

The constants $\beta = -1$ and $\mu_{min} = 1$ fulfil the sufficient conditions (6.76) and (6.78) for the discrete maximum principle for each $\tau > 0$. Hence, the LESFEM-IMEX Euler solution to (6.143) fulfils a discrete maximum principle unconditionally on τ . In order to appreciate the quadratic convergence in space we solve the problem on a sequence of eight Delaunay meshes Γ_i , $i = 1, \dots, 8$, whose mesh sizes at $t = 0$ fulfil $h_1(0) = 0.4013$ and $h_i(0) \approx \frac{h_{i-1}(0)}{\sqrt{2}}$, $i = 2, \dots, 8$. The corresponding timesteps τ_i fulfil $\tau_1 = 4e-2$ and $\tau_i = \left(\frac{h_i}{h_{i-1}}\right)^2 \tau_{i-1}$, $i = 2, \dots, 8$. In Fig. 6.2 we show a sequence of snapshots of the evolution of the numerical solution on the finest mesh Γ_8 . The experimental order of convergence is computed by measuring the error, in $L^\infty([0, T], L^2(\Gamma_h(t)))$ norm, between the numerical solution U and the piecewise linear interpolant $I_h(u)$ of the exact solution. The result is shown in Fig. 6.3: the convergence is experimentally optimal in that it is quadratic in the meshsize and linear in the timestep.

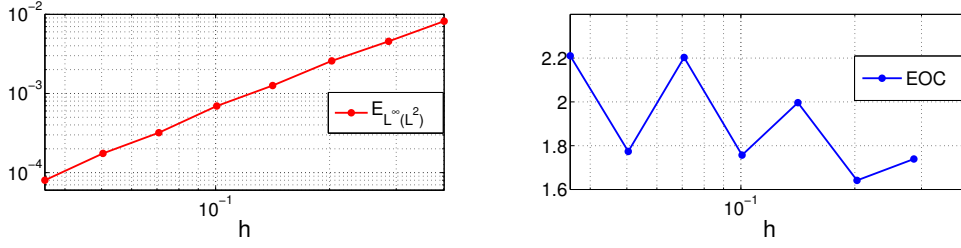


Figure 6.3: *Example 1*: Linear heat equation (6.143) on a sphere that evolves linearly with the material velocity field (6.144), with initial datum (6.146) and final time $T = 1$, solved on a sequence of eight Delaunay meshes Γ_i , $i = 1, \dots, 8$, and corresponding timesteps τ_i , $i = 1, \dots, 8$, as described in the text. Error in $L^\infty(0, T, L^2(\Gamma_h(t)))$ norm (left panel) and experimental rate of convergence (right panel). The quadratic convergence in space is optimal.

Numerical Example 2: RDS with Thomas kinetics and invariant regions

In this example, we show that the LESFEM-IMEX Euler preserves the invariant regions of RDSs on evolving surfaces. Let us consider the following RDS with Thomas kinetics

$$\begin{cases} \partial^\bullet u_1 + u_1 \nabla_\Gamma \cdot \mathbf{v} - d_1 \Delta_\Gamma u_1 = f_1(u_1, u_2) := \gamma \left(a - u_1 - \rho \frac{u_1 u_2}{1 + u_1 + K u_1^2} \right); \\ \partial^\bullet u_2 + u_2 \nabla_\Gamma \cdot \mathbf{v} - \Delta_\Gamma u_2 = f_2(u_1, u_2) := \gamma \left(\alpha(b - u_2) - \rho \frac{u_1 u_2}{1 + u_1 + K u_1^2} \right), \end{cases} \quad (6.147)$$

considered in Section 6.7.2, with the following reaction parameters:

$$a = 150, \quad b = 100, \quad \rho = 13, \quad K = 0.05, \quad \gamma = 1, \quad (6.148)$$

as in [95]. With these parameters, the system (6.147) admits, in the absence of domain growth, the homogeneous steady state $P \approx (37.7382, 25.1588)$ calculated using Newton-Raphson method on a stationary domain. Notice that the diffusion coefficient for u_2 has been normalised to 1 for convenience, and we choose $d_1 = 0.01$. The initial domain $\Gamma(0)$ is the *Dupin ring cyclide* considered in [59, Appendix B], rescaled for convenience, given by

$$\mathcal{D} := \left\{ (x, y, z) \in \mathbb{R}^3 : \left(9(x^2 + y^2 + z^2) + \frac{261}{100} \right)^2 - 4 \left(6x - \frac{\sqrt{39}}{10} \right)^2 - \frac{3249}{25} y^2 = 0 \right\}, \quad (6.149)$$

an orientable surface without boundary that is topologically equivalent to a torus. The surface evolves under the isotropic velocity field (6.46) with

$$S(t) = \frac{rK(K-1)}{K-1 + \exp(Krt)} > 0, \quad t \in [0, T], \quad (6.150)$$

with $r = 0.2$, $K = 3$ and undergoes a logistic growth, see Table 6.1. As final time we choose $T = 100$. From Theorem 20, it follows that the corresponding dilation rates fulfil

$$\mu_{min} = \mu_{min}^* \approx 0, \quad \mu_{max} = \mu_{max}^* = 0.8. \quad (6.151)$$

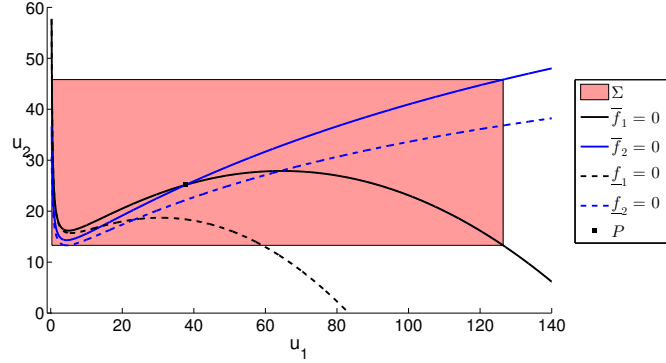


Figure 6.4: *Example 2*: Thomas RDS (6.147) with reaction parameters (6.148) on any surface that evolves logistically with the material velocity field defined by (6.46) and (6.150). Plot of the region (6.152), which is invariant for the considered system under the timestep restriction $\tau \leq 1.676e-3$. This region is obtained by considering the nullclines of the modified kinetics defined in (6.153)-(6.154).

From Theorem (26), model (6.147) possesses arbitrarily large bounded invariant regions contained in the positive orthant. Let

$$\Sigma = [\underline{\sigma}_1, \bar{\sigma}_1] \times [\underline{\sigma}_2, \bar{\sigma}_2] \approx [0.3366, 126.4194] \times [13.2938, 45.8182] \quad (6.152)$$

be the smallest bounded region that (i) contains P and (ii) meets the modified inward flux conditions (6.103)-(6.104) with $\tau = \bar{\tau} := 2e-3$ and thus (6.103)-(6.104) hold for all $0 < \tau \leq \bar{\tau}$. As illustrated in Fig. 6.4, Σ is obtained by considering the nullclines of the modified kinetics

$$\bar{f}_k(u_1, u_2) := f_k(u_1, u_2) - \mu_{min} u_k, \quad k = 1, 2; \quad (6.153)$$

$$f_k(u_1, u_2) := f_k(u_1, u_2) - \frac{e^{\bar{\tau} \mu_{max}} - 1}{\bar{\tau}} u_k, \quad k = 1, 2. \quad (6.154)$$

It is easy to see that, on a region of the form $\Sigma = [\underline{\sigma}_1, \bar{\sigma}_1] \times [\underline{\sigma}_2, \bar{\sigma}_2]$, the Lipschitz constants L_1 and L_2 of the kinetics f_1 and f_2 of (6.147) fulfil

$$L_1 \leq \hat{L}_1 := \gamma \sqrt{(1 + \rho \bar{\sigma}_2)^2 + \rho^2}, \quad L_2 \leq \hat{L}_2 := \gamma \sqrt{(\rho \bar{\sigma}_2)^2 + (\alpha + \rho)^2}.$$

Hence, the timestep restriction (6.105) becomes $\tau \leq \frac{1}{\max(\hat{L}_1, \hat{L}_2)} \approx 1.676e-3$. It follows that Σ is invariant for the LESFEM-IMEX Euler full discretisation under the timestep restriction $0 < \tau \leq \min\left(\bar{\tau}, \frac{1}{\max(\hat{L}_1, \hat{L}_2)}\right) \approx 1.676e-3$. We choose $\tau = 1e-3$. The region Σ is smaller than the invariant region provided in Theorem 26, which has a simple analytical expression but is not optimal. The following initial condition

$$\begin{cases} u_{1,0}(x, y, z) = \underline{\sigma}_1 + (\bar{\sigma}_1 - \underline{\sigma}_1)\psi(x, y, z); \\ u_{2,0}(x, y, z) = \underline{\sigma}_2 + (\bar{\sigma}_2 - \underline{\sigma}_2)\psi(x, y, z), \end{cases} \quad (6.155)$$

where $\psi(x, y, z) := \sqrt{1 - 25(\min(|y|, \frac{1}{5}))^2}$ fulfils $(u_{1,0}(\mathbf{x}), u_{2,0}(\mathbf{x})) \in \Sigma$ for all $\mathbf{x} \in \Gamma(0)$ and is shown in the first snap shot of Fig. 6.5. We solve the problem with $\tau = 1e-3$ on a sequence

i	$h_i(0)$	$\min_{t \in [\tau, T]} \underline{\eta}_1$	$\min_{t \in [\tau, T]} \bar{\eta}_1$	$\min_{t \in [\tau, T]} \underline{\eta}_2$	$\min_{t \in [\tau, T]} \bar{\eta}_2$
1	1.190e+00	8.482e-02	1.841e-01	-8.001e-01	5.214e-01
2	8.537e-01	8.005e-02	5.281e-01	-5.318e-01	6.397e-01
3	5.898e-01	5.860e-02	1.759e-01	-5.083e-01	7.626e-01
4	4.273e-01	2.259e-02	1.793e-01	-6.559e-01	5.147e-01
5	3.011e-01	-7.288e-02	1.791e-01	-6.338e-01	8.181e-01
6	2.114e-01	-3.555e-01	1.241e-01	-5.017e-01	4.297e-01
7	1.531e-01	-5.376e-01	1.321e-01	-3.816e-01	6.152e-01

Table 6.2: *Example 2*: Thomas RDS (6.147) on the Dupin ring cyclide (6.149) that evolves logarithmically with the material velocity field defined by (6.46) and (6.150), with reaction parameters (6.148), initial datum (6.155) and final time $T = 100$. Invariance analysis for ESFEM, carried out by solving the system on a sequence of seven meshes Γ_i , $i = 1, \dots, 7$ as described in the text with a fixed timestep $\tau = 1e-3$. The region Σ defined in (6.152) is not invariant for ESFEM for any $i = 1, \dots, 7$, as the method violates the minimum of U_1 for $i = 5, 6, 7$ and the minimum of U_2 for each $i = 1, \dots, 7$.

of seven meshes $\Gamma_{h,i}(t)$, $i = 1, \dots, 7$, with decreasing initial meshsizes $h_i(0)$, $i = 1, \dots, 7$, with both the LESFEM-IMEX Euler and ESFEM-IMEX Euler methods. Snap shots of the LESFEM-IMEX Euler numerical solution obtained on the finest mesh $\Gamma_{h,7}$ at different times are shown in Fig. 6.5. In particular, at the final time $T = 100$ (see last snap shot of Fig. 6.5), the surface is stationary up to machine precision and the numerical solution has reached a stationary pattern. For a given numerical solution (U_1, U_2) on the mesh $\Gamma_{h,i}$, $i = 1, \dots, 7$, consider the following functions

$$\bar{\eta}_k(t) := \min_{\mathbf{x} \in \Gamma_{h,i}(t)} (\bar{\sigma}_k - U_k(\mathbf{x}, t)), \quad \underline{\eta}_k(t) := \min_{\mathbf{x} \in \Gamma_{h,i}(t)} (U_k(\mathbf{x}, t) - \underline{\sigma}_k), \quad k = 1, 2.$$

These functions are the oriented distances of the numerical solution (U_1, U_2) from the edges of Σ . If the oriented distances $\underline{\eta}_k$ and $\bar{\eta}_k$, $k = 1, 2$, stay positive at all times, it means that (U_1, U_2) is in Σ at all times. For all $i = 1, \dots, 7$, we show the minima over the time interval $[\tau, T]$ (i.e. excluding the initial data) of $\underline{\eta}_k$ and $\bar{\eta}_k$, $k = 1, 2$, for both the ESFEM-IMEX Euler and LESFEM-IMEX Euler methods in Tables 6.2 and 6.3, respectively. We observe that ESFEM-IMEX Euler violates Σ for all $i = 1, \dots, 7$, while LESFEM-IMEX Euler preserves Σ for all $i = 1, \dots, 7$.

6.9 Conclusions

We have presented a LSFEM spatial discretisation and a LSFEM-IMEX Euler full discretisation of RCDSs on evolving compact surfaces. We have introduced indicators, called *dilation rates* that measure the rate of evolution of the continuous and triangulated surfaces.

We have proved sufficient conditions for a rectangular region in the phase-space to be invariant (i) for the LESFEM space discretisation and (ii) for the LESFEM-IMEX Euler full discretisation. These sufficient conditions account for the dilation rates of the discrete surface.

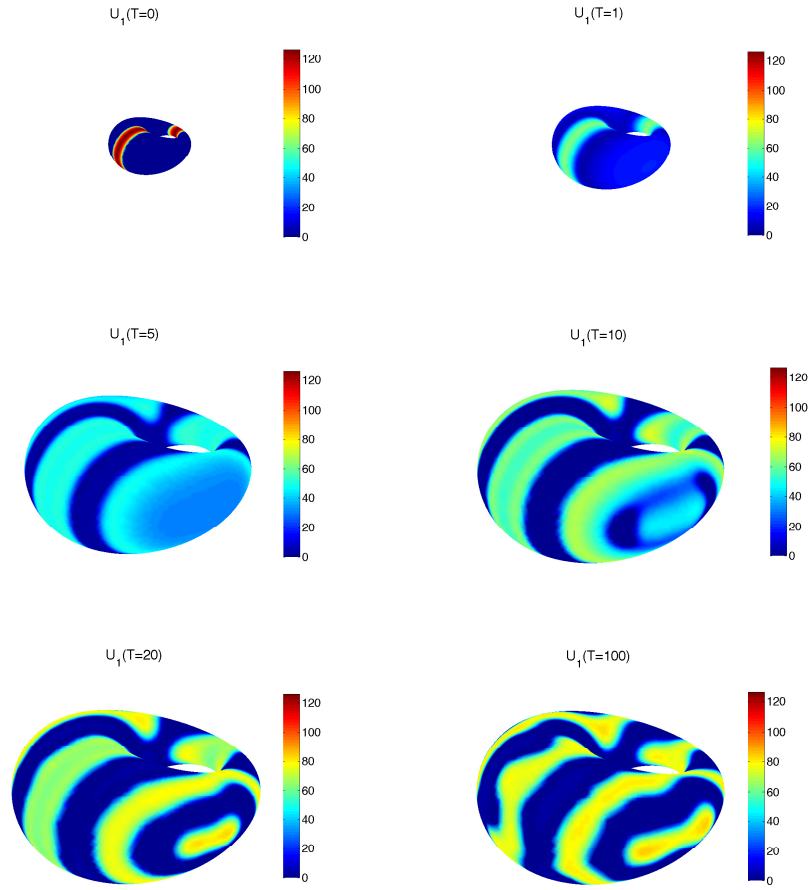


Figure 6.5: *Example 2*: Thomas RDS (6.147) on the Dupin ring cyclide (6.149) that evolves logarithmically with the material velocity field defined by (6.46) and (6.150), with reaction parameters (6.148), initial datum (6.155) and final time $T = 100$. Snap shots of the U_1 component of the LESFEM-IMEX Euler numerical solution at different times, obtained on the finest mesh Γ_7 (see text) with initial meshsize $h_7(0) = 1.531e-1$ and timestep $\tau = 1e-3$.

i	$h_i(0)$	$\min_{t \in [\tau, T]} \eta_1$	$\min_{t \in [\tau, T]} \bar{\eta}_1$	$\min_{t \in [\tau, T]} \eta_2$	$\min_{t \in [\tau, T]} \bar{\eta}_2$
1	1.190e+00	1.060e-01	1.738e-01	7.6017752487788e-02	2.665e-01
2	8.537e-01	1.060e-01	4.796e-01	7.6017752487775e-02	3.676e-01
3	5.898e-01	1.060e-01	1.958e-01	7.6017752487774e-02	5.336e-01
4	4.273e-01	1.060e-01	2.163e-01	7.6017752487768e-02	6.679e-01
5	3.011e-01	1.060e-01	1.934e-01	7.6017752487765e-02	9.708e-01
6	2.114e-01	1.060e-01	1.909e-01	7.6017752487761e-02	9.401e-01
7	1.531e-01	1.060e-01	1.899e-01	7.6017752487756e-02	9.367e-01

Table 6.3: *Example 2*: Thomas RDS (6.147) on the Dupin ring cyclide (6.149) that evolves logistically with the material velocity field defined by (6.46) and (6.150), with reaction parameters (6.148), initial datum (6.155) and final time $T = 100$. Invariance analysis for LESFEM, carried out by solving the system on a sequence of seven meshes Γ_i , $i = 1, \dots, 7$ as described in the text with a fixed timestep $\tau = 1e-3$. The region Σ defined in (6.152) is invariant for all $i = 1, \dots, 7$. The minima of $\underline{\eta}_1$ (and so the minima of U_1) coincide up to machine precision.

At the fully discrete level, a timestep restriction that depends on the Lipschitz constants of the kinetics is required.

By applying the proposed theory, we have classified some families of invariant regions for the LSFEM spatial discretisation of the Schakenberg, the Thomas, the Hodgkin-Huxley and the DIB models on evolving surfaces.

We have provided two numerical examples to show:

1. the $L^\infty([0, T], L^2(\Gamma(t)))$ optimal convergence (i.e. quadratic in the meshsize and linear in the timestep) of the LESFEM-IMEX Euler full discretisation of the linear heat equation on a linearly growing sphere, even though a theoretical convergence analysis is beyond the scope of this thesis;
2. the existence of an invariant rectangle for the LESFEM-IMEX Euler full discretisation of the Thomas RDS on a logistically growing Dupin cyclide.

Chapter 7

Conclusions and possible extensions

In this work we have proposed novel extensions of the SFEM for the numerical approximation of partial differential equations on stationary or evolving surfaces. The proposed methods address two problems in numerical analysis: (i) polygonal approximation of the surface and (ii) preservation of maximum principles and invariant regions under discretisation. The main findings of this thesis can be summarised as follows:

- In Chapter 3 we have presented a Surface Virtual Element Method (SVEM) for the numerical approximation of the Laplace-Beltrami equation on a stationary surface Γ . The method is well-defined on arbitrary (possibly discontinuous) polygonal approximations of the surface, rather than just on triangulations. The possibility of approximating the surface with arbitrary polygons can provide a computational advantage in several applications since (i) particular geometries can be approximated with fewer elements on equal number of nodes and (ii) multiple meshes can be easily pasted together through juxtaposition by imposing *virtual continuity*. We have proven optimal convergence in $H^1(\Gamma)$ norm (that is linear in the meshsize).
- In chapter 4 we have presented a Lumped Surface Finite Element Method (LSFEM) for a semilinear heat equation on a stationary surface Γ and a full discretisation based on the implicit-explicit (IMEX) Euler method of the LSFEM spatially discrete formulation. Both the spatial- and fully discrete methods preserve the maximum principle under discretisations if the mesh meets the Delaunay angle condition. No restriction on the meshsize is required, while a timestep restriction depending on the source term of the equation is required at the fully discrete level. We have proven optimal convergence in $L^\infty([0, T], L^2(\Gamma))$ norm for both the spatially- and fully discrete methods (that is quadratic in the meshsize and linear in the timestep).
- In Chapter 5 we have extended the LSFEM and the IMEX Euler-LSFEM considered in the previous chapter to solve reaction-cross-diffusion systems (RCDSs) on a stationary surface Γ . Both the spatial- and fully discrete methods preserve the invariant regions of the continuous PDE problem under discretisations if the mesh meets the Delaunay angle condition. No restriction on the meshsize is required, while a timestep restriction depending on the Lipschitz constants of the kinetics is required at the fully discrete level. As well as in the previous chapter, we have proven optimal convergence in $L^\infty([0, T], L^2(\Gamma))$ norm for both the spatially- and fully discrete methods.

- Finally, In Chapter 6 we have further extended the LSFEM and the IMEX Euler-LSFEM to solve the linear heat equation and reaction-diffusion systems (RDSs) on an evolving surface $\Gamma(t)$. We have introduced novel indicators, called *dilation rates*, that measure the rate of growth or contraction of both the continuous and triangulated surfaces. For the linear heat equation we have proven sufficient conditions for the maximum principle to hold at the spatially- and fully discrete levels. For RDSs we have proven sufficient conditions for a region in the phase-space to be invariant at the spatially- and fully discrete levels. We have conjectured that analogous sufficient conditions hold at the continuous level. These sufficient conditions account for the dilation rates of the surface, thus quantifying the impact of surface evolution on the maximum principle for the heat equation and on the invariance of sets in the phase-space for RDSs. We have classified families of invariant regions -depending on the dilation rates- for the *activator-depleted*, the Thomas, the DIB and the Hodgkin-Huxley RD models.

We now outline possible direction for future studies:

1. Nonlinear cross-diffusion. In [123] the authors consider RCDSs with nonlinear cross-diffusion on stationary planar domains. They prove that, in the absence of nonlinearities in the diffusion term, the only possible invariant regions have polygonal shape while, in the presence of nonlinear cross-diffusion, invariant regions with curved boundaries can exist. To the best of the author's knowledge, no numerical evidence of such invariant regions with curved boundaries is available in the literature. Hence, devising a numerical method that preserves the invariant regions of RCDSs with nonlinear cross-diffusion is a possible direction for future studies.
2. Higher order convergence in space. Higher orders of convergence can be achieved by adopting curved finite elements, as shown in [32]. However, raising the order of convergence of the presented methods provides additional challenges, in fact:
 - For the SVEM, the increased complexity arising from curved elements would require suitable techniques to retain computability;
 - For the LSFEM, the main bottleneck is the impossibility of formulating a Lagrangian finite element method of arbitrarily high order such that the resulting stiffness matrix is an M -matrix. In fact, if for linear Lagrangian elements it is sufficient to impose the Delaunay angle condition, the work in [74] shows that, for quadratic Lagrangian elements a much more restrictive angle condition is required, while for cubic Lagrangian elements there is no angle condition that guarantees a discrete maximum principle. Hence, novel machinery would be required.
3. Different time integrators. The LSFEM for stationary surfaces and the LESFEM for evolving surfaces could be combined with different time discretisation schemes for two reasons. First, by choosing a different time discretisation, the order of convergence in time can be increased. For instance, in [42] the authors consider Runge-Kutta time integrators combined with standard finite elements for parabolic problems on evolving surfaces. Second, some time integrators are suited for particular kinds of solutions. For instance, ESFEM and LESFEM could be combined with a symplectic time integrator to approximate oscillating solutions.

4. Preservation of the Delaunay condition under evolution. On evolving surfaces, the assumption that the mesh preserves the Delaunay condition under evolution is too restrictive in many cases in which non-isotropic growth is considered. Some adaptive mesh algorithms that produce quality evolving meshes (e.g. free of excessively distorted elements) have been proposed in the literature, we mention for instance the work in [77]. However, to the best of the author's knowledge, the preservation of the Delaunay condition under evolution remains an open problem.

Bibliography

- [1] B Ahmad, A Alsaedi, F Brezzi, L D Marini, and A Russo. Equivalent projectors for virtual element methods. *Computers & Mathematics with Applications*, 66(3):376–391, 2013. doi:10.1016/j.camwa.2013.05.015.
- [2] A Alphonse, C M Elliott, and B Stinner. An abstract framework for parabolic PDEs on evolving spaces. *Portugaliae Mathematica*, 72(1):1–46, 2015. doi:10.4171/pm/1955.
- [3] P F Antonietti, L Beirão Da Veiga, S Scacchi, and M Verani. A C^1 virtual element method for the Cahn-Hilliard equation with polygonal meshes. *SIAM Journal on Numerical Analysis*, 54(1):34–56, 2016. doi:10.1137/15m1008117.
- [4] T Aubin and Y-Y Li. On the best Sobolev inequality. *Journal de Mathématiques Pures et Appliquées*, 78(4):353 – 387, 1999. doi:10.1016/s0021-7824(99)00012-4.
- [5] B Ayuso de Dios, K Lipnikov, and G Manzini. The nonconforming virtual element method. *ESAIM: Mathematical Modelling and Numerical Analysis*, 50(3):879–904, 2016. doi:10.1051/m2an/2015090.
- [6] R Barreira, C M Elliott, and A Madzvamuse. The surface finite element method for pattern formation on evolving biological surfaces. *Journal of Mathematical Biology*, 63(6):1095–1119, 2011. doi:10.1007/s00285-011-0401-0.
- [7] D Becherer, M Schweizer, et al. Classical solutions to reaction–diffusion systems for hedging problems with interacting Itô and point processes. *The Annals of Applied Probability*, 15(2):1111–1144, 2005. doi:10.1214/10505160400000846.
- [8] L Beirão da Veiga, F Brezzi, A Cangiani, G Manzini, L D Marini, and A Russo. Basic principles of virtual element methods. *Mathematical Models and Methods in Applied Sciences*, 23(01):199–214, 2013. doi:10.1142/s0218202512500492.
- [9] L Beirão da Veiga, F Brezzi, L D Marini, and A Russo. The hitchhiker’s guide to the virtual element method. *Mathematical Models and Methods in Applied Sciences*, 24(08):1541–1573, 2014. doi:10.1142/S021820251440003X.
- [10] M F Benedetto, S Berrone, and S Scialò. A globally conforming method for solving flow in discrete fracture networks using the virtual element method. *Finite Elements in Analysis and Design*, 109:23–36, 2016. doi:10.1016/j.finel.2015.10.003.
- [11] N Benkemoun, A Ibrahimbegovic, and J-B Colliat. Anisotropic constitutive model of plasticity capable of accounting for details of meso-structure of two-phase composite

- material. *Computers & Structures*, 90:153–162, 2012. doi:10.1016/j.compstruc.2011.09.003.
- [12] M Bertalmío, L T Cheng, S Osher, and G Sapiro. Variational problems and partial differential equations on implicit surfaces. *Journal of Computational Physics*, 174(2):759–780, 2001. doi:10.1007/0-387-21810-6_20.
- [13] W G Bessler. A new computational approach for SOFC impedance from detailed electrochemical reaction–diffusion models. *Solid State Ionics*, 176(11):997–1011, 2005. doi:10.1016/j.ssi.2005.01.002.
- [14] K N Blazakis, A Madzvamuse, C C Reyes-Aldasoro, V Styles, and C Venkataraman. Whole cell tracking through the optimal control of geometric evolution laws. *Journal of Computational Physics*, 297:495–514, 2015. doi:10.1016/j.jcp.2015.05.014.
- [15] D Boffi and L Gastaldi. Stability and geometric conservation laws for ALE formulations. *Computer Methods in Applied Mechanics and Engineering*, 193(42-44):4717–4739, 2004. doi:10.1016/j.cma.2004.02.020.
- [16] S Brenner and R Scott. *The mathematical theory of finite element methods*, volume 15. Springer Science & Business Media, 2007. doi:10.1007/978-1-4757-4338-8.
- [17] F Brezzi and L D Marini. Virtual element methods for plate bending problems. *Computer Methods in Applied Mechanics and Engineering*, 253:455–462, 2013. doi:10.1016/j.cma.2012.09.012.
- [18] E Calabi et al. An extension of E. Hopf’s maximum principle with an application to Riemannian geometry. *Duke Mathematical Journal*, 25(1):45–56, 1958. doi:10.1215/s0012-7094-58-02505-5.
- [19] M A J Chaplain, M Ganesh, and I G Graham. Spatio-temporal pattern formation on spherical surfaces: numerical simulation and application to solid tumour growth. *Journal of Mathematical Biology*, 42(5):387–423, 2001. doi:10.1007/s002850000067.
- [20] P Chatzipantelidis, Z Horváth, and V Thomée. On preservation of positivity in some finite element methods for the heat equation. *Comp. Meth. Appl. Math.*, 15(4):417–437, 2015. doi:10.1515/cmam-2015-0018.
- [21] V Chellaboina, S P Bhat, W M Haddad, and D S Bernstein. Modeling and analysis of mass-action kinetics. In *Nonnegative and Compartmental Dynamical Systems*, chapter 9, pages 281–314. Princeton University Press, 2010. doi:10.1515/9781400832248.281.
- [22] J Chen. A memory efficient discontinuous Galerkin finite-element time-domain scheme for simulations of finite periodic structures. *Microwave and Optical Technology Letters*, 56(8):1929–1933, 2014. doi:10.1002/mop.28483.
- [23] Z Chen and J Zou. Finite element methods and their convergence for elliptic and parabolic interface problems. *Numerische Mathematik*, 79(2):175–202, 1998. doi:10.1007/s002110050336.

- [24] AY Chernyshenko and M A Olshanskii. Non-degenerate Eulerian finite element method for solving PDEs on surfaces. *Russian Journal of Numerical Analysis and Mathematical Modelling*, 28(2):101–124, 2013. doi:10.1515/rnam-2013-0007.
- [25] K N Chueh, C C Conley, and J A Smoller. Positively invariant regions for systems of nonlinear diffusion equations. *Indiana Univ. Math. J.*, 26(2):373–392, 1977.
- [26] P G Ciarlet. *The finite element method for elliptic problems*. SIAM, 2002. doi:10.1137/1.9780898719208.
- [27] F Corson, O Hamant, S Bohn, J Traas, A Boudaoud, and Y Couder. Turning a plant tissue into a living cell froth through isotropic growth. *Proceedings of the National Academy of Sciences*, 106(21):8453–8458, 2009. doi:10.1073/pnas.0812493106.
- [28] E J Crampin, E A Gaffney, and P K Maini. Reaction and diffusion on growing domains: scenarios for robust pattern formation. *Bulletin of Mathematical Biology*, 61(6):1093–1120, 1999. doi:10.1006/bulm.1999.0131.
- [29] J Cronin. *Mathematical aspects of Hodgkin-Huxley neural theory*, volume 7. Cambridge University Press, 1987. doi:10.1017/cbo9780511983955.
- [30] L Beirão Da Veiga, F Brezzi, and L D Marini. Virtual elements for linear elasticity problems. *SIAM Journal on Numerical Analysis*, 51(2):794–812, 2013. doi:10.1137/120874746.
- [31] F Dassi. *Advanced techniques for the generation and the aptation of complex surface meshes*. PhD thesis, Politecnico di Milano, 2014.
- [32] A Demlow. Higher-order finite element methods and pointwise error estimates for elliptic problems on surfaces. *SIAM Journal on Numerical Analysis*, 47(2):805–827, 2009. doi:10.1137/070708135.
- [33] A Demlow and G Dziuk. An adaptive finite element method for the Laplace–Beltrami operator on implicitly defined surfaces. *SIAM Journal on Numerical Analysis*, 45(1):421–442, 2007. doi:10.1137/050642873.
- [34] Q Du, L Ju, and L Tian. Finite element approximation of the Cahn–Hilliard equation on surfaces. *Comp. Meths. Appl. Mech. Eng.*, 200(29):2458–2470, 2011. doi:10.1016/j.cma.2011.04.018.
- [35] Z Du and B Lai. Transition layers for an inhomogeneous allen-cahn equation in riemannian manifolds. *Discrete & Continuous Dynamical Systems-A*, 33(4):1407–1429, 2013. doi:10.3934/dcds.2013.33.1407.
- [36] R Dyer. *Self-Delaunay meshes for surfaces*. PhD thesis, Simon Fraser University, 2010. URL: <http://summit.sfu.ca/system/files/iritems1/10038/etd5945.pdf>.
- [37] G Dziuk. Finite elements for the Beltrami operator on arbitrary surfaces. *Partial Differential Equations and Calculus of Variations*, pages 142–155, 1988. doi:10.1007/bfb0082865.

- [38] G Dziuk and C M Elliott. Finite elements on evolving surfaces. *IMA Journal of Numerical Analysis*, 27(2):262–292, 2007. doi:10.1093/imanum/drl023.
- [39] G Dziuk and C M Elliott. Surface finite elements for parabolic equations. *Journal of Computational Mathematics -International Edition-*, 25(4):385, 2007. URL: <http://www.jstor.org/stable/43693376>.
- [40] G Dziuk and C M Elliott. Finite element methods for surface PDEs. *Acta Numerica*, 22:289–396, 2013. doi:10.1017/s0962492913000056.
- [41] G Dziuk and C M Elliott. L^2 -estimates for the Evolving Surface Finite Element Method. *Mathematics of Computation*, 82(281):1–24, 2013. doi:10.1090/s0025-5718-2012-02601-9.
- [42] G Dziuk, C Lubich, and D Mansour. Runge–Kutta time discretization of parabolic differential equations on evolving surfaces. *IMA Journal of Numerical Analysis*, 32(2):394–416, 2011. doi:10.1093/imanum/drr017.
- [43] C Eilks and C M Elliott. Numerical simulation of dealloying by surface dissolution via the evolving surface finite element method. *Journal of Computational Physics*, 227(23):9727–9741, 2008. doi:10.1016/j.jcp.2008.07.023.
- [44] C M Elliott and T Ranner. Evolving Surface Finite Element Method for the Cahn–Hilliard equation. *Numerische Mathematik*, 129(3):483–534, 2015. doi:10.1007/s00211-014-0644-y.
- [45] C M Elliott and B Stinner. Modeling and computation of two phase geometric biomembranes using surface finite elements. *Journal of Computational Physics*, 229(18):6585–6612, 2010. doi:10.1016/j.jcp.2010.05.014.
- [46] C M Elliott, B Stinner, and C Venkataraman. Modelling cell motility and chemotaxis with evolving surface finite elements. *Journal of The Royal Society Interface*, 9(76):3027–3044, 2012. doi:10.1098/rsif.2012.0276.
- [47] C M Elliott and A M Stuart. The global dynamics of discrete semilinear parabolic equations. *SIAM J Num. Anal.*, 30(6):1622–1663, 1993. doi:10.1137/0730084.
- [48] C M Elliott and C Venkataraman. Error analysis for an ALE evolving surface finite element method. *Numerical Methods for Partial Differential Equations*, 31(2):459–499, 2015. doi:10.1002/num.21930.
- [49] I Faragó, J Karátson, and S Korotov. Discrete maximum principles for nonlinear parabolic PDE systems. *IMA J. Num. Anal.*, 32(4):1541–1573, 2012. doi:10.1093/imanum/drr050.
- [50] G E Fasshauer, F J Hickernell, and H Woźniakowski. On dimension-independent rates of convergence for function approximation with Gaussian kernels. *SIAM Journal on Numerical Analysis*, 50(1):247–271, 2012. doi:10.1137/10080138x.
- [51] S C Ferreira Jr, M L Martins, and M J Vilela. Reaction-diffusion model for the growth of avascular tumor. *Phys. Rev. E*, 65(2), 2002. doi:10.1103/physreve.65.021907.

- [52] N Flyer, E Lehto, S Blaise, G B Wright, and A St-Cyr. A guide to RBF-generated finite differences for nonlinear transport: Shallow water simulations on a sphere. *Journal of Computational Physics*, 231(11):4078–4095, 2012. doi:10.1016/j.jcp.2012.01.028.
- [53] N Flyer and G B Wright. Transport schemes on a sphere using radial basis functions. *Journal of Computational Physics*, 226(1):1059–1084, 2007. doi:10.1016/j.jcp.2007.05.009.
- [54] B Fornberg and N Flyer. Solving PDEs with radial basis functions. *Acta Numerica*, 24:215–258, 2015. doi:10.1017/s0962492914000130.
- [55] M Frittelli, A Madzvamuse, I Sgura, and C Venkataraman. Lumped finite elements for reaction-cross-diffusion systems on stationary surfaces. *Computers & Mathematics with Applications*, 74(12):3008 – 3023, 2017. doi:10.1016/j.camwa.2017.07.044.
- [56] M Frittelli, A Madzvamuse, I Sgura, and C Venkataraman. Preserving invariance properties of reaction-diffusion systems on stationary surfaces. *IMA Journal of Numerical Analysis*, 2017. Published online. doi:10.1093/imanum/drx058.
- [57] M Frittelli, A Madzvamuse, I Sgura, and C Venkataraman. Numerical preservation of velocity induced invariant regions for reaction-diffusion systems on evolving surfaces. *Journal of Scientific Computing*, 77(2):971–1000, 2018. doi:10.1007/s10915-018-0741-7.
- [58] M Frittelli and I Sgura. Virtual element method for the Laplace-Beltrami equation on surfaces. *ESAIM: Mathematical Modelling and Numerical Analysis*, 52(3):965–993, 2017. doi:10.1051/m2an/2017040.
- [59] E J Fuselier and G B Wright. A high-order kernel method for diffusion and reaction-diffusion equations on surfaces. *Journal of Scientific Computing*, 56(3):535–565, 2013. doi:10.1007/s10915-013-9688-x.
- [60] M R Garvie and C Trenchea. Finite element approximation of spatially extended predator–prey interactions with the Holling type II functional response. *Numerische Mathematik*, 107(4):641–667, 2007. doi:10.1007/s00211-007-0106-x.
- [61] A Gerisch and M A J Chaplain. Robust numerical methods for taxis–diffusion–reaction systems: Applications to biomedical problems. *Math. Comp. Mod.*, 43(1-2):49–75, 2006. doi:10.1016/j.mcm.2004.05.016.
- [62] S Ghorai and S Poria. Turing patterns induced by cross-diffusion in a predator-prey system in presence of habitat complexity. *Chaos, Solitons & Fractals*, 91:421–429, 2016. doi:10.1016/j.chaos.2016.07.003.
- [63] A Gierer and H Meinhardt. A theory of biological pattern formation. *Kybernetik*, 12(1):30–39, 1972. doi:10.1007/bf00289234.
- [64] D Gilbarg and N S Trudinger. *Elliptic partial differential equations of second order*. Springer, 2015. doi:10.1007/978-3-642-61798-0.

- [65] E González-Olivares and R Ramos-Jiliberto. Dynamic consequences of prey refuges in a simple model system: more prey, fewer predators and enhanced stability. *Ecological modelling*, 166(1):135–146, 2003. doi:10.1016/s0304-3800(03)00131-5.
- [66] J Grande and A Reusken. A higher order finite element method for partial differential equations on surfaces. *SIAM Journal on Numerical Analysis*, 54(1):388–414, 2016. doi:10.1137/14097820x.
- [67] J B Greer. An improvement of a recent Eulerian method for solving PDEs on general geometries. *Journal of Scientific Computing*, 29(3):321–352, 2006. doi:10.1007/s10915-005-9012-5.
- [68] A A Grigor’yan. The heat equation on noncompact riemannian manifolds. *Matematicheskii Sbornik*, 182(1):55–87, 1991. doi:10.1070/sm1992v072n01abeh001410.
- [69] Ø Grøn and A Næss. *Einstein’s Theory: A Rigorous Introduction for the Mathematically Untrained*. Springer Science & Business Media, 2011. doi:10.5860/choice.49-5120.
- [70] E Hebey and F Robert. Sobolev spaces on manifolds. In *Handbook of Global Analysis*, pages 375–415. Elsevier Science Ltd, 2008. doi:10.1016/b978-044452833-9.50008-5.
- [71] S Hittmeir and A Jüngel. Cross diffusion preventing blow-up in the two-dimensional Keller–Segel model. *SIAM J Math. Anal.*, 43(2):997–1022, 2011. doi:10.1137/100813191.
- [72] A L Hodgkin and A F Huxley. A quantitative description of membrane current and its application to conduction and excitation in nerve. *The Journal of physiology*, 117(4):500–544, 1952. doi:10.1016/s0092-8240(05)80004-7.
- [73] D Hoff. Stability and convergence of finite difference methods for systems of nonlinear reaction-diffusion equations. *SIAM J. Num. Anal.*, 15(6):1161–1177, 1978. doi:10.1137/0715077.
- [74] L Höhn and H D Mittelmann. Some remarks on the discrete maximum-principle for finite elements of higher order. *Computing*, 27(2):145–154, 1981. doi:10.1007/bf02243548.
- [75] T Kanai, H Suzuki, J Mitani, and F Kimura. Interactive mesh fusion based on local 3D metamorphosis. In *Graphics Interface*, volume 99, pages 148–156, 1999. URL: <http://mitani.cs.tsukuba.ac.jp/paper/InteractiveMeshFusion1999.pdf>.
- [76] E J Kansa. Multiquadrics—A scattered data approximation scheme with applications to computational fluid-dynamics—II solutions to parabolic, hyperbolic and elliptic partial differential equations. *Computers & Mathematics with Applications*, 19(8):147–161, 1990. doi:10.1016/0898-1221(90)90270-t.
- [77] B Kovács. Computing arbitrary Lagrangian Eulerian maps for evolving surfaces. 2016. arXiv:1612.01701.
- [78] B Kovács, B Li, C Lubich, and C A P Guerra. Convergence of finite elements on an evolving surface driven by diffusion on the surface. *Numerische Mathematik*, 137(3):643–689, 2017. doi:10.1007/s00211-017-0888-4.

- [79] D Lacitignola, B Bozzini, M Frittelli, and I Sgura. Turing pattern formation on the sphere for a morphochemical reaction-diffusion model for electrodeposition. *Communications in Nonlinear Science and Numerical Simulation*, 48:484–508, 2017. doi:10.1016/j.cnsns.2017.01.008.
- [80] D Lacitignola, B Bozzini, and I Sgura. Spatio-temporal organization in a morphochemical electrodeposition model: analysis and numerical simulation of spiral waves. *Acta Applicandae Mathematicae*, 132(1):377–389, 2014. doi:10.1007/s10440-014-9910-3.
- [81] D Lacitignola, B Bozzini, and I Sgura. Spatio-temporal organization in a morphochemical electrodeposition model: Hopf and Turing instabilities and their interplay. *Europ. J Appl. Math.*, 26(02):143–173, 2015. doi:10.1017/s0956792514000370.
- [82] O Lakkis, A Madzvamuse, and C Venkataraman. Implicit–explicit timestepping with finite element approximation of reaction–diffusion systems on evolving domains. *SIAM J Num. Anal.*, 51(4):2309–2330, 2013. doi:10.1137/120880112.
- [83] Alan J Laub. *Matrix analysis for scientists and engineers*. SIAM, 2005. doi:10.1137/1.9780898717907.
- [84] Q T Le Gia. Approximation of parabolic PDEs on spheres using spherical basis functions. *Advances in Computational Mathematics*, 22(4):377–397, 2005. doi:10.1007/s10444-003-3960-9.
- [85] J Lefèvre and J-F Mangin. A reaction-diffusion model of human brain development. *PLoS Computational Biology*, 6(4):e1000749, 2010. doi:10.1371/journal.pcbi.1000749.
- [86] H Li, Y Lin, R M Heath, M X Zhu, and Z Yang. Control of pollen tube tip growth by a rop GTPase–dependent pathway that leads to tip-localized calcium influx. *The Plant Cell*, 11(9):1731–1742, 1999. doi:10.1105/tpc.11.9.1731.
- [87] X Li and W Huang. Maximum principle for the finite element solution of time-dependent anisotropic diffusion problems. *Num. Meth. Part. Diff. Eqns.*, 29(6):1963–1985, 2013. doi:10.1002/num.21784.
- [88] C Lu, W Huang, and J Qiu. Maximum principle in linear finite element approximations of anisotropic diffusion–convection–reaction problems. *Numerische Mathematik*, 127(3):515–537, 2014. doi:10.1007/s00211-013-0595-8.
- [89] C Lubich and D Mansour. Variational discretization of wave equations on evolving surfaces. *Mathematics of Computation*, 84(292):513–542, 2015. doi:10.1090/s0025-5718-2014-02882-2.
- [90] C B Macdonald and S J Ruuth. The implicit closest point method for the numerical solution of partial differential equations on surfaces. *SIAM Journal on Scientific Computing*, 31(6):4330–4350, 2009. doi:10.1137/080740003.
- [91] A Madzvamuse. Time-stepping schemes for moving grid finite elements applied to reaction–diffusion systems on fixed and growing domains. *J Computat. Phys.*, 214(1):239–263, 2006. doi:10.1016/j.jcp.2005.09.012.

- [92] A Madzvamuse and R Barreira. Exhibiting cross-diffusion-induced patterns for reaction-diffusion systems on evolving domains and surfaces. *Physical Review E*, 90(4):043307, 2014. doi:10.1103/physreve.90.043307.
- [93] A Madzvamuse, E A Gaffney, and P K Maini. Stability analysis of non-autonomous reaction-diffusion systems: the effects of growing domains. *Journal of Mathematical Biology*, 61(1):133–164, 2010. doi:10.1007/s00285-009-0293-4.
- [94] A Madzvamuse, H S Ndakwo, and R Barreira. Cross-diffusion-driven instability for reaction-diffusion systems: analysis and simulations. *J Math. Biol.*, 70(4):709–743, 2015. doi:10.1007/s00285-014-0779-6.
- [95] A Madzvamuse, A J Wathen, and P K Maini. A moving grid finite element method applied to a model biological pattern generator. *Journal of Computational Physics*, 190(2):478–500, 2003. doi:10.1016/s0021-9991(03)00294-8.
- [96] M S McAfee and O Annunziata. Cross-diffusion in a colloid–polymer aqueous system. *Fluid Phase Equilibria*, 356:46–55, 2013. doi:10.1016/j.fluid.2013.07.014.
- [97] B Meyer. On the symmetries of spherical harmonics. *Can. J. Math*, 6:135–157, 1954. doi:10.4153/cjm-1954-016-2.
- [98] D Mora, G Rivera, and R Rodríguez. A virtual element method for the Steklov eigenvalue problem. *Mathematical Models and Methods in Applied Sciences*, 25(08):1421–1445, 2015. doi:10.1142/s0218202515500372.
- [99] T M Morton and M Neamtu. Error bounds for solving pseudodifferential equations on spheres by collocation with zonal kernels. *Journal of Approximation Theory*, 114(2):242–268, 2002. doi:10.1006/jath.2001.3642.
- [100] J D Murray. *Mathematical Biology. II Spatial Models and Biomedical Applications*. Springer-Verlag, New York, 2001. URL: <https://www.springer.com/us/book/9780387952284>.
- [101] Y-Y Nie and V Thomée. A lumped mass finite-element method with quadrature for a non-linear parabolic problem. *IMA J. Num. Anal.*, 5(4):371–396, 1985. doi:10.1093/imanum/5.4.371.
- [102] H F Nijhout, P K Maini, A Madzvamuse, A J Wathen, and T Sekimura. Pigmentation pattern formation in butterflies: experiments and models. *Comptes Rendus Biologies*, 326(8):717–727, 2003. doi:10.1016/j.crvi.2003.08.004.
- [103] L Nirenberg. A strong maximum principle for parabolic equations. *Communications on Pure and Applied Mathematics*, 6(2):167–177, 1953. doi:10.1002/cpa.3160060202.
- [104] F Nobile and L Formaggia. A stability analysis for the arbitrary Lagrangian Eulerian formulation with finite elements. *East-West Journal of Numerical Mathematics*, 7(EPFL-ARTICLE-176278):105–132, 1999. URL: https://infoscience.epfl.ch/record/176278/files/ale1_final.pdf.

- [105] R H Nochetto and C Verdi. Combined effect of explicit time-stepping and quadrature for curvature driven flows. *Numerische Mathematik*, 74(1):105–136, 1996. doi:10.1007/s002110050210.
- [106] S P Oliveira, A L Madureira, and F Valentin. Weighted quadrature rules for finite element methods. *Journal of Computational and Applied Mathematics*, 227(1):93–101, 2009. doi:10.1016/j.cam.2008.07.007.
- [107] P-O Persson. *Mesh generation for implicit geometries*. PhD thesis, Massachusetts Institute of Technology, 2004. URL: <https://dspace.mit.edu/bitstream/handle/1721.1/27866/60503856-MIT.pdf>.
- [108] P-O Persson and G Strang. A simple mesh generator in MATLAB. *SIAM review*, 46(2):329–345, 2004. doi:10.1137/s0036144503429121.
- [109] R G Plaza, F Sanchez-Garduno, P Padilla, R A Barrio, and P K Maini. The effect of growth and curvature on pattern formation. *Journal of Dynamics and Differential Equations*, 16(4):1093–1121, 2004. doi:10.1007/s10884-004-7834-8.
- [110] I Prigogine and R Lefever. Symmetry breaking instabilities in dissipative systems. II. *The J Chem. Phys.*, 48(4):1695–1700, 1968. doi:10.1063/1.1668896.
- [111] D Pruyne and A Bretscher. Polarization of cell growth in yeast. i. establishment and maintenance of polarity states. *J Cell Sci*, 113(3):365–375, 2000. URL: <http://jcs.biologists.org/content/joces/113/4/571.full.pdf?download=true>.
- [112] A Quarteroni and A Valli. *Numerical approximation of partial differential equations*, volume 23. Springer Science & Business Media, 2008. URL: <https://www.springer.com/us/book/9783540852674>.
- [113] K A Rahman, R Sudarsan, and H J Eberl. A mixed-culture biofilm model with cross-diffusion. *Bull. Math. Biol.*, 77(11):2086–2124, 2015. doi:10.1007/s11538-015-0117-1.
- [114] P-A Raviart. The use of numerical integration in finite element methods for solving parabolic equations. In J.J.H. Miller, editor, *Topics in Numerical Analysis*, pages 233–264, 1973. doi:10.1002/zamm.19750550226.
- [115] S J Ruuth and B Merriman. A simple embedding method for solving partial differential equations on surfaces. *Journal of Computational Physics*, 227(3):1943–1961, 2008. doi:10.1016/j.jcp.2007.10.009.
- [116] Y Saad. *Iterative methods for sparse linear systems*. SIAM, 2003. doi:10.1137/1.9780898718003.
- [117] P Sahlin and H Jönsson. A modeling study on how cell division affects properties of epithelial tissues under isotropic growth. *PloS one*, 5(7):e11750, 2010. doi:10.1371/journal.pone.0011750.
- [118] W E Schiesser. *The numerical method of lines: integration of partial differential equations*. Elsevier, 2012. doi:10.2307/2153182.

- [119] A Schmidt and K G Siebert. *ALBERTA - An adaptive hierarchical finite element toolbox*. Albert-Ludwigs Universität, Mathematik Fakultät, 2000. URL: http://www.alberta-fem.de/Downloads/Doc/landscape_doc.pdf.gz.
- [120] J Schnakenberg. Simple chemical reaction systems with limit cycle behaviour. *J Theoret. Biol.*, 81(3):389–400, 1979. doi:10.1016/0022-5193(79)90042-0.
- [121] V Shankar, G B Wright, R B Kirby, and A L Fogelson. A radial basis function (RBF) - finite difference (FD) for diffusion and reaction-diffusion equations on surfaces. *J Sci. Comp.*, 63:745–768, 2015. doi:10.1007/s10915-014-9914-1.
- [122] A Sharf, M Blumenkrants, A Shamir, and D Cohen-Or. Snappaste: an interactive technique for easy mesh composition. *The Visual Computer*, 22(9-11):835–844, 2006. doi:10.1007/s00371-006-0068-5.
- [123] J Smoller. *Shock waves and reaction-diffusion equations*. Springer Science & Business Media, New York, 1994. doi:10.1007/978-1-4684-0152-3.
- [124] M E Taylor. *Partial differential equations I: Basic Theory, 2nd Ed., Series: Applied Mathematical Sciences, Vol. 115*. Springer, 2011. doi:10.1007/978-1-4419-7055-8.
- [125] M E Taylor. *Partial differential equations III: Nonlinear Equations, 2nd Ed., Series: Applied Mathematical Sciences, Vol. 117*. Springer, 2011. doi:10.1007/978-1-4419-7049-7.
- [126] V Thomée. *Galerkin finite element methods for parabolic problems*. Springer-Verlag, Berlin Heidelberg, 1984. doi:10.1007/978-3-662-03359-3.
- [127] N Tuncer and A Madzvamuse. Projected finite elements for systems of reaction-diffusion equations on closed evolving spheroidal surfaces. *Communications in Computational Physics*, 21(3):718–747, 2017. doi:10.4208/cicp.oa-2016-0029.
- [128] A M Turing. The chemical basis of morphogenesis. *Philosophical Transactions of the Royal Society of London. Series B, Biological Sciences*, 237(641):37–72, 1952. doi:10.1016/s0092-8240(05)80008-4.
- [129] G Vacca. Virtual element methods for hyperbolic problems on polygonal meshes. *Computers & Mathematics with Applications*, 74(5):882–898, 2016. doi:10.1016/j.camwa.2016.04.029.
- [130] G Vacca and L Beirão da Veiga. Virtual element methods for parabolic problems on polygonal meshes. *Numerical Methods for Partial Differential Equations*, 31(6):2110–2134, 2015. doi:10.1002/num.21982.
- [131] V K Vanag. Waves and patterns in reaction-diffusion systems. Belousov-Zhabotinsky reaction in water-in-oil microemulsions. *Physics-Uspokhi*, 47(9):923–941, 2004. doi:10.1070/pu2004v047n09abeh001742.
- [132] V K Vanag and I R Epstein. Cross-diffusion and pattern formation in reaction-diffusion systems. *Phys. Chem. Chem. Phys.*, 11:897–912, 2009. doi:10.1039/B813825G.

- [133] C Varea, J L Aragón, and R A Barrio. Turing patterns on a sphere. *Phys. Rev. E*, 60(4):4588, 1999. doi:10.1103/physreve.60.4588.
- [134] C Venkataraman, O Lakkis, and A Madzvamuse. Global existence for semilinear reaction–diffusion systems on evolving domains. *Journal of Mathematical Biology*, 64(1-2):41–67, 2012. doi:10.1007/s00285-011-0404-x.
- [135] A Vergara, F Capuano, L Paduano, and R Sartorio. Lysozyme mutual diffusion in solutions crowded by poly(ethylene glycol). *Macromolecules*, 39(13):4500–4506, 2006. doi:10.1021/ma0605705.
- [136] F W Yang, C Venkataraman, V Styles, and A Madzvamuse. A robust and efficient adaptive multigrid solver for the optimal control of phase field formulations of geometric evolution laws. *Communications in Computational Physics*, 21(1):65–92, 2017. doi:10.4208/cicp.240715.080716a.